Xu, Feng (2006) *Transient natural convection in a differentially heated cavity with and without a fin on the sidewall.* PhD Thesis, James Cook University.

Transient natural convection in a differentially heated cavity with and without a fin on the sidewall

Thesis submitted by

Feng XU, B.Sc., M.Sc.

in September 2006

for the degree of Doctor of Philosophy

in the School of Engineering

James Cook University

Statement of access

I, the undersigned, author of this work, understand that James Cook University will make this thesis available for use within the University Library and, via the Australian Digital Theses network, for use elsewhere.

I understand that, as an unpublished work, a thesis has significant protection under the Copyright Act and;

I do not wish to place any further restriction on access to this work.

Signature | Date

Statement of sources declaration

I declare that this thesis is my own work and has not been submitted in any form for another degree or diploma at any university or other institution of tertiary education.

Information derived from the published or unpublished work of others has been acknowledged in the text and a list of references is given.

Signature Date

Electronic copy

I, the undersigned, the author of this work, declare that the electronic copy of this thesis provided to the James Cook University Library is an accurate copy of the print thesis submitted, within the limits of the technology available.

Signature   Date

Acknowledgements

Many people were involved in this thesis, and I gratefully appreciate their assistance here.

First of all, the help from my two supervisors, Prof. John Patterson and Dr. Chengwang Lei, is gigantic and is gratefully appreciated. In our regular weekly meetings, many good suggestions from them enabled me to take many shortcuts in my study, and many critical questions also made my thinking more logical. I have no doubt that these discussions will benefit my future research as well. Furthermore, marvelous ideas in many publications by them and co-authors enlightened me on my studies. Their direct and indirect help is acknowledged in depth.

I am also grateful to the technical staff in the workshop. In particular, Mr. Curt Arrosmith, Mr. Stuart Petersen and Mr. David Kauppila helped me enormously with my experiments.

It is a pleasure to thank Prof. Steve Armfield for kindly discussing some interesting results in my thesis.

I really appreciate the help from Ms. Helen Shorthouse who arranged and did many things for me when I attended those conferences.

Many thanks also go to my office mates: Mr. Suvash Saha and Dr. Li Shu. They gave me considerable assistance in many aspects when I quite desired.

I am pleased to thank the Australian government, James Cook University and the Australian Research Council, who sponsored all of my tuition and living cost as well as research cost during my study.

Finally, my thanks also go to my wife and daughter whose support allowed me to pay almost all of my attention to my study.

Abstract

Transient natural convection in a differentially heated cavity is a typical model of many flow processes in the ocean and atmosphere, and has extensive applications in industrial systems for which it is of significance to enhance or depress the heat transfer through the cavity. Therefore, transient natural convection with and without a fin on the sidewall of a differentially heated cavity is experimentally and numerically investigated in this thesis. One of the main objectives of this study is to investigate the effectiveness of the fin for the purpose of enhancing the heat transfer through the heated sidewall.

The shadowgraph technique is employed to visualize transient natural convection in a rectangular cavity, and thermistors are used to measure the time series of the temperatures at different locations adjacent to the hot sidewall. The numerical simulations in this thesis focus on the above experimental model. The SIMPLE scheme based on the finite volume method is adopted to solve the two dimensional governing equations using the commercial FLUENT software package.

The present flow visualizations demonstrate that the transition of the natural convection flow in the cavity from the start-up may be classified into three stages: an initial stage, a transitional stage and a quasi-steady stage. The initial stage includes the growth of the thermal boundary layer and the Leading Edge Effect. The correlation of the thickness of the thermal boundary layer with time obtained from the present experiments is consistent with that of a previous scaling analysis. In the transitional stage, the separation and trailing waves of the horizontal intrusion are observed and eventually a double-layer structure of the thermal boundary layer is visualized in shadowgraph images. The traveling waves of the inner layer in shadowgraph images become clear in the quasi-steady stage, and temperature measurements indicate that this is because the amplitude of the traveling waves in the thermal boundary layer increases as the stratification of the fluid in the cavity is enforced.

The corresponding numerical simulations validated by the experiments show that the bright strips of the double-layer structure in shadowgraph images correspond to the extrema of the second derivative of the temperature. In fact, the stratification of the fluid in the cavity results in a temperature distribution adjacent to the sidewall with a

maximum and a minimum of the second derivative of the temperature, which in turn leads to an opposing thermal diffusion directing to the temperature minimum.

The flow visualizations on transient natural convection with a fin on the sidewall of the cavity show that the transition from the start-up is likewise classified into three stages with variations from those without the fin, which also depend on the dimension of the fin. Two fins of different geometric parameters, one small square fin and the other large thin fin, are considered in the experiments. In the initial stage, a lower intrusion front appears underneath the fin and later bypasses the fin. The lower intrusion front bypassing the small square fin reattaches to the downstream thermal boundary layer, but the one bypassing the large thin fin moves upwards and strikes the intrusion under the ceiling. Although there are some variations of the transition of the thermal boundary layer flows between the cases with and without a fin, the double-layer structure of the thermal boundary layer appears in all cases in the quasi-steady stage. In particular, the presence of the large thin fin may cause the separation and vortex shedding of the thermal flow around the fin, which trigger the instability of the downstream thermal boundary layer.

The numerical simulations of transient natural convection with a fin on the sidewall of the cavity are consistent with the above-mentioned experimental results. The numerical results confirm that the transient strong convection flows such as the lower intrusion front and the oscillations of the thermal flow around the fin may enhance the heat transfer through the sidewall. Furthermore, the numerical results demonstrate that the enhancement of the heat transfer is dependent on the parameters of the fin, such as the dimension and position of the fin and the number of fins, with a maximum enhancement of 33% observed in the present simulations.

In summary, both numerical and experimental results show that the fin may significantly change the transient natural convection flows and improve the heat transfer through the cavity if properly configured. This research has great potential for industrial applications in which the enhancement of heat transfer is desirable.

Table of contents

List of figures

List of tables

Nomenclature

A	aspect ratio of the cavity
a, b	coefficients of the discretized equation (3.25)
$\vec{A}_e$	surface area vector enclosing the control volume
c_p	specific heat capacity at certain pressure
D	depth of the cavity (in the z-direction)
f	frequency of oscillations
$F(\phi)$	function of ϕ
F_i	body force
F_x, F_y, F_z	components of body force (in the x-, y- and z-directions)
Gr	Grashof number
g	acceleration due to gravity
H	height of the cavity
h	heat transfer coefficient of the sidewall
H_{fin}	heat transfer rate of the hot sidewall with a fin
H_{nofin}	heat transfer rate of the hot sidewall without a fin
$\hat{H}$	normalized difference of the heat transfer rate of the hot sidewall between the cases with and without a fin
I_0	illumination intensity entering the object
I_e	light intensity exiting the object
I_s	light intensity on the screen
k	thermal conductivity
L	width of the cavity
l	distance between the object and screen
n	refractive index
Nu	Nusselt number
Nu_{cen}	Nusselt number on the vertical centerline of the cavity
p	pressure
Pr	Prandtl number

q'	local heat flux of the sidewall
Ra	Rayleigh number
R_ϕ	residual of ϕ
S	temperature gradient in the center of the cavity
s_0, s_1	series number of the control volume
S_ϕ	sources of ϕ in the general transport equation (3.15)
T	temperature
t	time
T_0	temperature at the initial time
T_4, T_5	temperature readings of Thermistors 4 and 5
T_c	temperature of the cold sidewall
T_h	temperature of the hot sidewall
u, v	velocity components
V	volume of the control volume (or area of the control surface for 2D)
$\vec{v}$	velocity vector
v_{max}	maximum of y-direction velocity in the thermal boundary layer
x, y, z	coordinates
x_{ex}, y_{ex}, z_{ex}	coordinates of the light ray exiting the object
x_{in}, y_{in}, z_{in}	coordinates of the light ray entering the object
x_s, y_s	coordinates of the light ray on the screen

Greek symbol

α_r	under-relaxation factor
β	thermal expansion coefficient
ΔI	variation of the light intensity
$\Delta\vec{s}$	displacement vector from the upstream surface centroid to the edge
ΔT	temperature difference between hot and cold sidewalls
Δt	time step
Δ_x	displacement in the x-direction
Δ_y	displacement in the y-direction
$\Delta\phi$	variation of ϕ
δ_T	thickness of the thermal boundary layer
ϕ	quantity in the general transport equation (3.15)

$\overline{\phi}_e$	average of ϕ on the edges
ϕ_{old}	value of ϕ in the previous iteration
Γ_ϕ	diffusion coefficient for ϕ in the general transport equation (3.15)
κ	thermal diffusivity
μ	dynamitic viscosity
ν	kinematic viscosity
ρ	density
ρ_0	density at the initial time
τ	time from the start-up to the steady state
nb	number of edges enclosing the control volume

Subscript:

e	edge of the control volume
i, j	tensor indices
n	normal to the edge
nb	number of edges enclosing the control volume

Superscript:

n	time level

1 Introduction

1.1 Problem description

In warm summers, strong radiation from the sun heats the surface of a bitumen road so that the surface temperature is much higher than that of the air above. If we gaze at the far end of the road, it is often possible to see dark pixilated strips. This is actually a result of heated air moving away from the heated surface, and is an example of natural convection. Natural convection is defined as a flow driven by a density difference (or buoyancy), in contrast to other forced flows where a pressure difference or other body forces drive the flow. Such a density difference may result from a temperature difference, a concentration difference of chemical species in fluid or multiple phases of fluid.

Natural convection is present everywhere in nature. Present knowledge indicates that a large temperature difference between the polar and equatorial oceans may drive a global ocean circulation. Similarly, a density difference between the fresh and oceanic waters at an estuary, due to a salinity difference of water, may also result in a large-scale natural convection mixing. In fact, such thermohaline flows exist almost everywhere in the oceans.

Although temperature, concentration or phase can all cause a density variation of fluid and in turn drive natural convection, a temperature difference is apparently the most common factor. In particular for the fluid adjacent to a thermal boundary, which has a temperature difference from the ambient fluid, natural convection is easily induced. For instance, in contrast to the above-mentioned heated road surface, an icy stone cooled for a whole night may also drive the ambient air downwards along its surface. Likewise, natural convection often occurs around an iceberg, due to a temperature difference between the ice surface and the ambient oceanic water. For cases in which the external flow in an open environment is concerned, instead of natural convection the synonymous term, ‘free convection’, is often employed in some studies.

Natural convection adjacent to a thermal boundary is often idealized as a thermal infinite or semi-infinite flat plate flow. If the heated flat plate is horizontally placed, a typical natural convection, Rayleigh-Benard convection (see Bodenschatz et al. 2000), may arise. Idealized natural convection models adjacent to a horizontal or vertical thermal flat plate can represent many natural flow phenomena in some sense, and also are extensively applied in industry. For example, as the performance of the electronic chip is significantly improved, its power is largely increased and thus a greater amount of heat dissipation is generated. The heat output results in a temperature difference between the ambient fluid (usually air) and the chip, which can likewise drive natural convection.

Since boundaries are finite in both nature and industry, the application of the assumption of infinite and semi-infinite flat plates is limited. One needs to consider the presence of other boundaries in many real situations. Therefore, another natural convection model has been developed in which natural convection is completely enclosed by all boundaries – a cavity. Such a model is called the interior problem, in contrast to the exterior problem of the semi-infinite or infinite flat plate flow. Natural convection in a cavity, likewise, may be classified into two categories: the below-heating and side-heating. Both categories of natural convection are commonly present in industry, such as solar collectors, double glass windows, nuclear reactors and many other applications.

In studies of natural convection in a cavity, heat transfer is an essential component. Enhancing or depressing the heat transfer through the cavity is of significance in many industrial applications, and thus so far a variety of active and passive approaches have been employed in order to achieve different objectives. For example, a fin, placed on a thermal sidewall, a typical passive way, may be used to enhance or depress the heat transfer through the thermal sidewall by changing its shape or material. For the purpose of examining the effect of the fin on natural convection in a cavity, in this thesis experiments and simulations of transient natural convection in a rectangular differentially heated cavity with and without a fin on the sidewall are performed.

Figure 1.1 sketches a cavity with an aspect ratio (*A* height/length) of 0.24 and a thin fin on the sidewall. In the cavity (unless specified in this thesis, cavity hereinafter denotes a rectangular differentially heated cavity), one sidewall (on the left) is cooled to a lower temperature T_c and the other (with a fin) heated to a higher temperature T_h. The temperature difference between the heated wall and the average temperature of the fluid is equal to that between the cooled wall and the average temperature. In the corresponding numerical simulations, the top, bottom and fin are assumed insulated, and the initial fluid is treated as motionless and isothermal. However, these assumptions

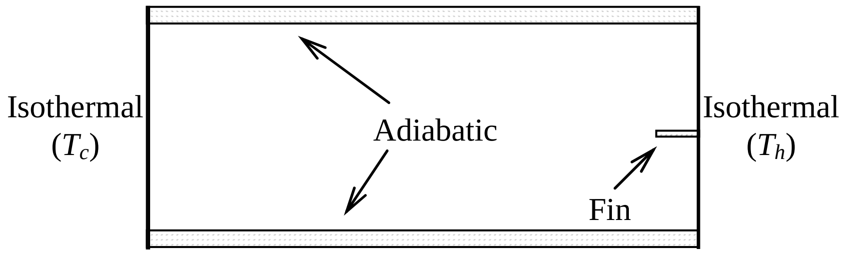

Figure 1.1 Schematic of the model cavity

are only an approximation of the experiment. A more detailed description of the experimental model will be discussed in Chapter 2.

It is worth noting that the emphasis in this thesis is placed on the transition from a stationary, isothermal ambient fluid following sudden heating and cooling of the sidewalls to the quasi-steady state, irrespective of the presence or otherwise of a fin on the sidewall.

1.2 Literature review

Natural convection adjacent to a thermal boundary is one of the major features of the dynamics of the oceans and the atmosphere and is also important in many industrial processes, as described in section 1.1. For over half a century the quest for the understanding of natural convection has motivated numerous experimental, numerical and theoretical studies. Naturally, the studies of natural convection in a differentially heated cavity, due to its simple geometrical shape and extensive applications, became the initial impetus for simulating the previously mentioned flow phenomena. Considerable attention in the last few decades has been paid to the transient flows following the sudden heating and cooling of the sidewalls. These studies have revealed important mechanisms of the complex transient flows and have provided insights into understanding similar flows adjacent to thermal boundaries in nature. Since these complex flows are determined by both linear and nonlinear effects, the elucidation of the flow processes becomes a challenging problem in physics and fluid mechanics.

An important aspect of studies of natural convection in the cavity is on heat transfer, and enhancement and depression of the heat transfer through the cavity may be relevant to a variety of industrial systems. Accordingly, the focus of this thesis is put on the impact of a fin on the sidewall on the flow and heat transfer, and the following literature review is organized in the following sequence: natural convection without a fin, natural convection with a single and multiple fins, and summaries.

In the following subsections, unless specified, the review of transient natural convection is basically based on those in the shallow cavity (i.e. $A \leq 1$) at Rayleigh numbers not larger than the critical value at which turbulence is present. Furthermore, since the working fluid in this investigation is water, those previous investigations, which are aimed at transient natural convection with the larger Prandtl number (e.g. >1), are mainly reviewed in the following sections. However, some of the others based on the smaller Prandtl number (<1, e.g. transient natural convection in an air-filled cavity) are also involved in the following subsections since they have transient features similar to those with the larger Prandtl number.

1.2.1 Natural convection without a fin

Studies of natural convection in a differentially heated cavity date back to 1950s, and a few reviews relevant to natural convection in a differentially heated cavity (see e.g. Catton 1978; Ostrach 1988; Hyun 1994) were reported. The focus of this review is placed on the more recent development of studies of transient natural convection in a cavity, and a few earlier representative studies are also involved. Furthermore, although this study is on transient natural convection in a differentially heated cavity, a few representative studies of natural convection adjacent to a vertical semi-infinite flat plate, due to the inherent relationship between the two types of natural convection problems, are also reviewed.

It is well known that, in spatially extended systems, convection occurs when a sidewall of a cavity containing an initially homogenous motionless fluid is suddenly heated. The spatial and temporal variations of the convection structures are often referred to as a variety of physical processes. Previous studies (see e.g. Batchelor 1954) demonstrated that these flows can be characterized by three important dimensionless parameters, the Rayleigh number (Ra), the Prandtl number (Pr), and the aspect ratio of the cavity (A), defined as follows,

$$Ra = \frac{\beta g \Delta T H^3}{\nu\kappa}, \tag{1.1}$$

$$Pr = \frac{\nu}{\kappa}, \tag{1.2}$$

$$A = \frac{H}{L}. \tag{1.3}$$

In some studies, the Grashof number (*Gr*) is also employed instead of the Rayleigh number, defined by

$$Gr = \frac{\beta g \Delta T H^3}{\nu^2}. \tag{1.4}$$

A scale analysis by Patterson and Imberger (1980) indicated that, following the sudden heating of the sidewall, the simplest flow which may occur in a cavity is characterized by the natural convection boundary layer flow adjacent to the vertical sidewall, the intrusion flow near the horizontal wall and the complex flow developed subsequently. This section will summarize the features and formation mechanisms of these flows, including the leading edge effect (LEE) and instability of the vertical boundary layer flow, the horizontal intrusion and subsequent development, the steady flow, and turbulent natural convection when the Rayleigh number is larger than the critical value.

1.2.1.1 LEE of the vertical boundary layer flow

For a suddenly heated vertical surface (which could be either a flat plate or a sidewall of a cavity), the early transient response was considered as one-dimensional (1D) by Illingworth (1950), and the heat transfer from the surface to the fluid is dominated by conduction. This implies that a transient temperature field adjacent to the surface is invariant along the streamwise direction, thus generating a corresponding buoyancy force and velocity distribution. A closed-form solution for such transient velocity and temperature distributions was obtained by Illingworth (1950).

In the initial stage, under the dominance of conduction, the following scales for the thickness and velocity of the vertical thermal boundary layer may be employed to represent the transient flow (refer to Patterson & Imberger 1980),

$$\delta_T \sim \sqrt{\kappa t}, \tag{1.5}$$

$$v \sim \frac{g\beta \Delta T t}{Pr}. \tag{1.6}$$

The thickness and velocity increase with the passage of time. When the heat conducted into this layer from the heated wall balances that convected away, a time scale for the steady state of the vertical thermal boundary layer flow can be obtained, as follows,

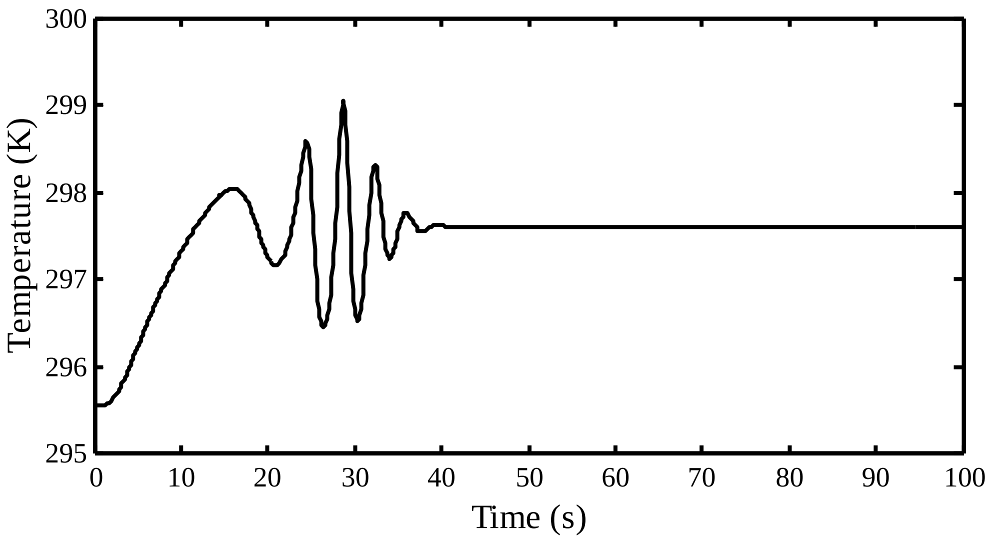

Figure 1.2 Temperature vs time at the point (0.498 m, 0.09 m) at $Ra = 3.8 \times 10^9$

$$\tau \sim \frac{H^2}{(\kappa Ra^{1/2})}. \tag{1.7}$$

At the steady state, the thickness and velocity scales are given by

$$\delta_T \sim \frac{H}{Ra^{1/4}}, \tag{1.8}$$

$$v \sim \frac{\kappa Ra^{1/2}}{H}. \tag{1.9}$$

It is worth noting that the term "steady state" here means a balance between conduction and convection in the initial stage. This set of scales (refer to Patterson and Imberger 1980 for details) portrays the initial growth of the transient flow.

The vertical thermal boundary layer flow approaches a steady state, with an overshoot of its thickness (see e.g. Xu et al. 2005c) and temperature (see e.g. Patterson et al. 2002) followed by a sequence of disturbances (also see Figure 1.2). The overshoot and disturbances (traveling waves) comprise the LEE, which originates from the leading edge of the sidewall or semi-infinite flat plate, and propagates downstream (refer to Gebhart 1988). The studies (see e.g. Gebhart 1988; Patterson *et al.*,2002) indicated that the passage of the LEE at a particular point was the mechanism by which the boundary layer was converted approximately from the unsteady one dimensional form to a steady two dimensional form. When the disturbances (traveling waves) of the LEE propagate and amplify far downstream, they become more complicated and thus also more interesting. Gebhart (1988) indicated that the LEE region was a combination of a transient and entrained upstream 2D flow and a 1D downstream flow. The LEE is one of the noticeable features in the initial development of the vertical thermal boundary layer flow.

An important aspect of describing the LEE propagation is to predict accurately its arrival time at a particular location. In order to obtain an analytical solution for the arrival time, Goldstein and Briggs (1964) simplified the momentum and energy equations, and kept only the unsteady, viscous, and horizontal conduction terms. By using the Laplace transform, a 1D analytical solution for the vertical velocity was obtained, as follows (for $Pr \neq 1$)

$$v(x,t) = \frac{4g\beta\Delta Tt}{1-Pr}\left(i^2 erfc\frac{x}{2\sqrt{\kappa t}} - i^2 erfc\frac{x}{2\sqrt{\nu t}}\right), \tag{1.10}$$

where i^2erfc is the second integral of the complementary error function (see Appendix).

Based on Equation (1.10), the LEE propagation distance at a particular time may be estimated by adopting the maximum value of the velocity integration with respective to time (see Goldstein & Briggs 1964). However, this prediction lags behind the experimental measurements (see e.g. Mahajan & Gebhart 1978; Joshi & Gebhart 1987). Therefore, Brown and Riley (1973) adopted another method of estimating the LEE propagation distance; that is, they replaced the maximum value of the velocity integration with the integration of the maximum velocity. Although the latter method improves the estimation of the LEE propagation speed in comparison with the former by Goldstein and Briggs (1964), the deviation from the experimental measurements is still significant (see Patterson et al. 2002). Mahajan and Gebhart (1978) suspected that such a big discrepancy between the prediction and the experimental measurement could be caused by the neglected pressure and convection terms in the analytical solution. In general, the 1D analytical solution cannot accurately represent the LEE.

Armfield and Patterson (1992) demonstrated that the speed of the unstable traveling waves in the vertical natural convection boundary layer, based on a linear stability analysis, is consistent with that of the LEE propagation. Therefore, the accuracy of predicting the LEE propagation is significantly improved, and this theoretical prediction is also supported by the experiments (refer to Patterson et al. 2002). This implies that the traveling waves present in the LEE region are a result of the thermal boundary layer instability. Further discussion, based on the numerical simulation by Armfield and Patterson (2000), suggests that the LEE propagation could be based on two speeds, a faster speed and a slower speed (the traveling wave speed).

Evidently, this speculation of the LEE propagation, based on two speeds, needs further validation, in particular on the mechanism.

1.2.1.2 Instability of the vertical thermal boundary layer flow

It is a typical unstable behavior that the traveling waves, associated with the LEE, amplify when they propagate downstream. Previous studies (see e.g. Gebhart 1988; Armfield & Patterson 1992) demonstrated that such an unstable behavior is dependent on the Rayleigh number and the Prantdl number. Since the unstable growth may ultimately result in turbulence (see e.g. Elder 1965b), the analysis of the unstable flow is an important aspect of studies of natural convection.

Although it is not straightforward to investigate experimentally the initial unstable growth, experimental observations can provide us with a clear description for the subsequent development of the instability, and in particular the transition to turbulence. Experimental results by Jaluria and Benjamin (1973) demonstrated that an initially small perturbation (e.g. a controlled 2D perturbation introduced into the thermal boundary layer by using a vibrating ribbon) may be amplified, initially as a sinusoidal disturbance, and then the amplified disturbance propagates along a plate heated with a uniform heat flux. A side view of the thermal boundary layer flow (see e.g. Szewczyk 1962) indicates that a double-row vortex is present in such an unstable boundary layer flow. Spanwise flow patterns visualized by Inagaki and Komori (1995) showed W-shaped 3D unstable structures and horseshoe-shaped low-temperature patterns. More detailed velocity and temperature fields were also measured by Jaluria and Benjamin (1974). It is worth noting that the vertical heated plate in the above-mentioned experiments is isoflux.

Since the experimental observation of the initial growth of small perturbations is difficult (primarily because of their small amplitudes), numerous earlier studies of instability were based on theoretical analyses (see e.g. Plapp 1957). For the purpose of understanding the instability of the vertical thermal boundary layer, three stability analysis methods (i.e. solving Orr-Sommerfeld equations or parabolized stability equations as well as direct stability analysis), which are extensively applied in studies of natural convection, are discussed in the following section together with the review of their results.

A linear stability theory was first presented by Plapp (1957); that is, small amplitude perturbation functions (stream function and temperature perturbations) are introduced into the Navier-Stokes equations which are then linearised, and thus a coupled set of stability equations (eigenvalue equations for the wavenumber and the phase speed of perturbations), similar to the Orr-Sommerfeld equations, are derived. There are two regular methods to numerically solve the eigenvalue equations. The first method is based on outward integration of the equations using a first-order Euler scheme along with an orthonormalization procedure (see Davey 1973; Daniels & Patterson 1997) to maintain accuracy. The asymptotic form of the outer boundary conditions is used to speed up convergence. The second method uses a fourth-order Runge-Kutta scheme to integrate the equations inwards from the wall to the outer boundary (Daniels & Patterson 1997, 2001). Results from these two procedures are found to be in excellent agreement for the primary mode of instability.

Based on the results of a linear stability analysis, Szewczyk (1962) suggested that the outer vortices in a double-row vortex control the thermal boundary layer flow development and transfer their effect into the more stable inner layer near the surface, provoking its instability. The results of the linear stability analysis also demonstrated that the amplitude distributions of the triple independent eigenmodes are present (see e.g. Hieber & Gebhart 1971). These have been experimentally supported by Yan and Zhang (2002). The basic characteristics of instability, such as its spectral components, wavelength and velocity, the location of its critical layer, and the growth rates of its temperature and velocity fluctuations, were also discussed by Yan and Zhang (2003).

In fact, a principal task of the linear stability analysis is to seek the neutral stability curves in the plane of the Rayleigh number (or Grashof number in some studies) and the wave frequency (see e.g. Knowles & Gebhart 1968). The previous results (see e.g. Gebhart 1973) showed that the neutral stability curve of the velocity fluctuation for the case of an isoflux vertical plate has a nose shape, but, for the temperature fluctuation, a ring-like region appears at a lower Rayleigh number before the nose-shaped main portion of the neutral stability curve. A detailed discussion of the neutral stability curves may be found in Gebhart (1973) and Gebhart and Mahajan (1982). Furthermore, the achievements of the linear stability analysis of general boundary layers were summarized by Mack (1984). His work, covering almost all aspects of the boundary-layer stability theory, is of significance for studying the natural convection boundary layer flow, although it has broader applications.

Linear stability analysis for the vertical natural convection boundary layer by Plapp (1957) is based on the approximation of parallel base-flow, and thus neglects the actual non-parallel properties of the boundary layer. For the purpose of overcoming the limitation of the parallel base-flow assumption, a non-parallel formulation by Bertolotti et al. (1992) has been applied to general boundary layers. This stability analysis method formulates parabolized stability equations (hereinafter referred to as PSE), assuming that the perturbation eigenfunctions have the same slow variation in the downstream direction as the base flow (see e.g. Herbert 1997). The PSE method, in some sense, may model the non-parallel effects and can be extended to nonlinear and three-dimensional effects (Brooker et al. 1997). The PSE equations may be solved by a marching procedure, and are valid for convectively unstable flows. Brooker et al. (1997) used the PSE method to analyze the stability of natural convection boundary layers, based on a non-parallel base flow. Their solutions, likewise, demonstrated that the spatial growth rate and wavenumber are highly dependent on the transverse location for a 2D thermal boundary layer flow and the flow parameters under consideration. The local solution of the PSE may accurately predict wave properties observed in direct numerical simulations. However, the conventional parallel stability analysis overpredicts the spatial amplification and the wavenumber. Moreover, discrepancies between the predictions by a linear stability analysis based on a quasi-stationary assumption and those by the PSE method based on non-stationary assumptions have been revealed by Brooker et al. (2000). Severin and Herwig (2001) discussed the variation between the parallel and nonparallel stability analyses using the PSE method and also developed an extended version of the Orr-Sommerfeld equation (EOSE) in order to deal with the effects of variable fluid properties.

Numerical integration of the momentum and energy equations may be used to validate various stability analyses by introducing perturbations at the upstream end of the boundary layer flow or in the boundary conditions. This analysis method, the so-called direct stability analysis (DSA) developed by Fasel and Konzelmann (1990), can reveal instability properties by examining the evolution of numerical solutions (which removes the need to solve the stability equations separately). Direct stability analysis has been applied to natural convection in a cavity (see e.g. Armfield & Janssen 1996; Janssen & Armfield 1996; Lei & Patterson 2003). In the DSA, two categories of perturbations are usually employed: perturbations of a uniform amplitude and randomly distributed wavenumbers, and those of a single wavenumber. In the first case, the amplitude spectrum of the resulting signal may describe the amplification properties of the flow as a function of wavenumber. In the second case, the amplitude of the surviving signals at the input wavenumber gives the amplification at that particular wavenumber, and a spectrum may be constructed from a range of input wavenumbers. The critical condition, at which the growth rate is greater than zero, may be determined by examining the amplitudes of the signals as a function of wavenumber. As natural convection in a cavity exhibits much more complex features than those adjacent to the semi-infinite flat plate, the DSA method is evidently more suitable for studying the stability of natural convection in a cavity.

It has been demonstrated by DSA that small perturbations to the wall boundary conditions can trigger an instability, and oscillatory behaviour in the boundary layer can be observed well before the transition to a steady 2D flow begins (see e.g. Brooker et al. 2000; Patterson et al 2002). Janssen and Armfield (1996) demonstrated that the initial evolution of artificial disturbances in a square differentially heated cavity is governed by linear effects, and may be used to accurately predict the frequency of bifurcation. They also found that the convective instability sets in at a much smaller Rayleigh number than those at which the absolute instability occurs. For small Prandtl numbers (<2), the unstable waves could be shear-driven, and a single frequency dominates in the flow after the bifurcation. For larger Prandtl numbers, the unstable waves are buoyancy-driven and no dominant single frequency is observed in the flow after the bifurcation.

1.2.1.3 Horizontal intrusion and subsequent development

The foregoing review of the development of the vertical natural convection boundary layer in the initial stage does not distinguish the natural convection flow adjacent to a vertical flat plate and a sidewall of a cavity. This is because the initial flow exhibits similar features (see e.g. Armfield & Patterson 1992) for the two categories of flows. However, as the flow develops further, the presence of other boundaries can make the subsequent flow in a cavity evidently different from that adjacent to the flat plate.

For natural convection in a differentially heated cavity, the presence of a horizontal ceiling forces a horizontal intrusion into the cavity (Patterson & Imberger 1980). The horizontal intrusion is an important physical process in a differentially heated cavity with a noticeable behavior – separation; that is, the intrusion may detach from the ceiling rather than moving smoothly across the cavity. This flow structure was initially regarded as a result of an internal hydraulic jump (Ivey 1984; Paolucci & Chenoweth 1989). However, this speculation was questioned by Patterson and Armfield (1990) on the basis that the densimetric Froude number for the intrusion flow was small.

A detailed discussion of the corner flow field by Ravi et al. (1994) also refuted the occurrence of the internal hydraulic jump, and suggested that the separation originated from thermal effects; that is, the relatively colder fluid detached from the ceiling under the action of gravity when it reached the top corner. However, the attribution of the flow separation to thermal effects is also questionable. As indicated by Schöpf and Patterson (1995), the fluid in the cavity is not stratified in the early intrusion stage, and thus there is no colder part of the intrusion fluid near the hot top corner.

From shadowgraph observations, Xu et al. (2005c) suggested that the entrainment development of the vertical boundary layer could be a mechanism to produce separation; that is, since the fluid beneath the intrusion is entrained by the vertical thermal boundary layer, the local pressure there becomes lower, compared with the pressure in the intrusion layer. If the vertical pressure gradient is sufficiently large to overcome the upward buoyancy force, the horizontal intrusion will separate from the ceiling. This was also supported by numerical results by Xu et al. (2005a).

Separation is usually followed by a series of trailing waves (see e.g. Ivey, 1984; Patterson & Armfield, 1990). Once the separated intrusion driven by the vertical pressure gradient deviates far from the ceiling, the vertical pressure gradient effect becomes weaker, and the buoyancy force forces the intrusion flow to reattach to the ceiling. The interaction between these two competing forces results in a set of trailing waves, which are clearly visible in shadowgraph images (see e.g. Schöpf & Patterson 1995, 1996; Xu et al. 2005c).

The horizontal intrusion is actually a gravity flow. Besides trailing waves, convection rolls in the spanwise cross section have been experimentally observed by Schöpf and Stiller (1997). This thermal instability is typical of Rayleigh-Benard convection. Stiller and Schöpf (1997) indicated that this is a result of a nonlinear velocity profile closer to the top or bottom walls, due to the viscosity. This nonlinear velocity profile (the closer to the wall, the smaller the velocity) of the horizontal intrusion may result in a nonlinear temperature profile in which the higher temperature is below and the lower temperature closer to the top wall. As a result, if this temperature difference of the fluid in the vicinity of the top or bottom wall exceeds a certain critical value, Rayleigh-Benard convection occurs (also refer to Stiller et al. 1998).

A scaling analysis by Patterson and Imberger (1980) indicated that, if the Rayleigh number is large enough ($Ra > Pr^{16}/A^{12}$), the inertial intrusion may reach another end wall and is not viscously damped. The striking of the intrusion can cause distortion and instability of the vertical thermal boundary layer at the opposite side (see e.g. Schladow 1990). Following the LEE perturbations, such instabilities, induced by the striking of the intrusion, are usually called the second set of the traveling waves of the vertical thermal boundary layer (see e.g. Armfield & Patterson 1991).

Since entrainment at the opposite wall cannot fully carry away the intrusion fluid, ‘piling up’ commences in the corner (see e.g. Patterson & Imberger 1980). A reverse flow, relative to the vertical thermal boundary layer flow adjacent to the opposite wall, arises, and induces a circulation in the corner. When the reverse flow moves away from the opposite corner, it may split the intrusion into two streams; that is, an upper warmer fluid layer moves along the horizontal wall and a lower fluid layer colder than the upper one discharges into the core region (see e.g. Patterson & Armfield 1990; Xu et al. 2004). As time increases, the split appoint moves back towards the emergent corner, which may be observed by showing a time series of a central Nusselt number (on the vertical centerline of the cavity), defined as follows (Schladow 1990),

$$Nu_{cen} = \int_0^H \frac{\lfloor k(\partial T / \partial x) - \rho c_p T u \rfloor}{2k\Delta T / H} dy. \tag{1.11}$$

The time series of a central Nusselt number is oscillatory, and the amplitude of oscillation significantly reduces with the passage of time. Armfield and Patterson (1991) speculated that it could result from a single perturbation rather than a continuous energy input. As there are no distinct oscillatory signals in the temperature time series, the oscillation of the Nusselt number is considered as primarily an oscillating advection effect. This has been validated by the presence of oscillatory signals in the horizontal velocity time series (Armfield & Patterson 1991).

The numerical simulation of a shallow cavity (usually $A \leq 1$; here $A = 0.24$) by Xu et al. (2004) gives consistent results with those for the square cavity. In the first period of the oscillation, the reverse flow moves across the whole cavity but the oscillation decays more rapidly (also see Chapter 5). At this time, the fluid in the cavity was considered as a three-layer system, i.e. an isothermal core with hot and cold intrusions (see e.g. Armfield & Patterson 1991). Evidently, this description is not sufficiently accurate. Due to the presence of the reverse flow, the horizontal intrusion is split into two streams, and thus the fluid should be considered as a seven-layer system, i.e. an isothermal core with a three-layer hot intrusion and a three-layer cold intrusion including a reverse flow and two split streams of each intrusion (refer to Chapter 5 for more details).

The transition of the vertical thermal boundary layer flow from the impact of the incoming intrusion to the steady state (or the quasi-steady state for sufficiently high Rayleigh numbers) has been visualized by Schöpf and Patterson (1996) and Xu et al. (2005c), using shadowgraph methods. A double-layer structure of the vertical thermal boundary layer was found if the Rayleigh number is large enough (Xu et al. 2005c). The corresponding numerical simulation by Xu et al. (2005a) demonstrated that the heat transfer in the double-layer structure is complex. In fact, there are few studies concerning the development of the flow after the intrusion strikes the far end wall. However, the transition from the impact of the incoming intrusion to the steady state is important because this process is associated with the stratification of the fluid in the core region. Accordingly, the study of the flow development during this stage will be a focus of this thesis.

1.2.1.4 Steady flow

As time elapses, the flow in a suddenly differentially heated cavity gradually approaches a steady state. Since the steady natural convection is of significance for extensive applications, most of the earlier studies were devoted to it. For the purpose of reviewing those relevant achievements, it is useful to date back to the earlier time of research on this topic.

One of the earliest studies of steady natural convection in a cavity was performed by Bachelor (1954) based on a prototype of a double-glass window. Bachelor (1954) found that, for a small Rayleigh number, conduction dominated the heat transfer through the cavity, and suggested the fluid in the core was isothermal. Evidently, the suggestion of an isothermal core is inappropriate. A later interferometer observation by Eckert and Carlson (1961) demonstrated that a stratified fluid is present in the core but there is an isothermal core only for a small distance between two sidewalls of the cavity. Based on the stratified core, the boundary layer and core solutions of natural convection dominated by convection were obtained by Gill (1966). The entrainment into the lower part of the warmer layer brings fluid from the cooler layer opposite to the warmer layer; that is, the flow across the core brings colder fluid into the lower half and warmer fluid into the upper half, thus leading to a stable vertical temperature gradient in the core. This vertical temperature gradient is also an important factor in determining the structure of the vertical thermal boundary layers (see Xu et al. 2005a).

The experimental observations of a slender cavity (with a large aspect ratio; that is, H is much larger than L) demonstrated that, for the case of $Ra \approx 10^9$ and $\Pr \approx 1000$, if $A > 50$, a weak stable unicellular circulation is generated (Elder 1965a). As the aspect ratio decreases but $A > 20$, a uniform vertical temperature gradient is established in the core, and the vertical boundary layer flow is similar to that near an isolated, heated, vertical plate; If $A < 20$ but $A > 10$, a steady secondary flow is generated in the core, in which a so-called ‘cats-eye’ i.e. multi cellular, pattern of streamlines may be observed.

Most of the earlier studies were devoted to natural convection in such a slender cavity. However, since flows in an enclosed shallow cavity can provide some insights into the dispersion of pollutants and heat waste in estuaries, air flows in a room and buoyancy flows in other industrial applications, the steady flow in a shallow cavity has been increasingly investigated using asymptotic, numerical and experimental methods (see e.g. Cormack et al. 1974a, b; Imberger 1974). A benchmark numerical solution for the air natural convection in a square cavity ($10^3 \leq \mathrm{Ra} \leq 10^6$) was reported by De Vahl Davis (1983). It has been found that, as Ra increases, the isotherms in the core changes from vertical to horizontal, and the flow field also changes from one cell in the core to multiple cells with two distinct vertical boundary layers.

Studies demonstrated that, if Ra becomes sufficiently large at $Pr < 1$ (e.g. air), natural convection displays a transitional flow (from laminar to turbulent flows, see e.g. Paolucci & Chenoweth 1989; Le Quere 1990; Henkes 1990). In such a transitional regime, a temperature time series taken in the vertical thermal boundary layer flow displays oscillations in the quasi-steady stage (here replacing the steady stage because the flow is periodic). The numerical results by Le Quere and Masud (1998) indicated that, for an air-filled square cavity, the critical Rayleigh number from the steady laminar flow to the oscillation flow is approximately 1.82×10^8. As Ra further increases, the oscillations become much more complex. Unfortunately, similar numerical results for a water-filled square cavity ($Pr \approx 7$) have not been obtained.

Shadowgraph observations by Schöpf and Patterson (1996) and Xu et al. (2005c) showed the presence of unstable traveling waves (which have higher frequencies than those of the air-filled cavity) in the vertical thermal boundary layer flow in the water-filled shallow cavity. Those traveling waves are considered as a result of convective instability of the vertical thermal boundary layer triggered by perturbations in the experiments.

In summary, for the laminar or transitional regime, the transition of natural convection in a suddenly differentially heated cavity to the quasi-steady stage usually involves multiple sets of waves, such as the LEE perturbations in the initial stage, trailing waves on the intrusion flows, unstable waves on the boundary layers triggered by the impact of the intrusions, horizontal oscillations, and traveling waves in the quasi-steady stage (refer to Xu et al. 2005c). These unstable waves, occurring at different stages of the transition, have different formation mechanisms and behaviors (e.g. in amplitude and frequency), and thus further discussion is of significance (refer to Chapter 5).

1.2.2 Natural convection with a single or multiple fins

Enhancement and depression of the heat transfer through a differentially heated cavity are of significance in industrial applications, such as solar collectors and nuclear reactors, and thus a considerable number of studies have been devoted to the problems of this aspect. The techniques of enhancing or depressing heat transfer are usually classified into two categories, i.e. the so-called 'active' and 'passive' approaches. The active approach denotes that some artificial perturbations are introduced into the natural convection flow in order to enforce convection or even trigger turbulence. For example, sound excitation, a typical active approach, may be used to perturb flows, induce flow instabilities and enhance heat transfer (see e.g. Kim et al. 2004). Perturbing temperature signals is also a useful active approach, which may destabilize flows and improve heat transfer, as described by Kwak and Hyun (1996) and Kwak et al. (1998).

Although the active approach is easier to 'control' the heat transfer through a cavity, its applications, in some sense, are limited since artificial perturbations need to be applied. In contrast, the passive approach may overcome this limitation, and thus extensive studies of the passive approach have also been reported. An easily implemented passive approach is to put a single or multiple fins in the cavity, which may enhance or depress heat transfer. In some studies, a fin could be called a roughness element, baffle, obstruction, partition, divider or even plate. For uniformity, the term 'fin' is adopted in this thesis. The review in this section is arranged as follows: natural convection induced by a single fin on the sidewall, multiple fins on the sidewall, and a single or multiple fins in locations in the cavity other than on the sidewall.

1.2.2.1 Single fin on the sidewall

One of the earliest studies of natural convection induced by a fin attached to a heated surface was reported by Eckert et al. (1960) who visualized transitional natural convection to turbulence, using smoke. It was found that a fin on a heated surface could reduce the critical Rayleigh number of transition to turbulence in comparison with those free-convection flows adjacent to a heated surface without a fin. A recent study of laminar natural convection adjacent to a heated plate with a square fin by Ichimiya (2000) indicated that the heat transfer through the heated surface is depressed in the region around the fin. If the fin is taken a small distance from the wall, the heat transfer may be slightly enhanced in the region of the heated surface opposite to the fin.

Studies of the natural convection flow in a cavity with a fin on an active wall (a heated or cooled sidewall) have also been extensively reported in the literature. An early study by Bejan (1983), based on the model of porous insulations heated from the side, indicated that the heat transfer dominated by convection decreases steadily and that dominated by conduction increases slightly, as the fin length increases. An adiabatic fin can generate the greater heat transfer through the cavity than that with a diathermal fin. Another early study by Ooshuizen and Paul (1985), who discussed the spatial distribution of the heat transfer for relatively higher Rayleigh numbers ($10^5 \sim 10^6$), showed that a fin on the cold wall enhances the local heat transfer rate on the upper portion of the hot wall and depresses it near the center, in comparison with those results without a fin. The overall effect is that the fin on the cold wall enhances the heat transfer at the hot wall if the ratio of the fin length to the cavity width is fairly small. Shakerin et al. (1988) experimentally and numerically investigated the thermal boundary layer flow along a sidewall with one and two square fins. Their results showed that there is no clear separation around a square fin attached at a low position on the hot wall in the laminar regime.

Besides these earlier results, a comprehensive discussion of the natural convection flow in a cavity with a fin on the sidewall has been reported in the recent literature. The effect of the shape, size, material, and position of the fin on the natural convection flow in the cavity has been the primary focus. In most studies, the fin is rectangular. A study of the thickness of the conducting fin varying from 0.5% to 10% (relative to the cavity height) by Nag et al. (1994) demonstrated that, as the thickness is reduced, the heat transfer through the cavity initially decreases until a critical thickness value is reached.

When the thickness is smaller than this critical value, the heat transfer increases as the thickness is further reduced. Clearly, such a large variation in thickness impacts on natural convection flows in the cavity. However, in most studies, for the purpose of examining other effects of the fin on heat transfer, thickness is usually considered to be small in comparison with the fin length, and thus may be neglected (a so-called thin fin).

The fin length is an important factor in controlling the natural convection flow in a cavity. If the length of a poorly conducting fin is sufficiently large, secondary circulations arise (see Frederick 1989). The heat transfer through the sidewall with a fin is reduced as the fin length increases. This is because the natural convection flow adjacent to the sidewall is depressed. However, since a long fin results in secondary circulations of the natural convection flow, secondary circulations, in some sense, increase the convective flow adjacent to the opposite sidewall and thus enhance the heat transfer through the opposite sidewall (see Frederick 1989). A long fin may also stimulate the appearance of multiple circulations, which arise at the upper and lower corner base of the fin respectively (refer to Nag et al. 1993).

The fin position, likewise, may change the natural convection flow in a cavity and heat transfer. It was confirmed by Nag et al. (1993) that the heat transfer through the opposite sidewall is dramatically reduced when the fin rises from a lower to an upper position. A more comprehensive discussion of the effect of the position of a highly conductive fin on natural convection has been performed by Shi and Khodadadi (2003) and Tasnim and Collins (2004). As the fin height increases, a significant separated region (a low velocity zone) appears between the fin and the top wall, and the varying local heat transfer is relevant to those flow patterns.

The Rayleigh number plays an important role in the natural convection flow in a cavity with a fin, similar to the case without a fin reviewed in section 1.2.1. When *Ra* increases, the natural convection flow in the cavity with a fin is enforced, and thus the heat transfer through the finned sidewall is enhanced (see e.g. Shi & Khodadadi 2003).

It is clear that a fin on the active sidewall depresses the convective flow in a cavity, trending to reduce the heat transfer through the finned sidewall (see e.g. Frederick & Valencia 1989). However, if the fin on a heated or cooled surface is perfectly conducting, it apparently increases the area of the heating or cooling surface (that is, increases conduction) and thus tends to enhance the total heat transfer through the cavity. Two counter-acting mechanisms (conduction and convection) determine the overall heat transfer through the cavity. Accordingly, depending on different applications (either maximizing or minimizing heat transfer), different fin parameters may be chosen to increase the conduction surface or depress the natural convection flow.

Most of the above-mentioned studies of the effect of a fin on natural convection and heat transfer focused on steady flows at low Rayleigh numbers (e.g. $Ra < 10^7$). However, for high Rayleigh numbers (e.g. $Ra > 10^7$) at which the natural convection flow in a cavity becomes an unsteady process (and a converged steady numerical solution cannot be obtained, see Shi & Khodadadi 2003), the conclusions from the steady laminar flow evidently need to be re-examined. Previous studies (see e.g. Patterson & Imberger 1980) demonstrated that the transition of the natural convection flow in the cavity without a fin is a complex flow process in which a vertical thermal boundary layer flow, a horizontal intrusion and core flows interact with each other. Therefore, it is of significance to investigate transient natural convection in a cavity with a fin on a sidewall at higher Rayleigh numbers.

Recently, a shadowgraph observation of the natural convection flow in a suddenly differentially heated cavity with a square fin was performed by Xu et al. (2005b, 2006), in which the transition of the natural convection flow from the start-up was classified into three stages: an initial stage, a transitional stage and a quasi-steady stage. It has been found that a fin, in the initial stage, blocks the upstream boundary layer flow and forces it to detach from the hot sidewall and eventually form a lower intrusion front (hereinafter referred to as front). The lower intrusion front reattaches to the downstream hot sidewall after it bypasses the fin. There are evidently quantitative differences in the flow structures and the wave properties between two cases with and without a fin in the transitional stage. A double-layer structure of the vertical thermal boundary layer with more circulations forms in the quasi-steady stage, in comparison with that without a fin. These results from shadowgraph observations were supported by the numerical simulations (see Xu et al. 2005d).

1.2.2.2 Multiple fins on the sidewall

Many studies have been devoted to the natural convection flow in a cavity with multiple fins on the active sidewall for over two decades. It has been demonstrated that flow patterns at the steady state are dependent on the Rayleigh number, the angle of inclination of the cavity, the aspect ratio, and the size and interval of fins (see e.g.

Scozia & Frederick 1991; Lakhal et al. 1997). For a slender cavity at low Rayleigh numbers (e.g. $Ra < 10^5$), a small cell may form in a 'small side-opened cavity', which consists of a sidewall and two adjoining fins (see e.g. Scozia & Frederick 1991; Facas 1993). As the number of fins increases, the flow pattern shows that a primary circulation is gradually restricted to the unfinned side (Scozia & Frederick 1991).

For the conduction regime (e.g. $Ra < 10^3$), if the fins are perfectly conducting, the heat transfer through the cavity increases with the increasing length and number of fins due to the increasing conducting surface area. For the convection regime, the heat transfer through the cavity exhibits a complex dependence on the length and number of fins. Yucel & Turkoglu (1998) indicated that with an increasing number of fins, the heat transfer first reaches a maximum and then approaches to a constant value, which is not affected by the number of fins. The numerical simulations by Lakhal et al. (1997) also showed that, if the cavity is inclined at 45^o, the heat transfer generally decreases considerably with the increasing fin length.

1.2.2.3 Single or multiple fins in locations other than on the sidewall

An emphasis in earlier studies was natural convection with one or multiple fins on the inactive wall (e.g. the horizontal adiabatic wall). An interferometer experiment by Bajorek and Lloyd (1982) showed that the core flow with one fin attached to the top wall and another symmetrically attached to the bottom wall is unsteady at Rayleigh numbers greater than 10^5. Bilgen (2002) indicated that two clear cells are separated by the two fins at low Rayleigh numbers ($10^4 < Ra < 10^6$). As the Rayleigh number increases up to 10^{11}, the two cells become indistinct and eventually evolve into a single cell, and the horizontal stratification of the fluid in the cavity is strengthened. Lin and Bejan (1983) indicated that if one of the two fins is removed (i.e. only a single fin on the top or bottom horizontal wall), the heat transfer through the cavity increases. The flow and heat transfer are strongly dependent on the fin length. As the fin length increases, the flow may be characterized by boundary layer flows along the heated or cooled wall and horizontally reverse flows through the aperture between the horizontal wall and the fin, and the heat transfer become smaller (Lin & Bejan 1983).

In order to depress the natural convection flow and heat transfer through the cavity as much as possible, the fin length may increase until it completely partitions one cavity into two cavities. Such a vertical fin (or a so-called partition), although conducting, may reduce by more than 60% of the heat transfer cross a cavity for the laminar regime (3.8

$\times 10^4 < Ra < 3.7 \times 10^5$, see Cuckovic-Dzodzo et al. 1999). For the turbulent regime, a complete vertical conducting fin, likewise, significantly reduces the heat transfer, which also decreases with the increasing number of complete fins (see e.g. Said et al. 1997).

Besides these wall-attached fins, a fin may be placed in the center of the cavity in order to dominate the natural convection flow. A study of natural convection with an arc-shaped adiabatic fin in the center of the cavity by Tasnim and Collins (2005) showed that the flow and temperature fields are dependent on the fin parameters, including the fin length and radius, and the heat transfer is reduced.

Considerable studies of other aspects of fins have also been reported. For example, weakly turbulent natural convection in a differentially heated side-finned cavity with two horizontal conducting walls has been experimentally investigated by Ampofo (2004, 2005), and velocity and temperature fields have been obtained. Bae et al. (2001) discussed the natural convection flow in a side-periodic-heated cavity with a horizontal fin in the center of the cavity, and indicated that the presence of the fin, likewise, depresses the fluctuating heat transfer through the cavity. Furthermore, the natural convection flow induced by an array of hot fins in a cavity has been paid considerable attention (see e.g. Heindel et al. 1996; Guvenc & Yuncu 2001; Yu & Joshi 2002), and the instability of the natural convection flow induced by hot fins has been discussed by Gadoin et al. (2001).

1.2.3 Summary

Although the focus of this thesis is on transient natural convection in a suddenly differentially heated cavity with and without a fin on the sidewall, more extensive studies of natural convection are reviewed so that the present study may be compared with a greater range of literature. Unfortunately, the present review is by no means exhaustive, and many other studies have not been covered here. Clearly, this review has shown some important aspects and significant achievements in the field. A few progresses may also be briefly summarized as follows.

Natural convection in a cavity without a fin:

- Major scales of flows in a suddenly differentially heated cavity were obtained;
- The critical Rayleigh number of the transition from laminar to period flows at certain Prandtl numbers was numerically gained;
- Some analytical solutions of the thermal boundary layer flow have been derived.

Natural convection in a cavity with a single or multiple fins:

- It has been found that fins on the sidewall depress the natural convection flow adjacent to the finned sidewall and the heat transfer for the laminar regime. Similarly, fins on the horizontal wall also significantly depress the heat transfer across the cavity.

Although these achievements have provided insights into natural convection and careful experiments and companion accurate computations have also shown very promising results toward a full understanding of natural convection in a differentially heated cavity, many important issues concerning the transient natural convection flow are not completely understood. Accordingly, the transient process and issues in this regard will be a long-term research topic in this field. For example, understanding the overall transition of the natural convection flow in a differentially heated cavity at the transitional regime from a stationary, isothermal ambient fluid following sudden heating to the quasi-steady state is still an unfinished task, and many mechanisms, responsible for transient features, need to be further discussed. Moreover, it is of significance to investigate the transient natural convection induced by a fin on the sidewall at higher Rayleigh numbers. This could lead to research in the direction of controlling the transition of the natural convection in the cavity, and thus a feasible method of the enhancement of the heat transfer through the cavity by employing a fin on the sidewall could be developed.

In summary, there are still a number of unexploited areas relevant to natural convection in a differentially heated cavity with and without a fin on the wall. In this section, only a few particularly interesting problems, due to their unique and significant aspects, are discussed briefly.

1.3 Thesis outline

Some fundamental problems of transient natural convection in a suddenly differentially heated cavity with and without a fin on the sidewall are the focus of this thesis. Experimental, numerical and analytical methods are employed here. The layout of this thesis containing eight chapters is as follows.

The basic descriptions of this thesis consist of Chapter 1 through Chapter 3. Chapter 1 presents the background and literature review. In Chapter 2, the experimental model system is described, and the methods by which the flow field is visualized and temperature measured are briefly introduced. The shadowgraph optical setup is illustrated and implications of shadowgraph patterns are discussed. The principle and accuracy of the thermistors used in temperature measurement are also given in this chapter. The physical problem of this thesis is formulated in Chapter 3, including simplification of the governing equations. The numerical procedures are introduced, and the testing results of the grid and time step dependences are discussed in this chapter.

The results of transient natural convection in a cavity without a fin are showed in Chapter 4 and Chapter 5. Chapter 4 presents shadowgraph observations and thermistor measurements of the transition of the natural convection flow from the start-up to the quasi-steady state. The mechanisms, responsible for the formation and evolution of the double-layer structure of the vertical thermal boundary layer, are discussed in Chapter 5 based on comparisons between numerical and experimental results. The heat transfer of the double-layer structure is analyzed.

Numerical simulations and experimental measurements of transient natural convection in a cavity with a fin on the sidewall are showed in Chapter 6 and Chapter 7 respectively. The experimental results of transient natural convection with a square and thin fin on a sidewall are presented in Chapter 6. Transient natural convection flows, such as the development of the lower intrusion front in the initial stage, is visualized. In addition, the oscillations of the thermal flow around a thin fin are observed and measured. The corresponding numerical simulations and comparisons with the experimental results are presented in Chapter 7. The effects of the lower intrusion front and the oscillations of the thermal flow around the fin on the heat transfer are discussed. Numerical simulations are also extended to transient natural convection flows for different fin parameters (e.g. dimension, position and number), and the effects of the fin parameters on the heat transfer through the finned sidewall is assessed in this chapter.

Discussion and conclusions comprises Chapter 8, where major conclusions are summarized, and the future research is also suggested.

2 Experimental apparatus and approaches

Due to the high relative cost in comparison to numerical investigations, fewer experimental studies of transient natural convection in a differentially heated cavity have been performed. However, experimental studies are still an important part of this thesis as a validation of numerical work. In the following sections, the experimental model and measurement techniques (the shadowgraph method and thermistors) are described before discussing the experimental results in later chapters.

2.1 Experimental apparatus

The laboratory study of natural convection in a suddenly differentially heated cavity is an important approach. However, there are considerable difficulties in modeling sudden heating of the walls to an isothermal state, since a step increase of temperature is only an idealized process. In an experiment, what one can do is to make the initial experimental heating process as short as possible in order to approximate the step increase of temperature. The regular heating approach, such as embedding electrical heaters in the hot wall (see e.g. Yewell et al. 1982), does not achieve this result since it takes a relatively long time for the wall to reach a specified temperature. The experiment by Yewell et al. (1982) showed that this process needed about 15 minutes. Although the time to reach a specified temperature varies for different electrical heaters and is shorter than the timescale of the overall flow development, it is long in comparison with the timescale of the growth of the vertical thermal boundary layer (e.g. the timescale of the thickness growth, see Equation (1.7)). Accordingly, the regular heating approach has been rarely applied to the suddenly heated isothermal boundary experiment.

For the purpose of investigating the transient response for the sudden heating problem, Ivey (1984) initiated the experiment by pouring pre-heated and pre-cooled water into water baths adjacent to the hot and cold sidewalls respectively. Such an initial heating process may be completed in a time of 5s and is much shorter than the

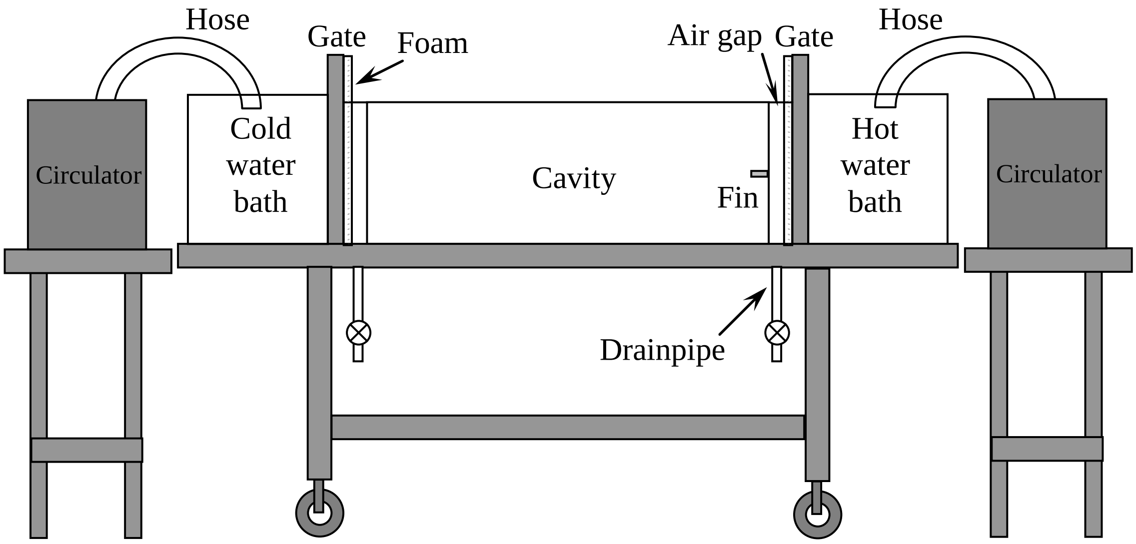

Figure 2.1 Schematic of the experimental configuration

procedure adopted by Yewell et al. (1982). Therefore, some transient effects may be better visualized.

Although the time of the initial sudden heating process was significantly reduced by Ivey (1984), it is still comparable with the timescale of the transient response following sudden heating, such as the set up time for the vertical thermal boundary layer (Patterson & Imberger, 1980). In order to minimize the effect of a relatively slow initiation, Patterson and Armfield (1990) employed a pneumatically operated apparatus, and their experiments showed that the step increase of temperature may be well approximated. The apparatus employed in Patterson and Armfield (1990) is the basis of the present experimental model system in this thesis, which will be thus introduced in the following section.

Figure 2.1 shows a schematic of the experimental system. The main parts are fixed on a steel frame, which may be moved and adjusted so that the cavity can be set up at a horizontal level. The movability of the apparatus is also convenient for measurements, such as shadowgraph observations (refer to Section 2.2).

The experimental cavity shown in Figure 2.2, except for the cooled and heated sidewalls, is made of 20 mm thick perspex with internal dimensions of 1 m (width, L) by 0.24 m (height, H) by 0.5 m (depth, D). Since perspex is transparent, the flow visualization may be performed both vertically and horizontally across the cavity. The two horizontal end sidewalls are made of gold-coated copper plates of 1.13 mm thickness. Since the gold-coated copper sidewalls are excellent conductors, they may be considered as isothermal. In contrast, the perspex walls are poor conductors in

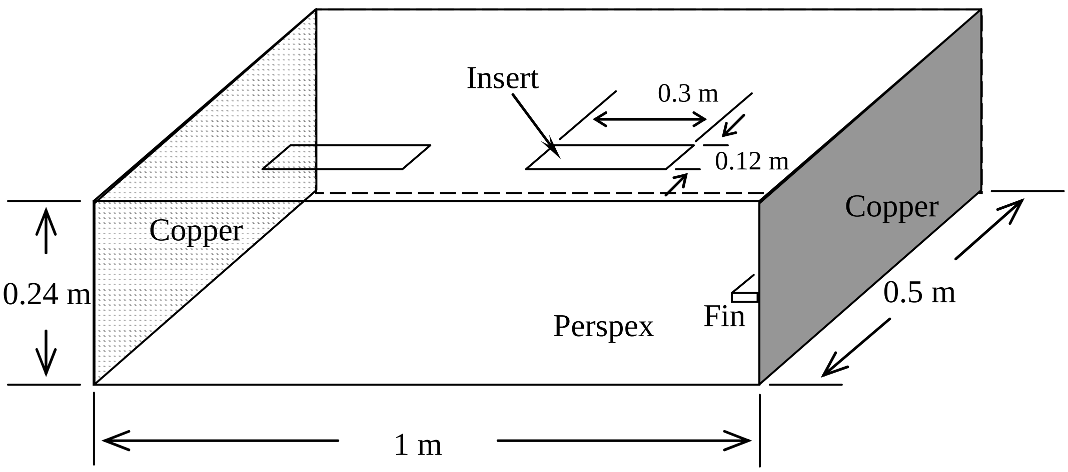

Figure 2.2 Three dimensional sketch of the model cavity

comparison with the copper walls, and thus may be regarded as adiabatic in the corresponding numerical simulations. In order to fill the cavity with the working fluid (here water) and provide a means of mounting thermistors, two rectangular holes of 0.3 m × 0.12 m are opened on the top wall. In the experimental process, two precisely matched perspex inserts are placed in the two holes so as to seal the cavity. For those experiments with a fin, a perspex fin is attached at the middle height of the hot sidewall. Two cross sections of fin are employed in the experiments; one square (10 × 10 mm^2) and the other rectangular (40 × 2 mm^2).

The model cavity is separated from two synchronously pneumatically operated gates by air gaps (see Figure 2.1) whose width is 30 mm, with a drainpipe under the air gap in order to drain the water there after the experiment finishes. The gate and gap are employed to minimize the heat transfer between the model cavity and the water bath before the experiment starts. However, it is impossible to completely insulate the cavity and the water bath, and effort is devoted to reducing the heat transfer as much as possible.

The synchronously pneumatically operated gates are used to produce a suddenly side-heated or side-cooled condition; that is, the copper sidewalls suddenly rises or falls to a constant temperature when water from the water bath flushes against them after the gates are rapidly lifted by the pneumatic actuators. Figure 2.3 shows a schematic of a gate. The gate is made of a PVC plate of 0.54 m (width) × 0.42 m (height) × 0.015 m (thickness), which is joined to the actuator shaft of the pneumatic actuator with a fixed joint. The pneumatic actuators are designed and manufactured by Festo Pty Ltd. The gates are constrained by fixed guides to minimize transverse vibrations. A piece of 15-

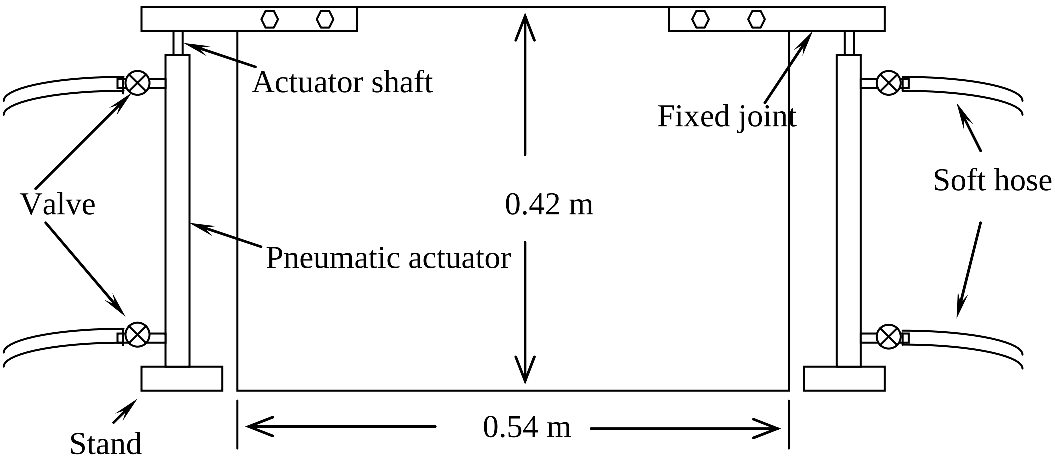

Figure 2.3 Sketch of the pneumatically operated gate

mm-thick polystyrene foam is attached to the air gap side of the gate to minimize the heat loss from the water in the water bath.

The pneumatically operated gate system comprises actuator shafts, actuator bodies (whose diameters are 26 mm and height 0.4 m), stands, inlet valves and outlet valves, as shown in Figure 2.3 (also see Patterson & Armfield 1990). The bottom end of the shaft is an airtight piston, which separates the actuator body into two air chambers. When the pneumatic switch is turned on, high-pressure air with a pressure range of 400~800 k Pa is allowed into the lower chamber via the bottom hoses. The high-pressure rapidly drives the piston and shaft upwards, lifting the gate. The time for the gate to be raised may be controlled by the pneumatic system, typically no more than 1 second. To avoid vibrations at the completion of the gate lifting, the final stage of the gate lifting is slow down by controlling the exit of the air from the upper air chamber.

The water baths, used to contain the hot or cold water, are at the other side of the gates. Each bath is made of perspex plates of 10 mm thickness with an open top, and is 0.53 m (length) × 0.64 m (width) × 0.35 m (depth). Each bath can contain up to 0.119 m^3 water. In order to prevent the heat loss from the water baths, the entire baths including the top are enclosed by polystyrene foam of 30 mm thickness. The gate and the water bath on either side of the model cavity are identical.

Table 2.1 Output power of JULABO circulators

Circulator model	F10	F33-HD	F33-MW	FP35
Output power (W)	170	2700	2700	2700

Four circulators (JULABO models listed in Table 2.1) are used to cool or heat water in two water baths respectively. Four circulators rather than two are employed in order to provide greater output power than two circulators, and thus a specified temperature is more quickly achieved. The circulators are also able to rapidly restore the water baths back to the specified temperature even though a large temperature perturbation may be produced, such as the sudden start-up at which time a large heat transfer occurs from the hot water bath to the water in the model cavity, with a corresponding heat gain at the cold end. The circulator parameters are listed in Table 2.1. The circulators maintain the temperature of the water in the water bath within a range of ±0.01 K at the specified temperature, which may also be controlled by an external digital input from a computer.

2.2 Flow visualization with the shadowgraph method

Because of its relative simplicity, the shadowgraph method has been extensively applied to the observation of buoyancy flows. Since it is very sensitive to a local density gradient, it is usually employed to visualize shock waves and turbulence; however the visualization of natural convection is also one of its important applications.

The shadowgraph technique was employed to visualize transient natural convection in a differentially heated cavity by Schöpf and Patterson (1995), in which the early flow properties were described, such as the first group of traveling waves along the hot boundary layer immediately following start-up, the initial horizontal intrusions and the second group of traveling waves originating from the interaction between the incoming intrusion and the boundary layer. These shadowgraph observations are also supported by numerical predictions (see e.g. Schladow et al. 1989; Patterson & Armfield 1990). Therefore, based on these previous studies, the shadowgraph technique is employed to visualize transient natural convection with and without a fin on the sidewall in this thesis.

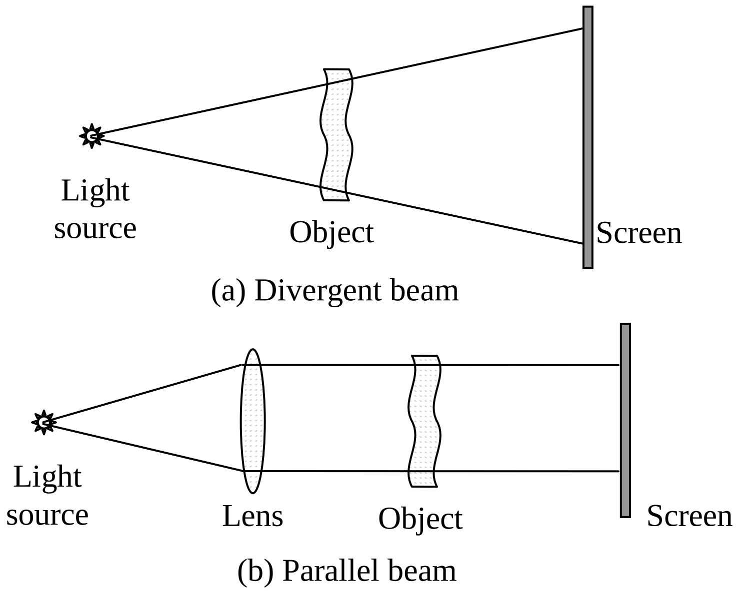

Figure 2.4 Schematic of the direct shadowgraph

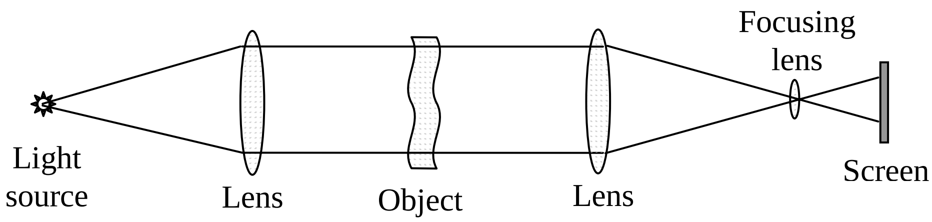

Figure 2.5 Schematic of the focused shadowgraph

2.2.1 Principle

As described in the beginning of this thesis, those dark pixilated strips characterize natural convection of air on a bitumen road, where the density difference of air results in a varying refractive index and in turn visible bright or dark strips. In fact, this is also a simple shadowgraph.

Various shadowgraph methods can be divided into two categories: direct and focused (see e.g. Settles 2001). The direct shadowgraph means that, in the simplest case, only a bright light, an object and a suitable surface on which to cast the shadowgraph image are required, as shown in Figure 2.4(a). The above-mentioned case of the patterns above a bitumen road is a direct shadowgraph. Figure 2.4(b) shows a schematic of the direct shadowgraph using a parallel light beam, which is superior to that in the divergent one (see Settles 2001 for details).

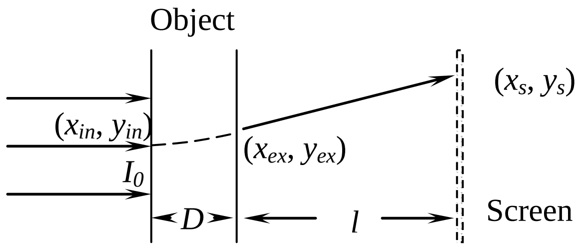

Figure 2.6 Shadowgraph light path through the object

Figure 2.5 shows a schematic of the focused shadowgraph. It is easily seen that a set of lenses (which may be substituted by a spherical mirror), focusing lens (placed at the focal point of the lens) and screen in Figure 2.5 replaces the single screen in Figure 2.4(b). The focusing lens and screen here may be a camera, and thus adjustment of the screen position may be replaced by camera focusing. Although the focused shadowgraph is more complex than the direct one, the focused shadowgraph can more easily adjust the imaging position by utilizing the camera focusing and thus has been extensively applied. For the purpose of obtaining the shadowgraph image close to the cavity, the focused shadowgraph is employed in this thesis.

The shadowgraph technique is developed on the basis of the optical refraction principle; that is, the shadowgraph pattern with the non-uniform gray levels results from the object (here a flow field) with a non-uniform refractive index field, which is a function of the fluid density (see Merzkirch 1974). Therefore, it is possible to find the correlation between the light intensity of the shadowgraph image and the varying refractive index of the object.

Figure 2.6 shows a schematic of the light path through the object, in which the light direction is the *z*-direction and thus the *x*-*y* plane is normal to the incident light direction. The point P_i (x_{in}, y_{in}) is the position in which the light ray enters the object, P_e (x_{ex}, y_{ex}) the exit position, P_s (x_s, y_s) the position in which the refracted light ray reaches on the screen, D the thickness of the object, and l the distance between the object and the screen. The screen is drawn using a dashed line because it is not a real screen but the imaging at that position for the focused shadowgraph.

According to Fermat's principle and the variational principle (refer to Schöpf et al. 1996), the differential equations of the light path parameterized by z may be expressed, as follows,

$$\frac{d^2x}{dz^2} = \frac{1}{n}(1+(\frac{dx}{dz})^2 + (\frac{dy}{dz})^2)(\frac{\partial n}{\partial x} - \frac{dx}{dz}\frac{\partial n}{\partial z}), \tag{2.1}$$

$$\frac{d^2y}{dz^2} = \frac{1}{n}(1+(\frac{dx}{dz})^2 + (\frac{dy}{dz})^2)(\frac{\partial n}{\partial y} - \frac{dy}{dz}\frac{\partial n}{\partial z}). \tag{2.2}$$

The *x*-*y* plane displacement of the parallel light from the entry point on one side of the object to the imaging point on the screen is

$$\overline{x_{in}x_s} = x_{ex} - x_{in} + l\frac{dx(z_{ex})}{dz}, \tag{2.3}$$

$$\overline{y_{in}y_s} = y_{ex} - y_{in} + l\frac{dy(z_{ex})}{dz}. \tag{2.4}$$

A direct numerical algorithm was first used to solve Equations (2.1) to (2.4) by Schöpf et al. (1996) and Brassington et al. (2002), and an artificial shadowgraph was obtained.

Since the shadowgraph pattern is a light intensity distribution (I_s), which is dependent on the illumination intensity I_0, the resulting intensity at P_s (x_s, y_s) is expressed (Schöpf et al. 1996),

$$I_s(x_s, y_s) = \sum \frac{I_0(x_{in}, y_{in})}{\left|\frac{\partial(x_s, y_s)}{\partial(x_{in}, y_{in})}\right|}. \tag{2.5}$$

Under the assumption that the displacement in the *x*-*y* plane is small, the Jacobian function in Equation (2.5) can be linearized, as follows,

$$\left|\frac{\partial(x_s, y_s)}{\partial(x_{in}, y_{in})}\right| = 1 + \frac{\partial\Delta_x(x_{in}, y_{in})}{\partial x} + \frac{\partial\Delta_y(x_{in}, y_{in})}{\partial y}. \tag{2.6}$$

If the object is thin, the deviation of light within the object may be neglected. Therefore, according to Equations (2.3) and (2.4), the displacements Δ_x and Δ_y may be given by (refer to Merzkirch 1974)

$$\Delta_x = l\frac{dx(z_{ex})}{dz} = l\int \frac{1}{n}\frac{\partial n}{\partial x}dz, \tag{2.7}$$

$$\Delta_y = l\frac{dy(z_{ex})}{dz} = l\int \frac{1}{n}\frac{\partial n}{\partial y}dz. \tag{2.8}$$

Equations (2.7) and (2.8) are substituted into Equation (2.6), and the relative intensity change becomes

$$\frac{I_0 - I_s}{I_s} = \frac{\Delta I}{I_s} = l\int (\frac{\partial^2}{\partial x^2} + \frac{\partial^2}{\partial y^2})(\ln n)dz. \tag{2.9}$$

Equation (2.9) demonstrates that the shadowgraph light intensity is roughly sensitive to the second derivative of the refractive index for the object; that is, the bright strips in a shadowgraph image corresponds to a maximum or minimum of the second derivative of the refractive index in the direction normal to the strip. However, the validation of Equation (2.9) relies on whether the above-mentioned conditions (the linear assumption) are satisfied; that is, the *x*-*y* plane displacement is much smaller than the path length through which the light passes.

Considering the present experimental cavity with a depth of 0.5 m, the assumption of a thin objective is not satisfied here, and thus the application of the above conclusions is not immediately justified.

Since the depth of the experimental cavity is large (0.5 m), it has been found that a clear shadowgraph pattern may be imaged at a position close to the cavity, such as on the wall of the cavity. If the shadowgraph pattern is imaged on the wall of the cavity, the distance *l* in Equations (2.3) and (2.4) is zero, and thus Equations (2.3) and (2.4) may be simplified to

$$\overline{x_{in}x_s} = x_{ex} - x_{in}, \tag{2.10}$$

$$\overline{y_{in}y_s} = y_{ex} - y_{in}. \tag{2.11}$$

This implies that the exit position P_e (x_{ex}, y_{ex}) is the same as the position P_s (x_s, y_s), where the refracted light ray reaches on the screen. Evidently, Equation (2.9), based on an assumption of a thin objective, cannot be applied to a deep cavity. For a deep cavity with a depth *D*, the *x*-*y* plane displacement of the light ray within the objective can be expressed as follows (see e.g. Merzkirch 1974),

$$\overline{x_{in}x_s} = \int_{z_{in}}^{z_{ex}}\int_{z_{in}}^{z_{ex}} \frac{1}{n}\frac{\partial n}{\partial x} dzdz = \int_{z_{in}}^{z_{ex}}\int_{z_{in}}^{z_{ex}} \frac{\partial}{\partial x}(\ln(n))dzdz. \tag{2.12}$$

$$\overline{y_{in}y_s} = \int_{z_{in}}^{z_{ex}}\int_{z_{in}}^{z_{ex}} \frac{1}{n}\frac{\partial n}{\partial y} dzdz = \int_{z_{in}}^{z_{ex}}\int_{z_{in}}^{z_{ex}} \frac{\partial}{\partial y}(\ln(n))dzdz. \tag{2.13}$$

Similar to Equation (2.5), a resulting intensity distribution (I_e) at P_e (x_{ex}, y_{ex}), dependent on the illumination intensity I_0, may be given by

$$I_e(x_{ex}, y_{ex}) = \sum \frac{I_0(x_{in}, y_{in})}{\left|\frac{\partial(x_{ex}, y_{ex})}{\partial(x_{in}, y_{in})}\right|}. \tag{2.14}$$

Under the assumption that the displacement in the x-y plane is sufficiently small, the Jacobian function in Equation (2.14) may again be linearized as follows,

$$\left|\frac{\partial(x_{ex}, y_{ex})}{\partial(x_{in}, y_{in})}\right| = 1 + \frac{\partial \Delta_x(x_{in}, y_{in})}{\partial x} + \frac{\partial \Delta_y(x_{in}, y_{in})}{\partial y}, \tag{2.15}$$

where the x-direction is assumed normal to the wall and the y-direction parallel to the wall.

Since the temperature variation in the y-direction of the thermal boundary layer is very much less than that in the x-direction, the variation of the refractive index in the y-direction, which depends on the temperature, may be neglected. Substituting Equations (2.12) and (2.13) into Equation (2.15) yields,

$$\frac{I_0 - I_{ex}}{I_e} = \frac{\Delta I}{I_e} = \int_{z_i}^{z_{ex}} \int_{z_i}^{z_{ex}} \frac{\partial^2}{\partial x^2}(\ln(n))dzdz. \tag{2.16}$$

Since the variation in the z-direction may be considered as very small (or dependent only weakly on z), Equation (2.16) can be further simplified as follows,

$$\frac{\Delta I}{I_e} = D^2 \frac{\partial^2}{\partial x^2}(\ln(n)). \tag{2.17}$$

Based on the linear (or weakly linear) dependence of the refractive index on temperature, an approximate relationship between the shadowgraph light intensity and the temperature of the thermal boundary layer flow is eventually given by

$$\frac{\Delta I}{I_e} \propto D^2 \frac{\partial^2 T}{\partial x^2}. \tag{2.18}$$

Equation (2.18) demonstrates that the shadowgraph light intensity is proportional to the squared depth of the cavity and the x-directional second derivative of the temperature of the thermal boundary layer flow; that is, the bright strips in the shadowgraph image correspond approximately to the maximum or minimum of the x-direction second derivative of the temperature. However, it is again worth noting that this equation is subject to the above-mentioned; that is, the x-y plane displacement is sufficiently small in comparison with the path length through which the light passes.

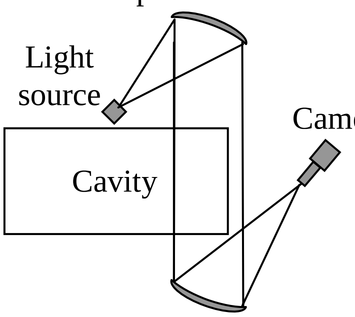

Figure 2.7 Schematic of the optic setup of the focused shadowgraph

2.2.2 Optical setup

For the purpose of obtaining shadowgraph imaging close to the sidewall of the cavity, a Z-shaped focused shadowgraph is employed in this thesis. Figure 2.7 sketches a top view of the shadowgraph optical setup, in which a point light source (a 12-W bulb in a small black box with a pin hole covered by a piece of ground glass) is placed at the focal point of a silver-coated spherical mirror with a diameter of 0.3 m and a focal length of 2.4 m. Such an optical set up results in a parallel light beam. When the parallel light beam passes through the model cavity filled with the non-uniform temperature fluid, it is deflected by the fluid due to variations of the refractive index of the fluid (based on Equations (2.1) to (2.4)). In fact, the refractive index depends on the fluid density, and in turn on the temperature. Therefore, a non-uniform pattern with varying light intensity is formed after the originally parallel light beam exits from the cavity. The distance from the light source to the mirror here is 2.4 m, and that from the mirror to the light-entering sidewall of the cavity is 2.6 m.

The exiting light beam is projected onto another identical spherical mirror, and refocused to a black-and-white CCD camera (Pulnix TM-6CN) at the focal point of this mirror. The distance from the light-exiting sidewall to the mirror is 1.8 m and that from the mirror to the camera is 2.4 m. The CCD camera is connected to a frame-grabber board (DT3120), which is implemented in a computer. The board digitizes the shadowgraph images received by the CCD camera into an array of 576 × 768 pixels with 256-bit grey-scale values. The shadowgraph images are stored on the hard disk of the computer at an adjustable sample rate of up to 5 frames per second. A time series of

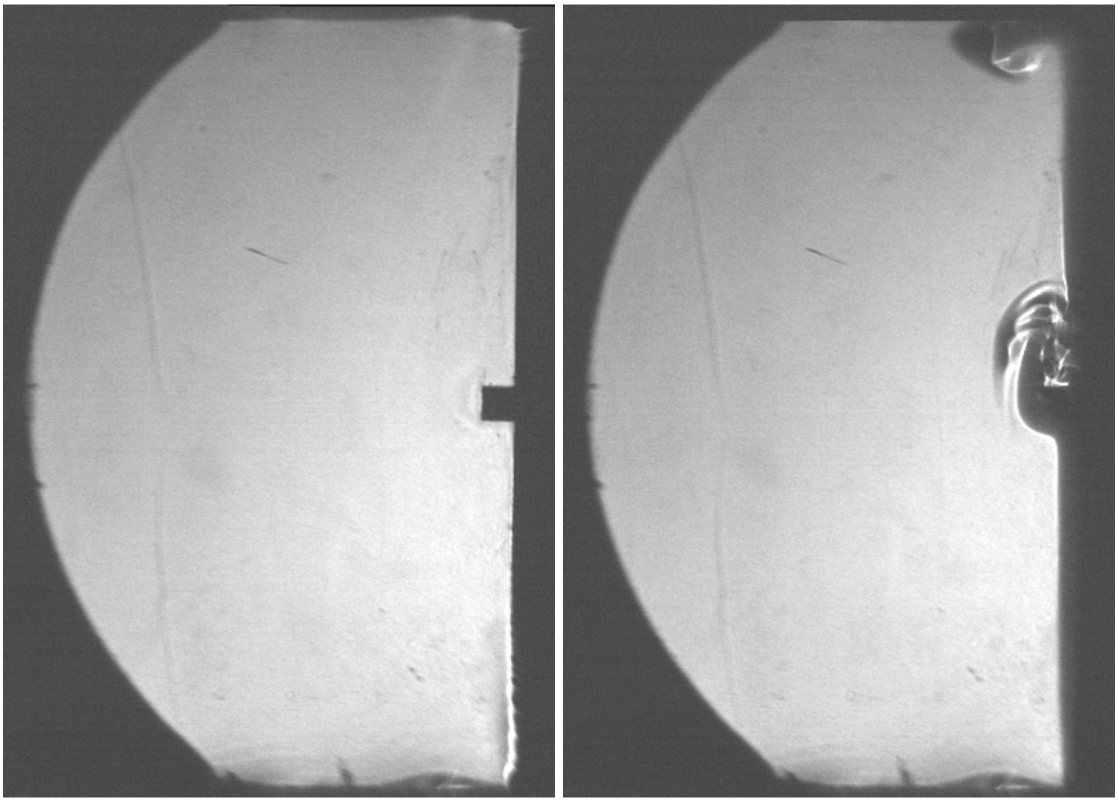

(a) Before experiment (b) t = 20 s

Figure 2.8 Shadowgraph images in the vicinity of the hot sidewall at $Ra = 3.9 \times 10^9$

the recorded shadowgraph images will display the temporal evolution of the temperature field.

In order to build a shadowgraph system, it is important to keep the light source, camera, and the center of each mirror in the same level plane, and make this plane normal to the sidewall of the cavity. Moreover, a parallel light beam, generated by adjusting the distance between the light source and the mirror, is also important in order to obtain a high-quality shadowgraph image. This means that the optical system must be carefully and accurately set up.

It is worth noting that, since the diameter of the mirror is 0.3 m, the parallel light beam generated by the mirror cannot fully cover the whole cavity, as shown in Figure 2.8. However, since the emphasis of this thesis is on flows adjacent to the sidewall with and without a fin, flows around the fin and adjacent to the hot sidewall are the primary interest. Figure 2.8(a) is taken before the experiment starts up, at which the fluid is motionless and isothermal. In fact, before each experiment, shadowgraph images need to be taken for later image processing. Figure 2.8(b) shows a shadowgraph image of the natural convection flow around a square fin on the hot sidewall at 20 s after the experiment starts up. Two intrusion fronts, close to the top and around the square fin, are clear. These are the result of temperature variations of the fluid. Discussion regarding the shadowgraph results is conducted in Chapters 4 and 6.

2.3 Temperature measurement with thermistors

Since the natural convection flow in a differentially heated cavity is driven by temperature differences, acquiring temperature data is an important component of studying natural convection and consequently temperature measurement has been paid considerable attention. A widely used technique, which can depict the temperature field of flows, is the interferometer. It played a role in the earlier studies of natural convection in a differentially heated cavity. For example, stratification in the cavity was first visualized by interferometer (see Eckert & Carlson 1961). Another technique, which can reveal the temperature information of flows, is the liquid crystal technique (refer to Rhee et al. 1984). Although both of these techniques can be applied to the temperature field measurements and provide the full temperature field information, their accuracies are unsatisfactory and in the latter case, implementation is difficult, particularly for the local measurements such as the thermal boundary layer. Consequently, their applications are limited to determining a qualitative view of the temperature field.

The most common method for the local temperature measurement is to employ a thermocouple, but it is poor in accuracy and sensitivity, in comparison with a resistance temperature detector (RTD) or a thermistor. Since a thermistor has a better sensitivity than a RTD, it has been extensively used to acquire a time series of the temperature of flows at fixed points (see Patterson & Armfield 1990; Patterson et al. 2002). Moreover, its high resistance can diminish the effect of inherent resistances in lead wires, which can cause significant errors in low resistance devices. In general, the thermistor is a good way for the temperature measurements at fixed locations with flows because of its high accuracy and sensitivity.

2.3.1 Description

A thermistor is in fact an electrical resistor whose resistance changes with temperature. It is usually manufactured from the metal oxide semiconductor material, and encapsulated in a glass or epoxy bead with a small tip outside. In this thesis, temperature measurements were implemented with fast response thermistors (Thermometrics FP07). The body of the thermistor has a maximum diameter of 2.2 mm and length of 12.6 mm, though the thermistor is contained in a small thin glass bead of the maximum diameter less than 0.2 mm. The thermistor has a time constant of 0.007 s in water. In order to minimize thermal disturbances caused by the presence of thermistor, the thermistor body is mounted in an insulated tube. The main parameters of the FP07 thermistor are listed in Table 2.2.

Table 2.2 FP07 thermistor parameters

Body (mm)		Lead-wires(mm)		Time constant in water (sec)	Dissipation constant in water (mW/K)	Power rating in air (W)
Diameter (max)	Length	Diameter	Length			
2.2	12.6	0.3	22	0.007	0.26	0.006

The FP07 thermistor, since it is a resistive device, needs current excitation, which is supplied by the SCXI-1581 module (manufactured by National Instruments Corporation). The SCXI-1581 can provide 32 channels of 100 μA current excitation; that is, up to 32 thermistors may be synchronously implemented in the experiment. Furthermore, the National Instruments SCXI-1102C analogue input module is used to acquire the output voltage signals from each thermistor.

Figure 2.9 shows a schematic of this temperature measurement system. The FP07 thermistor, through cables and SCXI-1300 terminal blocks, is connected to the SCXI-1581 current excitation and the SCXI-1102C amplifier modules respectively. The voltage signals are transferred to the PCI-6031E board plugged in the computer, which is used to perform the AD transformation. All of data acquisition devices of the temperature measurement and part of software are provided by National Instrument Corporation.

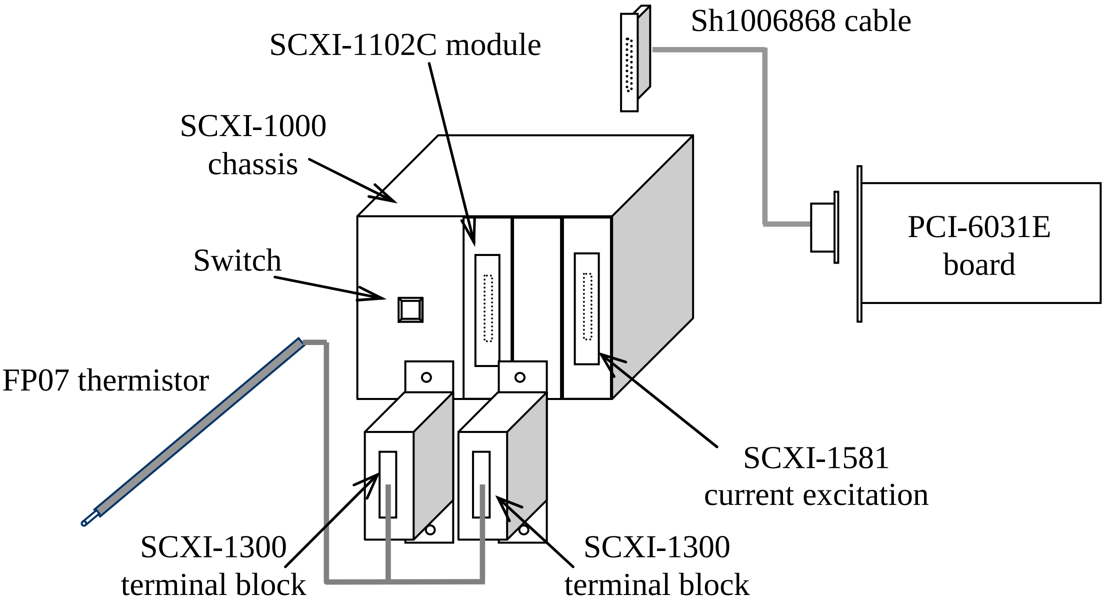

Figure 2.9 Schematic of the data acquisition system with FP07 thermistors

2.3.2 Calibration of thermistors

In section 2.3.1 the acquisition of the digital voltage time series using FP07 thermistors is described. In fact, the dependence of the thermistor resistance on temperature is usually prescribed by the specifications of the thermistor, and thus temperature may be calculated from the voltage value. Unfortunately, this correlation is approximate and has a poor accuracy for the full range of the sensor. Accordingly, calibration of each thermistor before it is used is important in order to acquire highly accurate measurement data.

When calibration is implemented, the range of the fluid temperature in experiments should be first considered. Since the temperature difference between the two sidewalls in experiments is up to 32 K, thermistors are calibrated with a range of 31K, from 283.05 to 314.05 K (with an average relative error of 0.24%), which will cover almost the entire range of the temperature variation of the fluid in the vicinity of the hot sidewall. Figure 2.10 shows the result of the temperature calibration of a thermistor, in which a third order polynomial function is well fitted to the temperature data.

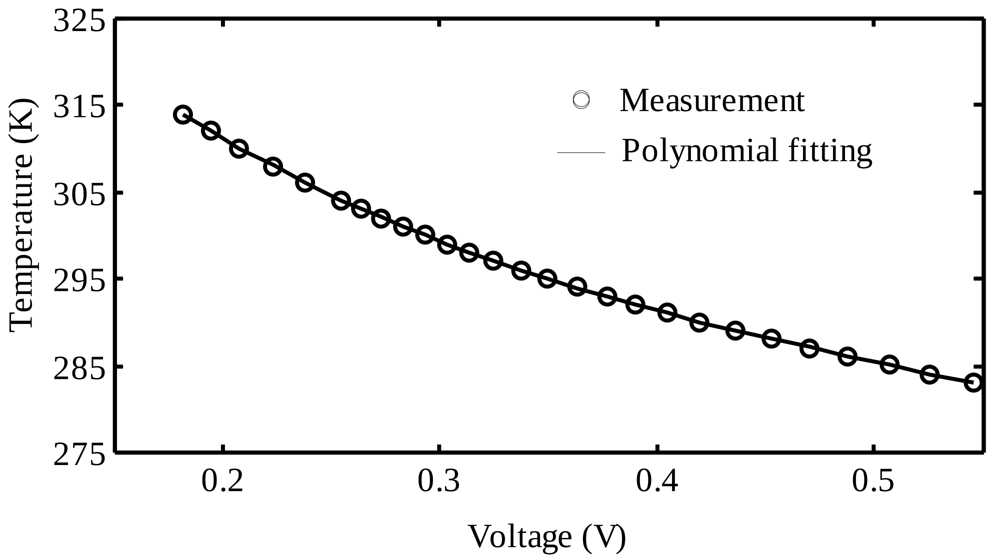

Figure 2.10 Calibration of a thermistor

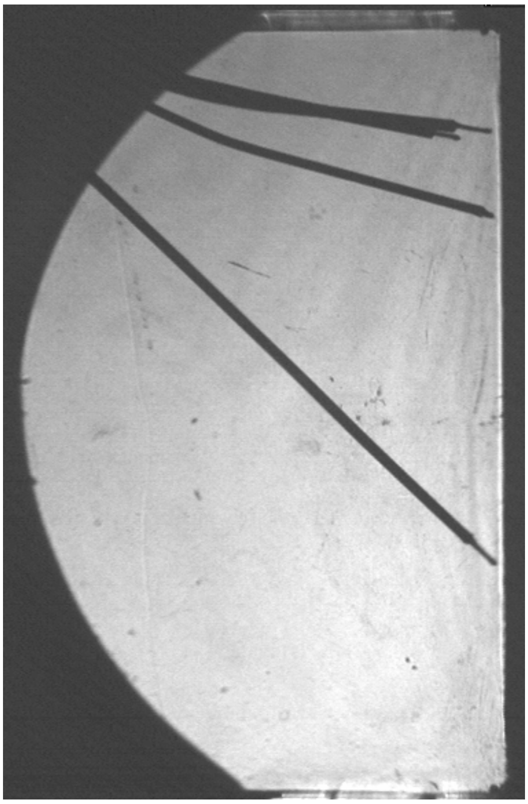

Figure 2.11 Thermistors mounted in the cavity

2.3.3 Temperature measurements

The first step of the temperature measurement is to fix a thermistor at a specified location. Since the thermal boundary layer flow is the focus of this study, thermistors are usually fixed in the vicinity of the hot sidewall or fin.

In order to minimize modifications to the cavity body due to thermistor mounting, thermistor tubes are fixed in the insert covering the opening of the cavity (see Figure 2.2) at a certain angle with sufficient length to allow the thermistor tips to be at their specified locations along the sidewall. Figure 2.11 shows fixed thermistors in a shadowgraph image. In practice, the thermistor is first located at a specified position, which is then validated using the shadowgraph image (see e.g. Figure 2.11). The final positions of different thermistors under different conditions are shown in Chapters 4 and 6.

When the experiment starts up, the pre-amplified and digitized output voltage signal from each thermistor is converted into a temperature signal using the polynomial fitting formula obtained from calibration, and is then recorded on the computer hard disk. The record comprises a time series of temperature at each location, which describes the time-dependent temperature variation.

2.4 Experimental procedures

Through considerable experimental observations and measurements, this experimental system and shadowgraph optical setup as well as thermistors have been tested thoroughly.

In practice, the present experiments indicate that it is necessary to carefully perform the experimental procedure in order to minimize external disturbances. For example, before an experiment starts, the measurement approaches need to be repeatedly tested, particularly the shadowgraph optical setup and the thermistor calibration. Since the quality of the shadowgraph image is significantly dependent on whether the shadowgraph optical setup is properly aligned, it is important to adjust the light source, camera, and the center of each mirror in the same level plane and make this plane normal to the sidewall of the cavity.

Apart from aligning the shadowgraph optical setup, calibration and mounting of thermistors, likewise, must be implemented before temperature measurements. Since the temperature variation in the thermal boundary layer is large, small errors in the location of the thermistors impacts on the temperature measurement. Therefore, the mounting and positioning of the thermistors must be carefully performed.

In an experiment, it is very important to maintain an appropriate initial experimental condition, at which the fluid in the cavity is motionless and isothermal. For the purpose of obtaining an isothermal ambient, it is necessary to fully stir the fluid in the cavity after the last experiment finishes or before the next experiment starts. This is because the fluid in a differentially heated cavity is stratified in the quasi-steady stage (also see Gill 1966). Furthermore, in order to make the fully disturbed fluid motionless, the fluid in the cavity needs to settle down for a long period (usually one day here) after the last experiment finishes. Ideally, after the above-mentioned two stages, a motionless and isothermal fluid ambient in the cavity may be achieved. However, since there always exist some external disturbances (such as the temperature variation of the air in the laboratory) in experiments, which cannot be completely removed, an idealized motionless and isothermal fluid in the cavity is only approximately achieved.

Once the above-mentioned initial experimental conditions are achieved, the water in the water bath may be heated or cooled to the specified temperature by the circulators. Two circulators are employed to heat the water in a water bath and the other two circulators in conjunction with an immersion chiller cool the water in the other water bath.

After the specified water temperature in each water bath is achieved and all experimental facilities (e.g. the data or image acquisition system) are ready, the experiment may be started. When the switch of the pneumatic system is turned on, the two pneumatically operated gates rapidly and synchronously lift, and the water from each water bath flushes against the copper walls of the experimental cavity. This process is completed in a fraction of a second; the actual time is controlled by the pneumatic system. Usually, the transition of the natural convection flow from the start-up to the quasi-steady state persists for more than one hour, depending on the Rayleigh number (e.g. experiments could persist for several hours at some Rayleigh numbers). After the experiment finishes, the switch of the pneumatic system is turned off and the gates shut down. Water remaining in the gap needs to be discharged through drainpipes for the next experiment. Therefore, the next experiment may be implemented in the above-mentioned procedures repeatedly.

In summary, a great number of experiments have been successfully performed and useful results have been obtained based on careful experiments (chapters 4 and 6).

3 Formulation and numerical procedures

In this chapter, the governing equations describing natural convection in a suddenly heated cavity are first presented and simplified. Numerical procedures for solving the governing equations by using the FLUENT package are introduced. A great number of tests of the grid and time step dependences for different cases with and without a fin on the sidewall have been performed and are described.

3.1 Formulation

3.1.1 Governing equations

It is critical to establish some basic assumptions and accurate formulas for describing a problem before any numerical procedures are implemented. Although this is always a challenge for the analyses of fluid flow and heat transfer problems, a great deal of fruitful work has been achieved. Natural convection in a differentially heated cavity satisfies the conservation of mass, momentum, and energy under the assumption of continuous media. The mathematical expressions of these conservation equations may be written together with the equation of state in Cartesian tensor notation as follows.

The continuity equation describing the conservation of mass:

$$\frac{\partial \rho}{\partial t} + \frac{\partial (\rho u_j)}{\partial x_j} = 0, \tag{3.1}$$

The momentum equation expressing the conservation of momentum based on Newton's second law:

$$\rho \frac{Du_i}{Dt} = -\frac{\partial p}{\partial x_i} + \rho F_i + \frac{\partial}{\partial x_j}\left[\mu\left(\frac{\partial u_i}{\partial x_j} + \frac{\partial u_j}{\partial x_i}\right)\right] - \frac{2}{3}\frac{\partial}{\partial x_i}\left(\mu \frac{\partial u_j}{\partial x_j}\right), \tag{3.2}$$

The energy equation representing the transport of the energy:

$$\rho c_p \frac{DT}{Dt} = u_j \frac{\partial p}{\partial x_i} + \frac{\partial}{\partial x_j}\left(k \frac{\partial T}{\partial x_j}\right) + \mu\left[\frac{\partial u_i}{\partial x_j}\left(\frac{\partial u_i}{\partial x_j} + \frac{\partial u_j}{\partial x_i}\right) - \frac{2}{3}\left(\frac{\partial u_j}{\partial x_j}\right)^2\right], \tag{3.3}$$

The equation of state:

$$\rho = \rho(p, T). \tag{3.4}$$

In the above equations, the body force F_i has three components: F_x, F_y and F_z in x-, y-, and z-directions. In addition, D/Dt is the material derivative operator defined as follows,

$$\frac{D}{Dt} = \frac{\partial}{\partial t} + u_j \frac{\partial}{\partial x_j}. \tag{3.5}$$

3.1.2 Simplifications of the governing equations

The governing equations presented in the previous section are highly non-linear and coupled, and are difficult to solve. Therefore, it is of significance to simplify these equations based on particular features of flows so that numerical discretizations and analyses may be easily performed.

For the present problem of transient natural convection in a differentially heated rectangular cavity (refer to Chapter 2 for more details about the model), it is understood that the fluid near the hot sidewall is heated and a temperature gradient forms. As discussed in Chapter 1, such a temperature gradient in turn results in a density gradient of the fluid in the vicinity of the hot sidewall, and with the presence of gravitational force, generates a buoyancy force. If the temperature difference between the two sidewalls in the cavity is not very large, the correlation between the density and temperature may be considered as a linear relation. As a result, the equation of state (3.4) may be given by

$$\rho = \rho_0 (1 - \beta(T - T_0)). \tag{3.6}$$

The thermal expansion coefficient (β) is generally of an order of magnitude between 10^{-2} and 10^{-4} for different fluids (Ostrach 1964). In the present study, the thermal expansion coefficient of water as the working fluid is assumed constant (approximately 0.00023 K^{-1}).

For natural convection flows with a relatively small temperature difference and a low velocity, the incompressible flow assumption is appropriate (see e.g. Batchelor 1954). Accordingly, the continuity equation (3.1) may be simplified as follows,

$$\frac{\partial u_j}{\partial x_j} = 0. \tag{3.7}$$

The Boussinesq approximation may be applied to natural convection in differentially heated cavities. Under the Boussinesq approximation, all fluid properties such as the viscosity and thermal conductivity are treated as constants except the density, and the variation of density is only considered when calculating the buoyancy force. Since there is no other volume force, the body force in Equation (3.2) has only the component (F_y) in the y-direction due to the density variation and may be written as (the positive direction points upwards, opposite to the accelerate under the gravity)

$$\rho F_y = (\rho - \rho_0) \times (-g). \tag{3.8}$$

Substitution of Equation (3.6) into Equation (3.8) leads to

$$F_y = g\beta(T - T_0). \tag{3.9}$$

Applying Equations (3.7) and (3.9) to Equation (3.2) yields a simplified momentum equation as follows

$$\frac{Du_i}{Dt} = -\frac{1}{\rho}\frac{\partial p}{\partial x_i} + \nu\frac{\partial^2 u_i}{\partial x_j \partial x_j} + F_i. \tag{3.10}$$

Here, the components of the body force (F_i) in the x- and z-directions are zero (i.e. F_x = F_y = 0)

Since the velocity of the natural convection flow in a cavity is normally small, the viscous energy dissipation and the pressure work (due to the incompressible assumption) may be neglected. The energy equation (3.3) may be simplified as

$$\frac{DT}{Dt} = \kappa\frac{\partial^2 T}{\partial x_j \partial x_j}. \tag{3.11}$$

The simplified continuity, momentum and energy equations consist of Equations (3.7), (3.10) and (3.11). Previous studies (see e.g. Dol & Hanjalic 2001) have also demonstrated that 2D numerical simulations can characterize major features of natural convection in a differentially heated cavity. Accordingly, in this thesis only 2D numerical simulations are performed. The complete set of 2D simplified governing equations are expressed as follows,

$$\frac{\partial u}{\partial x} + \frac{\partial v}{\partial y} = 0, \tag{3.12}$$

$$\frac{\partial u}{\partial t} + u\frac{\partial u}{\partial x} + v\frac{\partial u}{\partial y} = -\frac{1}{\rho}\frac{\partial p}{\partial x} + \nu(\frac{\partial^2 u}{\partial x^2} + \frac{\partial^2 u}{\partial y^2}), \tag{3.13}$$

$$\frac{\partial v}{\partial t} + u\frac{\partial v}{\partial x} + v\frac{\partial v}{\partial y} = -\frac{1}{\rho}\frac{\partial p}{\partial y} + \nu(\frac{\partial^2 v}{\partial x^2} + \frac{\partial^2 v}{\partial y^2}) + g\beta(T - T_0), \tag{3.14}$$

$$\frac{\partial T}{\partial t}+u\frac{\partial T}{\partial x}+v\frac{\partial T}{\partial y}=\kappa\left(\frac{\partial^2 T}{\partial x^2}+\frac{\partial^2 T}{\partial y^2}\right). \quad (3.15)$$

The above set of governing equations have been successfully adopted in previous numerical simulations of natural convection in a differentially heated cavity (refer to Schladow et al. 1989). However, it is worth noting that, in the case with a large temperature difference, the fluid does not satisfy the Boussinesq approximation, and thus cautions must be taken when adopting the above equations.

3.1.3 Initial and boundary conditions

The momentum and energy equations (Equations (3.13) through (3.15)) for velocity and temperature are parabolic in time and elliptic in space. Therefore, initial values must be defined for all quantities (at t = 0) and boundary conditions are required at each boundary of the computation domain.

Since a very weak stratification of the fluid and very weak flows are always unavoidable in the cavity before the start-up of experiments, as described in Chapter 2, the real initial fluid in the model cavity is neither motionless nor isothermal. Therefore, it is considerably difficult to specify the actual initial conditions of flows in the cavity. However, for the sudden heating problem considered in this study, the initial weak stratification and flows are unlikely to affect the development of natural convection and heat transfer, which is dominated by the thermal boundary layers adjacent to the sidewalls. Accordingly, an initially motionless and isothermal flow is adopted in all numerical simulations. These approximations of the initial conditions were also assumed by previous studies (see e.g. Patterson & Armfield 1990).

Due to the poor conduction of the top and bottom perspex walls of the model cavity, the top and bottom boundaries are considered adiabatic in the numerical simulations. The two copper sidewalls, which are very thin (only 1.13 mm) and highly conductive, are considered isothermal. In addition, the rigid and non-slip wall condition is applied to all interior surfaces. Similarly, all the surfaces of the perspex fin are considered adiabatic and non-slip. Figure 3.1 shows all the above-mentioned boundary conditions. In numerical simulations of this thesis, the initial and average temperature of the fluid in the cavity is 295.55 K and the temperature difference between the hot and cold sidewalls 16 K so that numerical results may be compared each other and with the corresponding experimental results.

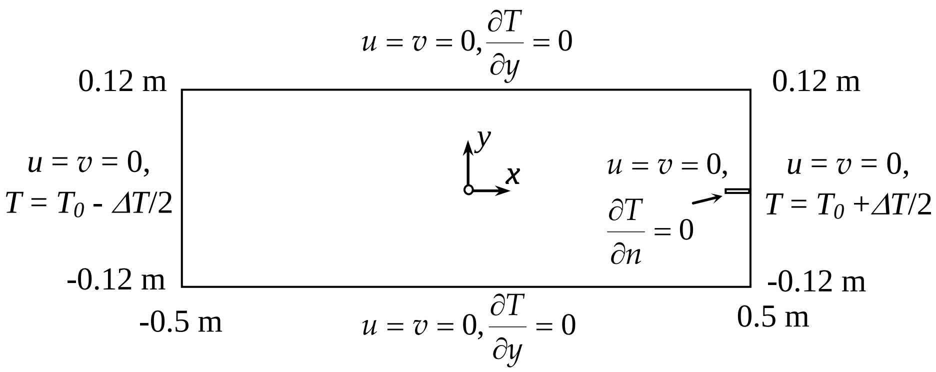

Figure 3.1 Schematic of the computational domain and boundary conditions

3.2 Numerical procedures

As mentioned previously, despite significant simplifications Equations (3.12) through (3.15) are still coupled and nonlinear, and cannot be solved analytically. Therefore, numerical methods are usually applied to obtain approximate solutions. Over the last three decades, a considerable number of commercial CFD (computational fluid dynamics) packages such as PHOENICS, CFX, and FLUENT have been developed. These commercial CFD packages have also been improved continuously over the years. In this thesis, FLUENT was employed to perform all numerical simulations.

3.2.1 Numerical Schemes

A number of finite volume and finite difference based schemes have been developed and applied to simulations of natural convection in the cavity. Studies (see e.g. De Vahl Davis 1983; Schladow et al. 1989; Le Quere 1990) showed that there is no remarkable discrepancy among various numerical schemes. However, it is still necessary to carefully test each scheme before it is applied to any new computational cases.

In the present study, the 2D finite volume scheme is used to discretize the governing equations, with a second order centre-difference scheme approximating the diffusion term, a second order upwind-difference scheme approximating the advection terms and a second order implicit time-marching scheme for the unsteady term; that is, the computational domain is divided into discrete control volumes (also called surfaces for 2D calculations) through a meshing process. The governing equations are integrated about each control volume to construct algebraic equations with respect to discrete unknown quantities such as velocities, pressure, and temperature. The linearized and discretized algebraic equations are then solved to update values of dependent quantities using Semi-Implicit Method for Pressure-Linked Equation (SIMPLE, see Partankar 1980; or FLUENT User's Guide for details).

The continuity, momentum and energy equations may be written as a united transport equation, which is then integrated over a control volume to yield the following integrated transport equation,

$$\int_V \frac{\partial \phi}{\partial t} dV + \oint \phi \vec{v} \cdot d\vec{A}_e = \oint \Gamma_\phi \nabla \phi \cdot d\vec{A}_e + \int_V S_\phi dV. \tag{3.16}$$

Since the numerical solutions are all 2D in this study, control volumes become control surfaces. Thus, the integration $\int_V$ is implemented on control surfaces (V), and the integration $\oint$ is implemented along the edges of control surfaces. The definitions of the quantities ϕ, Γ_ϕ and S_ϕ in Equation (3.16) corresponding to different conservation equations are listed in Table 3.1.

Table 3.1 Definitions of ϕ, Γ_ϕ and S_ϕ in Equation (3.16)

Equations	ϕ	Γ_ϕ	S_ϕ
Continuity Eq. (3.12)	1	0	0
x-Momentum Eq. (3.13)	u	ν	$-\partial p/\rho\partial x$
y-Momentum Eq. (3.14)	v	ν	$-\partial p/\rho\partial y + g\beta(T-T_0)$
Energy Eq. (3.15)	T	κ	0

In order to illustrate the discretization of the governing equations, the steady state transport equation (with the inertia term ignored, see below) is first considered as follows,

$$\oint \phi \vec{v} \cdot d\vec{A}_e = \oint \Gamma_\phi \nabla \phi \cdot d\vec{A}_e + \int_V S_\phi dV. \tag{3.17}$$

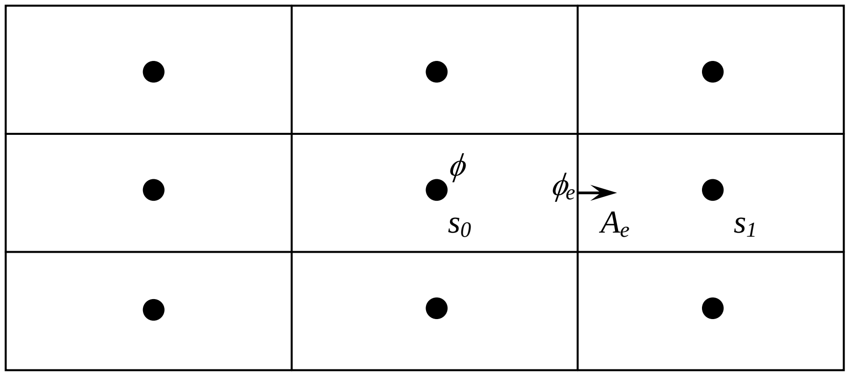

Figure 3.2 Control surfaces used to discretize the governing equations

To discretize Equation (3.17), the computational domain is meshed. Figure 3.2 shows an example of control surfaces to illustrate the discretization of the transport equation. Discrete values of the scalar ϕ are stored at the surface centers. Equation (3.17) may be discretized on a given surface (s_0) as follows,

$$\sum_{e}^{nb} \phi_e \vec{v}_e \cdot \vec{A}_e = \sum_{e}^{nb} \Gamma_\phi (\nabla\phi)_n \cdot \vec{A}_e + S_\phi V. \tag{3.18}$$

The values on the surface edges ϕ_e are required for the convection terms in Equation (3.18). They are interpolated from the surface center values. It may be computed using a second-order upwind scheme as follows,

$$\phi_e = \phi + \nabla\phi \cdot \Delta\vec{s}. \tag{3.19}$$

In Equation (3.19), the gradient $\nabla\phi$ may be determined according to the divergence theorem, which in the discrete form is written as

$$\nabla\phi = \frac{1}{V}\sum_{e}^{nb} \bar{\phi}_e \vec{A}_e. \tag{3.20}$$

Here $\bar{\phi}_e$ on the edge is computed by averaging ϕ on the two surfaces adjacent to the edge. Therefore, the gradient $\nabla\phi$ is in fact limited so that no new maxima or minima are introduced (refer to FLUENT User's Guide for more details).

It is worth noting that the momentum and continuity equations are solved sequentially, in which the continuity equation appears as an equation of pressure correction although pressure does not appear explicitly in the continuity equation for incompressible flows (i.e. the SIMPLE method). The numerical procedure of the SIMPLE method is shown in Figure 3.3.

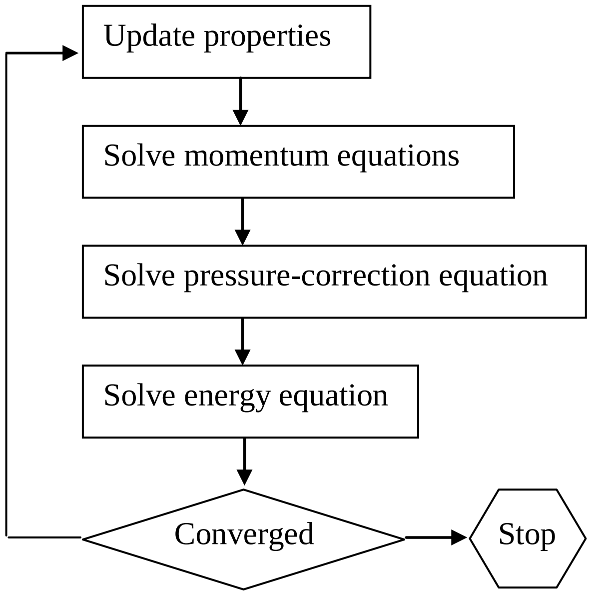

Figure 3.3 Flow chart of the SIMPLE method

The temporal discretization involves the integration of each term in the differential equations over a time step Δt. The integration of the transient terms is straightforward, and a generic expression for the time evolution of a quantity ϕ is given below,

$$\frac{\partial \phi}{\partial t} = F(\phi). \tag{3.21}$$

Here the function $F(\phi)$ incorporates any spatial discretization. The time derivative is discretized using backward difference, and a second-order scheme is written, as follows,

$$\frac{3\phi^{n+1} - 4\phi^{n} + \phi^{n-1}}{2\Delta t} = F(\phi^{n+1}). \tag{3.22}$$

Here, the implicit time integration is employed in order to evaluate $F(\phi)$ at the future time instance due to an advantage of the implicit scheme that it is unconditionally stable with respect to the time step. This implies that $\phi^{(n+1)}$ in a surface is related to $\phi^{(n+1)}$ in neighboring surfaces through $F(\phi^{n+1})$. The implicit equation may be solved by iterating the following equation,

$$\phi^{n+1} = \frac{4}{3}\phi^{n} - \frac{1}{3}\phi^{n-1} + \frac{2}{3}\Delta t F(\phi^{n+1}), \tag{3.23}$$

The iteration terminates until convergence criteria are met. The truncation error here is second-order with respect to the time step.

Because of the nonlinearity of Equations (3.12) to (3.15), it is necessary to control the change of ϕ during the iterations (see e.g. Henkes 1990). This is usually achieved by under-relaxation, which reduces the change of ϕ through an under-relaxation factor. In a simple form, the updated value of ϕ on a surface is calculated from the old value ϕ_{old}, the computed change $\Delta\phi$ and an under-relaxation factor α_r as follows,

$$\phi = \phi_{old} + \alpha_r \Delta\phi. \tag{3.24}$$

In the present study, the under-relaxation factor α_r is set to 0.3 for pressure, 0.7 for velocities, ant 1 for all others quantities.

3.2.2 Convergences

As indicated in Section 3.2.1, convergence criteria, which determine the efficiency and success of iterations, control the iteration processes. Therefore, selecting an appropriate convergence criterion is crucial for an iteration process. The appropriateness of a convergence criterion is measured by two factors: the convergence accuracy and speed. The former factor plays an important role in the numerical computations of unsteady transition and turbulence. This is because the numerical errors from previous time steps could be accumulated in subsequent ones. If the convergence criterion is inappropriately set, the numerical solution could deviate from the real physical flow.

In the present numerical solving using FLUENT 6.2.16, the sum of residuals of each equation is selected as the convergence criterion to control iterations; that is, at the end of each iteration, the sum of residuals of conserved variables is computed and compared with the set convergence criterion. The iterations will continue until the sum of residuals drops below the set convergence criterion.

The conservation equation for a general quantity ϕ at a surface s_0, after discretization (see Equations (3.18) to (3.20)), is written below,

$$a_{s_0}\phi_{s_0} = \sum_{nb} a_{nb}\phi_{nb} + b. \tag{3.25}$$

Therefore, the residual R_ϕ may be defined as the imbalance in Equation (3.25) summed over all computational surfaces as (see FLUENT User's Guide),

$$R_\phi = \frac{\sum_{s_0}\left|\sum_{nb} a_{nb}\phi_{nb} + b - a_{s_0}\phi_{s_0}\right|}{\sum_{s_0}\left|a_{s_0}\phi_{s_0}\right|}. \tag{3.26}$$

For the momentum equations and energy equation, ϕ is replaced by u, v or T respectively. For the continuity equation, the residual is defined by

$$R_{\phi} = \frac{\sum_{s_0} |\text{rate of mass creation in surface } s_0|}{\sum_{\text{Max in first five iterations}} |\text{rate of mass creation in surface } s_0|}. \tag{3.27}$$

Here, the denominator is the largest absolute value of the continuity residual in the first five iterations. A more detailed elucidation of Equations (3.26) and (3.27) may be found in FLUENT User's Guide, in which R_{ϕ} in Equations (3.26) and (3.27) is referred to as a scaled residual.

For double precision requirement, FLUENT permits residuals to drop down to twelve orders of magnitude (10^{-12}). However, in most numerical simulations of the present study, 10^{-3} is adopted as the convergence criteria of the continuity, momentum and energy equations after a number of tests are performed. In fact, a smaller criterion, such as 10^{-6}, is tested in some computational cases in which no distinction between the results obtained with two different residual criteria of 10^{-3} and 10^{-6} is identified. Therefore, a residual criterion of 10^{-3} is finally adopted in consideration of significant savings of computing time.

3.3 Grid and time step

3.3.1 Grid creation

The quality of the grid plays a key role in the accuracy and stability of numerical simulations. Since a continuous physical domain is discretized in numerical simulations, the degree to which the salient features of the flow (such as boundary layers) are resolved depends on the density and distribution of grid nodes. Poor resolution in critical regions could dramatically alter the representation of the flow features. Unfortunately, it is considerably difficult to determine the locations of significance before the calculation is actually carried out. Moreover, the grid resolution in complex flow fields is also constrained by computing resources (memory, storage space and CPU time etc). Although the numerical accuracy in general increases with the grid resolution, the required computing resources for both calculation and post-processing also increase. Therefore, it is necessary to compromise between the numerical accuracy and computing efficiency when considering numerical grid.

In regions with large gradients of flow variables the grid should be fine enough to minimize the change in flow variables from surface to surface. For example, the grid resolution in a boundary layer (i.e. grid spacing near a wall) is important for computing the wall shear stress and heat transfer coefficient.

Although it is difficult to predict the locations of large flow gradients, we can assume some regions of significance based on previous knowledge. Accordingly, a grid system may be constructed, which is then refined until the entire flow domain is properly meshed.

For natural convection in a differentially heated cavity, strong flows are present in the vicinity of the sidewalls (see e.g. Patterson & Armfield 1990). Therefore, a non-uniform grid is often adopted with concentrated grids in the boundary layer and relatively coarse grids in the interior region. For instance, the grid may expand at a rate from the wall until the interior edge of the boundary layer is reached. The expanding factor of the grid is usually limited in order to ensure that the solution is not degraded, and a factor of up to 10% may be used according to Patterson and Armfield (1990).

Experimental results have demonstrated that, in the transition of natural convection in the present experimental cavity from sudden heating to the quasi-steady state, strong flows usually occur within a region of 0.05-m width adjacent to the walls in the dimension of the present cavity (Figure 3.1). This region is defined as the boundary layer zones in this study. A non-uniform grid system with an expansion factor from the wall surface to the interior is adopted in the boundary layer zones. The rest of the flow domain (the central region of the cavity) is uniformly meshed.

Three grids are created for the case without a fin on the sidewall in order to test the grid dependence, and their parameters are listed in Table 3.2.

Table 3.2 Grid parameters without a fin

Grid ($H \times L$)	Boundary layer zone		Centre zone	
	GN	EF	Vertical GN	Horizontal GN
133×387	43	1.057	47	301
199×563	66	1.040	67	431
395×1155	127	1.018	141	901

Note: Hereinafter, the number of the grid is referred to as GN; the expansion factor is referred to as EF.

For the cases with a fin on the sidewall, different grids from those without a fin are created. Since the size of the fin is much smaller than that of the cavity, the grid distribution on the surfaces of the fin is uniform and finer than those in other zones, as

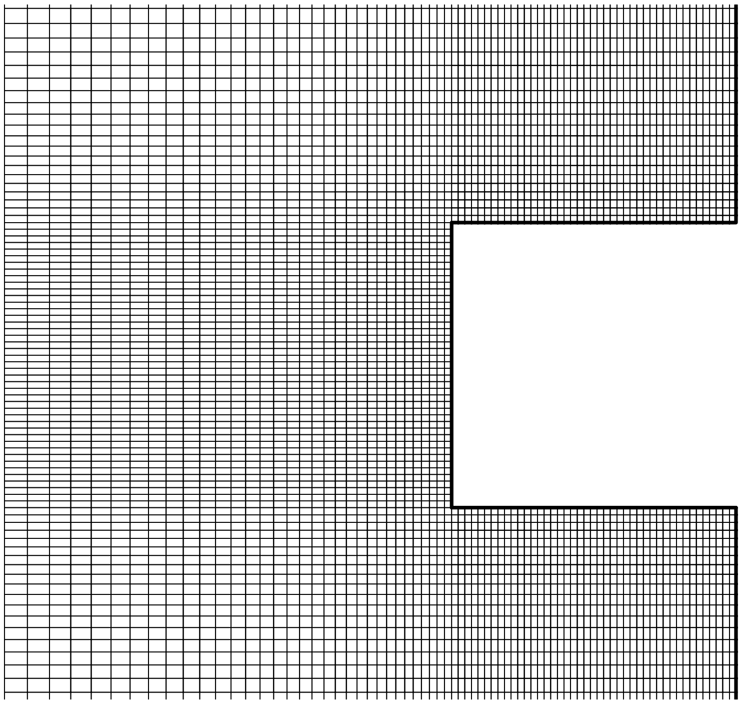

Figure 3.4 Grid distributions around a square fin

shown in Table 3.3. In the horizontal direction, two boundary layer zones of 0.1-m width adjacent to the sidewalls are defined, to which non-uniform grids are applied (see Table 3.3). Similar to those without a fin, the centre zone between the two boundary layer zones is uniformly meshed, and the number of the grid is listed in Table 3.3. In the vertical direction, grid distributions on the upper and lower halves of the cavity are symmetric with the grid symmetrically expanding toward the middle of each half cavity at certain rate (see Table 3.3). For the grid dependence tests, two grids are created for each case, as listed in Table 3.3.

Table 3.3 Grid parameters with a fin on the hot wall

Fin's cross section (mm^2)	Grid (H×L)	Grid distributions							
		Surfaces normal to fin	Horizontal					Vertical	
			Zone near cold wall		Centre zone (GN)	Zone near hot wall		GN	EF
		GN	GN	EF		GN	EF		
10 × 10	281 × 463	43 × 43	82	1.0334	231	73	1.0372	119	1.039
	425 × 671	63 × 63	119	1.023	331	107	1.0256	181	1.0258
20 × 2	211 × 467	9 × 87	82	1.0334	231	67	1.0414	101	1.0565
	259 × 596	9 × 87	105	1.0233	319	84	1.0293	125	1.0398
40 × 2	211 × 538	9 × 175	82	1.0334	231	50	1.056	101	1.0565
	259 × 743	9 × 175	105	1.0233	319	62	1.0395	125	1.0398

Figure 3.4 shows the grid distribution adjacent to a square fin. It is clear that a finer grid has been constructed around the fin.

3.3.2 Grid dependence tests

Selected results of the grid dependence tests for the case without a fin are listed in Table 3.4, which includes the temperature and *y*-velocity calculated at the point (0.498 m, 0.09 m) in the vertical boundary layer, the total heat transfer rate of the hot wall, and the normalized temperature gradient (S) in the center of the cavity at the quasi-steady state (see e.g. Janssen 1994 for definition). Except for the coarsest grid (133 × 387), the variations of the calculated results with different meshes are very small (less than 1%). This implies that either of the two finer grids may be used to resolve the quasi-steady state flow in the differentially heated cavity at a high Rayleigh number of 3.8×10^9.

Table 3.4 Grid dependence tests without a fin (t = 6000 s)

Grid ($H \times L$)	Temperature at point (0.498 m, 0.09 m) (K)	v at point (0.498 m, 0.09 m) (mm/s)	H_{nofin} (W)	$S = (H/\Delta T)\partial T/\partial y$
133 × 387	299.838	5.30007	706.368	0.40336
199 × 563	299.735	5.66113	742.598	0.42065
395 × 1155	299.731	5.67114	741.251	0.42264

The unsteady results calculated using different grids are shown in Figure 3.5, which plots the calculated time series of the temperature at the point (0.498 m, 0.09 m) within the hot boundary layer in the early stage. It is seen in this figure that the two time series of the temperature calculated using the two finer grids vary slightly during the period when unstable waves are present (corresponding to the period with distinct peaks and troughs on the plots). At other times, these two plots overlap. However, the temperature time series calculated using the coarsest grid is evidently different from the others. Therefore, in consideration of computing time and accuracy, the medium fine grid (199 × 563) is adopted in subsequent calculations.

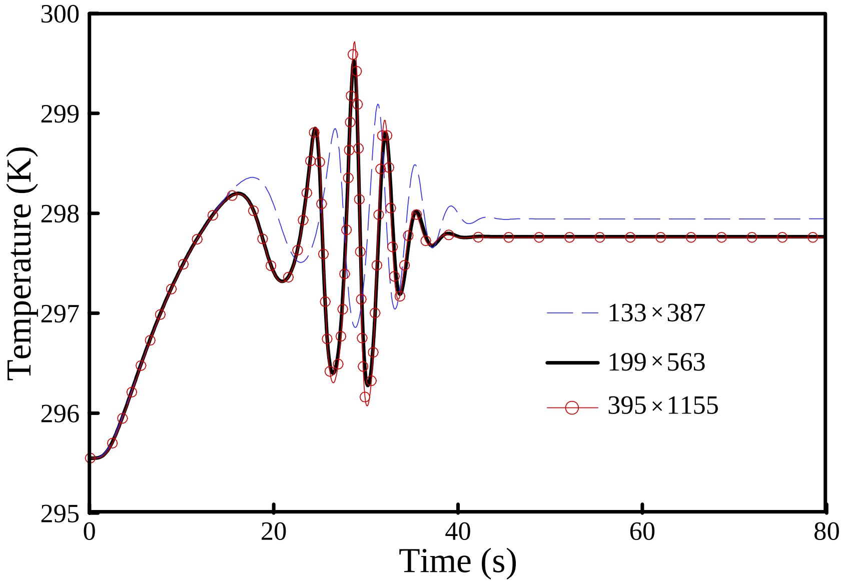

Figure 3.5 Temperature time series calculated by using different grids at the point (0.498 m, 0.09 m)

The results of the grid dependence test for the case with a square fin are presented in Table 3.5. It is found that the variations of the calculated quantities using the two different grids are considerably small (less than 2%), suggesting that either of the two grids may be used for this case.

Table 3.5 Grid dependence test with a square fin (t = 6000 s)

Fin's cross section (mm^2)	Grid ($H \times L$)	Temperature at point (0.498 m, 0.09 m) (K)	v at point (0.498 m, 0.09 m) (mm/s)	H_{fin} (W)	$S = (H/\Delta T)\partial T/\partial y$
10 × 10	281 × 463	299.608	5.53995	734.87	0.41927
	425 × 620	299.602	5.54749	734.75	0.41087

Figure 3.6 shows the calculated time series of the temperature at the point (0.498 m, 0.09 m) in the early stage. In spite of strong perturbations due to the presence of the fin on the sidewall, as can be seen from the comparison between Figures 3.5 and 3.6, the results calculated using the two grids are basically identical. This suggests that both grids can resolve the unsteady natural convection in the early stage. In consideration of the computing time, the coarser grid (281 × 463) is adopted in this thesis.

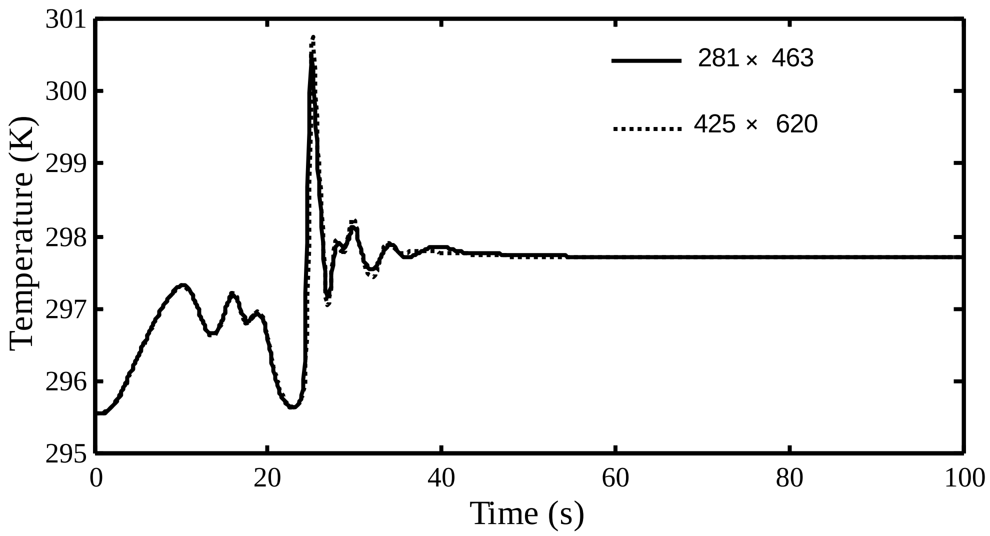

Figure 3.6 Temperature time series at the point (0.498 m, 0.09 m) calculated by using different grids for the case with a square fin of 10 × 10 mm^2

In the case with large thin fins, instability of the vertical boundary layer is induced (refer to Chapter 7). Accordingly, a different set of flow parameters (from those presented in Tables 3.4 and 3.5) is examined in the grid dependence tests. These include the average amplitude and frequency of temperature waves and the total heat transfer rate of the hot wall (see Table 3.6). It is clear that the frequency of traveling waves in the vertical thermal boundary layer, the average temperature at the point (0.498 m, 0.09 m) and the heat transfer rate of the hot wall are not sensitive to the present grid resolutions. Although the calculated amplitude changes slightly between different grids, these variations are unlikely to change the overall features of the unsteady natural convection induced by the thin fin.

Table 3.6 Grid dependence test with thin fins (5900 s ~ 6000 s)

Fin's cross section (mm^2)	Grid ($H \times L$)	Temperature at point (0.498 m, 0.09 m)			H_{fin} (W)
		Average (K)	Amplitude (K)	Frequency (Hz)	
20 × 2	211 × 467	299.520	2.3091	0.1563	729.40
	259 × 596	299.472	2.4154	0.1563	735.85
40 × 2	211 × 538	299.449	1.2856	0.1172	746.39
	259 × 743	299.309	1.3825	0.1172	742.87

In fact, the unsteady natural convection flows at t = 6000 s, with the presence of the thin fins, have not reached a quasi-steady state yet; that is, they are still in a

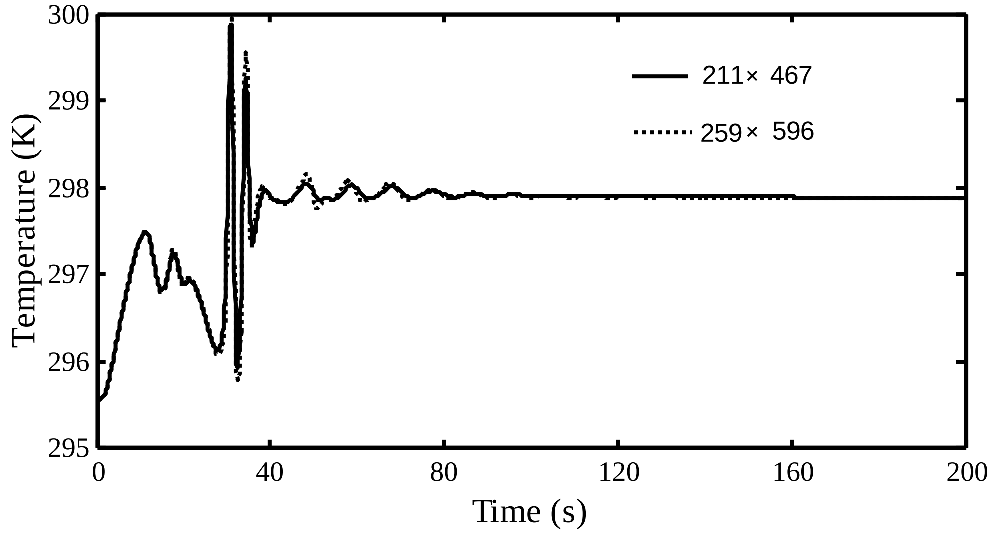

(a) For the case with a fin of 20 × 2 mm^2

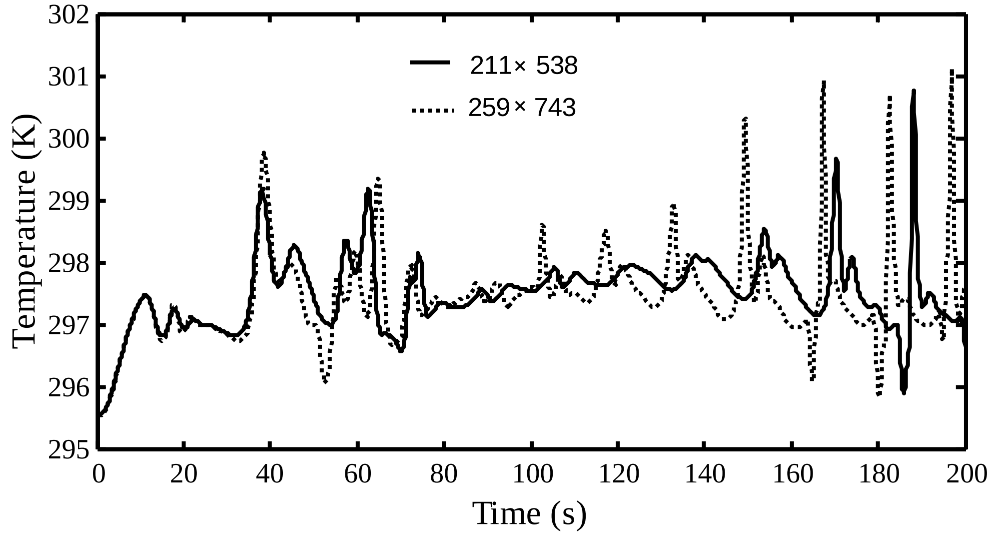

(b) For the case with a fin of 40 × 2 mm^2

Figure 3.7 Temperature time series at the point (0.498 m, 0.09 m) calculated by using different grids for the cases with different thin fins

transition from the start-up flow to a periodic flow, and the traveling waves in the vertical thermal boundary layer continue to grow. Therefore, the grid dependence test results for the cases with thin fins do not characterize the differences between different grids at the quasi-steady state. However, since the computation of the unsteady natural convection with a thin fin is extremely time-consuming, it is not feasible to carry the mesh dependence tests further in order to examine the variations of the numerical results at the quasi-steady state.

Figure 3.7 shows the time series of the temperature at the point (0.498 m, 0.09 m) in the early stage calculated using different grids for the cases with thin fins. The results for the case with the smaller thin fin (20 × 2 mm^2) are shown in Figure 3.7(a). It is clear that the calculated temperature in the early stage is not sensitive to the grid. Therefore, the coarser (211 × 467) of the two grids is adopted in this thesis. For the case with the larger thin fin (40 × 2 mm^2), Figure 3.7(b) indicates that there are major differences in the calculated amplitude and phase of the traveling waves using the two grids. Since the emphasis of this study is not on the details of individual traveling wave but the statistical features of the traveling waves (refer to Table 3.6), the grid of 211 × 538 is used to simulate the flow for the case with the larger thin fin.

3.3.3 Time step dependence tests

The time step refinement is also important for accurately resolving the natural convection flow with and without a fin on the sidewall in a differentially heated cavity through numerical simulations; that is, tests of the time step are necessary in order to obtain reliable numerical solutions.

Figure 3.8 shows the test results obtained using different time steps for various cases. It is clear that a time step of 0.1 second (significantly smaller than 0.7 s used by Patterson and Armfield 1990) is sufficiently small to capture various features of the natural convection flow in this study, and the stability of the scheme is guaranteed with this time-step. Except for the case with the larger thin fin (40 × 2 mm^2), the time series of the calculated temperatures are not sensitive to the time step (see Figures 3.8b and c), and thus a time step of 0.1 s is adopted for these cases. For the case with the larger thin fin (40 × 2 mm^2), although there are distinct variations between the results calculated using the two time steps (see Figure 3.8d), a time step of 0.1 s is also used in the present study due to the consideration of the computing time.

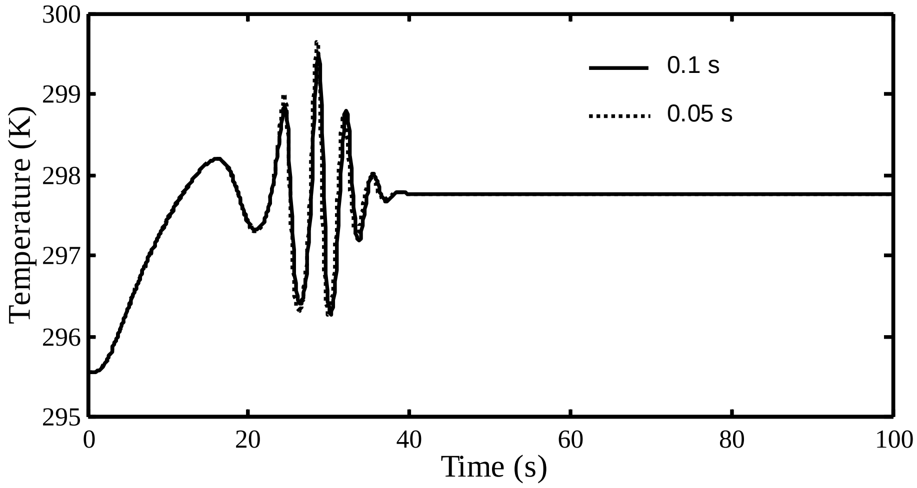

(a) For the case without a fin

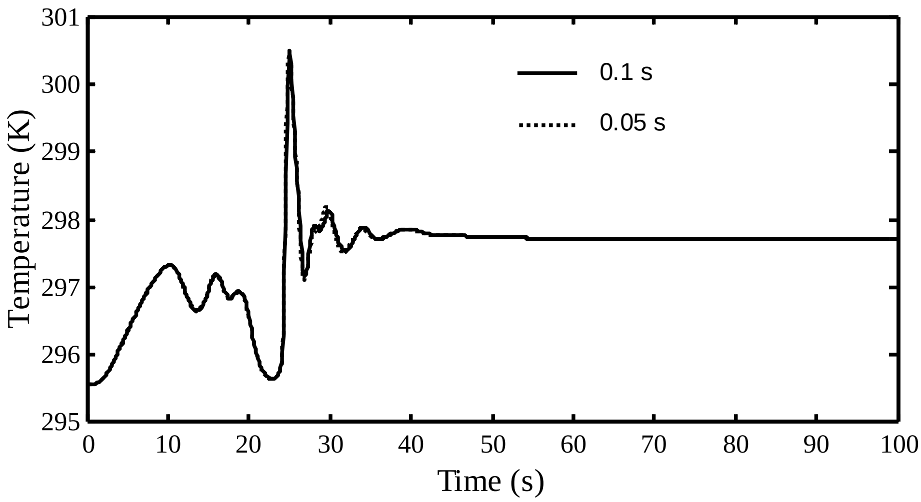

(b) For the case with a fin of 10×10 mm^2

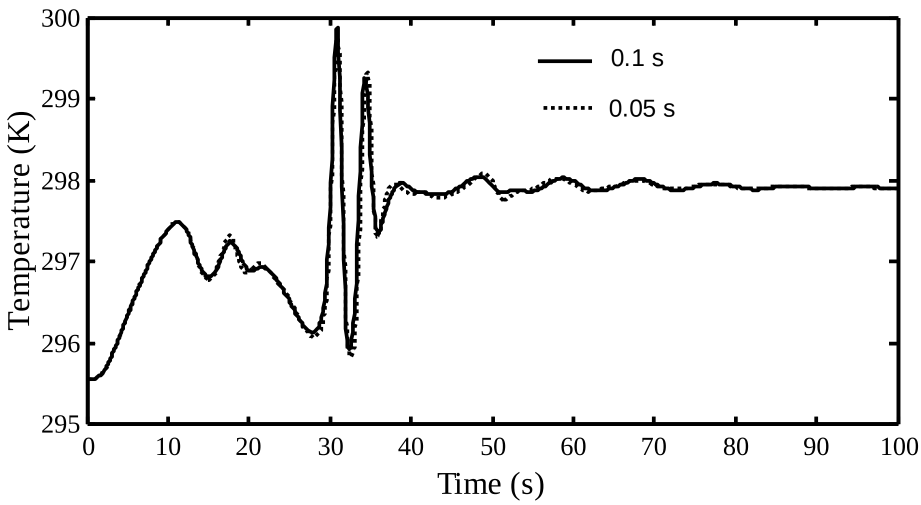

(c) For the case with a fin of 20×2 mm^2

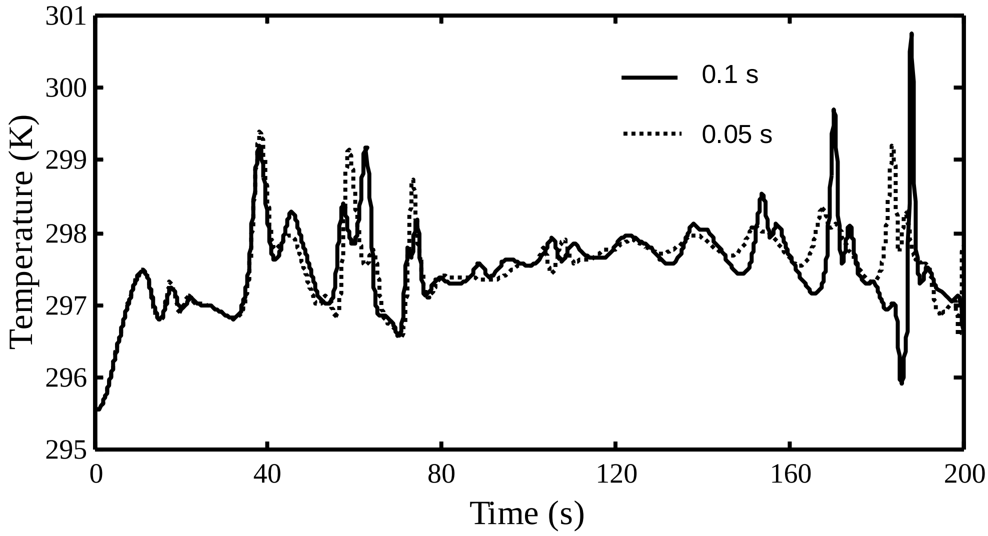

(d) For the case with a fin of 40 × 2 mm^2

Figure 3.8 Temperature series at the point (0.498 m, 0.09 m) calculated by using different time steps

3.4 Summary

In this Chapter, the 2D governing equations for numerical simulation of transient natural convection in a differentially heated cavity with and without a fin on the sidewall are presented. A finite volume method is used to discretize the governing equations. The linearized and discretized algebraic equations are then solved using the SIMPLE scheme. The above numerical procedures are performed using the FLUENT package. Since the FLUENT package has been validated in various flow simulations (see FLUENT User Guider), the further validation here has been neglected.

For different computation cases with and without a fin on the sidewall, mesh and time step dependences are tested. It has been demonstrated that the meshes and time steps to be adopted for different computation cases in the following chapters are appropriate.

4 Experimental investigations of the thermal boundary layer without a fin

Most of previous experimental studies focused on the early development of the flows, and the early transient features have been well characterized (see e.g. Patterson & Armfield 1990). For example, the LEE propagation in the vertical thermal boundary layer was visualized by Schöpf and Patterson (1995), and perturbations of temperature signals of the LEE were discussed by Patterson et al. (2002). These experiments validate and support the corresponding theories and numerical simulations (see e.g. Armfield & Patterson 1992; Schladow 1990). It is worth noting that many more experiments of the vertical thermal boundary layer were done by Gebhart and his co-workers (refer to Gebhart 1988), as reviewed in Chapter 1. Although their studies are the focus of flows adjacent to an isoflux flat plate, due to similar early transient features between the two categories of thermal boundary layer flows adjacent to an isothermal sidewall of a differentially heated cavity and an isoflux flat plate (see Patterson et al. 2002), some conclusions obtained from the case of the flat plate (e.g. the LEE) are likewise appropriate for those thermal boundary layer flows in the cavity. Furthermore, a representative transient natural convection experiment by Ivey (1984) also visualized the early horizontal intrusion flow, and the separation and trailing waves of the intrusion were discussed although the argument concerning the mechanism of separation remains unresolved (also refer to Patterson & Armfield 1990).

The above-mentioned cavity experiments were all aimed at the early transient flows for a sudden heating problem. However, the subsequent development of natural convection in a cavity to a steady or quasi-steady state has not been well documented except the experimental observations by Schöpf and Patterson (1996) in which the features of the traveling waves in the quasi-steady state were visualized. Therefore, flow visualizations and temperature measurements aimed at a complete transition of natural convection from the start-up to the quasi-steady state, and particularly at the further development of the vertical thermal boundary layer, are motivated and naturally become the focus of this thesis. In this chapter, flow visualizations are described in Section 4.1, temperature measurements are shown in Section 4.2, and a summary is given in Section 4.3.

4.1 Flow visualizations

All experiments described in this section are all performed on the experimental rig described in Chapter 2. The mean temperature of the water in the cavity in the experiments ranges from 293.2 to 295.9 K, and the temperature difference between the heated and cooled sidewalls varies from 2 to 31.6 K. The corresponding ranges of the experimental Rayleigh and Prandtl numbers are $4.5 \times 10^8 \sim 7.2 \times 10^9$ and 6.6 ~ 7.1, respectively. Unless specified otherwise, the images reported in this section are for the case with $Ra = 3.8 \times 10^9$ and $Pr = 6.6$. The parameters of all experiments shown in this section are listed in Table 4.1. In the following experimental illustrations, the origin of coordinates is defined at the center of the cavity, and the same coordinate system as defined in Chapter 3 is used (the hot sidewall is on the right); that is, the vertical coordinate is measured from the middle of the hot sidewall with the positive direction pointing upwards.

Table 4.1 Parameters of shadowgraph experiments in Section 4.1

Number	Initial temperature of water in the cavity (K)	Temperature difference between sidewalls (K)	Ra ($\times 10^8$)	Pr
1	295.55	4.0	9.4	6.6
2	295.55	16.0	38	6.6
3	295.50	20.0	47	6.7
4	295.00	32.0	72	6.7

The thermal boundary layer flow in a differentially heated cavity is an internal flow, and is, after the initial start up phase, strongly impacted by the top and bottom boundaries as well as the opposing wall. In the following context, the detailed transition from the start-up to the quasi-steady state and the corresponding kinematical properties of the thermal boundary layer are described. Three stages of the transition can be identified according to its dynamical and kinematical properties; these are an initial stage, a transitional stage and a quasi-steady stage.

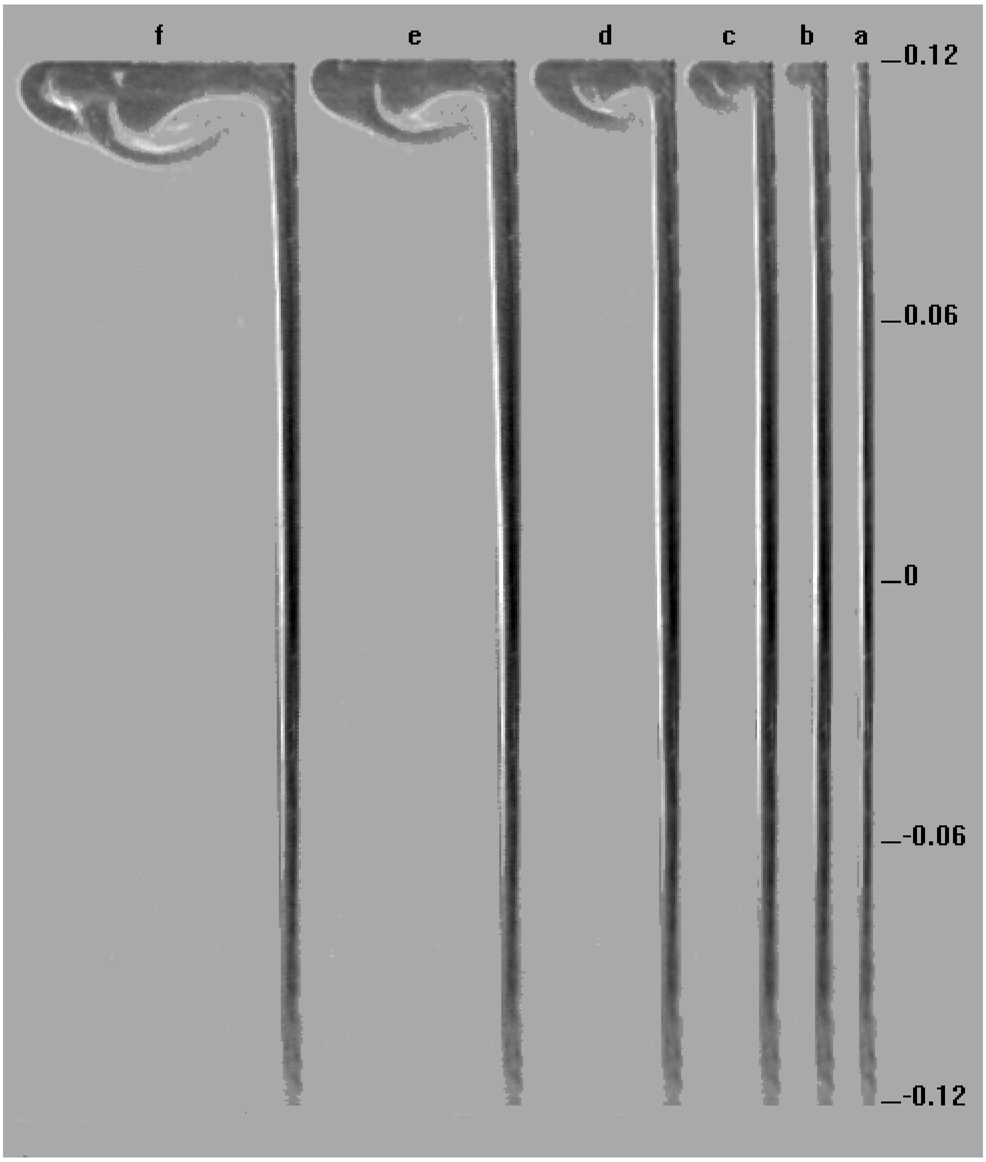

Figure 4.1 Transient response of the thermal boundary layer in the initial stage (The vertical position, relative to the origin at mid height, is shown on the right hand side) (a) t = 4 s. (b) t = 8 s. (c) t = 12 s. (d) t = 16 s. (e) t = 20 s. (f) t = 24 s

4.1.1 Initial stage

The initial stage lasts only for a short time, and displays two important kinematical features: the boundary layer thickness growth and the LEE perturbation in the transient response of the thermal boundary layer flow.

Figure 4.1 presents a series of shadowgraph images demonstrating the growth of the thermal boundary layer on the hot wall in this stage. In the shadowgraph images, the thermal boundary layer is approximately represented by the vertical dark regions,

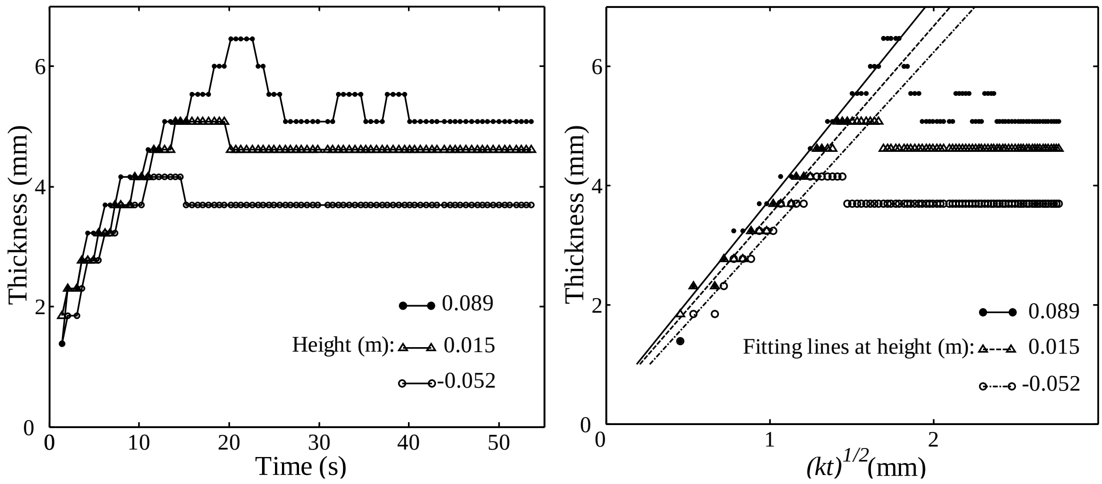

(a) Thicknesses against time (b) Thicknesses against $(\kappa t)^{½}$

Figure 4.2 Thickness growth of the thermal boundary layer at different heights

bonded by a clear bright strip. In accordance with the discussion in Chapter 2, these bright strips are associated with the extremum of the second derivative of the temperature in approximately the horizontal direction. This position may be used as a measure of the boundary layer thickness. It is clear in Figure 4.1 that the thickness of the boundary layer increases from upstream to downstream, and also grows with time. The shadowgraph images in Figure 4.1 have been processed by subtracting a background image recorded immediately before the start of the experiments in order to display more clearly the thickness variations of the thermal boundary layer.

A simple scaling relation (see Equation (1.5), also refer to Patterson & Imberger 1980) may be used to describe the thickness growth with time in the initial stage. This scaling is appropriate if heat transfer is dominated by conduction, which is true for the initial development of the thermal boundary layer. Figure 4.2(a) plots time series of the thicknesses measured at three different locations along the vertical wall. The thickness is determined as the width of the dark strips, or the position of the inner edge of the bright strip, typically shown in Figure 4.1, although the measurements have been taken from the full time series of images. The thickness values in Figure 4.2 show step changes with time. This is because the resolution of the imaging system is 0.44 mm per pixel in the present experimental set-up, and any variations of less than 0.44 mm cannot be detected by the imaging system. The same method for estimating the boundary layer thickness has been employed in Lei and Patterson (2002).

Figure 4.2(b) replots the measured thickness of the thermal boundary layer against the scaling prediction, and reveals that the experimental measurements fit well with the theoretical prediction of $(\kappa t)^{1/2}$ for the initial 10 seconds although the slopes of the fitting lines are not equal to unity. As time increases, the measurements deviate from the scaling (the deviating times at heights -0.052, 0.015 and 0.089 m are about 10 s, 14 s and 20 s, respectively), suggesting that convection effects become important. After approximately 20 seconds, the thickness at the height of 0.089 m starts to fluctuate and eventually approaches a constant value. The waves shown in Figure 4.2(a) are caused by the LEE.

Following the evolution in the initial stage, the horizontal intrusion and entrainment of the thermal boundary layer dominate the subsequent transition of the thermal boundary layer flow to the quasi-steady state. Therefore, the flow enters into the second stage, the transitional stage.

4.1.2 Transitional stage

The horizontal intrusion, which emanates from the downstream end of the thermal boundary layer, is the means by which the convective heat transfer occurs across the cavity. Figure 4.3(a) shows the intrusion front and the initial separation of the intrusion flow, and Figure 4.3(b) displays some trailing waves located at the upstream end of the intrusion front. Ravi et al. (1994) suggested that such a flow structure was the result of the relatively colder fluid separating from the ceiling after it reaches the top corner. However, as shown in Figure 4.3(b), the entire hot intrusion detaches from the ceiling after it leaves the corner. In fact, since there does not exist a strong stratification of the fluid in the cavity in the early intrusion stage (also see numerical results in Chapter 5), there is no colder part of the intrusion relative to the fluid near the corner.

Equations (3.13) and (3.14) indicate that the driving force for the intrusion flow may include the buoyancy force and the pressure gradient. In the early stage of the intrusion, the temperature of the intrusion is much higher than that of the fluid in the upper part of the cavity so that the buoyancy force is in the upward direction and against the separation of the intrusion from the ceiling. This implies that the driving force of the separation is not the buoyancy force but the pressure gradient. Detailed discussion concerning the mechanism of the separation, based on numerical simulations, is given in Chapter 5.

Figures 4.3(b) and (c) show the evolution of the separation and trailing waves at the early time. It is seen from Figure 4.3(c) that the intrusion jets from the corner toward

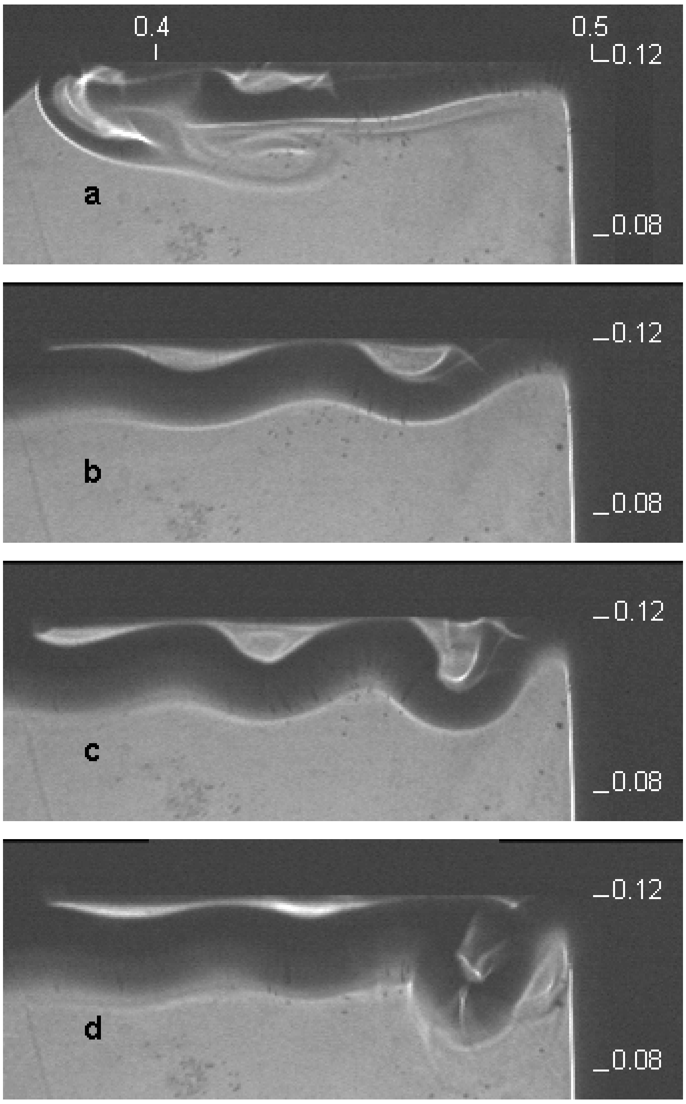

Figure 4.3 Early evolution of the horizontal intrusion
(a) t = 38 s. (b) t = 132 s. (c) t = 199 s. (d) t = 278 s

the core. As time elapses, the jet flow gradually trends to the vertically downward direction, thus leading to larger amplitude trailing waves. The non-linear effect of the large amplitude waves (Drazin 2001) can cause the first trailing wave to form a close roll structure near the corner, as shown in Figure 4.3(d). As the jet flow from the corner further trends to the vertical downward direction, the roll structure starts to destabilize. The variations of the grey values of the shadowgraph image around the roll structure in Figure 4.3(d) indicate the presence of a secondary instability.

In order to display the flow structures in the corner more clearly, Figure 4.4(a) shows a close roll structure at a smaller Rayleigh number of 9.4×10^8. About 80 seconds later, the roll structure in the corner reshapes as an upright flow structure and is drawn closer to the thermal boundary layer under the action of the strong entrainment

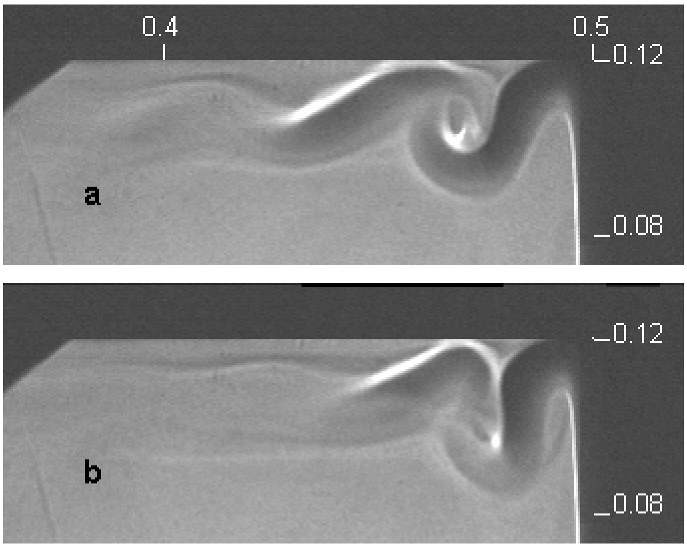

Figure 4.4 Roll structure at the Rayleigh number of 9.4×10^8

(a) t = 413 s. (b) t = 496 s

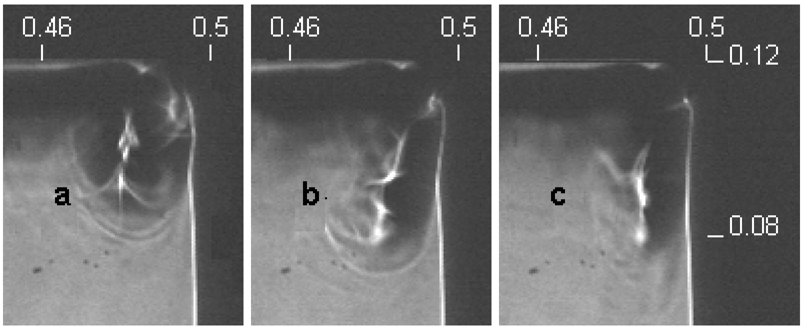

(a) t = 432 s (b) t = 680 s (c) t = 792 s

Figure 4.5 Evolution of the corner roll

(Figure 4.4b). This upright flow includes a downward jet (almost vertical) and an upward return flow.

Following the flow structure shown in Figure 4.3, Figure 4.5 shows the further evolution of the corner flow. It is seen that the destabilizing roll firstly forms an upright return flow similar to that shown in Figure 4.4(b). With the passage of time, the intrusion flow is split into two streams by the horizontal oscillation flow (refer to numerical results in Chapter 5). One stream of the intrusion flow continues to travel across the cavity along the ceiling, and the other jets into the core region as indicated by the bright strip in Figure 4.5(b). After 792 seconds, the latter stream of the hot intrusion jets almost vertically downward (Figure 4.5c).

While the flow in the top corner is developing, a different flow feature appears near the bottom corner after the cold intrusion front from the cold wall strikes the hot

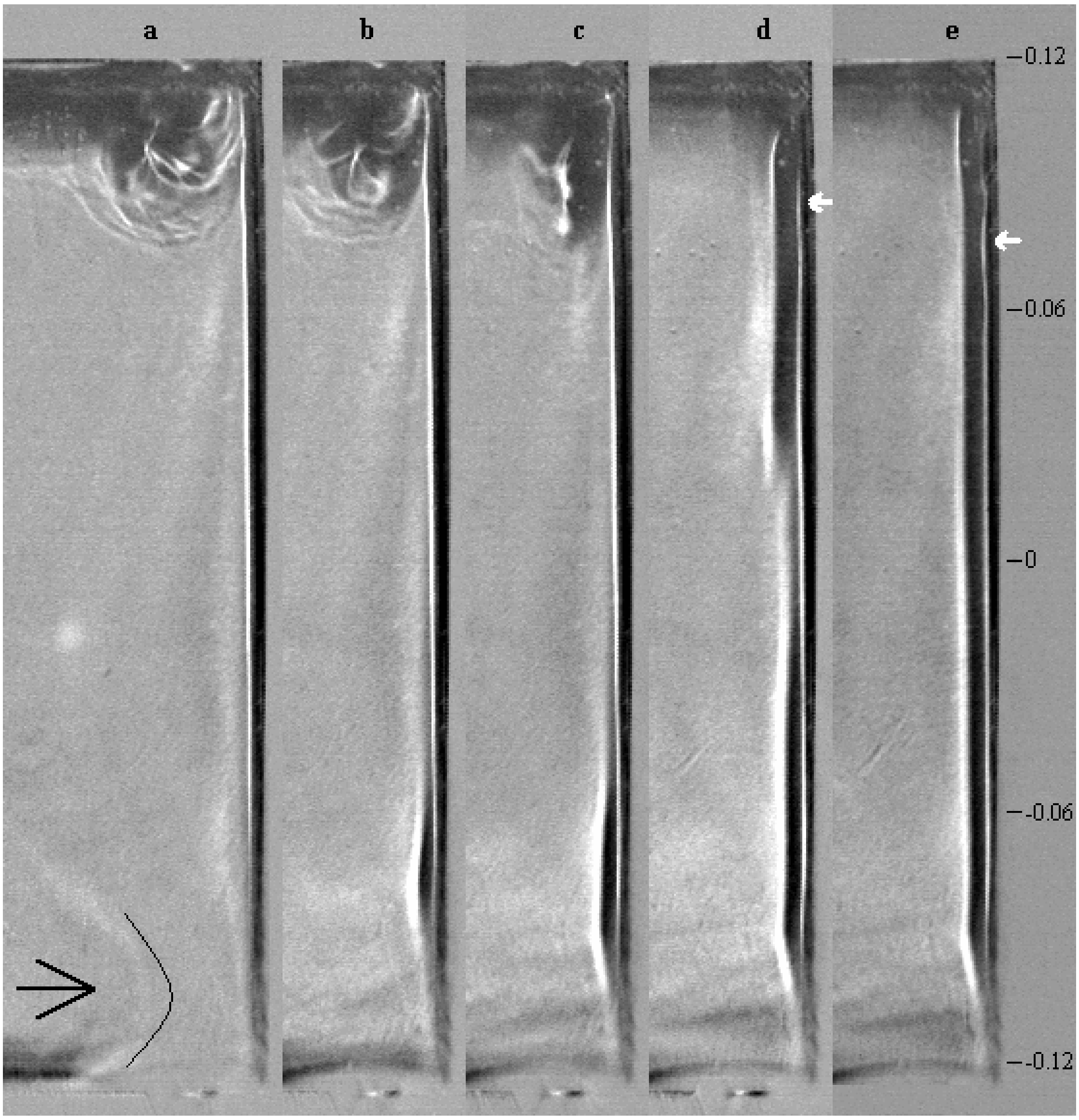

Figure 4.6 Formation of the double-layer structure

(a) t = 330 s. (b) t = 480 s. (c) t = 792 s. (d) t = 2509 s. (e) t =4961 s

wall. This is shown in Figure 4.6 (The images in this figure are processed in the same way as those presented in Figure 4.1).

Figure 4.6(a) shows that the cold intrusion, indicated by a black arrow and line, is approaching the thermal boundary layer. As the cold intrusion is entrained by the thermal boundary layer, another bright strip appears outside the thermal boundary layer near the bottom corner as shown in Figure 4.6(b). The additional bright strip outside the thermal boundary layer is related to the formation of the upward thermal tongue due to the cold incoming fluid being entrained by the thermal boundary layer (see Chapter 5). A similar temperature structure exists near the upper corner due to the downward jet of the hot intrusion flow, which results in two bright strips in the region (see Figure 4.6c which shows the extended shadowgraph image of Figure 4.5c). As the thickness of both the hot intrusion discharged toward the core and the entrained cold intrusion increases, the upper bright strip extends downward and the lower bright strip extends upward. Since the structure of the developing bright strips is forming outside the normal thermal boundary layer, it is referred to as the outer layer hereinafter, whereas the normal thermal boundary layer is referred to as the inner layer.

By 2509 seconds, the two bright strips of the outer layer meet at approximately the half height of the vertical wall as shown in Figure 4.6(d). However, the two bright strips do not align vertically; the one from the top is further out from the hot wall than the one from the bottom. Subsequently, there is some adjustment of the velocity and temperature fields around the middle section of the vertical wall. By 4691 seconds, the two bright strips align vertically, and a continuous outer layer is formed (Figure 4.6e). The structure shown in Figure 4.6(e) has the appearance of a double-layer structure.

Table 4.2 Measured thicknesses of the double-layer at different heights

Heights (m)	Thicknesses of the inner layer (mm)		Distance between outer layer and sidewall at the quasi-steady state (mm)
	Maximum at the initial stage	Mean value at the quasi-steady state	
0.089	6.5	3.2	8.8
0.06	5.6	3.2	8.7
0.015	5.1	3.2	8.3
-0.06	4.6	2.3	6.9

It is worth noting that the inner layer becomes thinner with time during this stage of the flow development, as shown in Figure 4.6. Table 4.2 lists the measured thickness of the inner layer at different heights and different stages. It is seen that the thickness decreases by about half from the maximum in the initial stage to the mean values in the quasi-steady stage. Meanwhile, the outer layer is gradually entrained closer to the sidewall as shown in Figure 4.6, and eventually trends to steady values at different heights. The measured distances between the bright strip of the outer layer and the sidewall at different heights in the quasi-steady stage are listed in the Table 4.2.

In summary, the transition of the boundary layer flow to a quasi-steady structure may be described as a process during which the mass and heat transfer approaches a new balance. As discussed previously, one stream of the intrusion outflow near the top

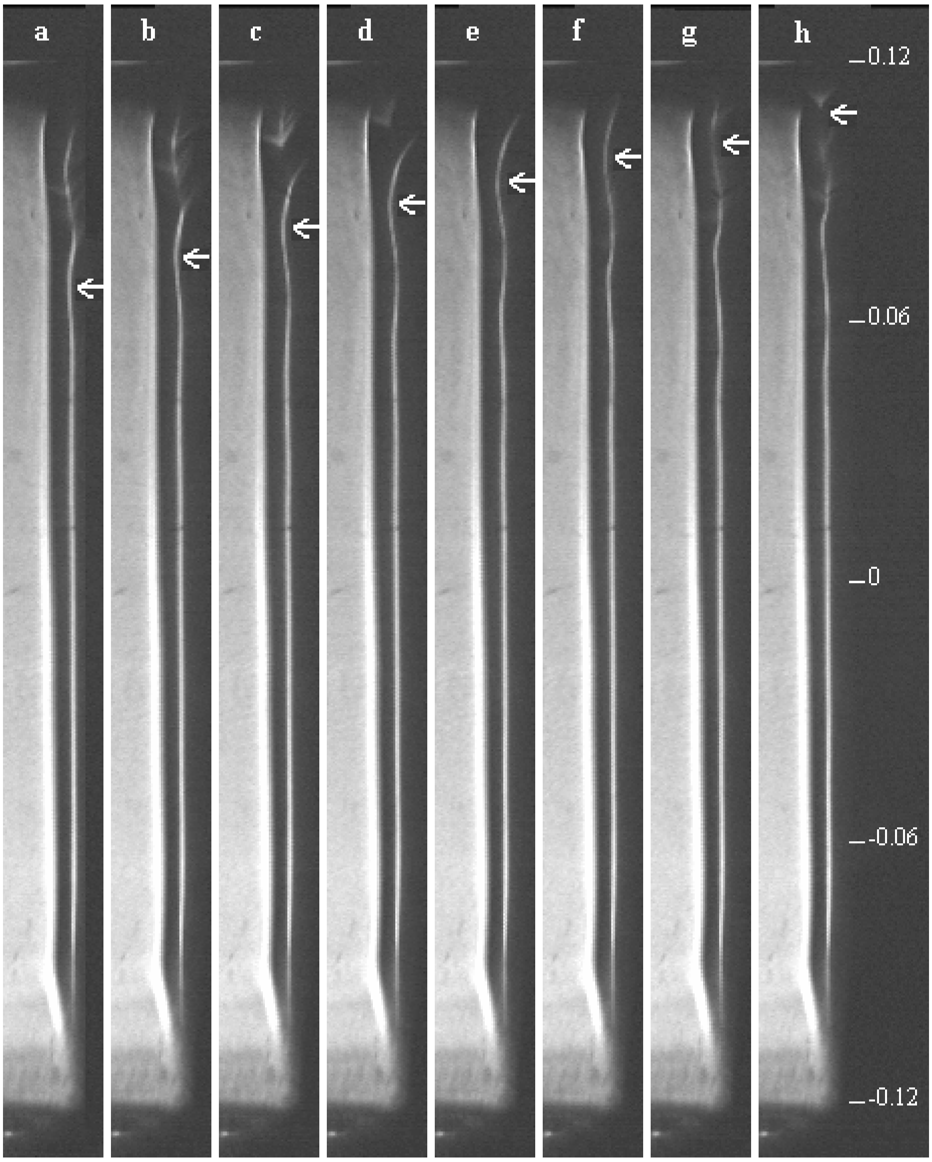

Figure 4.7 Evolution of a traveling wave in the quasi-steady stage

(a) to (h) start from t = 4806 s with an even time interval of 1 s

corner is gradually compressed in the horizontal direction and elongated in the vertical direction so that an outer layer is formed close to the inner layer. Associated with the formation of the double-layer structure, some traveling waves are observed which will be discussed in the following section.

4.1.3 Quasi-steady stage

The major feature of the quasi-steady state flow shown in the shadowgraph images is the presence of traveling waves in the thermal boundary layer, which arise in association with the formation of the double-layer structure during the late transitional

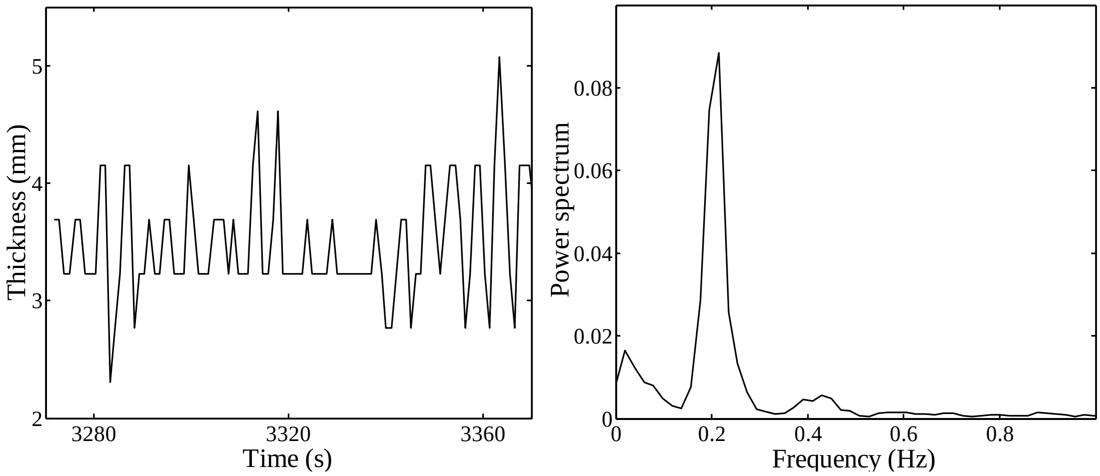

(a) Time series of the thickness (b) Spectrum of the thickness time series

Figure 4.8 Time series of the thickness at 0.089 m in the quasi-steady stage and the corresponding spectrum

stage. The traveling waves can be identified clearly in Figure 4.6(e) (indicated by a white arrow) and weakly in Figure 4.6(d). However, in the early transitional stage, no distinct traveling wave is observed (e.g. Figures 4.6a and b). While the outer layer strip is extending toward the middle of the cavity, waves start to appear in the inner layer. As the outer layer strip extends further, those traveling waves also become more distinct (refer to Figures 4.6d and e), and some of them even break down near the top corner. Therefore, it is likely that the reverse flow in the outer layer may be responsible for the appearance of the traveling waves at the quasi-steady state in shadowgraph images.

The set of shadowgraph images shown in Figure 4.7 exhibits the evolution of a traveling wave, as indicated by arrows. This wave is first sighted on the shadowgraph image at 4806 seconds (Figure 4.7a); its amplitude grows with time (Figures 4.7b to g); and eventually the wave breaks down near the corner (Figure 4.7h).

Figure 4.8(a) displays a time series of the measured thickness of the inner layer at the height of 0.089 m at the quasi-steady stage. The corresponding power spectrum shown in Figure 4.8(b) shows a peak frequency of 0.22 Hz.

Apart from the wave breaking in the corner as shown in Figure 4.7(h), another nonlinear process of the unstable traveling waves is also observed at higher Rayleigh numbers such as $Ra = 4.68 \times 10^9$ shown in Figure 4.9. The arrows in Figure 4.9 indicate the crest of the unstable wave. The appearance and growth of this unstable wave can be seen in Figures 4.9(a) through (c). As the amplitude of the unstable wave increases, a breakpoint of the bright strip of the inner layer firstly appears at the wave crest in Figure

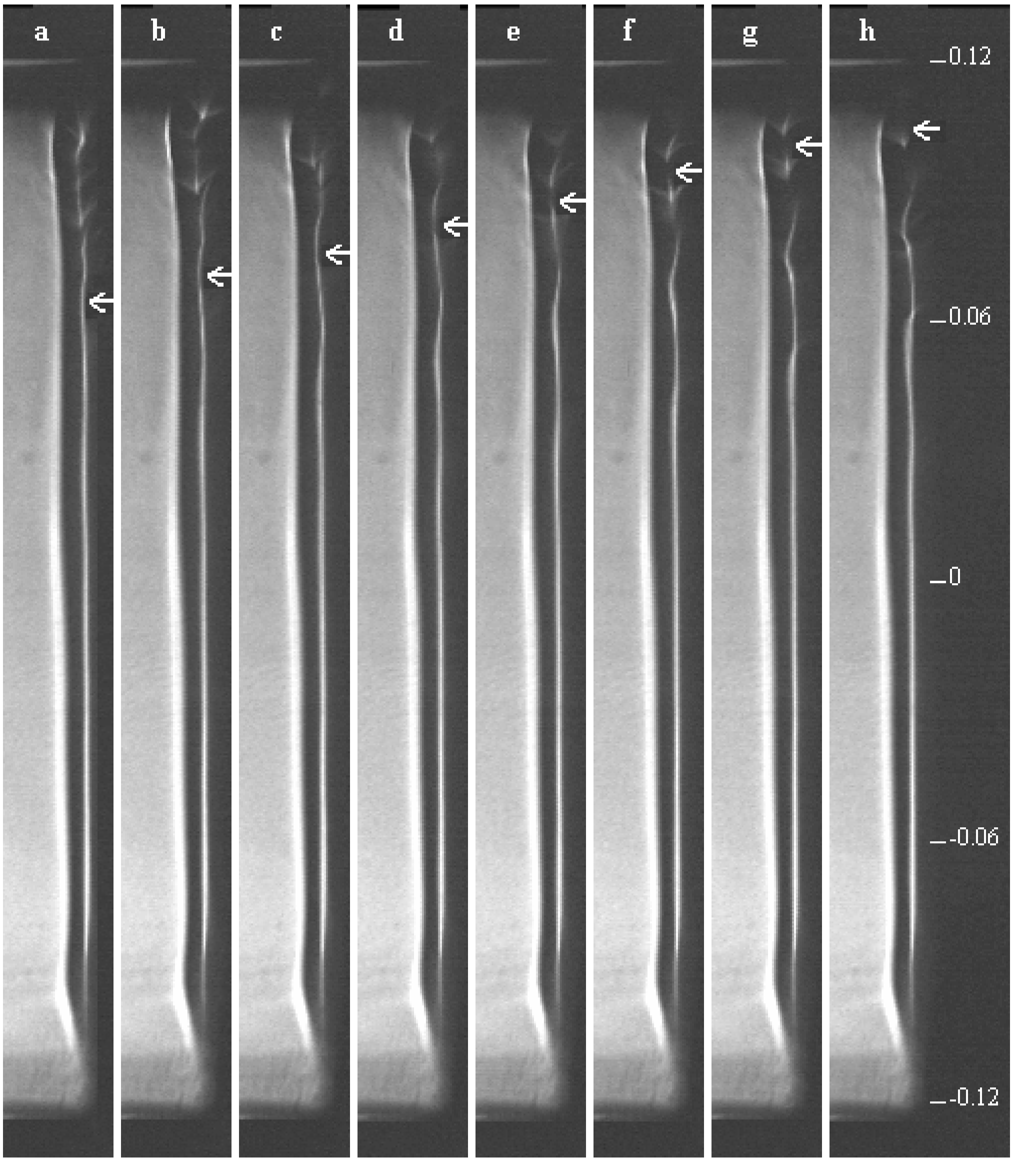

Figure 4.9 Breakdown of the wave at $Ra = 4.7 \times 10^9$ in the quasi-steady stage (a) to (h) start from t = 4032 s with an even time interval of 1 s

4.9(d), suggesting that the breakpoint originates from the non-linear effect of large amplitudes (Drazin 2001). After the breakpoint appears, the distance between the two separated parts of the wave split by the breakpoint rapidly increases as shown in Figure 4.9(e). As a consequence, one wave eventually breaks into two new waves as seen in Figures 4.9(f) and (g). Figure 4.9(h) shows that the two waves eventually vanish in the corner.

When the Rayleigh number is increased to 7.2×10^9, the thermal boundary layer exhibits certain different features from those at lower Rayleigh numbers (Figure 4.10 in comparisons with Figures 4.7 and 4.9). At this Rayleigh number, the wavy bright strip in Figure 4.10 is indistinct. The unstable waves of the inner layer display small dimmed

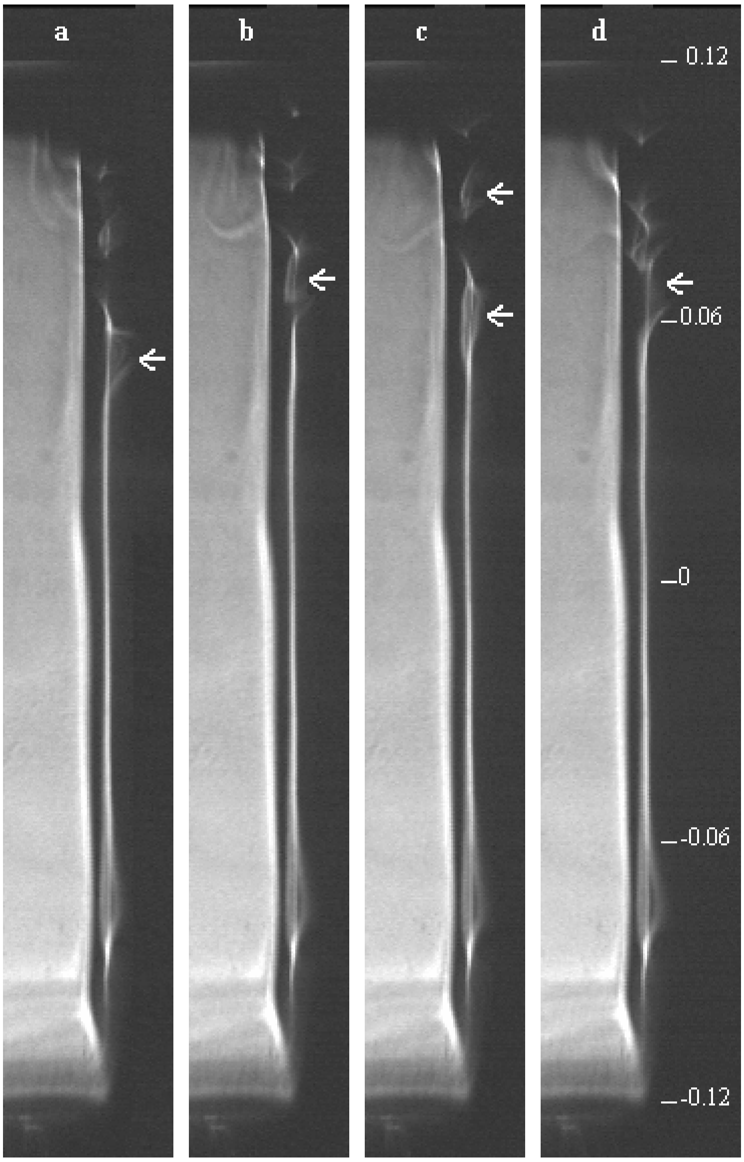

Figure 4.10 Traveling waves at $Ra = 7.2 \times 10^9$ in the quasi-steady stage

(a) to (d) start from t = 3126 s with an even time interval of 2 s

patches (indicated by arrows) of plume-like structures toward the hot sidewall. This is likely the result of the rapid nonlinear growth of the unstable waves at such a high Rayleigh number; that is, the unstable wave breaks down after a very short growth time. Moreover, the outer layer flow with a reverse velocity starts to become unstable as seen in Figure 4.10. The instability of the outer layer flow originates near the upper corner and travels downward with the flow (Figures 4.10a through c). It eventually dissipates completely into the stratified fluid in the cavity as shown in Figure 4.10(d).

For all the experiments conducted within the Rayleigh number range of $4.5 \times 10^8 \sim 7.2 \times 10^9$ in this section, it is found that the traveling waves in the thermal boundary layer last as long as the experiments are continued. However, different kinematic

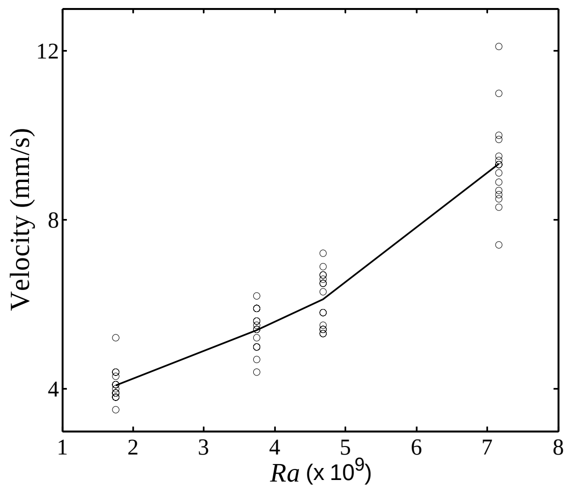

Figure 4.11 Velocity of the traveling waves at different Rayleigh numbers

properties are observed at different Rayleigh numbers as shown in Figures 4.7 through 4.10.

Figure 4.11 presents the statistical results of the measured wave velocity for different Rayleigh numbers, which clearly indicate that the velocity of the traveling waves increases with the Rayleigh number. The smallest Rayleigh number plotted in Figure 4.11 is $Ra = 1.8 \times 10^9$. For Rayleigh numbers below this value, observations demonstrate that the double-layer flow structure becomes very indistinct and the traveling waves become very weak. Therefore, it is difficult to measure the wave velocity accurately. Schöpf and Patterson (1996) reported a traveling wave velocity of 4.7 mm/s for a Rayleigh number of 7.3×10^8 at the quasi-steady state, which is higher than the expected wave velocity for the same Rayleigh number from the present measurements. The discrepancy may be attributed to the aspect ratio effect. As mentioned previously, the present experiments are conducted on a long cavity model with a depth-to-length ratio of 0.24. It is expected that the traveling wave activities in such a long cavity are considerably weaker than those present in the square cavity adopted by Schöpf and Patterson (1996).

4.2 Temperature measurements

There have been many temperature measurements (refer to Gebhart 1988) concerning thermal flows adjacent to a vertical flat plate, some of which may be applied to the discussion of the transient natural convection flow in the cavity in the very early stage for the case of sudden heating. However, due to distinctions between the two categories of thermal flows (exterior and interior flows), temperature measurements of the transient natural convection flows in the cavity cannot be replaced by those measurements of flows adjacent to the vertical flat plate of isoflux heating. Unfortunately, few experiments concerning the natural convection flow in the cavity with isothermally heated and cooled sidewalls were performed, and also they focused on the early transient natural convection (see e.g. Patterson & Armfield 1990; Patterson et al. 2002). Accordingly, temperature measurements in this section for the complete transition of natural convection from the start-up to the quasi-steady stage have been conducted in this thesis and are reported in this section.

Table 4.3 Flow parameters for temperature measurements in Section 4.2

Number	Initial temperature of water in cavity (K)	Temperature difference between sidewalls (K)	*Ra* ($\times 10^8$)	*Pr*
5	294.50	4.0	8.8	6.8
6	294.50	8.0	18	6.8
7	295.55	16.0	38	6.6
8	294.20	32.0	69	6.9

The temperature measurements here are based on those flow visualization experiments described in Section 4.1 for comparisons the experimental results. Experiments with four temperature differences between the sidewalls ranging from 4 to 32 K, corresponding to those in Section 4.1, are performed. The ranges of the Rayleigh number and Prandtl number are $8.8 \times 10^8 \sim 6.9 \times 10^9$ and $6.7 \sim 6.9$ respectively and the experimental parameters are listed in Table 4.3. Since it is difficult to repeat an experiment at the exactly same conditions, only Experiment 7 in Table 4.3 was conducted at the same experimental conditions as those of Experiment 2 in Table 4.1 were performed; the others have approximately the same conditions as those of the corresponding flow visualization experiments.

Since the thermal flow adjacent to the hot sidewall is the focus of this thesis, four thermistors are employed and located in the vicinity of the hot sidewall. Among them, three thermistors have a distance of 2 mm between the thermistor tip and the sidewall at different heights, and the fourth one is placed at a distance 10 mm from the sidewall. All positions of the thermistors are listed in Table 4.4.

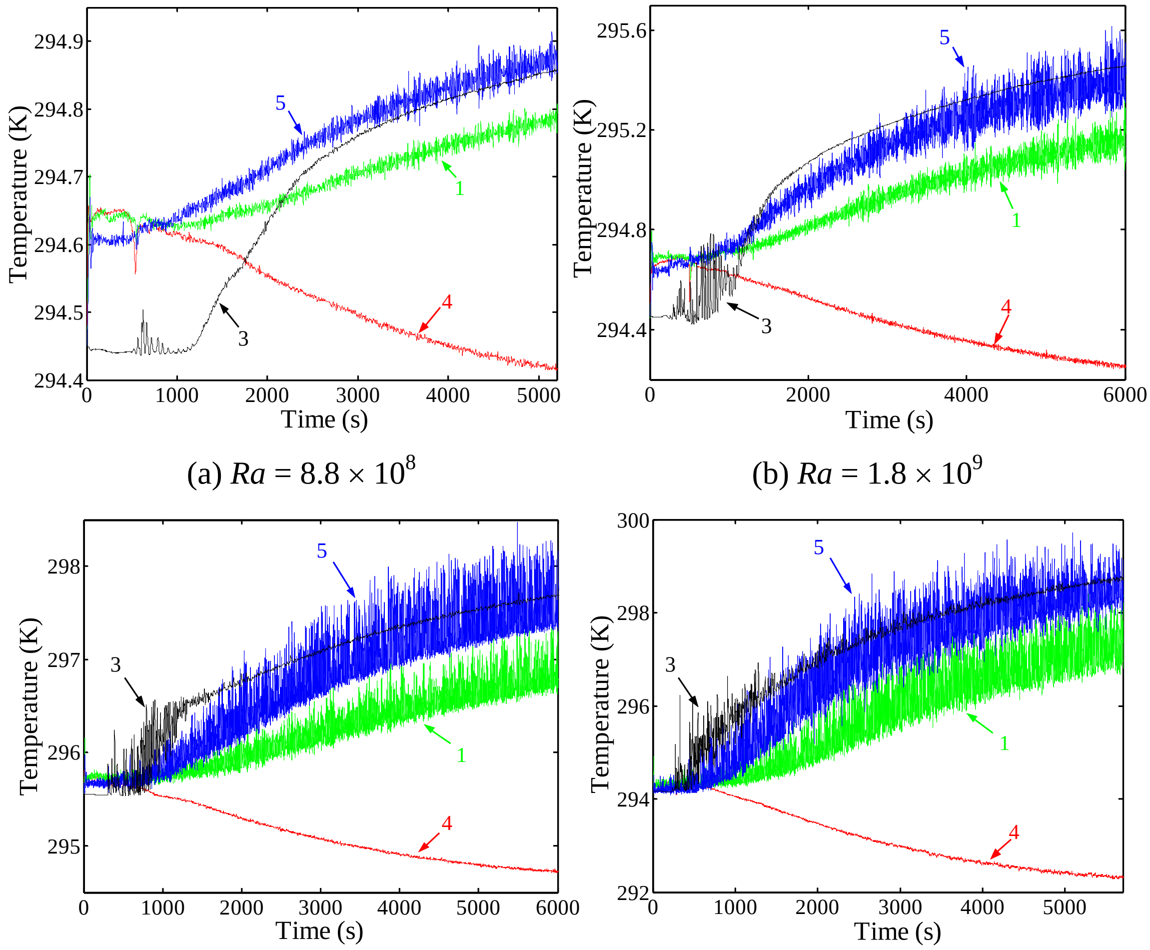

(a) $Ra = 8.8 \times 10^8$ (b) $Ra = 1.8 \times 10^9$

(c) $Ra = 3.8 \times 10^9$ (d) $Ra = 6.9 \times 10^9$

Figure 4.12 Time series of the temperatures measured at different positions and at different Rayleigh numbers

Table 4.4 Thermistor locations (relative to the center of the cavity)

Thermistor number	*x* coordinate (m)	*y* coordinate (m)
1	0.498	0.06
3	0.490	0.09
4	0.498	-0.055
5	0.498	0.09

Figure 4.12 shows time series of the temperatures at four positions for four different Rayleigh numbers. The time series of the temperatures at different points adjacent to the hot sidewall are oscillatory, and the amplitude of oscillation increases with the passage of time. This implies that the traveling waves visualized in the quasi-steady stage in the shadowgraph images in Section 4.1 result from the increasing amplitudes of traveling waves; that is, only if the amplitudes of traveling waves are

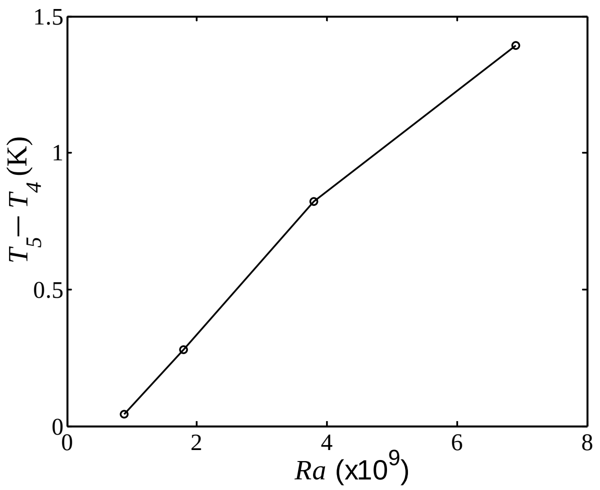

Figure 4.13 Vertical temperature differences (average from 5000 s to 5100 s) against Rayleigh numbers

larger than some value can these waves be visualized in the shadowgraph images. Furthermore, the time series of the temperatures from the three thermistors closest to the hot sidewall show that the traveling waves in the thermal boundary layer grow significantly when they convect downstream. The spatial growth of traveling waves becomes clearer as the Rayleigh number increases, as seen in Figures 4.12(c) and (d).

Apart from traveling waves of the thermal boundary layer, stratification of the core fluid in the cavity is another feature of the transition. The increasing temperature differences between the upper and lower sections in the cavity (see Thermistors 5 and 4) indicate that stratification of the fluid is significantly enforced. Such stratification, relevant to the Rayleigh number, is shown in Figure 4.13, in which a temperature difference between two series of temperatures recorded by Thermistors 5 and 4 denotes stratification.

Figure 4.12 shows distinctive features of the complete transition. However, some details can not be clearly due to the large time scale. Therefore, in the following subsections, details of the temperature time series are redrawn for different stages in order to discuss these transient features.

4.2.1 The Leading Edge Effect

The time series of the temperatures from different thermistors for two Rayleigh numbers in the early stage are shown in Figure 4.14. The time series of the temperature recorded by Thermistor 4 displays features of the LEE, similar to those results given by

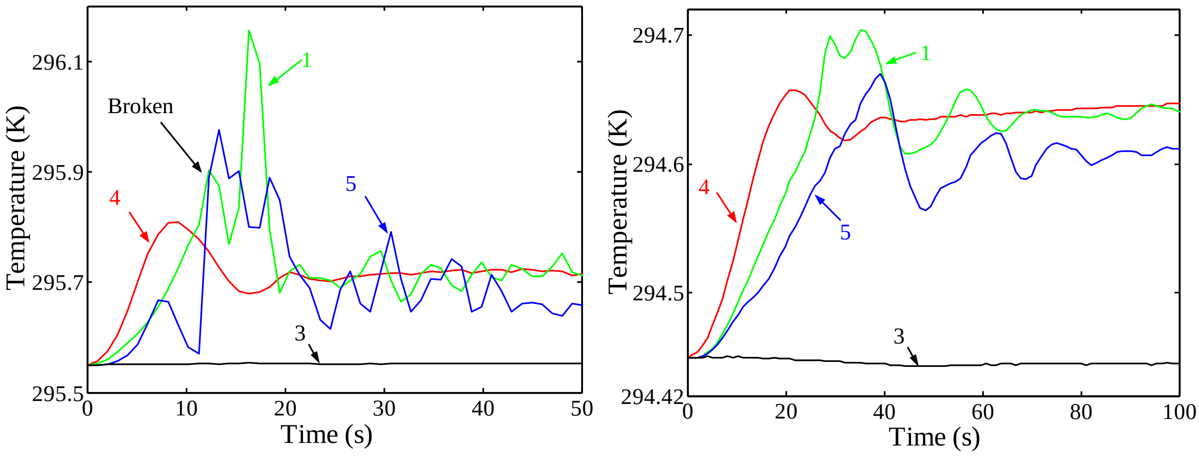

(a) $Ra = 3.8 \times 10^9$ (b) $Ra = 8.8 \times 10^8$

Figure 4.14 Time series of the temperatures at different positions in the early stage

Patterson and Armfield (1990) and Patterson et al. (2002), including an overshoot and subsequent traveling waves. However, a complete overshoot of the temperature can not be found at higher locations (Thermistors 1 and 5) for $Ra = 3.8 \times 10^9$ as seen in Figure 4.14(a). Instead, a broken overshoot of temperatures at higher locations arises, and clearly unstable traveling waves follow (Figure 4.14a). Unfortunately, the early broken overshoot of the temperatures at higher locations is not predicted by corresponding numerical simulations (refer to e.g. Armfield & Patterson 1991).

It is found from Figure 4.14(a) that the temperature at a lower position (e.g. Thermistor 4) increases more rapidly than that at higher positions. This is possibly because the temperature time series by thermistors is sensitive to the position relative to the hot wall and due to very small errors in locating the thermistors, Thermistor 4 could have been located closer to the sidewall compared with the others (also see Patterson et al. 2002).

For the case with the Rayleigh number of $Ra = 8.8 \times 10^8$, Figure 4.14(b) shows that an overshoot of the temperature (e.g. data recorded by Thermistor 4) may also be found, even at a higher position (see, for example, as recorded by Thermistor 5), which is followed by clearly unstable traveling waves.

For the purpose of illustrating the dependence of the early transient flow features on the Rayleigh number, the time series of the temperatures recorded by Thermistor 4 (y = -0.055 m) at different Rayleigh numbers are replotted in Figure 4.15 for comparison. It is clear that, as the Rayleigh number increases, the peak value of the overshoot increases, and unstable traveling waves become clearer with distinctively different

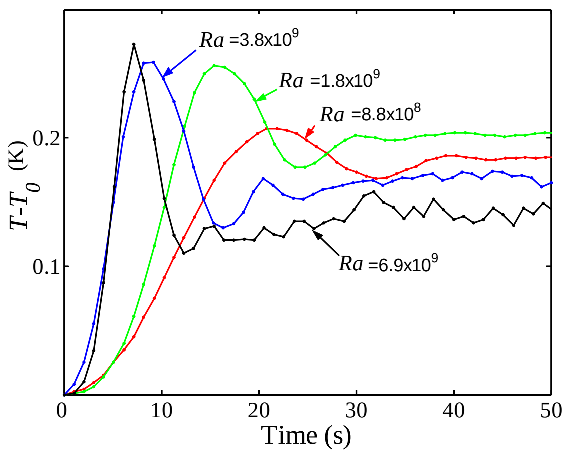

Figure 4.15 Time series of the temperatures at the point (0.498 m, -0.055 m) at different Rayleigh numbers

frequencies (which are also discussed in the following section). This observation implies the dependence of the traveling waves in the thermal boundary layer flow on the Rayleigh number.

4.2.2 Time series of temperatures in the transitional stage

As seen in Figure 4.12, the transition of natural convection from the start-up to the quasi-steady state is always associated with the development of traveling waves in the thermal boundary layer.

Figure 4.16(a) shows time series of temperatures recorded by different thermistors in the transitional stage. It is clear that, as the cold intrusion reaches the hot sidewall at approximately 330 s (also refer to Figure 4.6), the amplitude of the unstable traveling waves recorded by thermistors at higher positions (Thermistors 1, 3 and 5) increase significantly. In particular, the time series of the temperature recorded by Thermistor 3 suddenly changes from the flat line at 300 s to an oscillation with large amplitudes. This is because the location of thermistor 3 (x = 0.49 m, y = 0.09 m) is outside the vertical thermal boundary layer, and thus the traveling waves in the thermal boundary layer does not impact on the temperature at this location before the arrival of the cold intrusion. However, when the cold intrusion approaches the hot sidewall, the discharged flow from the downstream end of the thermal boundary layer destabilizes, and the destabilizations are recorded by Thermistor 3, as seen in Figure 4.16(a). The instability of the discharged flow, which has a lower frequency of 0.06 Hz, is different from the

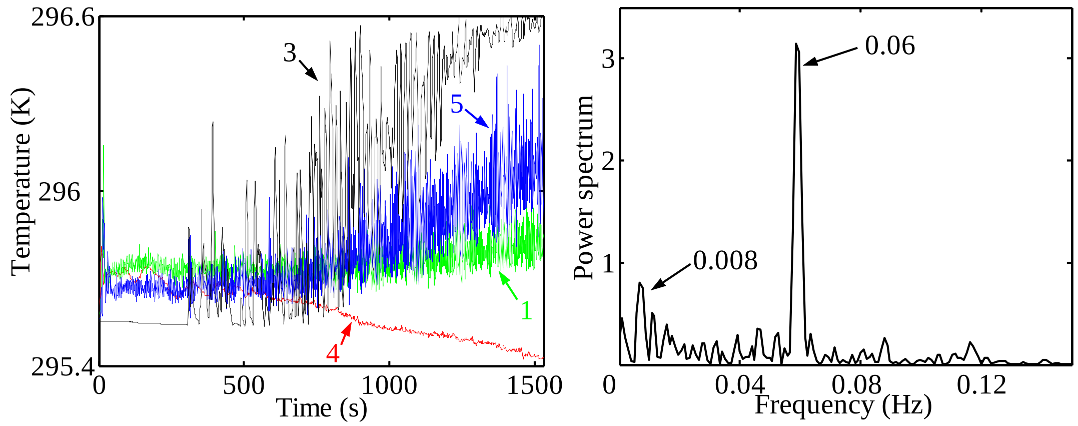

(a) Temperatures at different positions (b) Spectrum of the temperature from Thermistor 3

Figure 4.16 Time series of the temperatures in the transitional stage at $Ra = 3.8 \times 10^9$ and a corresponding spectrum

traveling waves (whose frequency is 0.23 Hz, referring to the next subsection) in the thermal boundary layer. The spectrum of the temperature time series recorded by Thermistor 3 is shown in Figure 4.16(b).

Apart from the wave features, stratification of the core fluid is enforced after the arrival of the cold intrusion. For example, the time series of the temperatures at different heights (Thermistor 1, 4 and 5) diverge as time elapses (Figure 4.16a). It is worth noting that in Figure 4.16(a) the temperature recorded by Thermistor 3 is higher than others because the discharged flow from the downstream end of the thermal boundary layer is fully mixed and is passing through the location of Thermistor 3 in this stage (also refer to Figure 4.6a).

4.2.3 Traveling waves in the quasi-steady stage

According to the temperature time series shown in Figure 4.12, the temperatures at different positions still changes with time even though the experiments lasted for more than two hours. Therefore, only results which approximately represent those at quasi-steady stage can be obtained. It is clear in Figure 4.12 that the transition approaches a quasi-steady state, which is supported by the earlier experiments of Schöpf and Patterson (1996). As a consequence, a time series of the temperature at some large time (e.g. 6000 s here) is considered representative of that at the quasi-steady state.

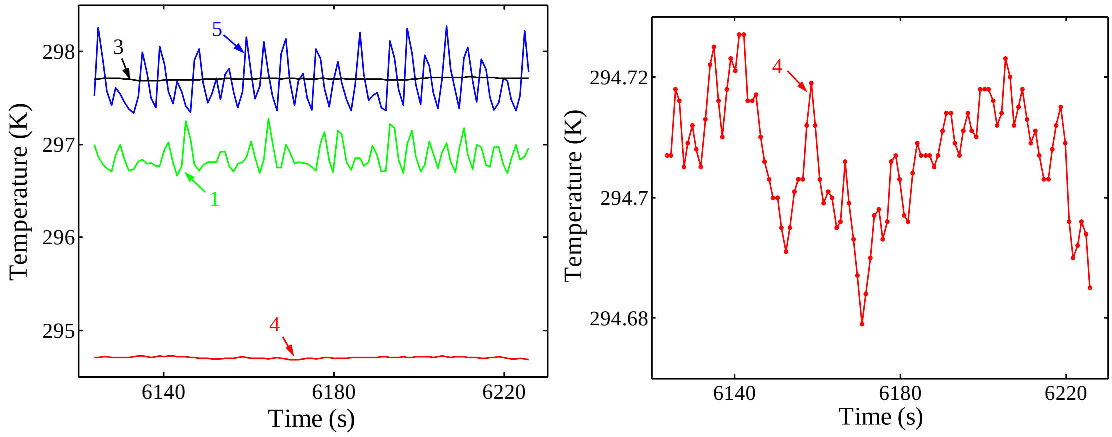

(a) At different positions (b) At point (0.498 m, -0.055 m)

Figure 4.17 Time series of the temperatures in the quasi-stage stage at $Ra = 3.8 \times 10^9$

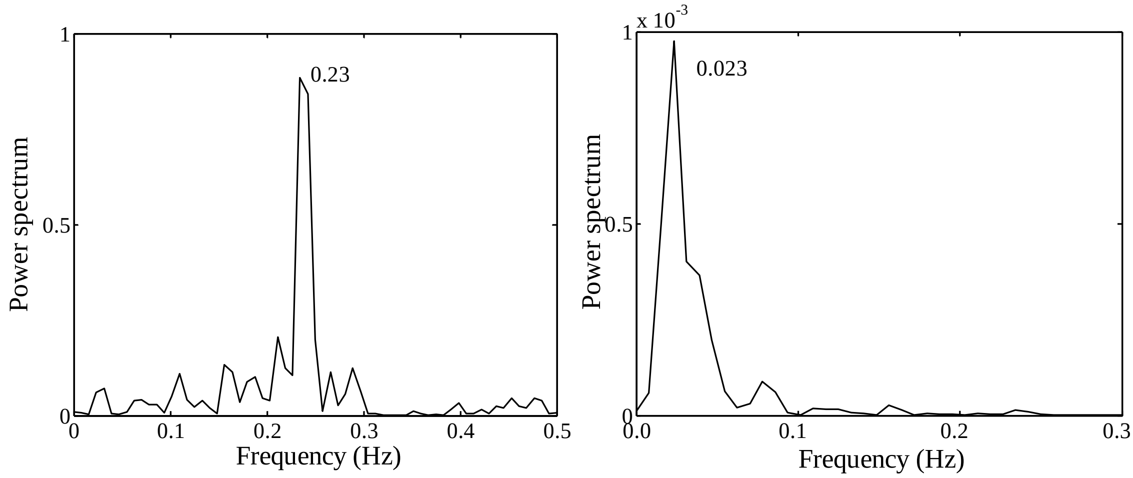

(a) At point (0.498 m, 0.09 m) (b) At point (0.498 m, -0.055 m)

Figure 4.18 Spectra of the temperature time series at different positions at $Ra = 3.8 \times 10^9$

Figure 4.17 shows the time series of the temperatures in the quasi-steady stage, in which the amplitude of the traveling waves does not grow apparently with time (see Figure 4.17a). However, the spatial growth of the traveling waves with height is evident by comparing the time series of the temperatures recorded by Thermistors 1, 4 and 5. Figure 4.17(b) shows the time series of the temperature recorded by Thermistors 4 (at a lowest position). It is clear that even at such a low position there still exist high-frequency traveling waves.

The spectra of the traveling waves recorded by the thermistors at different heights are shown in Figure 4.18. Figure 4.18(a) indicates that the traveling waves at a higher position in the thermal boundary layer have a principal frequency of 0.23 Hz, which does not change in the transition and matches exactly with the shadowgraph observation in Section 4.1 (refer to Figure 4.8b). However, apart from such high-frequency traveling waves, the spectrum of the temperature recorded by the thermistor at a low position (Figure 4.18b) shows that another spectrum peak is present; that is, there exist the low-frequency waves (0.023 Hz) in the cavity.

4.3 Summary

In this chapter, the formation of the double-layer structure of the thermal boundary layer in a differentially heated cavity is described, and the transition of the thermal boundary layer from the start-up to the quasi-steady state is classified into three stages based on the different kinematic properties of the flow. The three stages are the initial stage, the transitional stage and the quasi-steady stage. For each of the three stages, the responsible dynamic mechanisms are briefly discussed based on flow visualizations and temperature measurements. The major flow features at each stage are summarized below.

In the initial stage, there exist two distinct kinematic properties. One is the boundary layer growth, involving overshoots of thickness and temperature as shown in Figures 4.1 and 4.14 respectively; the other is the LEE perturbation as shown in Figures 4.2 and 4.14, which induces high-frequency traveling waves in the laminar flow regime.

In the transitional stage, there also exist two distinct flow properties: the horizontal intrusion and the entrainment of the vertical boundary layer as shown in Figures 4 through 7. This stage lasts for a relatively long time, depending on the Rayleigh number. Through the discussion of the dynamic mechanism of the horizontal intrusion and the vertical boundary layer entrainment, the evolution of a reverse flow outside the inner thermal boundary layer is described. Time series of temperatures at different heights show that the fluid in the cavity is continuously stratified (Figure 4.16a).

In the quasi-steady stage, one important flow property is a double-layer structure of the thermal boundary layer as shown in Figure 4.6(e). In addition, the traveling waves at the quasi-steady stage may be clearly visualized by the shadowgraph technique. The corresponding temperature time series indicate that the traveling waves at the quasi-steady stage have larger amplitudes than those at other stages (see Figure

4.12), and the reverse flow in the outer layer of the double-layer structure is likely to be responsible for the amplitude growth of the traveling waves.

In summary, in order to unveil the full transition of the thermal boundary layer from the start-up to the quasi-steady state, flow visualizations and temperature measurements are performed in this chapter. Based on the present experimental results, it is found that the transition is very different from that of the natural convection flow near a semi-infinite plate immersed in an isothermal fluid. In particular, for the quasi-steady stage flow, the suitability of the semi-infinite plate assumption for the stability analyses of the thermal boundary layer in a differentially heated cavity needs to be re-examined. The experimental data here are extensive in comparison with those previous experiments, and may be used to validate corresponding numerical simulations.

5 Numerical simulations of transient natural convection without a fin

Numerical simulations serve the purpose of proving insights into the transition of the natural convection flows in a differentially heated cavity from the start-up to the quasi-steady state. Considerable transitional numerical results have been reported in the literature (see e.g. Schladow et al. 1989), and most of the previous numerical studies focused on the early part of the transitional flow. Similar to those experimental investigations, few of the existing numerical studies paid attention to the subsequent development of the transition to the steady or quasi-steady state. The lack of comprehensive numerical data and the need to understand the mechanisms responsible for some transient features of the early transitional flows motivate the present numerical investigation, which is aimed at simulating the overall transitional process from the start-up to the quasi-steady state as observed experimentally in Chapter 4.

In this chapter, Experiment 2 described in Chapter 4 with $Ra = 3.8 \times 10^9$ and $Pr = 6.6$ is numerically simulated. A two-dimensional rectangular domain based on the experimental model, which is 0.24-m high and 1-m wide, is considered. The initial temperature of the fluid in the cavity is 295.55 K, and the temperature difference between two sidewalls 16 K (the temperature of the hot sidewall is 303.55 K). Details regarding the initial and boundary conditions as well as other basic flow parameters may be found in Chapter 3.

5.1 Overview of the transient flow

For the purpose of illustrating the overall transition of the thermal boundary layer flow in a suddenly differentially heated cavity, Figure 5.1(a) plots a time series of the calculated temperature at the point (0.498 m, 0.09 m), which is located at the downstream section of the thermal boundary layer adjacent to the heated sidewall. The same time series of the temperature is re-plotted on a logarithmic scale in Figure 5.1(b) in order to demonstrate more clearly the early-stage features of the transient thermal boundary layer flow. Although the time series of the temperature at a discrete location in the thermal boundary layer cannot fully describe the complex transition of the natural

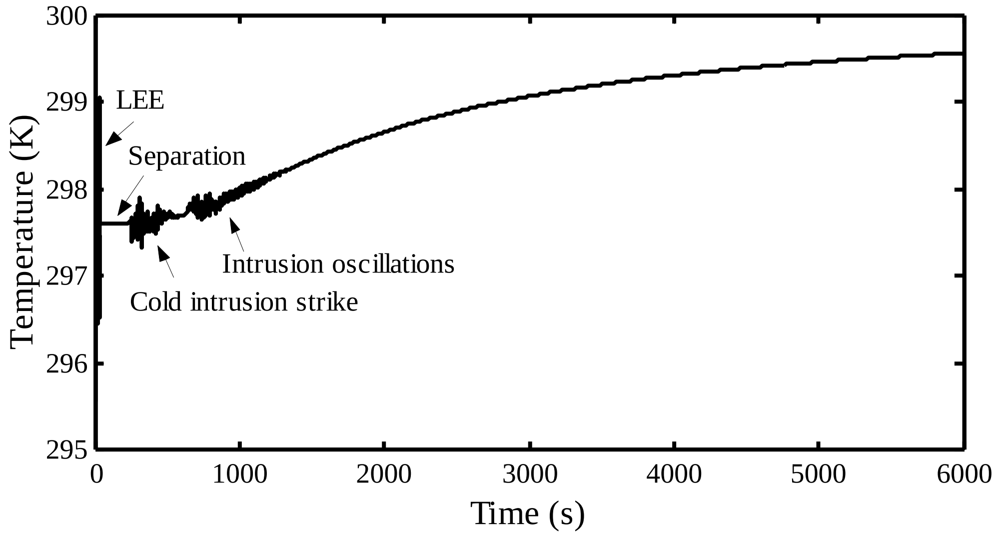

(a) On a linear time scale

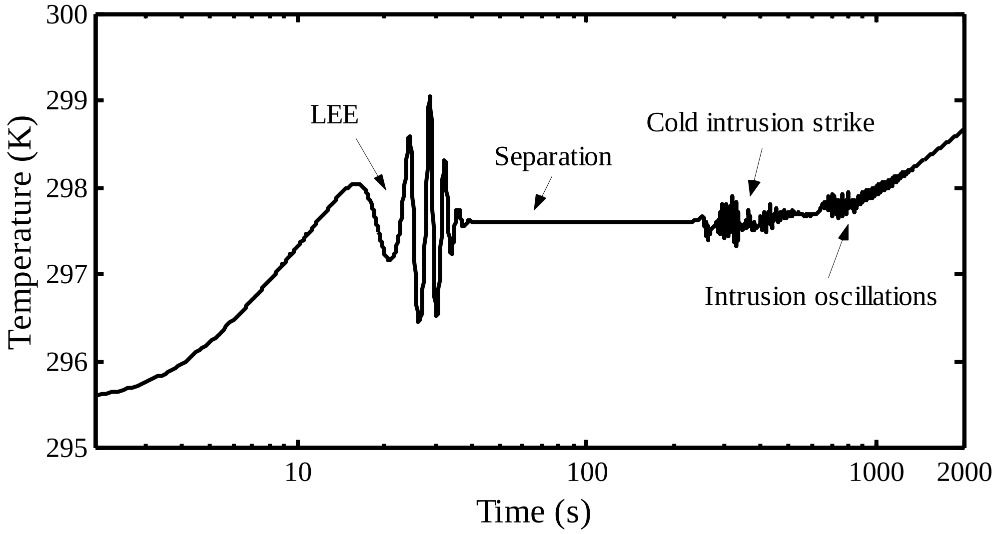

(b) On a logarithmic time scale

Figure 5.1 Time series of the temperature in the thermal boundary layer calculated at the point (0.498 m, 0.09m)

convection flow in the cavity, it does demonstrate the major flow features of the transition (marked in Figure 5.1), particularly those pertinent to the vertical thermal boundary layer.

In general, the overall transition of the natural convection flow may be characterized as follows: in the very early stage, the leading-edge effect (LEE) results in an instability of the thermal boundary layer, as indicated by the first group of traveling waves in Figure 5.1(b). After the LEE perturbations are convected away, the temperature time series in the thermal boundary layer flow becomes steady (This is different from the corresponding temperature measurements which clearly show traveling waves, see Figure 4.14) until the arrival of the intrusion flow from the opposite sidewall. Separation of the horizontal intrusion also happens in this stage (see e.g. Ivey 1984). When the cold intrusion from the opposite sidewall strikes the hot sidewall, instability of the thermal boundary layer flow is triggered again, as indicated by the second group of traveling waves in Figure 5.1(b). At a certain stage after the arrival of the intrusion from the opposite sidewall, the intrusion flow oscillates and as a consequence, it induces instability of the discharged flow of the thermal boundary layer, which is represented by the third group of waves in Figure 5.1(b). Subsequently, the thermal boundary layer flow enters a slow evolution process toward a quasi-steady state, as described by the smooth curve of the temperature plot in Figure 5.1(a) (for $t >$ 2000 s). The expected traveling waves in the thermal boundary layer in the later transition, as indicated by those temperature time series recorded by thermistors in Chapter 4, are not observed in the present numerical simulations, as discussed below. Similar numerical results have been reported in Schladow et al. (1989) and Armfield and Patterson (1991). Previous stability analyses (e.g. Brooker et al. 2000; Tao and Le Quere 2003) indicate that the measured traveling waves in the thermal boundary layer are associated with a thermal convective instability. Due to the lack of appropriate perturbations in the numerical simulations in comparison with experiments, such convective instability does not normally manifest itself in the numerical simulations. Exceptions are expected in the events with the presence of strong perturbations such as at the times when the sudden heating is started and when the cold intrusion strikes the hot sidewall.

Despite the above-mentioned discrepancies between the numerical and experimental results concerning the thermal convective instability, the numerical simulations characterize the major flow features of the transition well. In the following sections, the numerical results are discussed in comparison with the experimental observations and measurements. The discussion will be in the order of the flow development in the cavity which includes the LEE of the vertical thermal boundary layer in the initial stage, the horizontal intrusion, the formation of the double-layer structure of the vertical thermal boundary layer, and the flow and thermal features in the quasi-steady stage.

5.2 The Leading-Edge Effect

For the natural convection flow in a suddenly differentially heated cavity, similar to the case with a semi-infinite plate, heat conduction through the wall results in the thickness growth of a vertical thermal boundary layer which dominates the initial flow development, as shown in Chapter 4. The scaling analysis by Patterson and Imberger (1980) (see Equation (1.7)) indicates that the time scale for the growth of the thermal boundary layer is small, which has been validated by the experimental measurements in Chapter 4.

Associated with the initial thickness growth, convection arises within the thermal boundary layer. Previous studies (see e.g. Gebhart 1988) indicated that convection was one-dimensional in the initial stage, and then became two-dimensional after the LEE passed. Although considerable studies concerning the LEE have been reported, the mechanisms responsible for the generation and propagation of the LEE still remain unclear. Accordingly, further discussion of the LEE is given in this section based on the present numerical simulations.

5.2.1 Origin of the Leading-Edge Effect

In a differentially heated cavity, the leading edge of the thermal boundary layer is the joint of the isothermal vertical sidewall and the adiabatic horizontal bottom wall at the upstream corner. In order to obtain some insights into the dynamic mechanisms responsible for the generation and propagation of the LEE, the discussion here starts from the origin of the LEE, i.e. the upstream corner.

Figure 5.2 shows the pressure, velocity and temperature fields near the upstream corner of the thermal boundary layer in the initial stage. Although the times are very small (1 s and 3 s), it is evident that the flow near the corner is two-dimensional. This is a result of the mass transfer in the corner region; that is, following the sudden heating, the heated fluid in the upstream corner is convected upwards due to the buoyancy effect, and in the meantime the fluid outside the upstream corner, which is colder than that in the upstream corner, is entrained into the corner, as seen in Figure 5.2. Figure 5.2(a) indicates that the pressure minimum firstly arises in the upstream corner in the initial stage, resulting in a negative pressure gradient toward the corner. Figure 5.2(b) shows

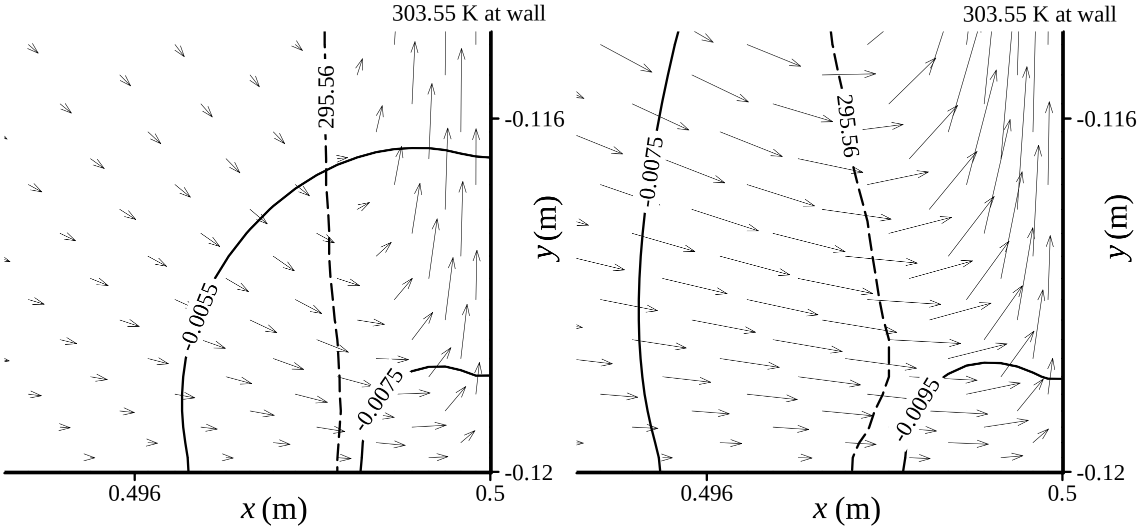

(a) t = 1 s (b) t = 3 s

Figure 5.2 Isotherms (dashed line), isobars (solid line), and velocity vectors near the bottom corner at two early times

that the low pressure zone near the corner extends outwards and the entrainment into the corner becomes increasingly stronger (indicated by the relative length of the velocity vectors). The temperature contours at different times in Figures 5.2(a) and (b) indicate that the thickness of the vertical thermal boundary layer grows with time. Since the temperature of the fluid entrained into the upstream corner is lower than that of the heated fluid in the upstream corner and the viscous effect of the velocity field due to the adiabatic bottom boundary is present, a temperature contour (T = 295.56 K), convex to the hot sidewall, results as seen in Figure 5.2(b). Clearly, this temperature structure is different from that of a semi-infinite plate (see e.g. Wright & Gebhart 1994) since the entrainment from the interior here is confined by a bottom boundary.

Since the pressure gradient is the only one force in the horizontal direction in the thermal boundary layer (see Equation (3.13)), it is necessary to observe the pressure distribution in the vicinity of the hot sidewall in the initial stage. Figure 5.3(a) shows the pressure contours at t = 5 s. It is clear that the pressure maximum and minimum are present in the downstream and upstream corners respectively, resulting in a non-uniform pressure distribution in the cavity. Figure 5.3(b) shows a zoomed view of the pressure contours. It is seen from this figure that the pressure contours are not normal to the surface of the vertical sidewall and thus a horizontal pressure gradient is established. According to the horizontal momentum equation (3.13), the horizontal pressure gradient

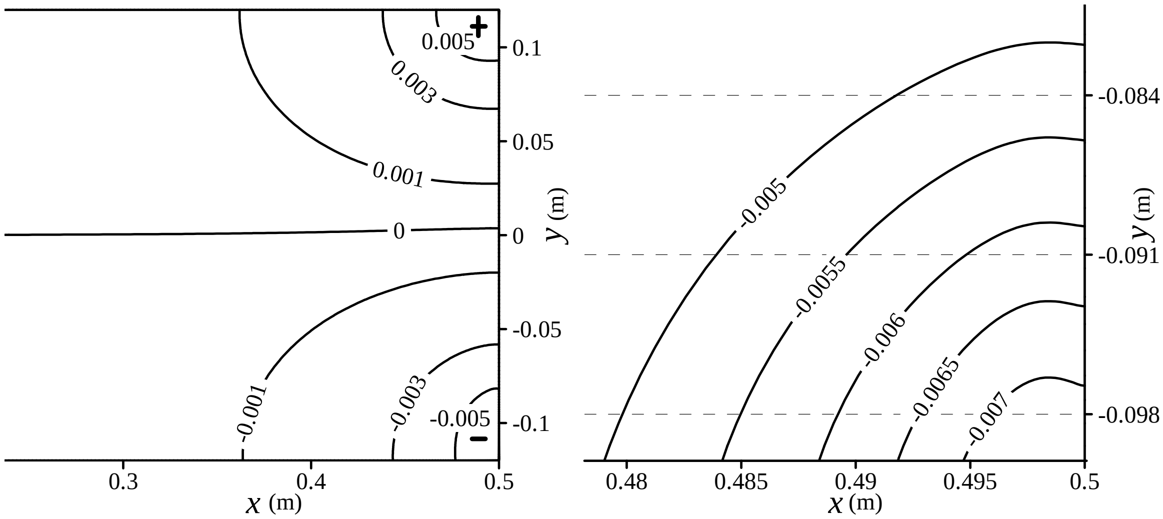

(a) Pressure contours adjacent to the hot sidewall (b) Zoom view of (a)

Figure 5.3 Pressure contours at t = 5 s (Pa)

may in turn drive a horizontal motion in the thermal boundary layer even in the initial stage.

In order to illustrate the initial evolution of major physical variables in the thermal boundary layer, Figure 5.4 plots the profiles of the temperature, pressure and velocities at x = 0.499 m, very close to the hot sidewall. For the sudden heating case, the boundary condition of the temperature is in fact similar to a ‘step’ increase. Due to the leading edge effect (the horizontal entrainment), a large temperature gradient in the streamwise direction near the leading edge is produced at the early time, which is slightly larger than that at the time when thermal conduction balances thermal convection (comparing the earlier temperature profiles with that at t =150 s shown in Figure 5.4a). Figure 5.4(b) shows the pressure profiles at different times (see different colorful curves). The pressure fluctuations near the leading edge are evident. Furthermore, associated with the pressure fluctuations, the disturbances of the horizontal and vertical velocities are also clear, as shown in Figures 5.4(c) and (d).

In summary, the sudden heating of the sidewall results in a temperature variation (distribution) of the fluid in the vicinity of the sidewall by conduction in the initial stage, which in turn produces a buoyancy force driving the heated fluid upwards adjacent to the sidewall. When the heated fluid near the leading edge is convected away, the mass balance induces a pressure distribution (that is, a pressure minimum arises near the leading edge) which drives the horizontal entrainment near the leading edge (see

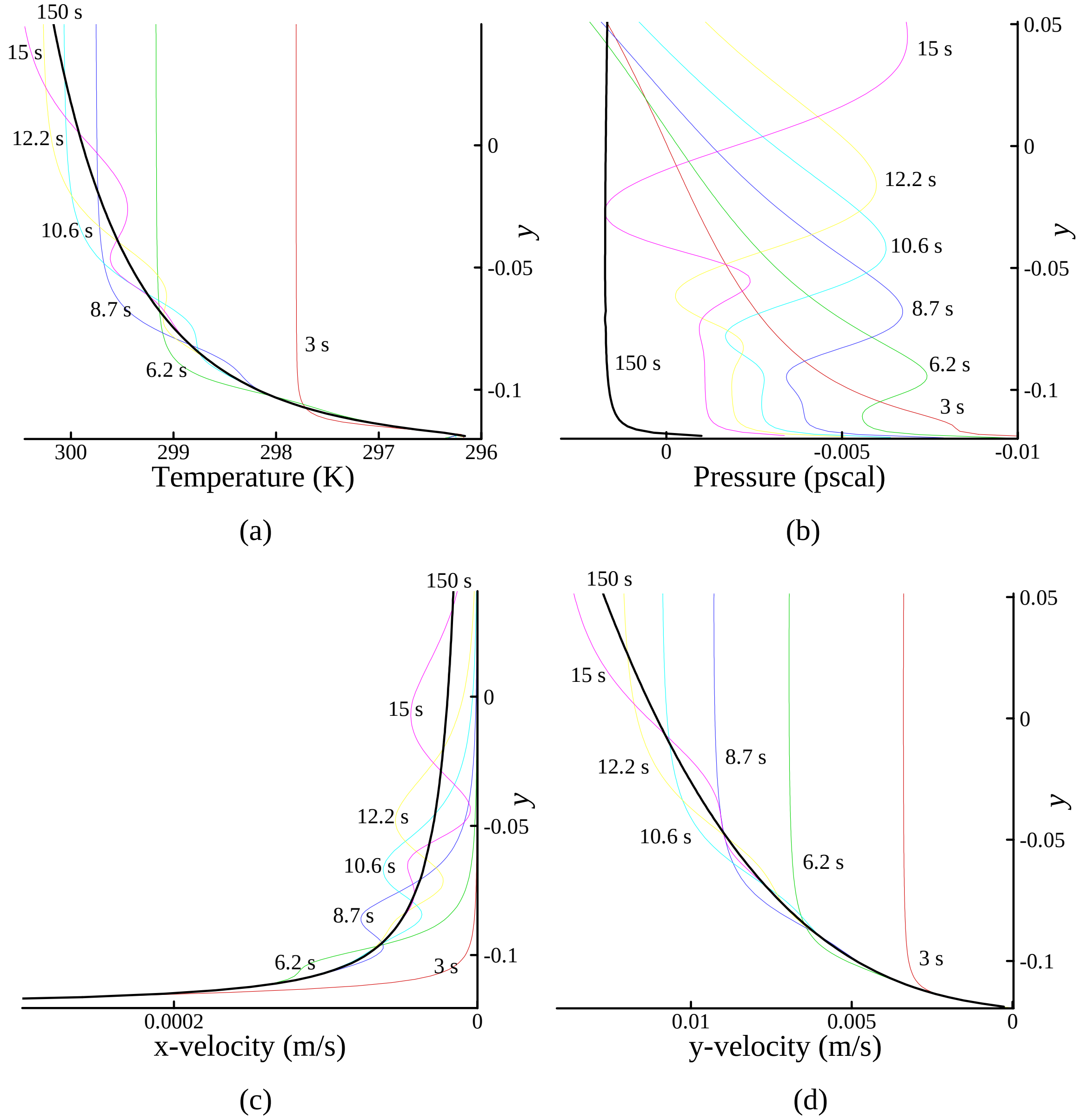

Figure 5.4 Profiles of the temperature, pressure and velocities at x = 0.499 m at different times

Figures 5.2 and 5.3). As a consequence, the pressure gradient as the only one horizontal force plays a key role in the origination of the LEE

5.2.2 Propagation of the LEE

The pressure minimum, induced by the vertical convection flow in the upstream corner, moves downstream, as indicated by the pressure profiles in Figure 5.4(b). For the purpose of illustrating the propagation of the pressure perturbations, Figure 5.5 shows the pressure contours and the corresponding streamlines at different times. As the

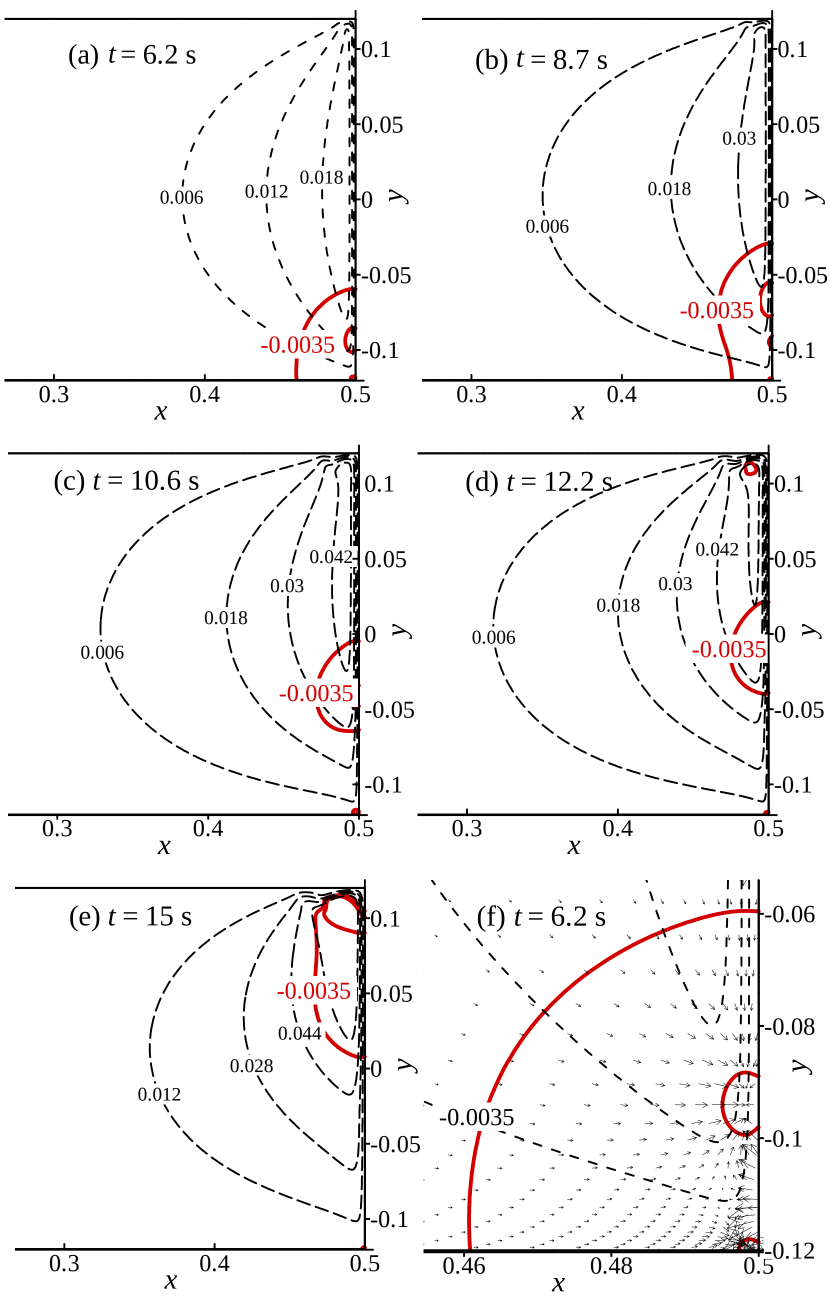

Figure 5.5 Isobars (solid lines) and streamlines (dashed lines) adjacent to the hot sidewall (vectors in f: negative pressure gradients)

pressure minimum moves downstream, by comparing stream function values at different times, it is seen from Figure 5.5 that the convection at the upstream side of the pressure minimum is apparently enforced. In particular, the horizontal convection in which the pressure gradient is the only one driving force significantly increases with time.

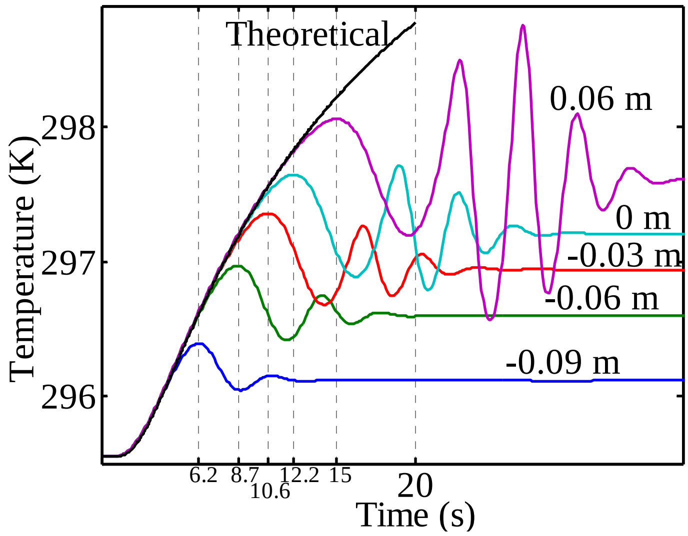

Figure 5.6 Time series of the temperatures at different heights (x = 0.498 m)

Figure 5.5(f) shows the vectors of the negative pressure gradient at t = 6.2 s. Clearly, the horizontal entrainment is driven by the pressure gradient near the location of the pressure minimum.

In order to observe further the temperature variation associated with the propagation of the LEE, Figure 5.6 plots time series of the temperatures at different heights. Distinct properties of the LEE propagation, such as the overshoot of the temperatures and the increasing amplitude of the traveling waves with the height following the overshoot, are consistent with those temperature measurements presented in Chapter 4. However, it is also seen that the variation of the temperatures between the numerical results and experimental measurements (refer to Figure 4.14) is significant; that is, the measured temperature is apparently smaller than the numerically calculated one. Two major factors in the experiments may have contributed to the significant variation between the numerical simulations and experimental measurements, as previously discussed in Chapters 2 and 4. One is that the measured temperature is sensitive to the location of the thermistor within the thermal boundary layer, and thus a slight variation of the thermistor position may cause a significant variation of the measured temperature (also see Patterson et al. 2002). The other is that a smaller temperature difference between the sidewalls is achieved in the experiments than the specified temperature difference in the numerical simulations due to the nature of the adopted heating method in the experiments, as discussed by Patterson and Armfield (1990).

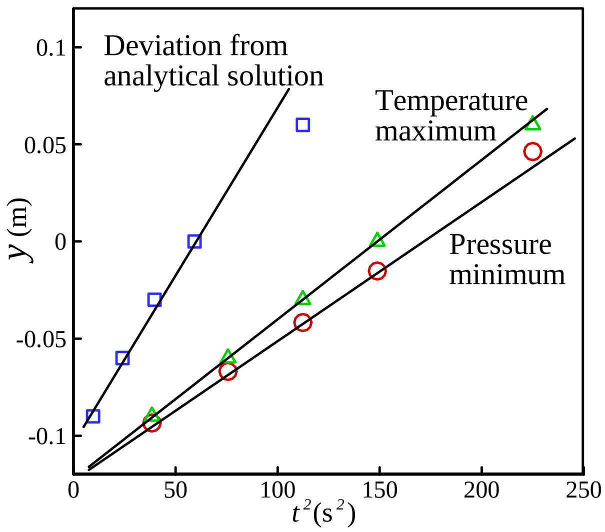

Figure 5.7 Locations of the pressure minimum, the temperature maximum and the deviation of the numerical solution from the theoretical solution against t^2

The times when the temperature achieves the first peak at different heights in Figure 5.6 correspond to those in Figure 5.5 at which the pressure contours and stream functions are shown. By comparing the location of the temperature peak (see the height of each curve in Figure 5.6) with that of the pressure minimum (see the pressure contour within the contour of -0.0035 Pa) at the same time, it is seen that the former location is higher than the latter one; that is, the temperature maximum first arises at a certain point in the thermal boundary layer, and then the pressure minimum arrives.

It is worth noting that at each height the numerically calculated temperature apparently deviates from the theoretical solution given by Goldstein and Briggs (1964) after some time, as seen in Figure 5.6 (see Gebhart 1988; Armfield & Patterson 1992; Patterson et al. 2002). Such deviation is due to the fact that when the temperatures are analytically solved the convection terms in the energy equation is neglected (Goldstein & Briggs 1964, see the next subsection for details).

For the purpose of measuring the propagation of the LEE, Figure 5.7 plots the locations of the pressure minimum, the temperature maximum and the deviation of the numerical solution from the theoretical solution against the time squared. Clearly, there is a very good linear correlation between the locations and the time squared for the three sets of data in the initial stage; that is, the propagation speeds of the pressure minimum, the temperature maximum and the deviation of the numerical solution from the theoretical solution are a linear function of time, which is also coincidently consistent

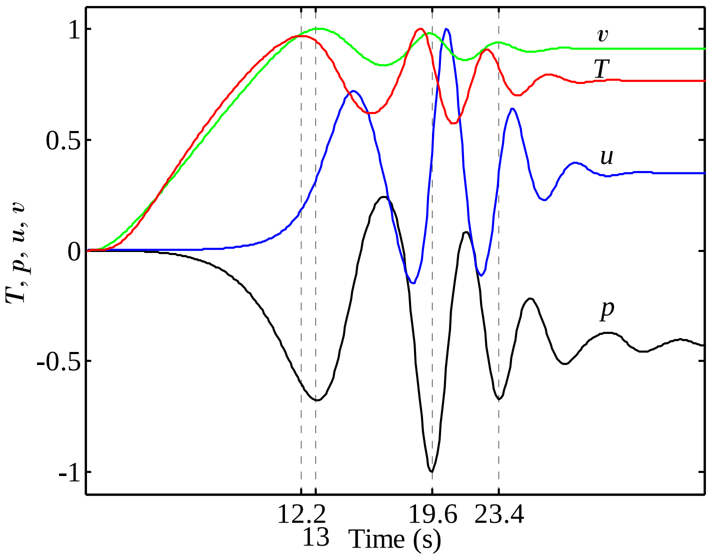

Figure 5.8 T, u, v, and p normalized against time at the point (0.498 m, 0 m)

with the scaling prediction of the initial-stage flow velocity (i.e. $v \sim t$) in Patterson and Imberger (1980).

For the purpose of illustrating the coupling of variables in the LEE propagation, Figure 5.8 plots the time series of normalized T, p, u and v (i.e. $T = (T - T_0)/(|T|_{max} - T_0)$, $p = (p - p_0)/(|p|_{max} - p_0)$, $u =(u - u_0)/(|u|_{max} - u_0)$ and $v =(v - v_0)/(| v|_{max} - v_0)$) at the point (0.498 m, 0 m). It is clear that the arrival of the pressure minimum coincides with the appearance of the overshoot of the vertical convection velocity but slightly lags behind that of the temperature maximum.

In summary, the vertical mass transfer near the leading edge, due to the sudden heating, induces an initial pressure perturbation. When the pressure perturbation propagates downstream, it further induces the velocity perturbation and through the heat convection impacts on the temperature field (also see the local energy balance in the next subsection 5.2.3). Clearly, the LEE behaviors of the thermal boundary layer flow for the case of sudden heating are an interaction coupling the temperature, pressure and velocities.

5.2.3 Heat balance in the initial stage

In order to obtain insights into the deviation of the numerical solution from the theoretical solution (Goldstein & Briggs 1964), the components of the energy equation of the thermal boundary layer are discussed in the following section. This is because

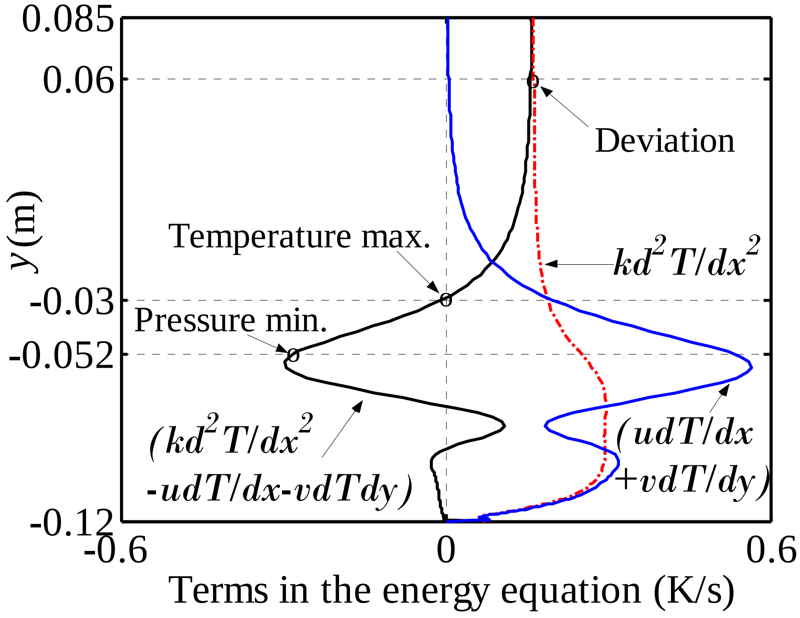

Figure 5.9 Terms in the energy equation at x = 0.498 m at t = 10.6 s

both the numerical and theoretical solutions for temperature are obtained by solving the energy equation.

Figure 5.9 shows the vertical profile of each term in the energy equation at t = 10.6 s. It is clear that the diffusion term ($\kappa\partial^2T/\partial x^2$) is approximately constant downstream, far from the location of the pressure minimum, and significantly increases upstream of the pressure minimum point. Similarly, the convection terms ($u\partial T/\partial x + v\partial T/\partial y$) are approximately zero downstream of the deviation point (y = 0.06 m, see Figure 5.9). However, upstream of y = 0.06 m, the convection terms increase as the distance from the deviation point increases. As a consequence, the unsteady temperature term ($\kappa\partial^2T/\partial x^2 - u\partial T/\partial x - v\partial T/\partial y$) also deviates from the diffusion term. This observation indicates the reason why the numerical solution deviates from the theoretical solution (also see Figures 5.6 and 5.7); that is, the theoretical solution (Goldstein & Briggs 1964) neglects the convection terms in the theoretical solution of the energy equation, however these terms become important once the LEE has passed.

As the convection term increases and eventually balances the diffusion term at y = -0.03 m, the unsteady temperature term becomes zero at this point (refer to Figure 5.9) and the temperature reaches a maximum (refer Figure 5.6). The pressure minimum point is upstream of the temperature maximum position and does not coincide with the maximum of the convection terms as seen in Figure 5.9. Upstream of the pressure minimum, perturbations of the LEE are clear. Armfield and Patterson (2000) indicated that the propagation speed of the LEE perturbations is determined by the speed of the traveling waves based on a stability analysis.

In summary, as indicated in Figures 5.2 to 5.5, the LEE is an interaction between the major flow quantities including the temperature, pressure and velocities. In particular, the pressure (i.e. the pressure gradient) plays a key role in the origination and propagation of the LEE. A good linear correlation of the locations of the pressure minimum, the temperature maximum and the deviation with the time squared illustrates that the different propagation speeds of these quantities describing the LEE linearly increase with time in the initial stage (Figure 5.7). Furthermore, by examining the individual components of the energy equation (Figure 5.9), it is demonstrated that the numerical solution significantly deviates from the theoretical solution due to the neglect of the convection terms in the theoretical solution.

5.3 Intrusion

5.3.1 Separation and trailing waves

As previously described, the thermal boundary layer becomes stable following the passage of the LEE for a certain period of time (see Figure 5.1b), and in the meantime the horizontal intrusion separates from the ceiling of the cavity.

Figure 5.10 shows comparisons between the shadowgraphs and the isotherms generated by the numerical simulation at the downstream end of the thermal boundary layer during that period of time. It is seen in Figure 5.10 that the numerical simulations are consistent with the experimental results in portraying the intrusion front structure, the separation position and the trailing waves, although the numerical results indicate that the numerical flow develops slightly faster than the experimental flow. This discrepancy in timing originates from a smaller actual Rayleigh number in the experiment than that in the numerical simulation, as indicated in the previous section (also refer to Patterson & Armfield 1990). Figure 5.10 also shows that, as the time increases, the angle of the intrusion separation becomes larger, resulting in a set of trailing waves with an increasing amplitude and a decreasing wavelength. Moreover, the isotherms in Figure 5.10 clearly indicate that the temperature of the intrusion is higher than that of the ambient fluid in the cavity. This generates an upward buoyancy force, which tends to resist the occurrence of the separation.

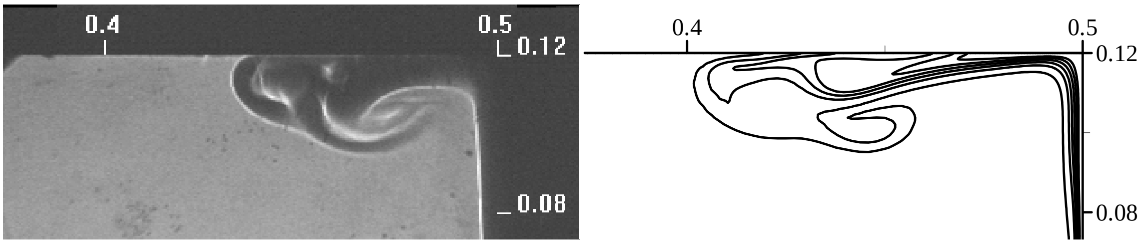

(a) t = 25 s

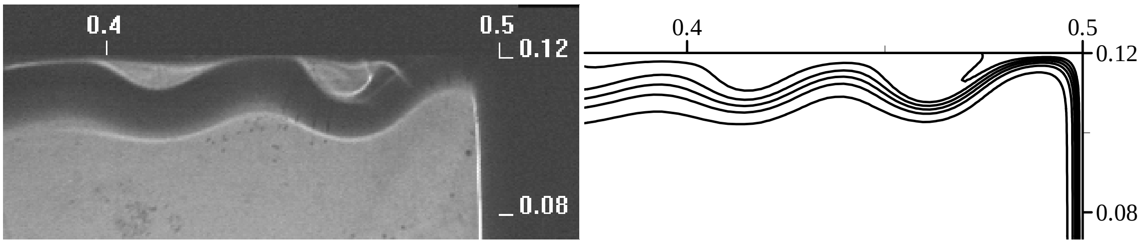

(b) t = 150 s

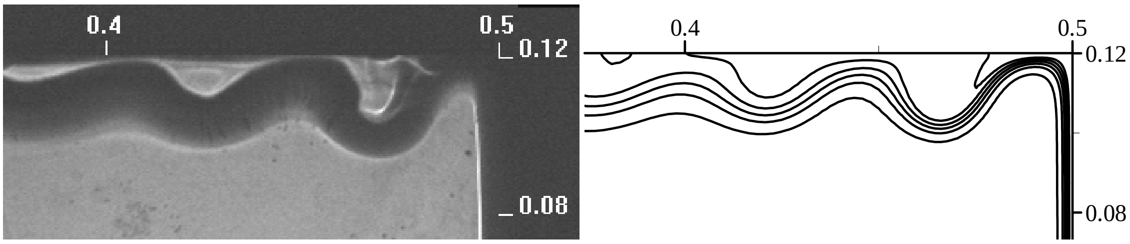

(c) t = 200 s

Figure 5.10 Shadowgraph images from the experiment and isotherms from the numerical simulation (contours between 295.77 and 300.77 K with an interval of 1 K)

To examine the mechanism of the intrusion separation, Figure 5.11(a) shows the numerically generated streamlines adjacent to the hot wall at t = 8 seconds, and Figure 5.11(b) gives a detailed view with a single isotherm overplotted near the top corner at the same time. It is clear that, although the time is small (8 s), separation of the intrusion front has already commenced, as shown by the isotherm in Figure 5.11(b). The streamlines in Figure 5.11(a) indicate that the flow outside the thermal boundary layer is an overall circulation in an anti-clockwise sense, in which the outflow from the upper end of the thermal boundary layer is entrained at the lower end, upstream of the LEE position. At t = 150 s (Figure 5.11c) the streamlines show that, although the anti-clockwise circulation is convected away, a strong reverse flow towards the thermal boundary layer forms under the hot intrusion, occupying most of the core region. This reverse flow may generate a significant pressure gradient, as shown in Figure 5.11(d) in which detailed pressure contours near the upper corner are plotted. The pressure contours indicate that a low-pressure region arises under the separation. This pressure

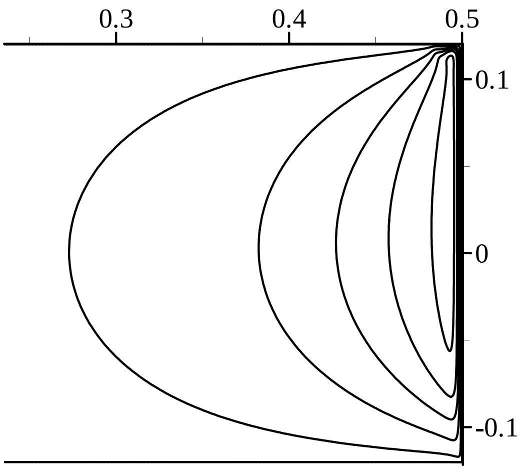

(a) t = 8 s

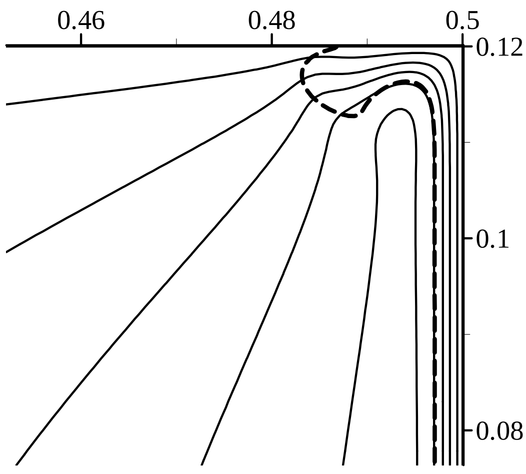

(b) t = 8 s

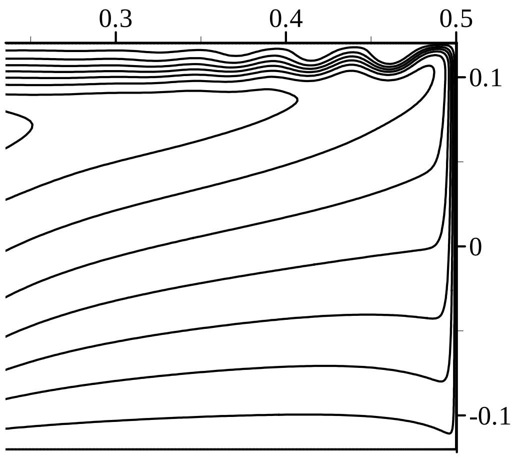

(c) t = 150 s

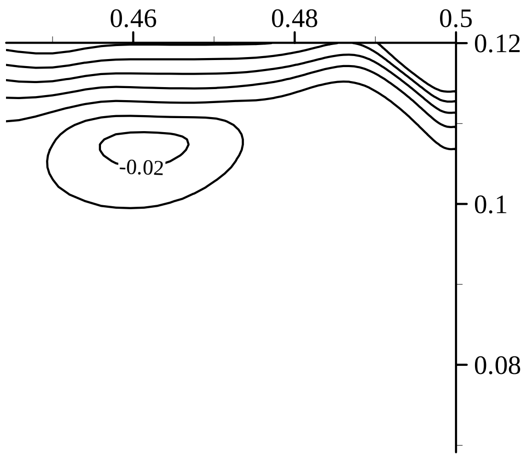

(d) t = 150 s

Figure 5.11 Separation at the early stage.

(a) Streamlines (contours between 2.00×10^{-6} and 2.79×10^{-5} m^2/s with an interval of 6.50×10^{-6} m^2/s). (b) A zoomed view of (a) near the upper-right corner with an isotherm (dashed line) of T = 296 K. (c) Streamlines (contours between 1.66×10^{-5} and 1.83×10^{-4} m^2/s with an interval of 1.66×10^{-5} m^2/s). (d) Isobars near the top corner (contours between -0.02 and 0.1 Pa with an interval of 0.02 Pa)

gradient drives the hot intrusion to separate, as shown in Figure 5.11(c). As the intrusion travels further into the cavity, the pressure gradient becomes less significant, and buoyancy drives the flow back towards the ceiling, leading to reattachment. The competing buoyancy and pressure forces therefore result in a set of trailing waves, as shown in Figure 5.11(c).

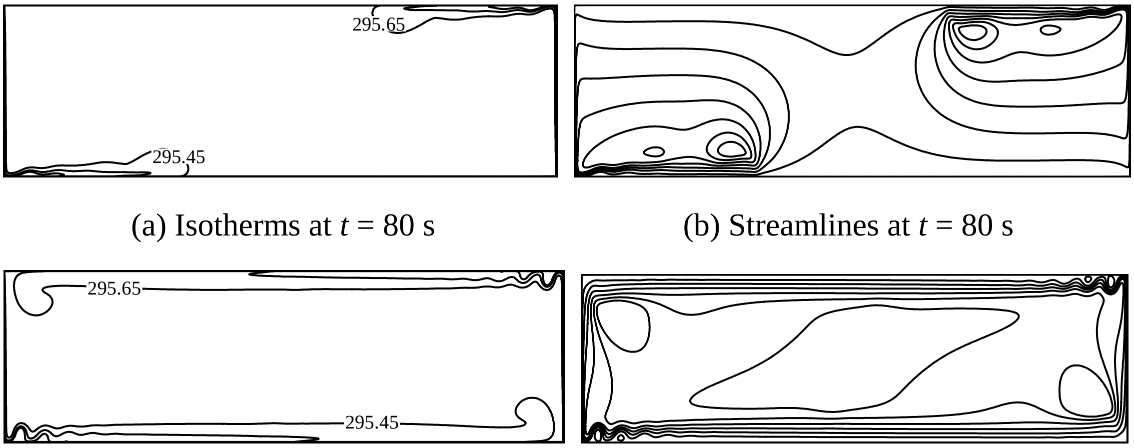

(a) Isotherms at t = 80 s (b) Streamlines at t = 80 s

(c) Isotherms at t = 260 s (d) Streamlines at t = 260 s

Figure 5.12 Development of the intrusion front before it strikes the opposite sidewall (Isotherm contours: 291.45, 293.45, 295.45 295.65, 297.65 and 299.65 K; Streamline contours between 1.35×10^{-5} and 1.35×10^{-4} m^2/s with an interval of 1.35×10^{-5} m^2/s)

5.3.2 Oscillations of intrusion

The subsequent development of the hot intrusion is shown in Figure 5.12 in which the temperature contours and stream functions at different times are plotted. It is seen in Figure 5.12(a) that the hot intrusion front moves to the mid cavity along the ceiling. In the meantime, the large anticlockwise circulation (hereinafter referred to as the front circulation, and see Figure 5.12a) under the intrusion front is horizontally extended, in comparison with that at the earlier time (see Figure 5.11a). With the passage of time, those trailing waves gradually regress to the hot top corner as shown in Figure 5.12(c), and the front circulation arrives at the cold sidewall in Figure 5.12(d). Symmetrically, the cold intrusion arrives at the hot sidewall (see the bottom-right corner).

Due to the limitation of the dimensions of the spherical mirrors in the shadowgraph visualization, only the flow adjacent to the hot sidewall was visualized in the experiments. However, as seen in Figure 5.12, the flow in the cavity is symmetrical. Figure 5.13 shows a comparison between the experimental and numerical results in the vicinity of the hot sidewall at the time when the cold intrusion strikes the hot sidewall. It is noted previously that the development of the flow described by the numerical results is slightly faster than that observed in the experiment in the early stage. As time elapses, this timing difference accumulates. Therefore, the comparison between the experimental image and the numerical simulation in Figure 5.13, which depicts the event when the

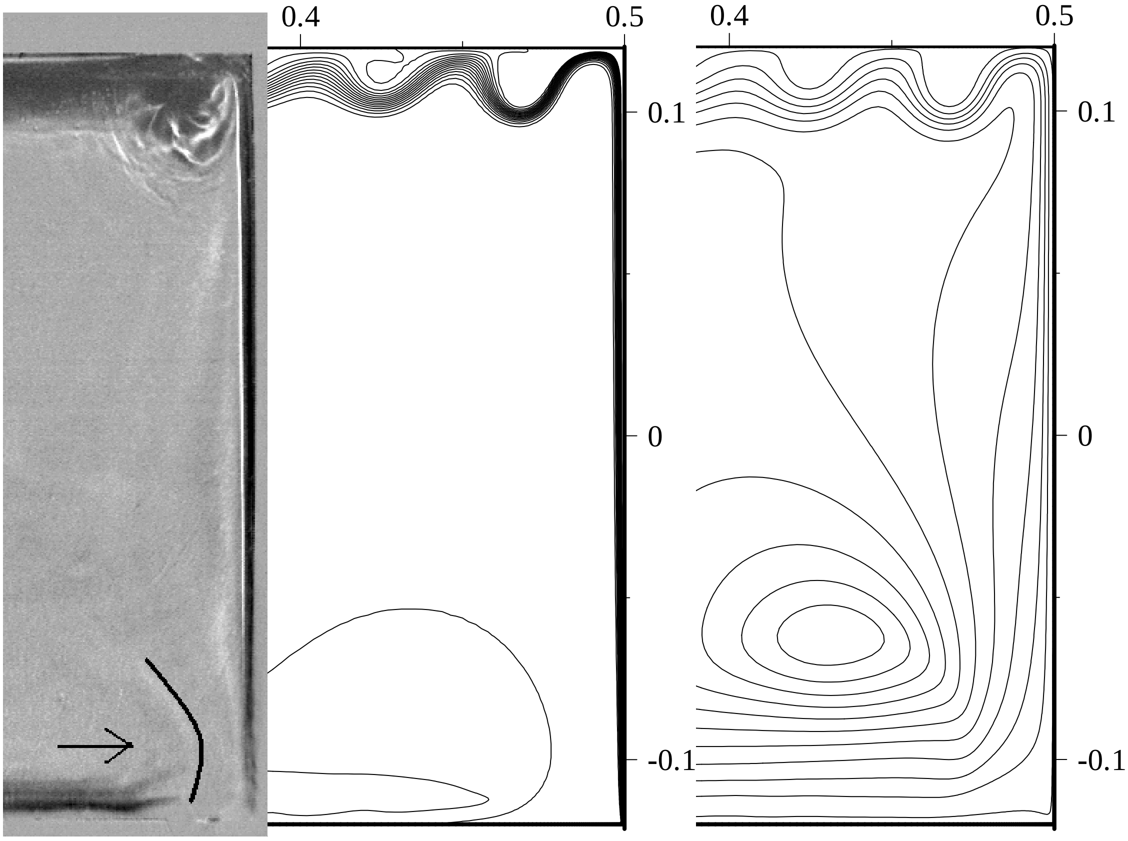

(a) t = 335 s (b) t = 235 s (c) t = 235 s

Figure 5.13 Cold intrusion strikes the hot wall

(a) Shadowgraph image. (b) Isotherms (contours between 295.23 and 300.19 K with an interval of 0.31 K). (c) Streamlines (contours between 1.77×10^{-5} and 1.95×10^{-4} m^2/s with an interval of 1.77×10^{-5} m^2/s)

cold intrusion from the far sidewall is about to impact the base of the hot boundary layer, is based on significantly different times. Since the kinematic properties are the same, it suffices to make comparisons based on the events rather than the actual times in this figure.

Figure 5.13(a) is a processed shadowgraph image in which the background image recorded immediately before the start of the experiment is subtracted from the original shadowgraph image (also see Figure 4.1). At this time the LEE has passed, and the cold intrusion, marked by the solid line overdrawn at the bottom of the figure, is approaching the hot wall. The thermal boundary layer thickness, measured by the distance between the vertical bright strip and the sidewall on the shadowgraph image (the bright strip corresponds to the position of the maximum of the second derivative of the temperature, as discussed in Section 2.1), is approximately constant before the cold intrusion strikes

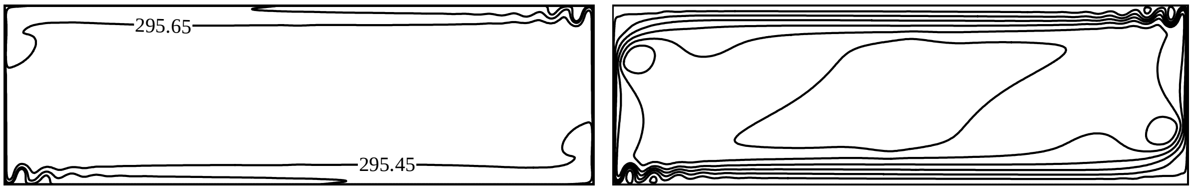

(a) Isotherms at t = 272 s (b) Streamlines at t = 272 s

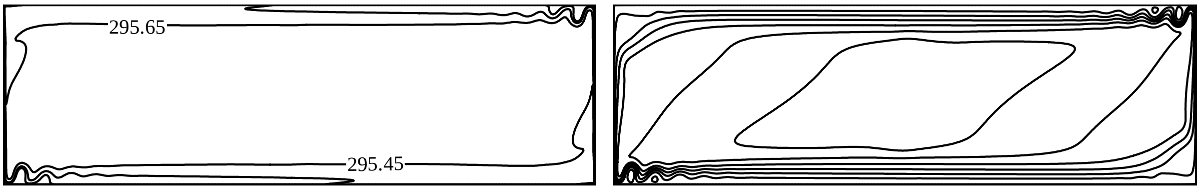

(c) Isotherms at t = 280 s (d) Streamlines at t = 280 s

Figure 5.14 Subsequent development of intrusion after striking the opposite sidewall (Isotherm contours: 291.45, 293.45, 295.45 295.65, 297.65 and 299.65 K; Streamline contours between 1.35×10^{-5} and 1.35×10^{-4} m^2/s with an interval of 1.35×10^{-5} m^2/s)

the hot wall. Likewise, the time series of the temperature in the thermal boundary layer are also constant at this stage, as seen in Figure 5.1. However, once the cold intrusion strikes the hot wall, it triggers the convective instability of the thermal boundary layer, as described by those temperature waves in Figure 5.1, and the convective instability propagates and amplifies downstream. As a consequence, the outflow in the top corner becomes clearly unstable, and is no longer a simple discharge flow into the cavity, as shown in Figure 5.13(a). The complex roll structure in the top corner causes strong mixing in this region, which is believed to be responsible for the disappearance of the downstream trailing waves that are present in the intrusion before the arrival of the cold intrusion. Figure 5.13(b) plots the corresponding isotherms of the numerical simulation at the same time. However, the numerically generated corner flow structure remains stable, compared with the experimental flow. It is suggested that the presence of various perturbations in the experiment could lead to the destabilization of the roll structure in the top corner. Furthermore, the streamlines shown in Figure 5.13(c) imply that the entrainment of the thermal boundary layer is all from the cold intrusion at this time, opposing to the situation at earlier times when the entrainment is from the discharge at the top end of the thermal boundary layer, as shown in Figure 5.11(a).

Following the discussion in Figure 5.12, Figure 5.14 shows the subsequent development of the hot intrusion. The front circulation moves downstream along the cold sidewall in Figure 5.14(b) and eventually dissipates into the core in Figure 5.14(d).

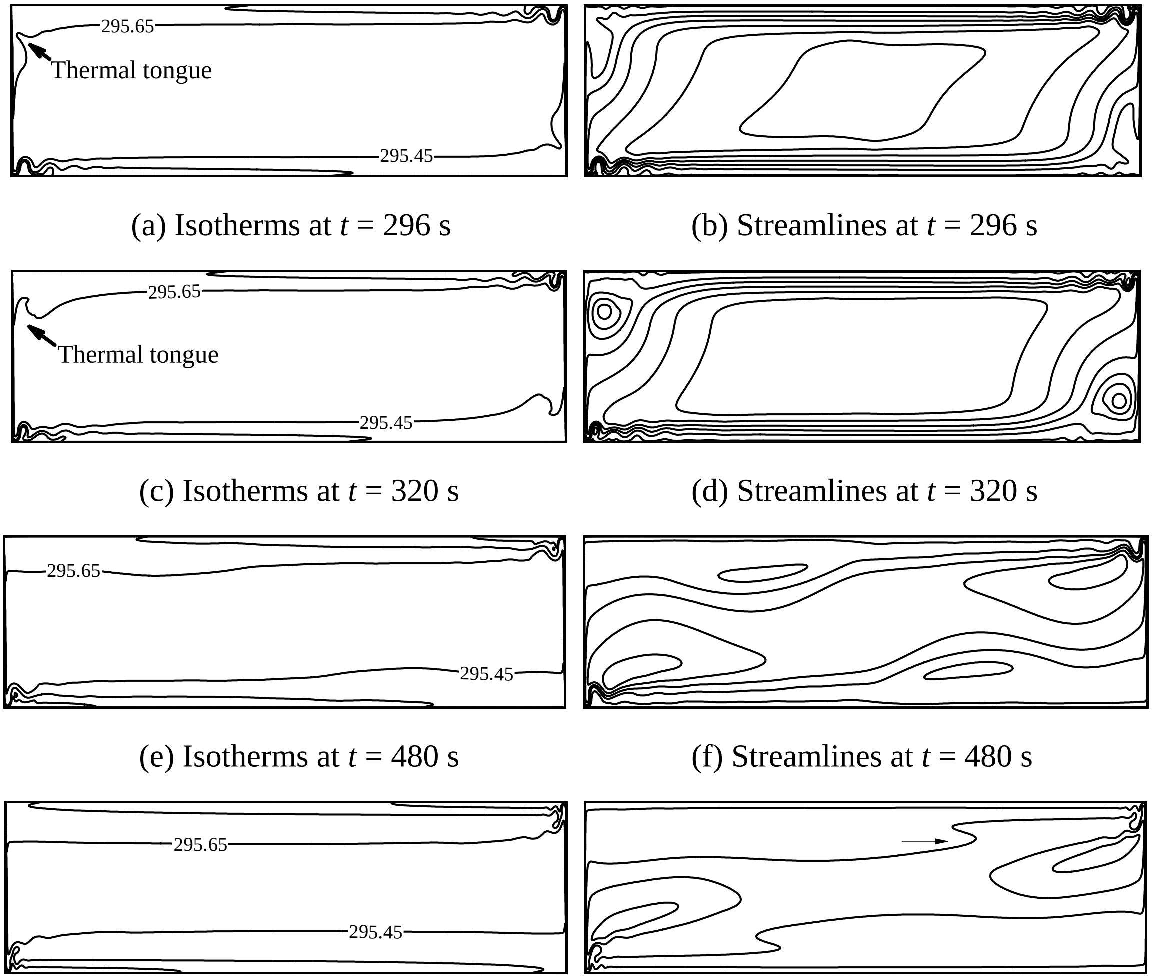

(a) Isotherms at t = 296 s (b) Streamlines at t = 296 s

(c) Isotherms at t = 320 s (d) Streamlines at t = 320 s

(e) Isotherms at t = 480 s (f) Streamlines at t = 480 s

(g) Isotherms at t = 720 s (h) Streamlines at t = 720 s

Figure 5.15 Formation and development of the reverse flow

(Isotherm contours: 291.45, 293.45, 295.45 295.65, 297.65 and 299.65 K; Streamline contours between 1.35×10^{-5} and 1.35×10^{-4} m^2/s with an interval of 1.35×10^{-5} m^2/s)

Since the cold sidewall cannot cool and entrain all the hot intrusion to the bottom, increasing hot fluid is accumulating in the cold top corner (the upper-left corner). As a consequence, a tilted flow field forms near the cold top corner as shown in Figure 5.14(d). In addition, the intrusion front stretches gradually downward along the cold sidewall, as indicated by the temperature contours shown in Figures 5.14(a) and (c). As a consequence, the tilted temperature contours near the upper-left cold corner produce buoyancy forces.

Figure 5.15 shows the further development of the intrusion. Due to the above-mentioned buoyancy effect, a reverse flow near the cold sidewall is generated, as shown in Figure 5.15(b). At this time, the temperature contours exhibit an upward ‘thermal tongue’ near the upper-left corner of the cold sidewall in Figure 5.15(a). As the hot

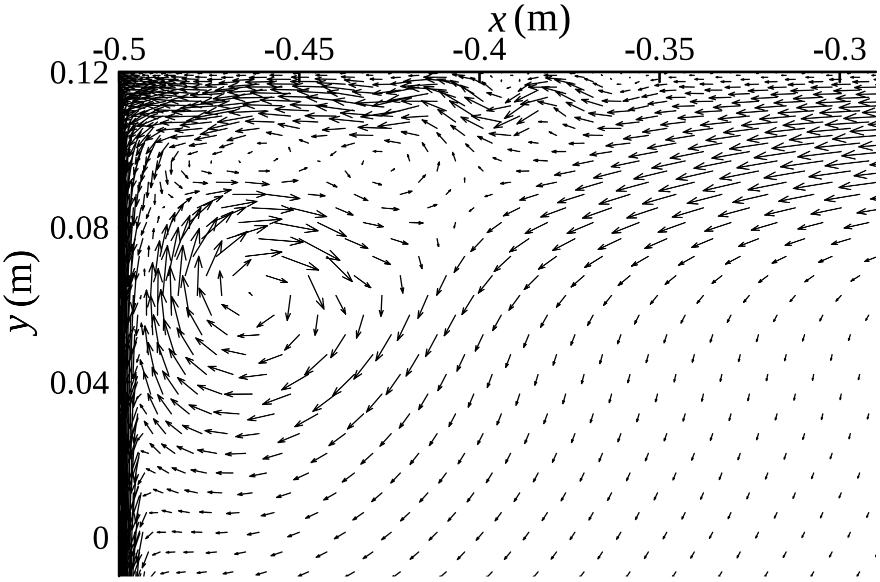

Figure 5.16 Velocity vectors in the cold top corner at 320s

intrusion further accumulates in the cold top corner, the increasing buoyancy effect forces the thermal tongue to rotate in the clockwise direction (see Figure 5.15c), and eventually, a clockwise circulation as shown in Figure 5.15(d) is formed in the region.

In order to observe the details of the flow near the cold top corner when the hot intrusion reaches the cold wall, Figure 5.16 shows the velocity vector field at the same time as of Figure 5.15(d). It is seen in this figure that the strong shear between the clockwise circulation and the hot intrusion underneath the ceiling induces some smaller scale circulations in the region as well as some waves in the coming hot intrusion.

Figure 5.15(f) shows that this clockwise circulation is traveling toward the hot sidewall, although it has been weakened significantly. Moreover, the clockwise circulation splits the hot intrusion into two parts, one of which continues to run to the cold sidewall along the ceiling and the other jets into the core as seen in Figure 5.15(f). After about 720 seconds, the clockwise circulation is completely dissipated and forms a reverse flow relative to the hot intrusion as indicated by an arrow in Figure 5.15(h). This reverse flow then pushes the jet stream (into the core) closer to the hot sidewall (Figure 5.15g), and causes it to be unstable. The instability of the jet stream into the core in turn impacts on the vertical thermal boundary layer flow, resulting in the waves of the temperature time series in the vertical thermal boundary layer, as seen in Figure 5.1. The corresponding frequency spectrum analyses are shown in Figure 5.17. Clearly, the instability of the jet stream induced by the reverse flow (with a principal frequency of 0.07 Hz) is different from the thermal convective instability in the thermal boundary

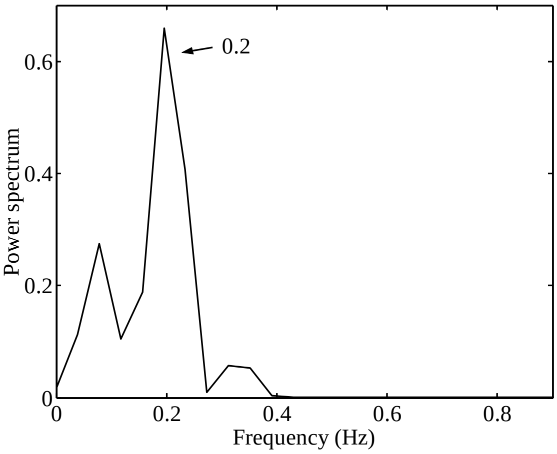

(a) Convective instability

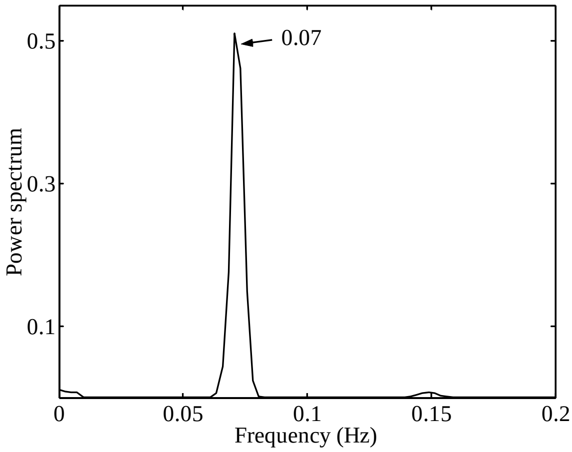

(b) Instability of the jet stream

Figure 5.17 Spectra of the temperature waves of the thermal boundary layer flow and jet stream

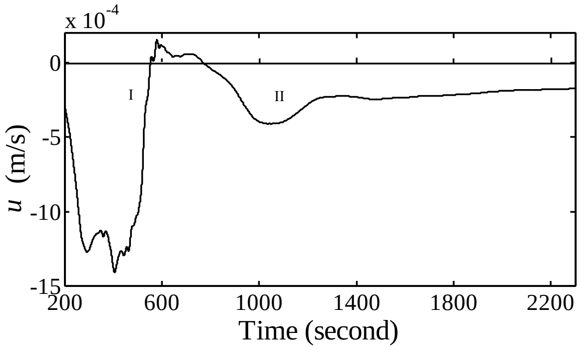

(a) u versus time at point (x = 0, y = 0.07)

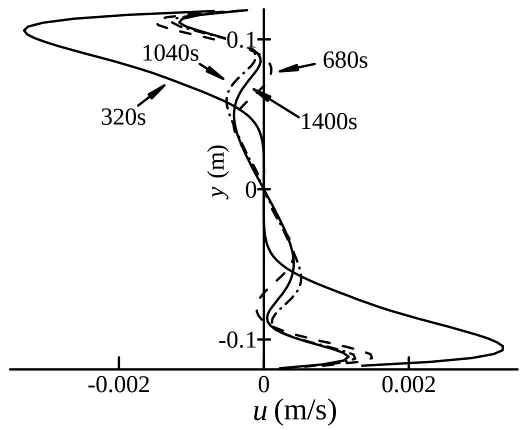

(b) Profiles of u at x = 0 at different times

Figure 5.18 Oscillations of the intrusion

layer induced by the cold intrusion striking the hot sidewall (with a higher frequency of 0.2 Hz), which is consistent with the experimental measurements presented in Chapter 4 (see Figures 4.16 and 4.18).

It is worth noting that the temperature contours in the upper part of the cavity in Figure 5.15 move downward toward the core as the reverse flow moves back to the hot sidewall. This implies that the reverse flow speeds up the core stratification.

As shown in Figure 5.15(h), the reverse flow has been significantly dissipated when it moves toward the hot sidewall. However, this flow does not disappear, and eventually it causes a cavity-scale oscillation in the upper part of the cavity (a back and forth flow between the hot and cold walls). Figure 5.18(a) shows this cavity-scale horizontal oscillation using a time series of the horizontal velocity obtained at the point

(x = 0 m, y = 0.07 m). It is seen that the amplitude of the oscillation reduces significantly after the first oscillation cycle as indicated by ‘I’ in Figure 5.18(a). The first two cycles (‘I’ and ‘II’ in figure 5.18a) are completed by 1400 seconds, but the oscillation actually lasts for a longer time with reduced amplitude. At the point shown, the time duration for which the velocity is positive (the reverse flow) is more than 200 seconds. Despite the reduced intensity of the cavity-scale oscillation, it plays a key role in the stratification of the core, as shown in Figure 5.15.

Similarly, there always exists a symmetric oscillation of the cold intrusion in the lower part of the cavity. Figure 5.18(b) shows the horizontal velocity profile at x = 0 at different times. Two symmetrical oscillations, one in the upper part and the other in lower part of the cavity respectively, can be clearly observed.

In general, oscillations of the horizontal intrusion can play a key role in the transition of natural convection in a differentially heated cavity, particularly in the stratification of the fluid in the cavity and the development of the instability of the vertical boundary layer flow.

5.4 Formation of the double-layer structure

As indicated by the temperature plot in Figure 5.1, the subsequent development of the natural convection flow is a slow transition to the quasi-steady state. Therefore, the timing difference between the experiment and numerical simulation noted above becomes less significant. In the following figures the experimental and numerical results at the same times are compared.

Figure 5.19 shows the subsequent development of the thermal boundary layer after the reverse flow moves back to the hot wall. In the bottom corner, a second bright strip in the shadowgraph image arises outside the thermal boundary layer (the inner layer) and is roughly parallel to the inner layer (Figure 5.19a). In the meantime, a similar bright strip is also noticeable in the top corner, although it is further out from the hot wall. These two outer bright strips correspond to the positions of the minima of the second derivative of the temperature (indicated by the dashed lines in Figure 5.19b). It is seen in Figure 5.19(b) that an upward thermal tongue (with fluid colder than that on both sides) of isotherms close to the sidewall near the lower corner is present, and the thermal tongue is fed by the incoming cold intrusion. Near the upper corner, due to the

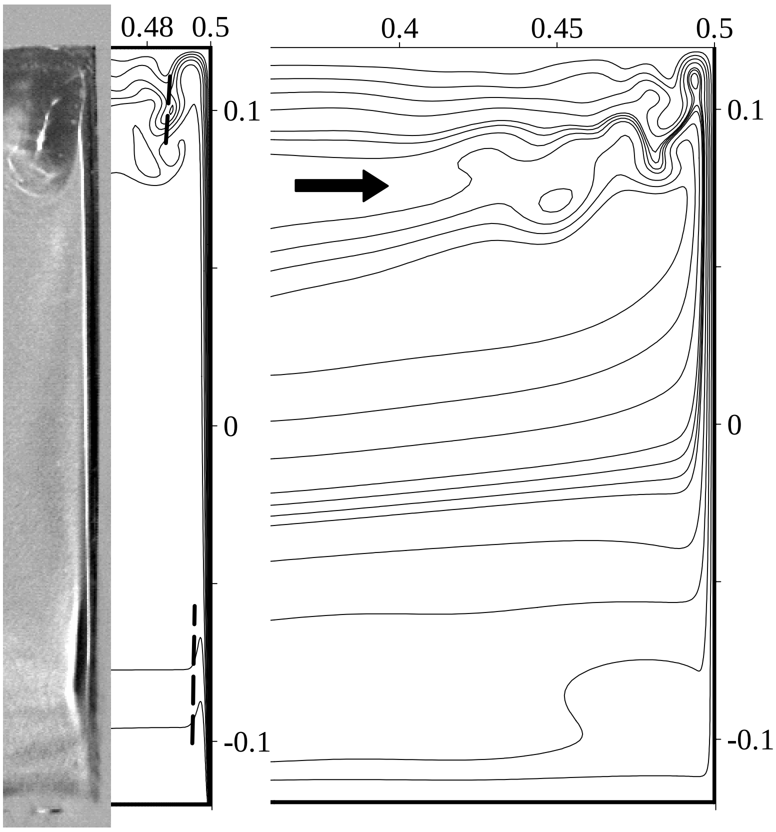

(a) (b) (c)

Figure 5.19 Formation of the double-layer structure at t = 695 s

(a) Shadowgraph image. (b) Isotherms (solid lines showing contours between 294.1 and 301.1 K with an interval of 1 K) and lines of the minimum second derivative of temperature (dashed lines). (c) Streamlines (contours between 6.70×10^{-6} and 6.70×10^{-5} m^2/s with an interval of 7.50×10^{-6} m^2/s)

separation of the intrusion flow, a thermal structure similar to that near the lower corner but at a much larger scale forms.

The corresponding streamlines (Figure 5.19c) display further evolution of the flow adjacent to the hot wall. As described in Section 5.3, the resulted reverse flow (indicated by the arrow in Figure 5.19c) splits the hot intrusion into two parts, an upper part that moves to the cold wall under the ceiling and a lower part that discharges into the cavity and forms a circulation, trapping cold fluid between itself and the boundary layer.

The two outer bright strips slowly extend toward the mid height of the cavity as the interior fluid in the cavity is further stratified. Figure 5.20 shows the shadowgraph image, isotherms and streamlines when the two outer bright strips eventually meet near the mid height. It is evident in this figure that the two bright strips do not align

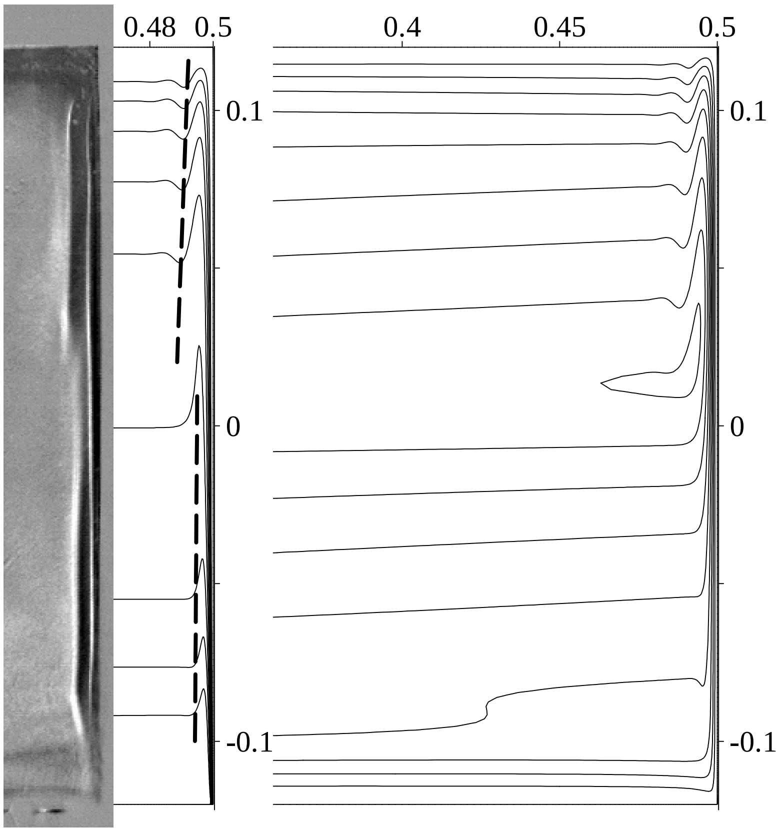

(a) (b) (c)

Figure 5.20 Formation of the double-layer structure with the misalignment of the two outer strips at t = 2500 s

(a) Shadowgraph image. (b) Isotherms (solid lines showing contours between 292.55 and 300.55 K with an interval of 1 K) and lines of the minimum second derivative of temperature (dashed lines). (c) Streamlines (contours between 3.30×10^{-6} and 3.33×10^{-5} m^2/s with an interval of 3.30×10^{-6} m^2/s)

vertically, with the descending strip further away from the hot wall than the ascending one. The upward thermal tongue in the upper part is much greater than that in the lower part (Figure 5.20b), and a clear circulation, driven by the misalignment of the two outer strips, is present near the meeting point (Figure 5.20c).

Figure 5.21 shows the shadowgraph image, isotherms and streamlines of the flow adjacent to the hot wall at a much later time. Compared with those in Figure 5.20(a), the two outer strips have aligned vertically and a continuous outer layer has formed, as shown in Figure 5.21(a). The corresponding isotherms in Figure 5.21(b) indicate that the width of the upward thermal tongue decreases continuously from the top to the bottom. The fluid in the cavity has been further stratified, as shown in Figure 5.21(b). Figure 5.21(c) shows that the circulation at the mid height shown in Figure 5.20(c) has

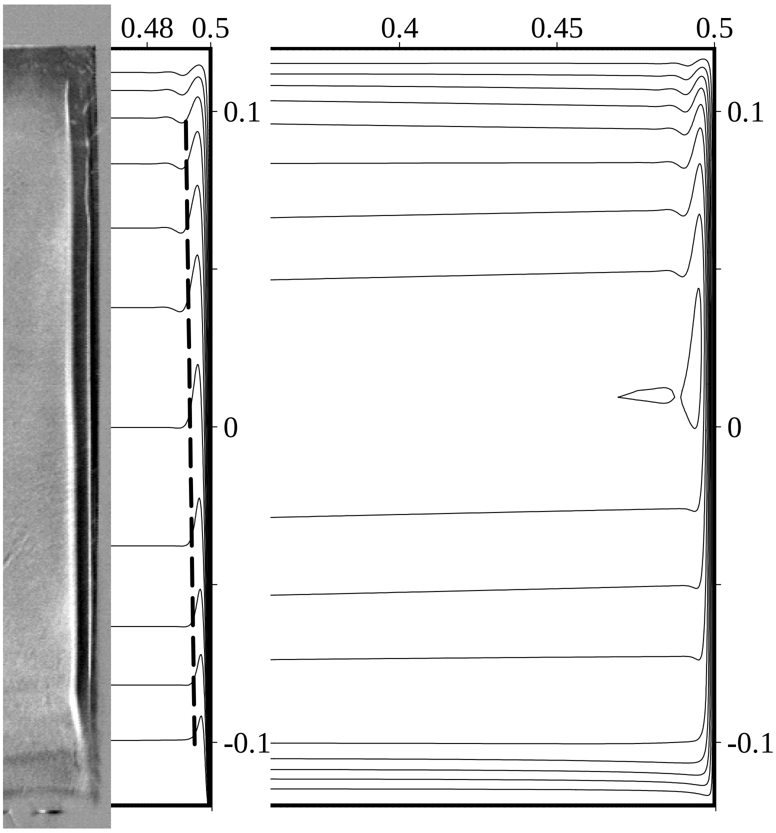

(a) (b) (c)

Figure 5.21 Double-layer structure at t = 4700 s

(a) Shadowgraph image. (b) Isotherms (solid lines showing contours between 291.55 and 301.55 K with an interval of 1 K) and lines of the minimum second derivative of temperature (dashed lines). (c) Streamlines (contours between 2.50×10^{-6} and 2.46×10^{-5} m^2/s with an interval of 2.80×10^{-6} m^2/s)

been split into two smaller circulations. The flow structure at this stage is referred to as a double-layer structure.

5.5 Flow features in the quasi-steady stage

In the previous sections, the transition of natural convection is described, and the formation and evolution of the double-layer structure of the vertical thermal boundary layer observed in shadowgraph images are represented through comparisons with the numerical simulation. It has been demonstrated that the numerical simulation is consistent with the experiment at all stages of the flow development. In order to gain

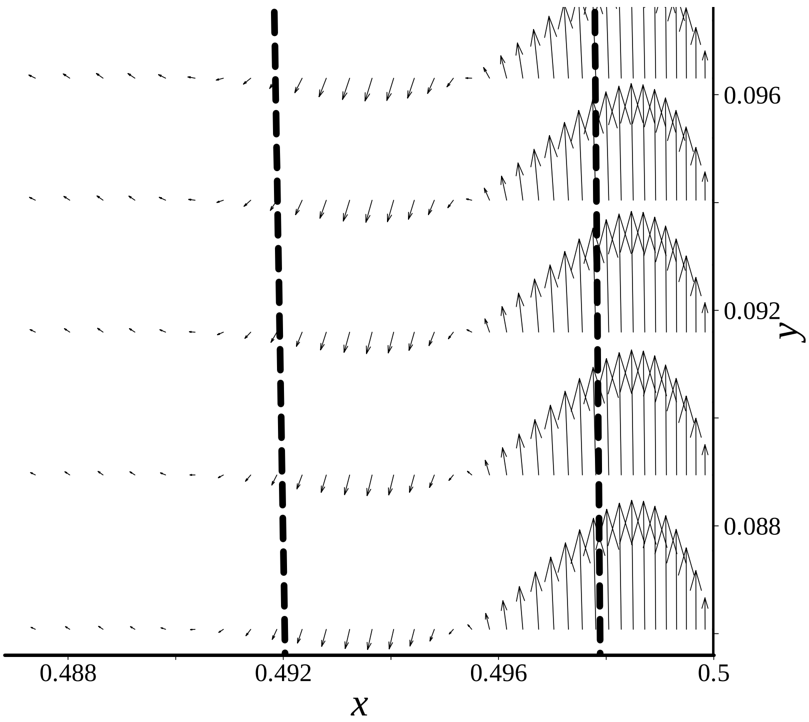

Figure 5.22 Details of the velocity vector adjacent to the hot wall at t = 4700 s
The dashed lines indicate the minimum (left one) and maximum (right one) of the second derivative of the temperature

further insight into the double-layer structure, this section discusses the velocity fields of the double-layer structure, based on the numerical results.

It is clear from Figures 5.21(b) and (c) that there is a small dip on the interior side of the upward thermal tongue in both the isotherm and streamline contours. This indicates that a reverse flow is present in the outer layer (also see Tao & Le Quere 2003). Figure 5.22 shows a detailed view of the velocity vectors of the thermal boundary layer, in which the reverse flow (flowing downwards) outside the inner layer is clear although it is much weaker than the upward flow of the inner layer. The locations of the maximum and minimum second derivatives of the temperature in the x-direction, corresponding to the two bright strips in the shadowgraph images (refer to Section 5.6 for quantitative comparisons between the experimental and numerical results), are marked by the dashed lines in Figure 5.22. It is worth noting that the dashed lines do not match with the maximum and minimum of the velocity; that is, the bright strips in Figures 5.19(a), 5.20(a) and 5.21(a) do not correspond to the maximum and minimum of the velocity boundary layer, although they are a result of the flows.

The flow structure in Figure 5.22 may be attributed to combined buoyancy and inertial effects. After the cold fluid is entrained from the lower part of the cavity, it is

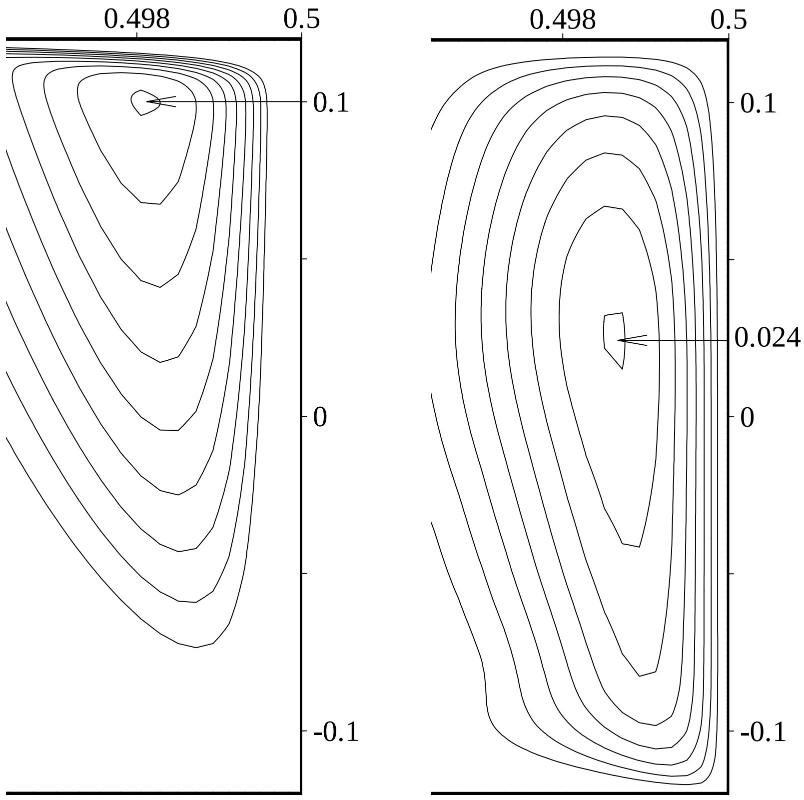

(a) t = 150 s (b) t = 4700 s

Figure 5.23 Velocity magnitudes of the flow adjacent to the hot wall at different times (a) Contours between 0.0076 and 0.0166 m/s with an interval of 0.0011 m/s. (b) Contours between 0.002 and 0.009 m/s with an interval of 0.001 m/s

heated by the hot sidewall and thus driven upwards by the buoyancy effect. The buoyancy force accelerates the fluid if the temperature of the fluid is higher than the locally ambient. As the fluid moves up, the temperature of the fluid approaches the locally ambient because the interior is stratified (i.e. the higher the position, the higher the local ambient temperature). However, the inertial effect drives the fluid upwards over its position of neutral buoyancy so that it reaches a position at which its temperature is lower than the locally ambient. Once the fluid passes its position of neutral buoyancy, gravity resists this upward motion until it stops, and the fluid is discharged from the boundary layer. The discharged fluid firstly falls, due to its lower temperature, until it reaches its position of neutral buoyancy in the stratified interior.

Figures 5.23(a) and (b) compare the velocity magnitude in the vicinity of the hot wall at different times. Associated with the flow transition (see Figures 5.18 through 21), the velocity maximum in the thermal boundary layer reduces as the outer reverse flow extends downwards, changing from approximately 0.0166 m/s in the initial stage

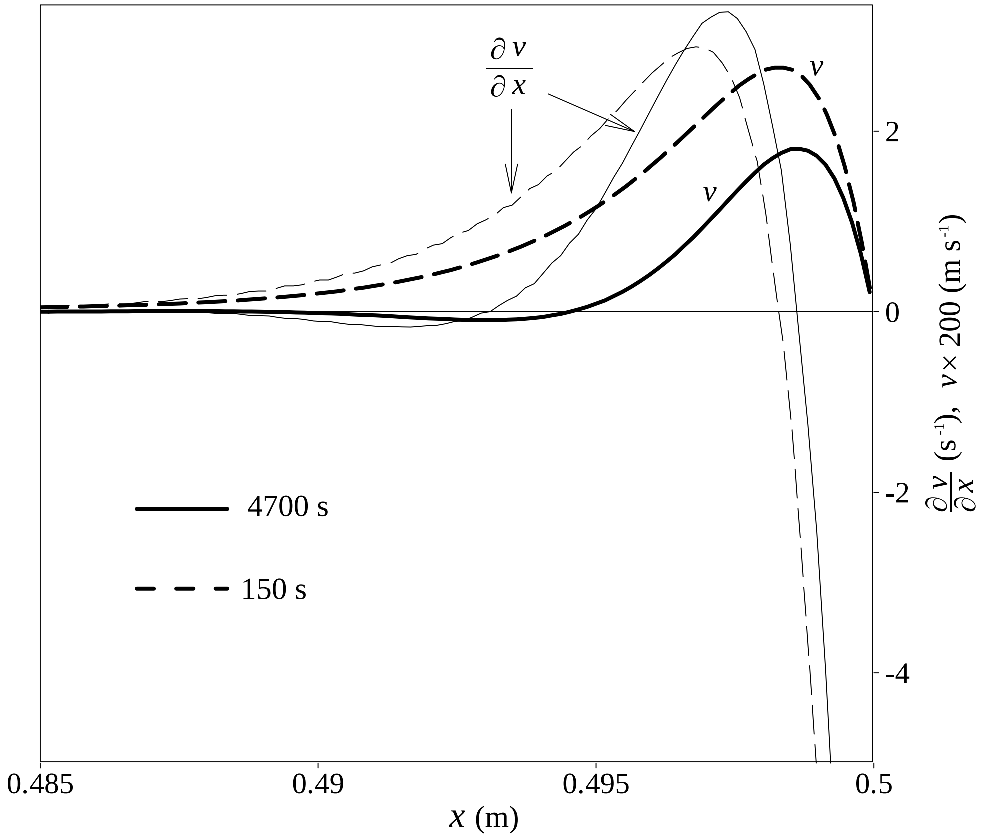

Figure 5.24 Velocity profiles and the *x*-direction derivatives of the upward velocity at y = 0.024 m at different times

to 0.009 m/s in the quasi-steady stage. This is consistent with the scaling result v_{max} = $0.089(g\beta\Delta TH)^{1/2}$ reported by Henkes and Hoogendoorn (1993) with only a small variation between the scaling analysis and the present simulation, which may be attributed to the different aspect ratios (A = 0.24 here but 1 in Henkes & Hoogendoorn 1993). The position of the velocity maximum also moves downwards from the top (y = 0.1 m) to approximately the middle of the cavity (y = 0.024 m) and closer to the hot wall, as shown in Figures 5.23(a) and (b).

Figure 5.24 shows the profiles of the upward velocity and its x-direction derivatives across the thermal boundary layer at y = 0.024 m (where the velocity magnitude peaks at t = 4700 s) at different stages. Compared with that at the earlier stage (e.g. t = 150 s), the occurrence of the reverse flow in the outer layer narrows the inner layer at the later stage (e.g. t = 4700 s). As a result, the position of the maximum velocity in the inner layer moves closer to the sidewall at the quasi-steady stage. This leads to an increase of the local shear ($\partial v/\partial x$) between the outer and inner layers, as seen in Figure 5.24, in which the maximum of the velocity derivative with respect to the x-direction at the quasi-steady stage is evidently greater than that at the earlier time.

5.6 Heat transfer in the quasi-steady stage

In the previous sections, the transition of the thermal boundary layer flow is portrayed by shadowgraph images and numerical results. The outer bright strips in the shadowgraph images (refer to Figures 5.19a, 5.20a, 5.21a) are considered to correspond to the position of the minima of the second derivatives of temperature (refer to Chapter 2), the computed positions of which are shown with dash-dotted lines in Figures 5.19(b), 5.20(b), 5.21(b) and 5.22. Quantitative comparisons between the computed positions of the maxima and minima of the second derivative of the temperature and the observed positions of the bright strips in the shadowgraph image (which corresponds to Figure 5.21) are given in Table 5.1. The positions shown in Table 5.1 are measured as the distance from the hot wall. It is seen that the predicted positions compare well with the observations, but are consistently slightly smaller than the observed positions. This is consistent with the experiments achieving a slightly smaller *Ra* value than intended.

Table 5.1 Positions of the computed maxima and minima of the second derivative of the temperature and the observed bright strips on the shadowgraph image at t = 4700 s

	Distance measured from the hot wall (mm)			
y (m)	Computed $\left.\frac{\partial^2 T}{\partial x^2}\right\rvert_{\max}$	Inner bright strip	Computed $\left.\frac{\partial^2 T}{\partial x^2}\right\rvert_{\min}$	Outer bright strip
-0.06	1.4	2.3	5.4	6.9
0.06	2	3.2	7.5	8.7

The correspondence between the bright strips in the shadowgraph images (Figure 5.21a) and the maxima and minima of the second derivative of the temperature in the direction normal to the strip implies that those bright strips also correspond to the positions of the maximum and minimum horizontal thermal diffusion. For the purpose of examining the horizontal thermal diffusion in the double-layer structure and its interaction with thermal convection, the energy equation (3.15), subject to the usual boundary layer assumptions, is rewritten for the steady state thermal boundary layer flow as

$$\kappa \frac{\partial^2 T}{\partial x^2} + \left(-u \frac{\partial T}{\partial x} \right) + \left(-v \frac{\partial T}{\partial y} \right) = 0. \tag{5.1}$$

Equation (5.1) describes, in a differential sense, the heat balance between thermal diffusion ($\kappa\partial^2 T/\partial x^2$) and convection (horizontal component $-u\partial T/\partial x$ and vertical component $-v\partial T/\partial y$) in a control element near the wall at a steady state. If the value of a certain term is positive, the term contributes heat to the control element, whereas a negative term means a loss of heat from the control element.

Figure 5.25 plots the horizontal profiles of the temperature, velocity and the different terms of Equation (5.1) at t = 4700 s for two different locations along the heated sidewall (y = 0.06 m and -0.06 m, representing the upper and lower parts of the double layer structure respectively). In this figure, the vertical dashed lines indicate the positions of the minimum and maximum of the horizontal thermal diffusion, and the vertical solid lines indicate the positions of the temperature minimum. These vertical lines serve to delineate the inner boundary layer (from the wall to the maximum diffusion line) and the outer layer (from the maximum to the minimum diffusion line).

It is seen in Figure 5.25 that, for both the upper and lower parts of the cavity, in the inner layer both thermal diffusion and convection increase with the distance from the wall. In the outer layer, all terms in Equation (5.1) reduce significantly with increasing distance.

For the upper cavity, Figure 5.25(a) shows that in the inner layer vertical thermal convection carries away the heat transferred in by thermal diffusion and horizontal convection from the hot wall. Due to the stratification of the interior flow at this time, the thermal diffusion is relatively weak in the upper cavity, and the horizontal convection from the hot wall is comparable with the thermal diffusion. In the outer layer up to the point of the temperature minimum, heat balance is similar to that in the inner layer. Although the heat transfer beyond the point of the temperature minimum significantly reduces, it is worth noting a feature of interest regarding the direction of the thermal diffusion on either side of the temperature minimum. Clearly, thermal diffusion in the inner layer side of the temperature minimum is directed from the sidewall towards the interior, whereas on the interior side of the temperature minimum, thermal diffusion is directed from the interior towards the minimum.

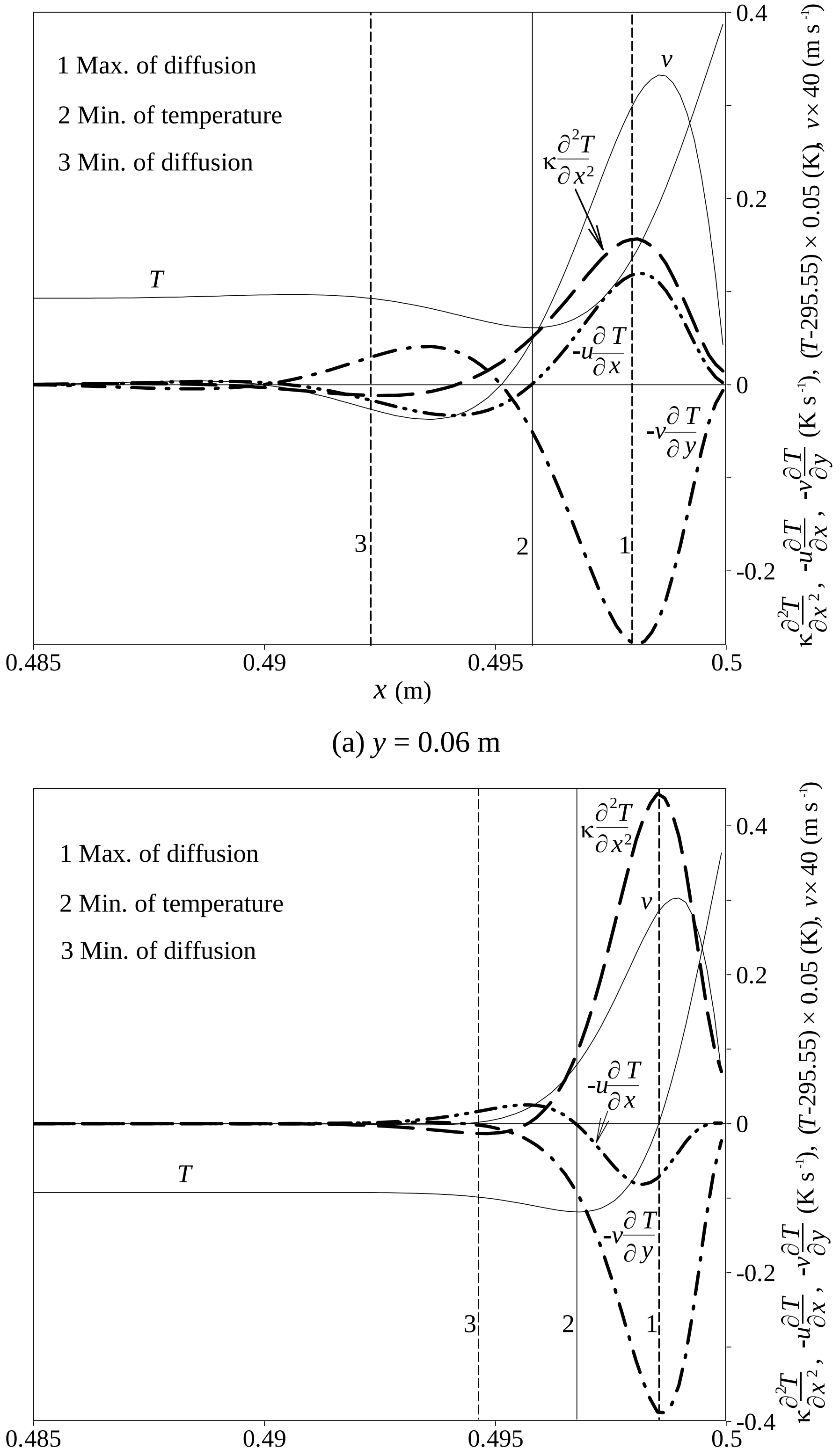

(a) y = 0.06 m

(b) y = -0.06 m

Figure 5.25 Thermal diffusion and convection at t = 4700s

Compared to the flow in the upper cavity, thermal diffusion and vertical convection in the lower cavity are much stronger due to the stratification of the interior flow. The horizontal convection remains at approximately the same order as in the upper cavity but with an opposite sign. Figure 5.25(b) shows that, in the lower cavity, the heat balance in the inner layer is mainly between the thermal diffusion from the hot wall and the vertical convection. This heat balance extends to the outer layer up to the point of the temperature minimum, beyond which heat transfer becomes very weak. The opposing thermal diffusion at the point of the temperature minimum is also present in the lower part of the cavity.

In summary, the heat transfer in the upper and lower regions is governed by similar balances, with the role of horizontal convection changing between the two regions due to the change of the magnitudes of thermal diffusion and vertical convection. A transitional region is expected to be present near the mid height, where the horizontal velocity changes direction.

5.7 Summary

In this chapter, the transition of natural convection in a differentially heated cavity from the start-up to the quasi-steady state is numerically investigated, and the mechanisms responsible for certain important flow features during the transition are discussed. Numerical simulations are basically consistent with the corresponding experimental observations.

For the case of sudden heating, the generation and propagation of the LEE are the important features of the transient thermal boundary layer flow in the initial stage. Based on the present numerical results, it is clear that the LEE phenomenon is an interaction between the temperature, pressure and velocities. When the sidewall is suddenly heated, thermal conduction through the wall surface generates a temperature distribution of the fluid in the vicinity of the sidewall, which in turn induces buoyancy. The buoyancy force drives the fluid in the vicinity of the sidewall upwards. However, since the fluid near the leading edge convected away cannot be complemented from the upstream due to the presence of the horizontal wall, a pressure gradient is induced; that is, a pressure minimum appears in the upstream corner. The pressure minimum may propagate downstream at the speed which is linearly dependent on time (Figure 5.7). The further discussion of the components of the energy equation demonstrates that the deviation of the numerical solution from the theoretical solution is because the theoretical solution neglects the convection terms.

The numerical results also demonstrate that a double-layer structure of the vertical thermal boundary layer simultaneously develops from the top and bottom, respectively. The stratification of the internal fluid in the cavity is a key dynamical mechanism supporting this transition. In the upper part of the cavity, the outer layer develops initially from the separation of the horizontal intrusion induced by the entrainment of the adjacent ambient fluid by the thermal boundary layer. In the meantime, in the lower part of the cavity a similar outer layer develops from the entrainment of the incoming cold intrusion. The two branches of the outer layer eventually meet at the mid height and align vertically, forming a double-layer structure with an approximately uniform thickness over the length of the vertical boundary. In the quasi-steady stage, the flow in the double-layer structure is complex, which includes an inner layer adjacent to the hot wall and an outer layer of a reverse flow with a strong shear between the two layers, as seen in Figure 5.23. Due to the presence of the strong shear, the double-layer structure is considered as a potential cause responsible for the appearance of the unstable traveling waves observed in shadowgraph images at the quasi-steady stage (see Chapter 4). It is clear that the inner and outer bright strips observed in shadowgraph images approximately correspond to the maximum or minimum of the second derivative of the temperature as previously described (see e.g. Figures 5.19, 20, and 21).

The present numerical results indicate that heat transfer near the wall is rather complex, and significantly depends on the development of the flow. After the formation of the double-layer structure, a dip of the temperature profile adjacent to the hot wall appears in the outer layer, resulting in the opposing horizontal thermal diffusion on the two sides of this dip. That is, thermal diffusion is directed toward the dip on both sides of the dip.

Associated with the transition of the vertical thermal boundary layer flow, the physical properties of the intrusion and flows in the core are also described, and a back and forth flow between the hot and cold walls is observed. The numerical results show that the separation of the intrusion driven by the pressure gradient occurs, and a large anticlockwise circulation below the hot intrusion front forms. With the passage of time, this anticlockwise circulation moves horizontally to the cold sidewall and eventually dissipates. Subsequently, another clockwise circulation, close to the cold sidewall, is generated under the buoyancy effect. This clockwise circulation produces a strong shear with the hot intrusion underneath the ceiling, inducing some smaller scale circulations and waves in the hot intrusion. The clockwise circulation moves back to the hot sidewall and forms an oscillation (a back and forth flow between the hot and cold walls). The oscillation is a typical internal gravity wave of natural convection in a side-heated cavity, and can impact on both the vertical boundary layer flow and the stratification of the fluid in the core to some extent. This is because, on one hand, the oscillation flow pushes the trailing waves in the hot top corner closer to the hot wall, thus changing the properties and structure of the hot vertical thermal boundary layer flow; on the other hand, the hot intrusion into the core is split by the back and forth flow and speeds up the core stratification.

In conclusion, although a great number of numerical simulations concerning the transient natural convection in a differentially heated cavity were reported and many flow features were described, the mechanisms responsible for certain major flow features during the transition remain uncovered until the present investigation. Apart from revealing a double-layer structure at the quasi-steady state, which has not been properly documented previously in the literature, the present study has also provide both numerical and experimental evidences for understanding the flow mechanisms behind the LEE propagation, the separation of the intrusion, and the formation of the double-layer structure.

6 Experimental modelling of the thermal flow around a fin on the sidewall

Studies (see e.g. Bilgen 2005) have demonstrated that a fin on the sidewall of a differentially heated cavity may change natural convection flows, which in turn impact on the heat transfer through the finned sidewall. Therefore, it is of interest and significance to visualize the flows induced by the fin and measure the corresponding temperatures. Unfortunately, as reviewed in Chapter 1, even fewer experiments of this aspect have been performed than those for the case without a fin (see e.g. Shakerin et al. 1988). As a consequence, the need for flow visualizations and temperature measurements for the case with the fin on the sidewall is the motivation for this chapter.

Based on the understanding of natural convection flows without a fin, transient thermal flows around the fin on the sidewall are the focus of this chapter. Since the geometric parameters of the fin, such as its shape and dimension, could be critical for the development of flows in the cavity, two sets of experiments are performed here. The first is the visualization of the thermal flow around a square fin, documented in Section 6.1, and the second is that around a longer, thin fin, described in Section 6.2. Furthermore, temperature measurements of the thermal flow around the thin fin are given in Section 6.3.

6.1 Visualizations of the thermal flow around a square fin

In this section, the flow around a square fin with a cross-section of 10 mm × 10 mm is visualized, and the focus is placed on the Rayleigh number effects and the comparisons between the cases with and without the square fin.

In order to obtain results at different Rayleigh numbers, temperature differences between the heated and cooled sidewalls are varied from 1 K to 32 K. The corresponding ranges of the experimental Rayleigh and Prandtl numbers are 2.6×10^8 to 8.3×10^9 and 6.2 to 6.6 respectively, and are listed Table 6.1. Unless specified otherwise, the results reported in this section are for the case with $Ra = 4.0 \times 10^9$ and $Pr = 6.5$. Similar to the convention adopted in Chapters 3 and 4, the hot sidewall is on the right; the vertical coordinate is measured from the middle of the hot sidewall with the positive direction pointing upwards.

Table 6.1 Parameters of flow visualization experiments with a square fin

Number	Initial temperature of water in cavity (K)	Temperature difference between sidewalls (K)	Ra ($\times 10^8$)	Pr
9	297.1	1.0	2.6	6.4
10	297.1	2.0	5.2	6.4
11	296.4	4.0	9.9	6.5
12	298.4	8.0	22	6.2
13	296.6	15.9	40	6.5
14	295.55	16.0	38	6.6
15	297.20	32	83	6.4

The development of the thermal boundary layer flow adjacent to a heated wall without a fin has been described in Chapter 4. In this section, the experimental observations will focus on the effect of the square fin on the flow structures adjacent to the sidewall, in comparison with the case without a fin. The transition of the thermal boundary layer flow from the start-up to the quasi-steady state and the corresponding kinematic properties are described. Similar to the transition of the thermal boundary layer flow without a fin, three stages of the transition can be classified for the thermal boundary layer flow with a square fin. They are an initial stage, a transitional stage and a quasi-steady stage.

6.1.1 Initial stage

When a sidewall without a fin is heated suddenly, heat conduction through the sidewall results in a thermal boundary layer adjacent to the sidewall, which grows with both space and time, as described in Chapter 4. However, for the case with a square fin at the mid height of the heated sidewall, the thermal boundary layer is initially split into an upper and a lower section, as seen in Figure 6.1(a). Figure 6.1(b) shows a processed image similar to Figure 4.1. As can be seen in Figure 6.1(b), the processed image clearly displays the variation of the thickness of the thermal boundary layer along the

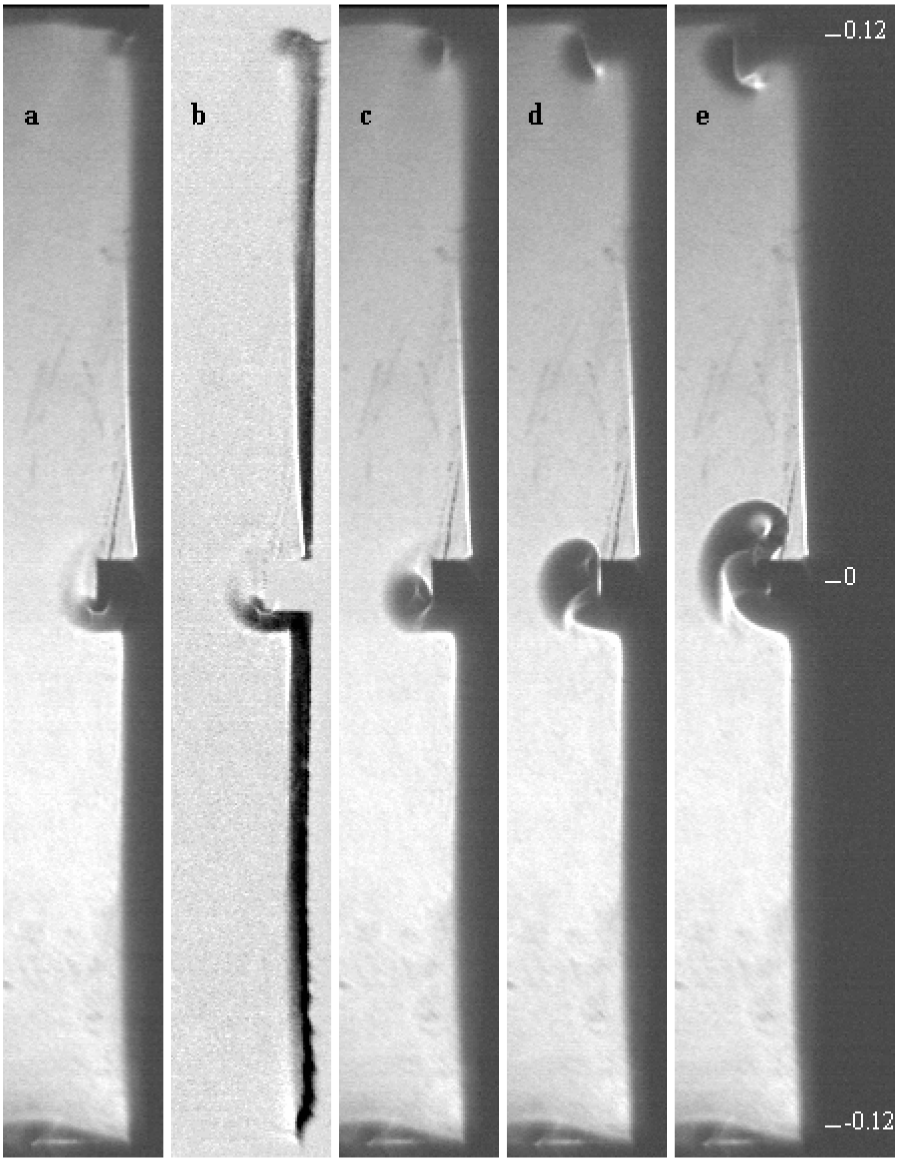

Figure 6.1 Formation of the lower intrusion front

(a) t = 9s. (b) t = 9s. (c) t = 11s. (d) t = 13s. (e) t = 15s

sidewall. The structure with clearly separated upper and lower sections of the thermal boundary layer persists only for a short time, which is dependent on the dimension of the square fin and the Rayleigh number (also refer to Section 6.2).

In the present case, the horizontal dimension of the square fin attached to the heated sidewall is greater than the thickness of the thermal boundary layer, and thus the ascending hot fluid from the lower thermal boundary layer initially accumulates under the fin, and then discharges horizontally. Due to the relatively small dimension of the square fin, the discharging hot fluid overwhelms the fin (see Figures 6.1a and b). As a consequence, a clear intrusion front (hereinafter referred to as a lower intrusion front) forms next to the fin (see Figure 6.1c). Figure 6.1(d) shows that the continuous feeding

Figure 6.2 Reattachment of the lower intrusion front

(a) t = 17s, each interval of 2s from (a) to (f)

of the hot fluid from the lower thermal boundary layer leads to further growth of the lower intrusion front. Subsequently, the buoyancy effect drives the lower intrusion front upwards, and the front bypasses the fin, as shown in Figure 6.1(e). This process persists for approximately 15 seconds at the Rayleigh number of 4.0×10^9. In fact, the greater the Rayleigh number, the shorter the time it takes for the lower intrusion front to bypass the fin.

The subsequent development of the thermal boundary layer flow displays more complex flow features. The lower intrusion front continues to rise due to the buoyancy effect. In the meantime, its size grows rapidly. These features of the lower intrusion front are similar to those of rising hot plumes. However, in the present situation, the

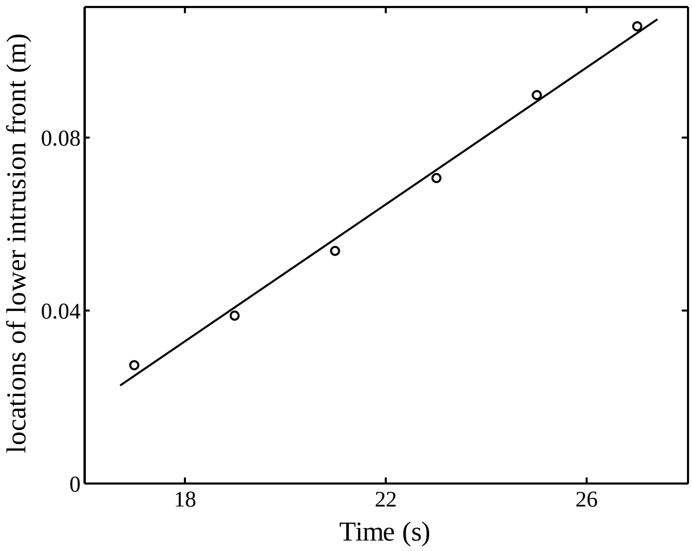

Figure 6.3 Measured positions of the lower intrusion front versus time

growth of the ascending lower intrusion front is also strongly influenced by the entrainment of the upper thermal boundary layer, which is a significant feature of the thermal boundary layers. The entrainment causes the lower intrusion front to reattach to the wall, as shown in Figure 6.2(a). The reattachment is a rather complex process with associated mixing and heat transfer. When the lower intrusion front is drawn close to the thermal boundary layer, it causes firstly a local deformation of the thermal boundary layer, followed by mixing in the local region, as shown in Figure 6.2(a) and (b). With the further development of the reattachment, the region of mixing between the front and the thermal boundary layer extends downstream (Figure 6.2c).

After part of the lower intrusion front merges into the upper thermal boundary layer, a large region with distinct interaction between the intrusion front and the thermal boundary layer results (see Figure 6.2d). This interaction eventually leads to the collapse of the original structure of the lower intrusion front, as shown in Figure 6.2(e). The strip pattern in Figure 6.2(f) indicates that the low intrusion front rotates while it is convected downstream. In fact, this is a result of the non-uniform velocity distribution of the thermal boundary layer (refer to Chapter 7 for a detailed discussion).

Figure 6.3 plots the measured positions (heights) of the lower intrusion front against time, which are also indicated by the dark lines in Figure 6.2. The good linear correlation shown in Figure 6.3 implies that the lower intrusion front convects at an approximately constant velocity, which is obtained from Figure 6.3 as 7.8 mm/s.

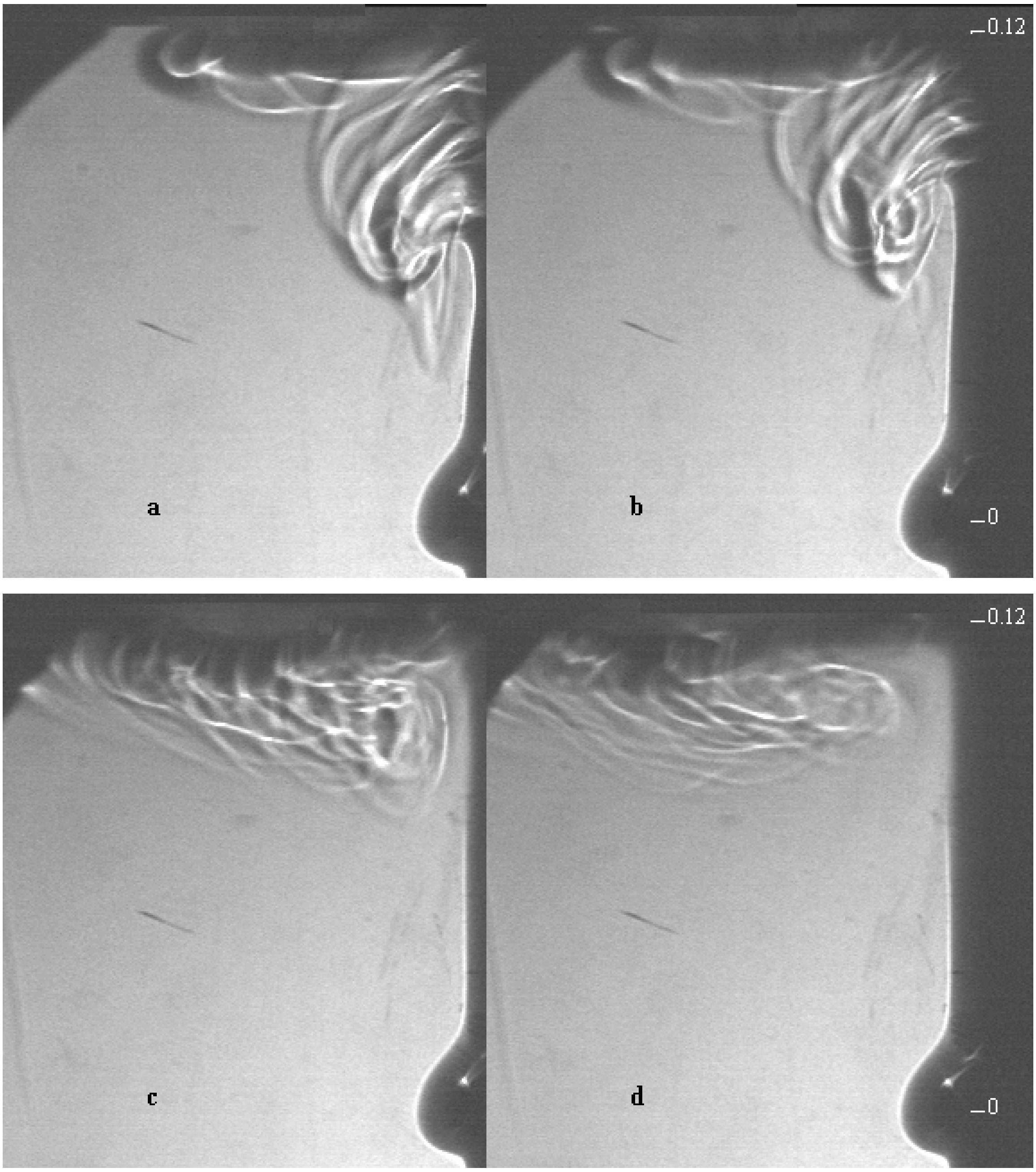

Figure 6.4 Formation and evolution of the local circulation in the upper right corner (a) t = 29s. (b) t = 31s. (c) t = 40s. (d) t = 44s

With the passage of time, the lower intrusion front is convected further away from the square fin, as shown in Figure 6.4(a), and the destabilization of the downstream thermal boundary layer is clear. The layered strip patterns in the vicinity of the wall indicate that the interaction between the lower intrusion front and the upper thermal boundary layer may have resulted in some temperature waves in the thermal boundary layer (also see Figure 7.1b). Due to the presence of the non-uniform velocity profile, the rotation of the lower intrusion front is further accelerated, and a large anticlockwise

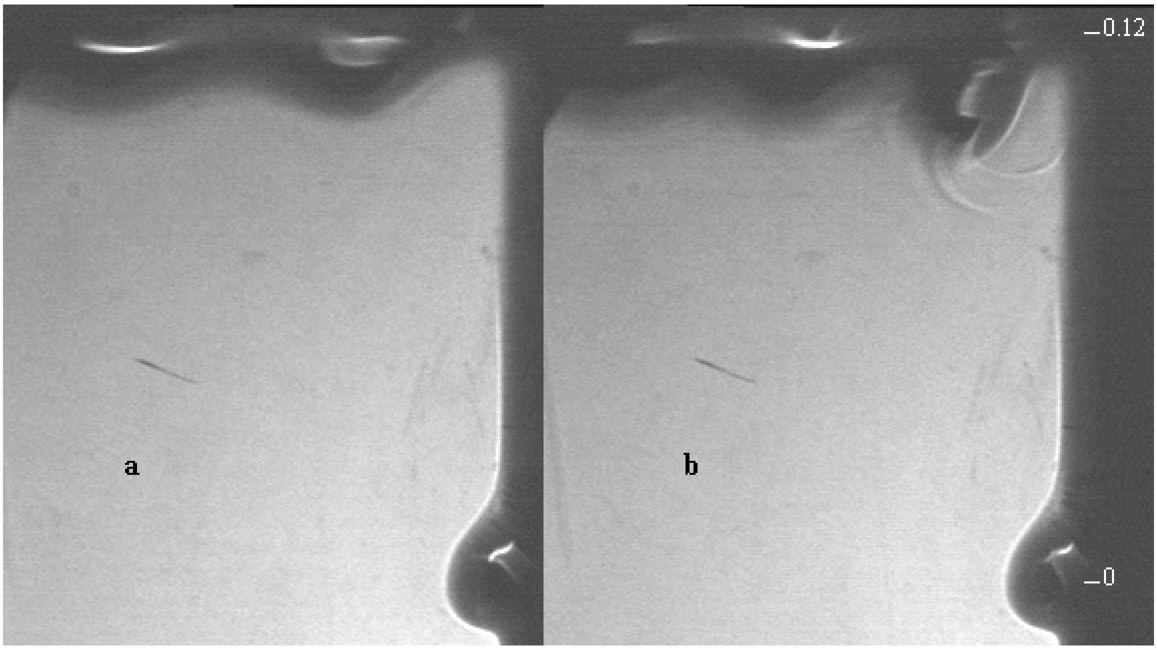

Figure 6.5 Early development of the intrusion

(a) t = 132 s. (b) t = 237 s

circulation is formed near the top corner of the hot wall (see Figure 6.4b). Such a circulation eventually merges into the horizontal intrusion under the ceiling, and is convected away horizontally, as shown in Figures 6.4(c) and (d).

The above flow visualizations suggest that the mass transfer associated with a series of complex flow processes is a distinct feature of the thermal boundary layer flow in the initial stage.

6.1.2 Transitional stage

As shown in Figure 6.4, the lower intrusion front provokes the early flow structure of the intrusion under the ceiling of the cavity, compared with the case without a fin (see Figure 4.3a), and even impacts on the development of the intrusion. Figure 6.5 shows the development of the hot intrusion after the lower intrusion front is convected away. Compared with the case without a fin (refer to Figures 4.3b to 4.3d), the separation and trailing waves of the intrusion becomes less distinct, as shown in Figure 6.5(a). Figure 6.5(b) also indicates that the square fin destabilizes the flow structure of trailing waves earlier than that without a fin, before the cold intrusion arrives at the hot sidewall.

After the lower intrusion front is convected away, the development of the thermal boundary layer enters into a slow transition period, as shown in Figure 6.6. Here the

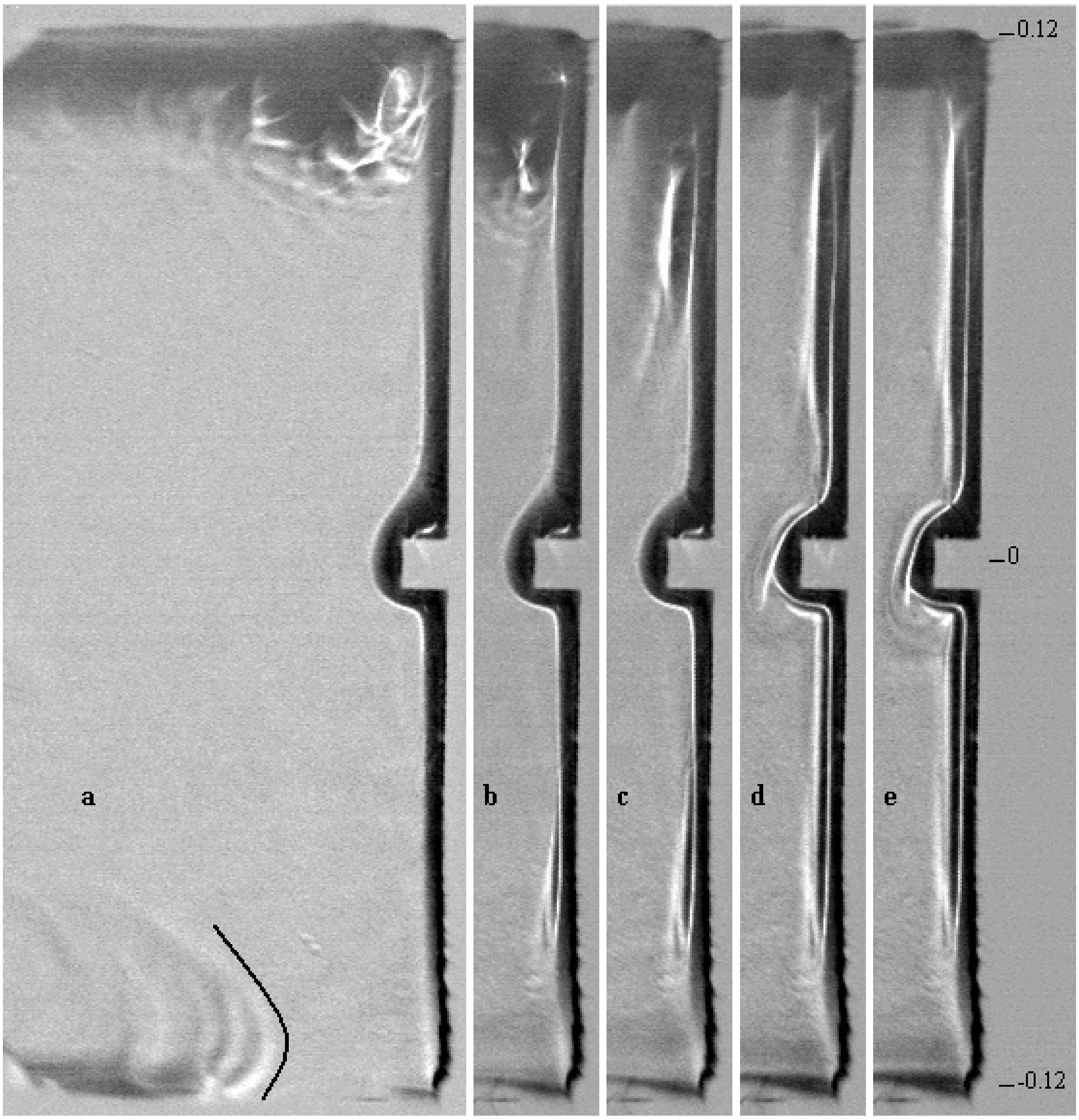

Figure 6.6 Development of the thermal boundary layer at the transitional stage
(a) t = 364s. (b) t = 769s. (c) t = 1,354s. (d) t = 4,308s. (e) t = 8,164s

images are processed in the same way as that for the image shown in Figure 4.1. It will be demonstrated that the transition of the thermal boundary layer in the present case with a square fin exhibits certain kinematic properties similar to the case without a fin.

Figure 6.6(a) shows that the cold intrusion front from the cold wall (indicated by the solid line overdrawn near the bottom) is approaching the hot wall at the time of 364s, which is slightly longer than the arrival time in the case without the square fin (330s) at approximately the same Rayleigh number. In addition, the outflow in the top corner displays certain features marking the beginning of the transitional stage, in which the interaction between the intrusion and the thermal boundary layer flow results in a double layer structure. After the cold intrusion strikes the hot wall, a bright strip appears in the vicinity of the bottom corner outside the thermal boundary layer (see Figure 6.6b). In the meantime, a similar bright strip forms near the top corner.

As time goes on, the upper and lower bright strips outside the thermal boundary layer extend towards the middle of the hot wall, as shown in Figure 6.6(c). This process is associated with the stratification of the interior fluid in the cavity, which is caused by the expansion of the hot and cold intrusion toward the middle of the cavity, as described in Chapter 4. Eventually, the two bright strips outside the thermal boundary layer reach the square fin (see Figure 6.6d). As a consequence, a double-layer flow structure forms although the outer layer is broken due to the presence of the fin, which is different from the double-layer structure observed without a fin in Chapter 4. As the thermal boundary layer flow approaches a quasi-steady state, the double-layer structure becomes more distinct, as seen in Figure 6.6(e). Certain flow patterns caused by the circulation (refer to numerical results in Figure 7.9c) under the square fin are also noticeable in Figure 6.6(e).

Similar to the case without a fin described in Chapter 4, the transition of the thermal boundary layer with the square fin displays a physical process in which one stream of the hot intrusion near the top corner extends downwards in the vertical direction so that an outer layer is eventually formed close to the inner layer above the square fin. In the meantime, another bright strip extends upwards from the bottom and eventually forms an outer layer below the fin while the interior fluid in cavity is stratified. However, variations between the thermal boundary layer flows with and without the square fin are also evident. For instance, the outer layer of the double-layer structure is broken with the presence of the square fin, as shown in Figure 6.6, but is continuous in the case without a fin (refer to Chapter 4), and as a consequence, the layer thicknesses of the thermal layers are different.

6.1.3 Quasi-steady stage

As shown in Figure 6.6, although the double-layer structure is still present, the square fin splits the outer layer into an upper and a lower section. Moreover, the strip pattern in Figure 6.6(e) implies that there exists a complex flow structure around the square fin in the quasi-steady stage (refers to Chapter 7 for details).

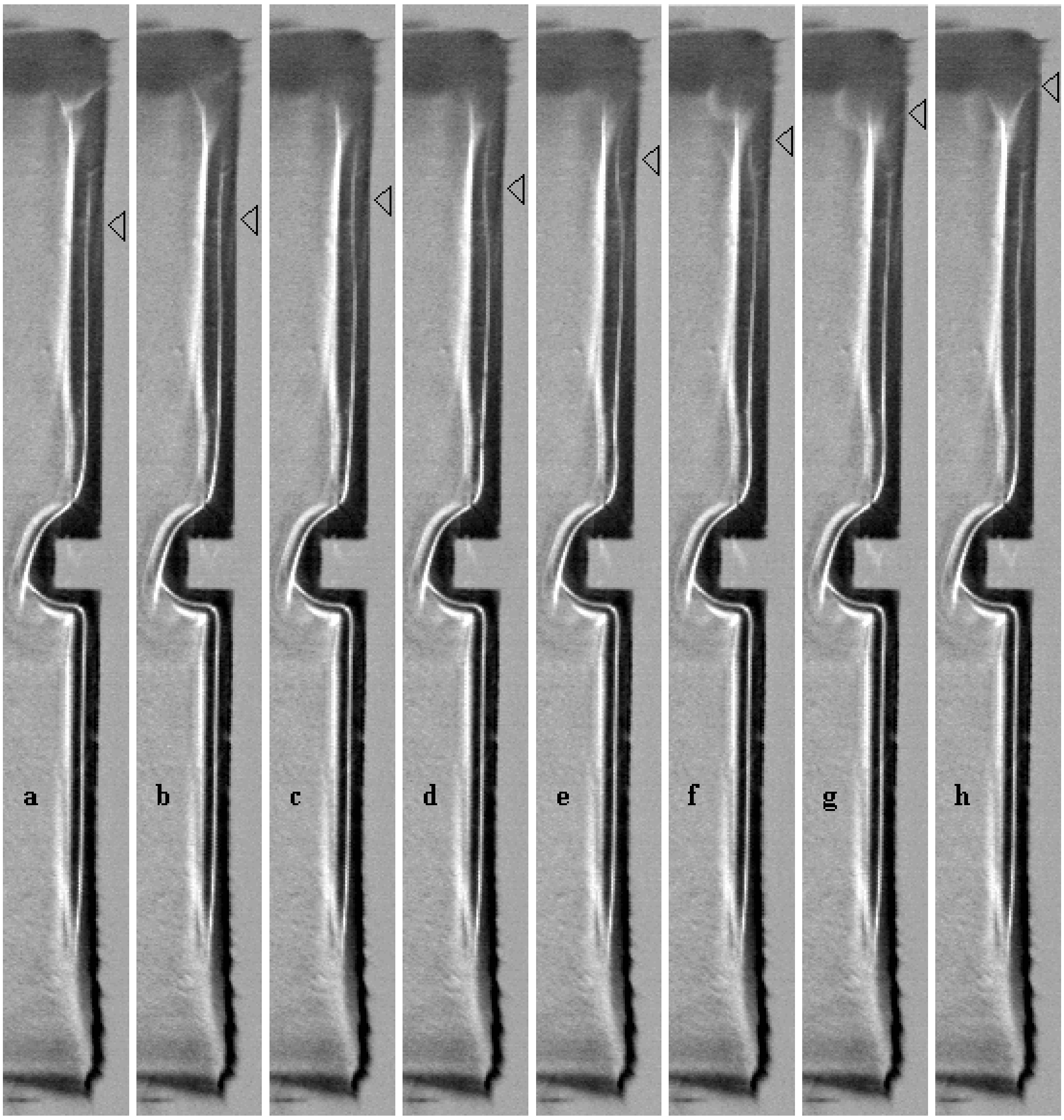

Figure 6.7 Traveling waves in the thermal boundary layer

(a) t = 5,706s, each interval of 1 s from (a) to (h)

In the quasi-steady stage, another important feature of the thermal boundary layer is the presence of the traveling waves. For the purpose of observing the traveling waves in the thermal boundary layer, a time series of shadowgraph images obtained for $Ra = 4.0 \times 10^9$ is shown in Figure 6.7. The triangle signs in Figure 6.7 indicate the positions of the wave peak. Compared with the case without a fin, the traveling waves in the present case with the square fin show a similar evolution, but may be observed at lower positions including the upstream side of the fin. These traveling waves grow more rapidly than those observed without a fin, and most of the traveling waves break in the top corner. In the case without a fin, the breaking of the traveling waves can be observed only for higher Rayleigh numbers.

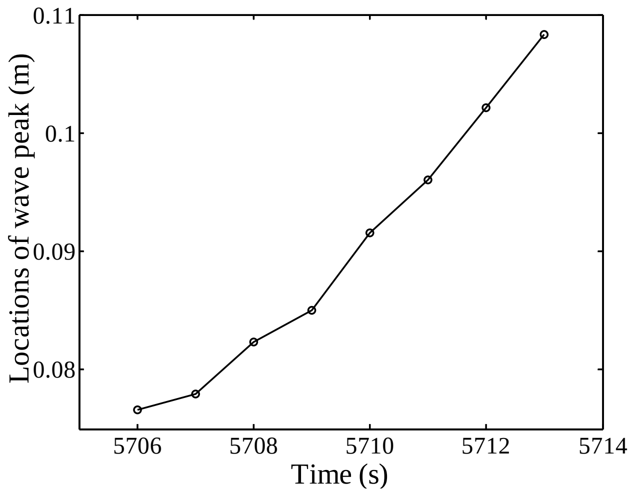

Figure 6.8 Measured wave peak positions against time

The positions of the traveling wave peak marked in Figure 6.7 are also plotted against time in Figure 6.8. It is clear that the correlation between the wave peak position and the time is not linear, which means that the velocity of the traveling wave is not constant. The mean velocity of the traveling wave is approximately 4.5 mm/s, which is smaller than that measured without a fin (5.7 mm/s). This may be attributed to the presence of the fin because, in some sense, the fin blocks the thermal boundary layer flow.

The measured thicknesses of the double-layer structure at different heights and different stages with and without the square fin are listed in Table 6.2. It is seen from the table that, in the upper section of the heated wall, both the inner and outer layers with the fin are slightly thinner than those without the square fin. However, in the lower section of the heated wall, the inner layer with the fin is thicker than that without a fin, and the outer layer is slightly thinner than that without a fin. It is also clear from the table that, in both cases with and without the square fin, the inner thermal boundary layer at the quasi-steady state is remarkably thinner than that at the initial stage.

Table 6.2 Thicknesses of the double layers at different heights and different stages

Heights (m)		Thickness of the inner layer (mm)		Distance between outer layer and sidewall at quasi-steady state (mm)
		Maximum in initial stage	Mean value at quasi-steady state	
0.089	No fin	6.5	3.2	8.8
	Square fin	5.7	3.1	7.5
-0.052	No fin	4.2	2.3	7.4
	Square fin	4.4	3.5	6.6

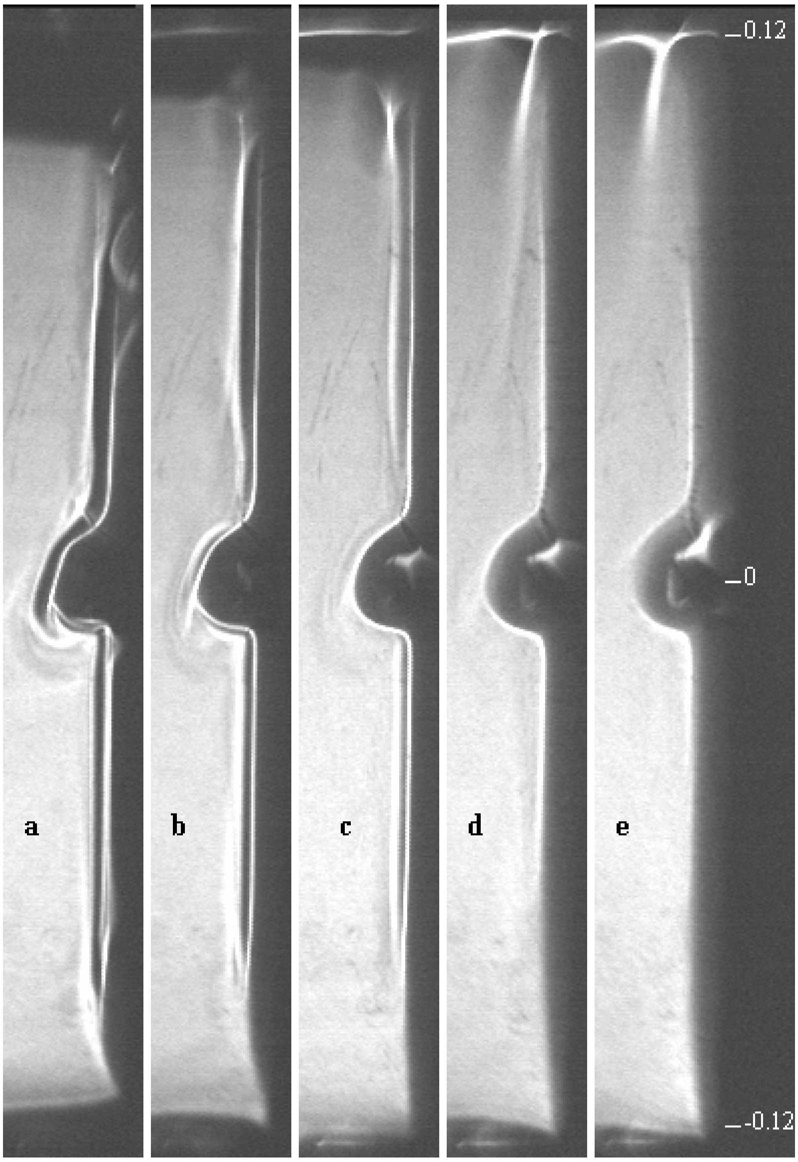

Figure 6.9 Double-layer structures at different Rayleigh numbers at t = 5100s
(a) $Ra = 8.3\times10^9$. (b) $Ra = 4.0\times10^9$. (c) $Ra = 2.2\times10^9$. (d) $Ra = 9.9\times10^8$. (e) $Ra = 5.2\times10^8$

Figure 6.9 shows the double layer structures in the quasi-steady stage for different Rayleigh numbers. It is found that, in the case of high Rayleigh numbers such as $Ra = 8.3 \times 10^9$ (Figure 6.9a), the double-layer structure is clear; the traveling waves in the thermal boundary layer are evident; and even the local flow with layered strips around the square fin may be observed. However, within the present range of the Rayleigh numbers between 5.2×10^8 and 8.3×10^9, the double layer structure becomes less distinct as the Rayleigh number decreases (see Figures 6.9b to e). At the Rayleigh number of $Ra = 9.9\times10^8$, the outer layer cannot be observed in the lower section (Figure 6.9d). As the

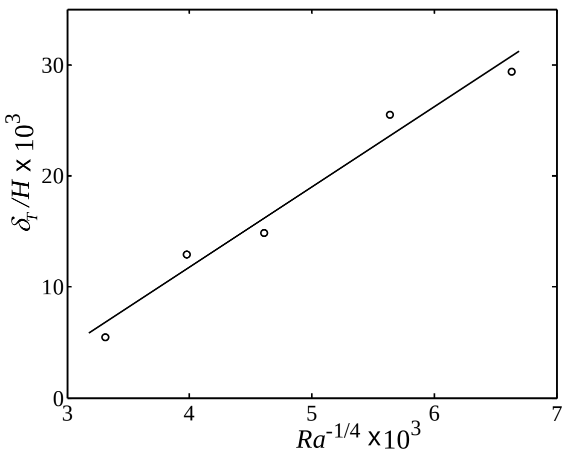

Figure 6.10 Normalized thickness of the inner layer against $Ra^{-1/4}$ at the height of 0.089 m at the quasi-steady state (t = 5100s)

Rayleigh number decreases further to $Ra = 5.2 \times 10^8$, almost the entire outer layer becomes indistinct, as shown in Figure 6.9(e). It is also difficult to observe traveling waves in the thermal boundary layer at low Rayleigh numbers.

Another noticeable phenomenon of interest shown in Figure 6.9 is that a horizontal bright strip under the ceiling becomes more distinct as the Rayleigh number decreases. A possible explanation of this phenomenon is that the horizontal intrusion has a distinct extreme position of the second derivative of the temperature field for the lower Rayleigh numbers, which results in the bright strip on the shadowgraph images. However, the strong mixing in the region for the higher Rayleigh numbers (see e.g. Figure 6.9a) leads to a more uniform temperature structure, which has no distinct extreme position of the second derivative of the temperature field, and thus no bright strip is observed on the shadowgraph images.

Figure 6.10 presents the thickness of the inner boundary layer measured at the height of 0.089 m at the quasi-steady state for a range of Rayleigh numbers. In this figure, the thickness of the inner layer, normalized by the height of the cavity, is plotted against the predicted scale for the dimensionless thickness of the thermal boundary layer, $Ra^{-1/4}$ (Patterson & Imberger 1980). Since the outer layers are indistinct and difficult to measure at low Rayleigh numbers, the results of the outer layer are not presented here. It is evident in Figure 6.10 that the thickness of the inner layer decreases as the Rayleigh number increases. The approximately linear correlation between the dimensionless thickness of the inner layer and $Ra^{-1/4}$ confirms the scale analyses of Patterson and Imberger (1980).

6.2 Visualizations of the thermal flow around a thin fin

For the purpose of testing the effect of the fin dimension on the thermal boundary layer flow, the thermal flow around a thin fin with a cross-section of 40 mm × 2 mm, attached to the mid height of the hot sidewall, is visualized using shadowgraph techniques. Experiments with temperature differences between the sidewalls varying from 4 K to 32 K were performed. The corresponding ranges of the experimental Rayleigh and Prandtl numbers are 9.5×10^8 to 7.7×10^9 and 6.6 to 6.8, respectively (refer to Table 6.3). The results shown in this section are for the case with $Ra = 3.8 \times 10^9$ and $Pr = 6.6$ unless specified otherwise.

Table 6.3 Parameters of visualization experiments with a thin fin

Number	Initial temperature of water in cavity (K)	Temperature difference between sidewalls (K)	Ra ($\times 10^8$)	Pr
16	295.8	4.0	9.5	6.6
17	294.9	8.0	18	6.8
18	295.55	16.0	38	6.6
19	295.70	32.0	77	6.6

Similar to the case with a square fin on the sidewall, the thermal boundary layer flow around a larger thin fin also displays the formation and dissipation of the lower intrusion front in the initial stage, the development of the double-layer structure in the transitional stage and traveling waves in the quasi-steady stage. However, the development of the thermal flow around the thin fin is clearly different from that around the square fin described previously in Section 6.1.

6.2.1 Initial stage

Similar to the case with a square fin, the thermal boundary layer flow initially accumulates under the thin fin and forms a lower intrusion front after the sidewall is suddenly heated, as shown in Figure 6.11(a). As time goes on, the lower intrusion front convects horizontally toward the tip of the thin fin due to further accumulation of the

Figure 6.11 Formation of the lower intrusion front

(a) t = 14 s. (b) t = 16 s. (c) t = 18 s. (d) t = 20 s

heated fluid (see Figures 6.11b and c). It is clear that the motion of the lower intrusion front is almost synchronized with that under the ceiling, and the flow structures of the two fronts are also similar. After approximately 20 s, the lower intrusion front arrives at the tip of the thin fin, as seen in Figure 6.11(d). Since the length of the thin fin is much larger than that of the square fin, the development of the lower intrusion front under the thin fin lasts longer (also refer to Figure 6.1).

After the lower intrusion front arrives at the tip of the thin fin, it overwhelms the thin fin due to buoyancy. Figure 6.12 shows the subsequent development of the lower intrusion front bypassing the thin fin. Figure 6.12(a) exhibits the curling up of the lower intrusion front driven by the buoyancy force. As a consequence, a new front, similar to a

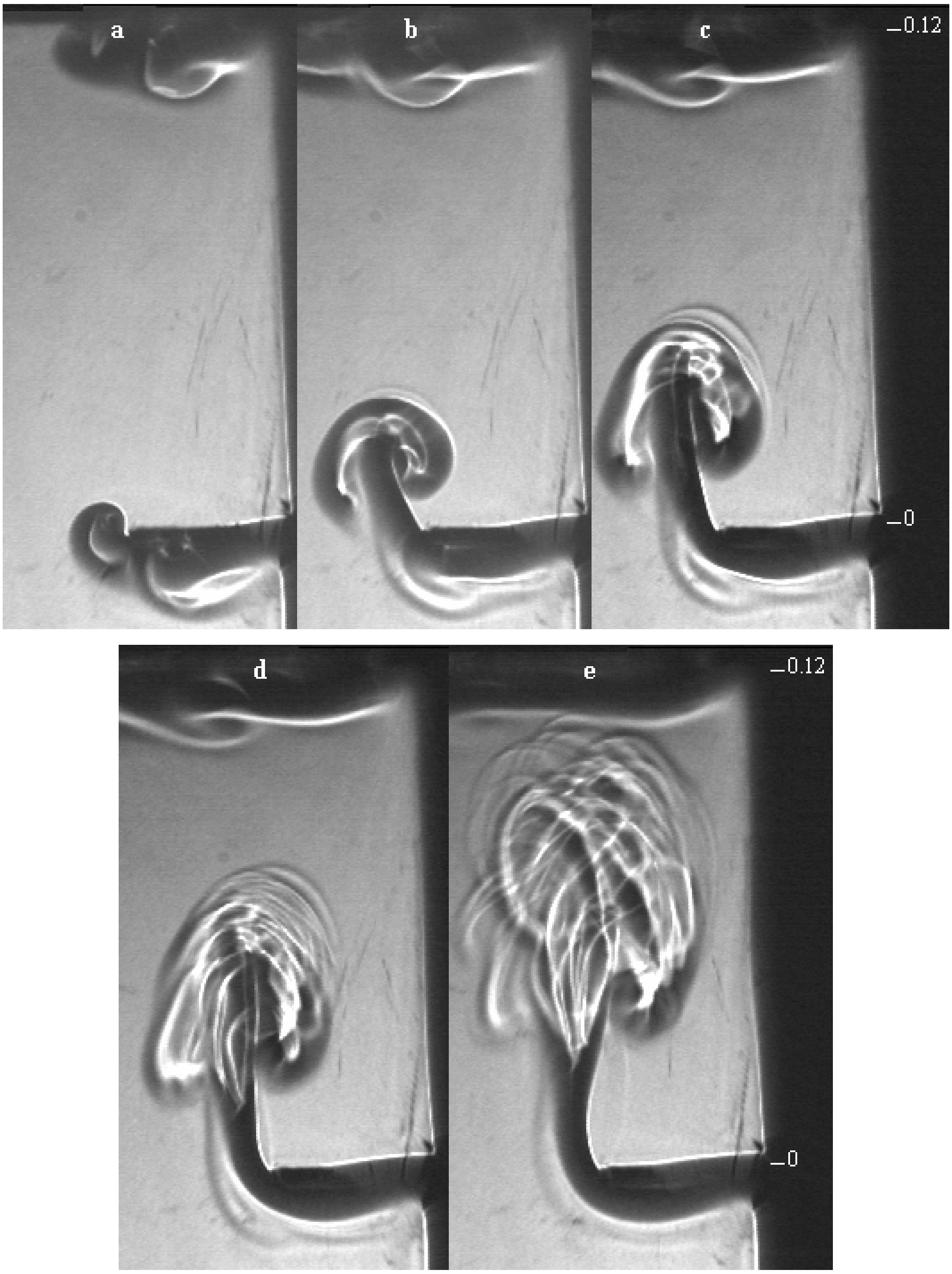

Figure 6.12 Lower intrusion front bypassing the thin fin

(a) t = 24 s. (b) t = 30 s. (c) t = 33 s. (d) t = 36 s. (e) t = 41 s

buoyant plume directing upwards, forms after the lower intrusion bypasses the thin fin, as shown in Figure 6.12(b).

Subsequently, the plume is driven upwards by buoyancy and becomes increasingly unstable, as indicated in Figure 6.12(c) by the strip-like patterns near the front. When the front moves upwards, the strip-like patterns become more complex, as seen in Figure 6.12(d). The chaotic strip patterns in Figure 6.12(e) indicate that the front breaks up before it strikes the intrusion under the ceiling.

It is worth noting that, in the case of a square fin, the lower intrusion front bypassing the fin is immediately entrained by the downstream thermal boundary layer. However, the lower intrusion front bypassing the larger thin fin here moves vertically due to the increased length of the fin and thus the distance of the bypassing front from the downstream thermal boundary layer. In addition, since the speed of the flow closer to the sidewall except for the viscous inner layer in the thermal boundary layer is larger than those further from the sidewall, the front entrained into the thermal boundary layer for the case of the square fin moves upwards more quickly (at a speed of 7.8 mm/s, see Figure 6.3) than the front bypassing the thin fin further from the sidewall (at approximately 7.3 mm/s here).

Figure 6.13 shows the interaction between the lower intrusion and the thermal boundary layer flow at a much later stage. Figure 6.13(a) indicates that the entrainment by the upper thermal boundary layer eventually draws the lower intrusion front and its trailing flow closer to the hot sidewall. As a consequence, the broken lower intrusion front spreads all over the top corner as seen in Figure 6.13(a), and the trailing flow behind the lower intrusion front retains strip-like patterns. During this stage, the mixing in the top corner is thorough and displays some features of turbulence, which significantly impacts on the heat transfer through the hot sidewall (also refer to Chapter 7 for details based on numerical simulations).

As time elapses, this trailing flow is drawn further toward the hot sidewall by entrainment, and a distinct clockwise circulation forms in the lower corner of the downstream section of the hot sidewall (i.e. above the thin fin, see Figure 6.13b). Figures 6.13(c) and (d) show that, after the perturbations induced by the lower intrusion front are convected away, the trailing flow exhibits distinct strip-like patterns, and is drawn closer to the hot sidewall. The above observations clearly indicate that reattachment of the lower intrusion front to the downstream thermal boundary layer, as observed in the case of a small square fin in Section 6.1, does not occur for the present case of a large thin fin. However, the trailing flow of the lower intrusion front eventually reattaches to the hot sidewall (Figures 6.13c and d).

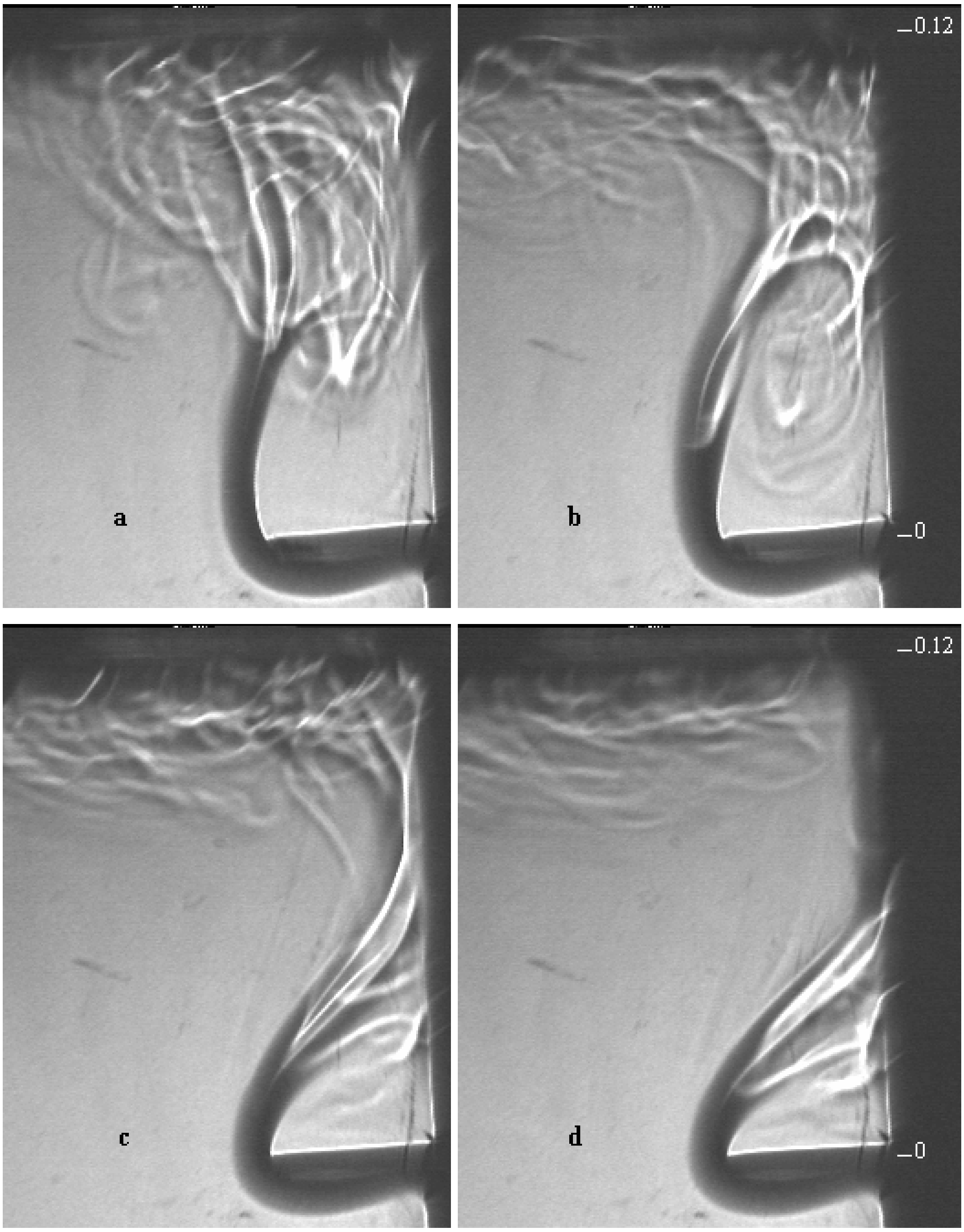

Figure 6.13 Interaction between the lower intrusion and the thermal boundary layer

(a) t = 48 s. (b) t = 56 s. (c) t = 78 s. (d) t = 88 s

6.2.2 Transitional stage

After the perturbations of the lower intrusion front are convected away, the subsequent development of the thermal boundary layer enters a slow transition process, and exhibits distinct variations from the case of a square fin.

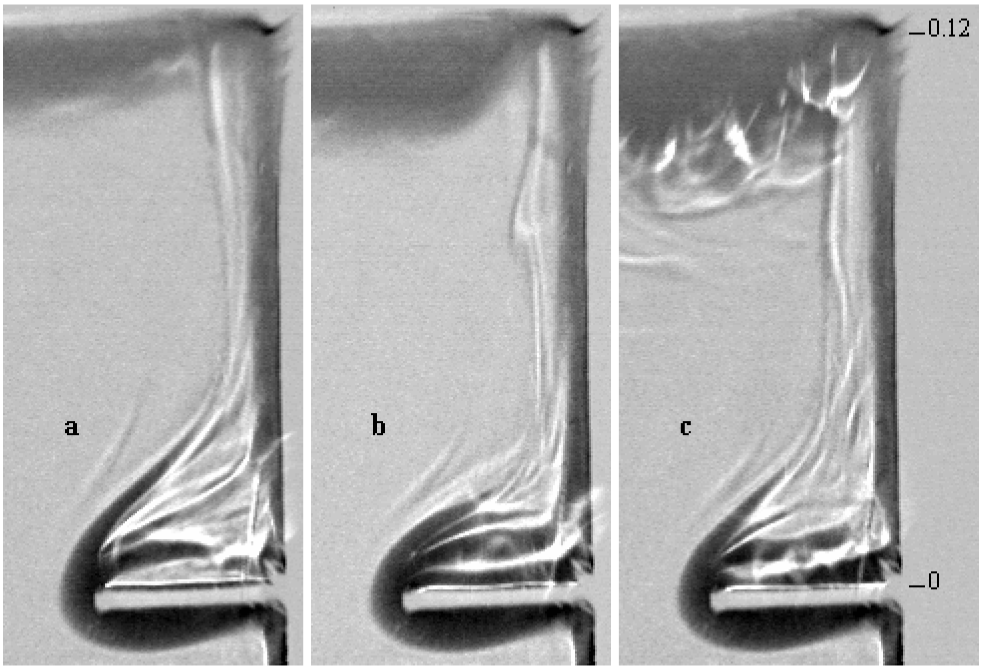

Figure 6.14 Development of the thermal flow around the thin fin

(a) t = 140 s. (b) t = 193 s. (c) t = 232 s

Figure 6.14 shows the development of the thermal flow around the thin fin before the cold intrusion front from the cold wall strikes the bottom of the hot sidewall. It is worth noting that the images shown in this figure have been processed by subtracting a background image recorded immediately before the experiment starts, similar to that in Figure 6.1(b). As a consequence of the image processing, the shape of the thin fin is clearly displayed in Figure 6.14. It is evident that the bypassing flow around the thin fin is drawn closer to the thin fin, compared with that in Figure 6.13(d). Furthermore, it is also seen in Figures 6.14(a) and (b) that the chaotic flow structure observed previously under the ceiling (refer to Figure 6.13) has disappeared. However, as the cold intrusion is approaching the hot sidewall, a distinct unstable flow structure of chaotic strip-like patters in the top corner shown in Figure 6.14(c) reappears. In fact, this is a result of amplified perturbations from the cold intrusion; that is, the instability of the thermal boundary layer, triggered by the cold intrusion approaching the sidewall, significantly amplifies when it propagates downstream (also see temperature measurements in Figure 6.25 and numerical results in Figure 7.25).

After the cold intrusion strikes the hot wall, a double-layer structure of the thermal boundary layer, similar to those observed for other cases with and without a square fin on the sidewall (see Figures 4.6 and 6.6), eventually forms. Figure 6.15 shows the subsequent development of the thermal boundary layer, to which the same image

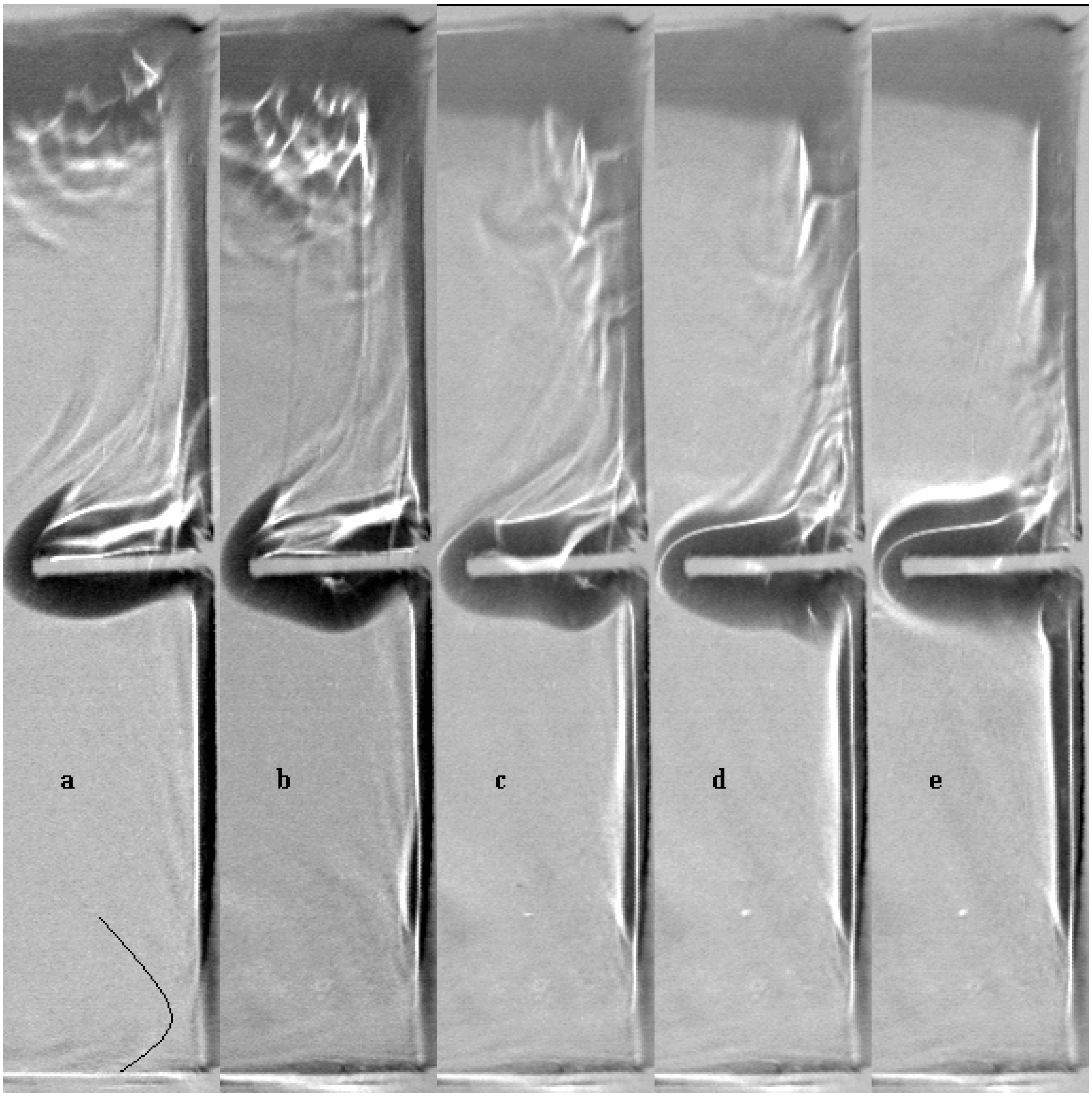

Figure 6.15 Development of the thermal boundary layer after the cold intrusion strikes the hot sidewall

(a) t = 405 s. (b) t = 741 s. (c) t = 2139 s. (d) t = 3247 s. (e) t = 11786 s

processing used in Figure 6.14 has been applied. The cold intrusion front is overdrawn in the bottom corner in the Figure 6.15(a) by a dark solid line. After the strike of the cold intrusion, a bright strip appears in the vicinity of the bottom corner outside the thermal boundary layer, as seen Figure 6.15(b). The flow in the top corner is characterized by a completely destabilized structure (also see temperature time series in Figure 6.24), which is different from the case of a small square fin in which the flow structure in the top corner is less unstable.

As time increases, the lower bright strip outside the thermal boundary layer extends toward the thin fin, as shown in Figure 6.15(c). In the meantime, the chaotic strip-like pattern in the top corner becomes weaker, but the horizontal strip-like pattern occurs in the upper thermal boundary layer (Figure 6.15c). Figure 6.15(d) shows that another short bright strip, which originates from the top corner, extends downwards, and a horizontal indistinct bright strip arises above the flow around the thin fin. The subsequent development of the flow indicates that the two bright strips outside the inner layer above the thin fin become clearer, as seen in Figure 6.15(e), and the bright strip from the top corner continuously extends downwards. However, the upper bright strip from the top corner does not extend to the fin as that in the case with a smaller square fin (see Figure 6.6), even though the experiment is extended for a long period. As a consequence, the outer bright strip is distinct below the thin fin, but is broken above the fin. Based on the discussion concerning the outer bright strip in Chapter 5, the outer bright strip in the shadowgraph images denotes the minimum of the second derivative of the temperature, as indicated in Chapter 2, 4 and 5. This means that the stratification of the fluid in the core leads to a stable temperature distribution below the fin in which there is a minimum of the second derivative of the temperature outside the inner layer, and in turn results in a clear outer bright strip. However, strong perturbations of the thermal flow around the thin fin provoke the stratification on the downstream side of the fin and thus break the outer bright strip above the fin (also refer to Figure 7.18 for more details).

In summary, the transition of the thermal boundary layer flow with the thin fin displays certain different features from that in the case with a smaller square fin at this stage, particularly for the flow on the downstream side of the fin.

6.2.3 Quasi-steady stage

As shown in Figure 6.15(e), a double-layer structure of the thermal boundary layer is formed at the upstream side of the thin fin. However, at the downstream side of the fin, strong perturbations have resulted in an indistinct inner layer and a broken outer layer.

For the purpose of observing the thermal flow around the thin fin, a time series of shadowgraph images obtained for $Ra = 3.8 \times 10^9$ is shown in Figure 6.16, in which the white arrows indicate the separation of the flow from the thin fin. In contrast to the present case, separation of the thermal flow around the smaller square fin was not observed (see Figure 6.6). This implies that the flow separation above the thin fin is

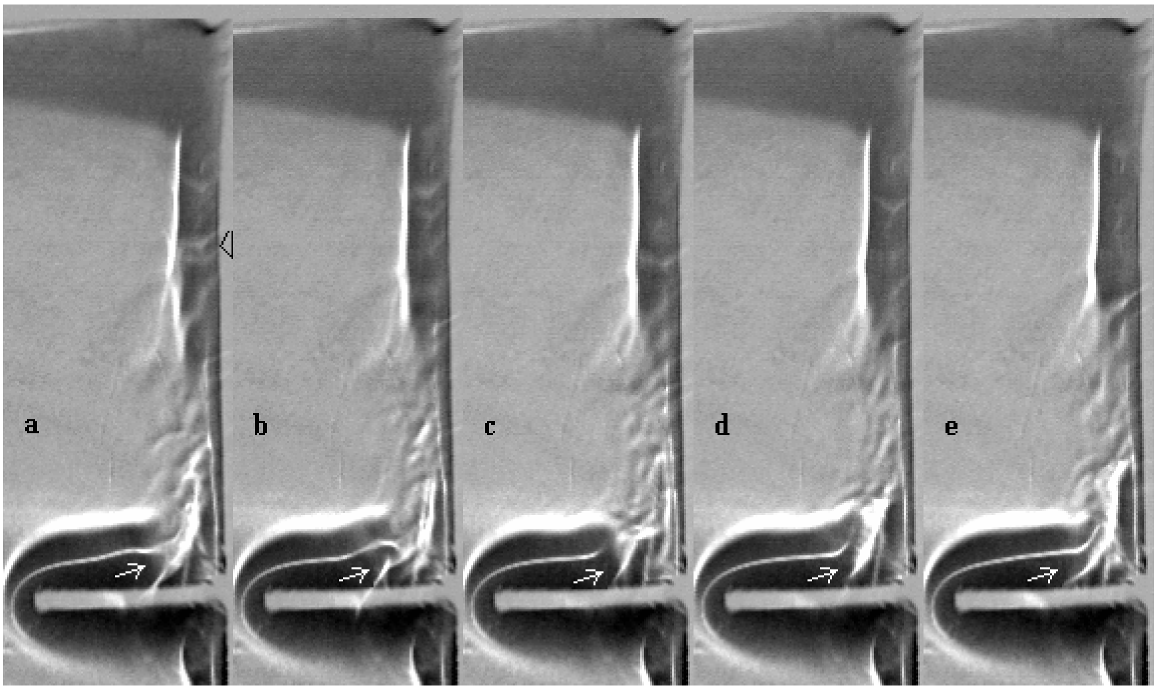

Figure 6.16 Oscillations of the thermal flow around the fin at the quasi-steady state (a) t = 11840 s, each interval of 2 s from (a) to (e)

sensitive to the geometric parameters of the fin. Further discussion of the effects of the geometric parameters based on numerical simulations will be given in Chapter 7.

In the quasi-steady stage, a noticeable feature of the flow is the presence of oscillations after the thermal flow separates from the thin fin. This flow feature is qualitatively similar to a vortex shedding flow but is more complex. This is because there are combined effects of the entrainment by the thermal boundary layer and an adverse temperature gradient in which the fluid temperature of the thermal flow around the fin is higher than that of the fluid above it. A series of broken inner bright strips between the outer bright strip and the sidewall, as indicated by a triangle sign in Figure 6.16(a), implies that oscillations destabilize the flow of the inner layer at the downstream side of the fin, which is different from those with and without a smaller square fin (also see Figures 4.9 and 6.6).

The frequency of oscillations of the thermal flow around the thin fin is dependent on the Rayleigh number and the dimension of the fin. By recording the time within which the certain number of consecutive oscillations pass, the frequency of oscillations may be calculated, which is equal to the ratio of the number to time (also refer to temperature measurements in Section 6.3). Figure 6.17 shows the dependence of the frequency of oscillations on the Rayleigh number. It is clear that the correlation between

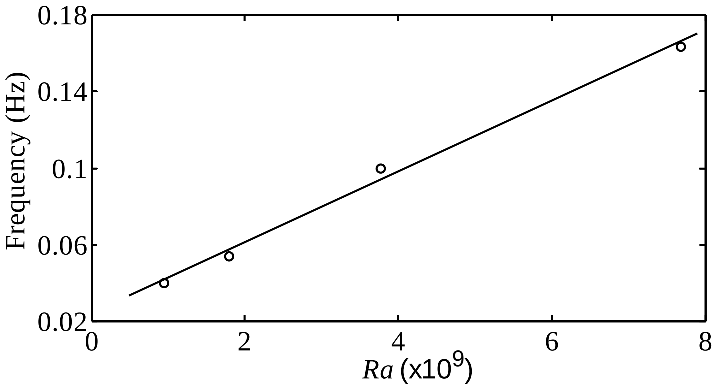

Figure 6.17 Frequency of oscillations against Rayleigh numbers

the frequency and Rayleigh number is approximately linear in the range of the present Rayleigh numbers. For the case of $Ra = 3.8\times10^9$, the frequency of oscillations is 0.1 Hz, which is approximately half of the frequency of traveling waves observed in the case without a fin (also see Figure 4.8).

In order to observe the effect of the Rayleigh number on the quasi-steady state flow structure, Figure 6.18 shows the thermal boundary layers in the quasi-steady stage at different Rayleigh numbers. It is clear from this figure that, as the Rayleigh number increases, both the double-layer structure under the thin fin and the instability of the thermal boundary layer become more distinct. At a Rayleigh number of $Ra = 9.54\times10^8$, the bright strip in the upper section is hardly identifiable (see Figure 6.18a), and the lower outer bright strip is also indistinct. However, in the case of $Ra = 1.8 \times 10^9$, the upper outer bright strip may be clearly identified; the instability of the upper thermal boundary layer is distinct; and the local flow with layered strips around the thin fin is also evident (see Figure 6.18b). When the Rayleigh number increases to 7.7×10^9, the instability of the thermal boundary layer flow at the downstream side of the thin fin becomes more easily identifiable (see Figure 6.18d), and the mixing of the lower inner layer, indicated by the thickening of the inner bright strip, may be observed.

It is worth noting that in Figure 6.18(d) the outer bright strip above the thin fin horizontally extends toward the core (also see Figure 6.18c, although it is less distinct there). This is because, at high Rayleigh numbers, there is a larger temperature gradient in the middle between the horizontal outflow discharged from the upper thermal boundary layer and the thermal flow bypassing the fin from the lower thermal boundary layer. Such a temperature distribution yields the extrema of the second derivative of the

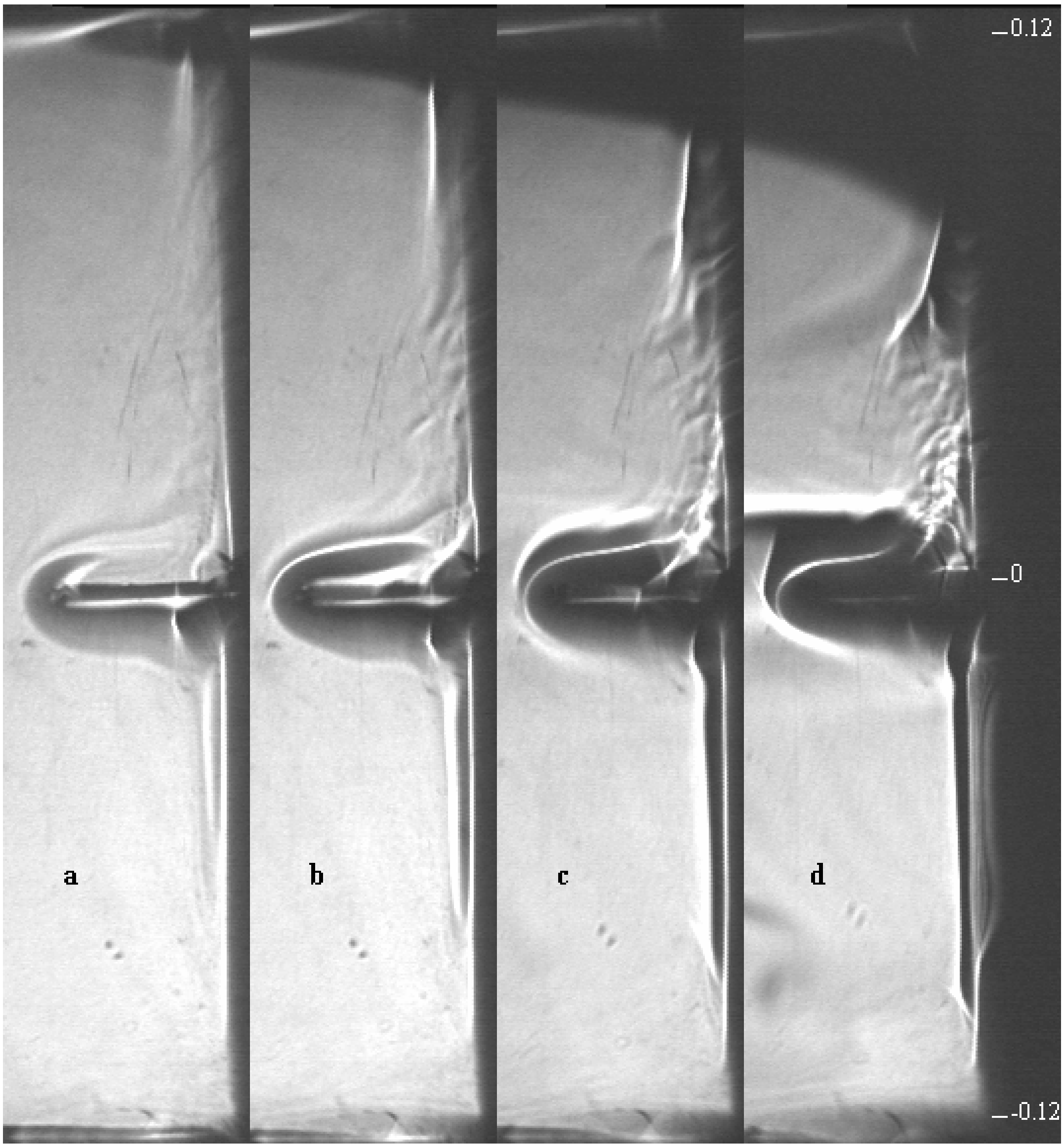

Figure 6.18 Thermal boundary layer flows at different Rayleigh numbers at t = 7200s
(a) $Ra = 9.5\times10^8$. (b) $Ra = 1.8\times10^9$. (c) $Ra = 3.8\times10^9$. (d) $Ra = 7.7\times10^9$

temperature near the fin and in turn leads to an outer bright strip horizontally extending toward the core above the thin fin, as seen in the shadowgraph image (Figure 6.18d).

6.3 Measurements of temperature in the thermal flow around a thin fin

Temperature measurements in this section are likewise aimed at the thermal flow around the same thin fin as that described in Section 6.2. Similar to those in Chapter 4, experiments with four temperature differences between sidewalls from 4 to 32 K are

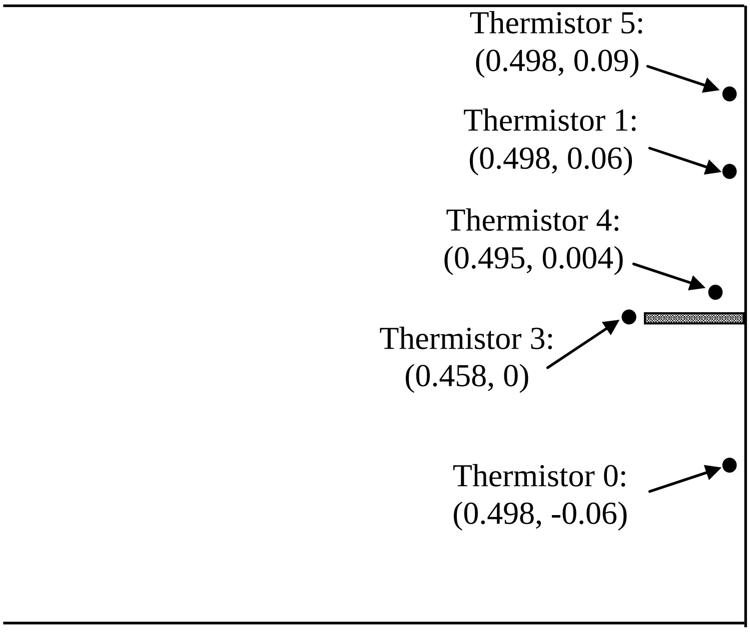

Figure 6.19 Thermistor locations relative to the center of the cavity

carried out. The corresponding ranges of the Rayleigh number and Prandtl numbers are $1.0 \sim 7.5 \times 10^9$ and $6.5 \sim 6.6$ respectively, as listed in Table 6.3. In order to compare with the previous flow visualizations and other temperature measurements without a fin, Experiment 22 was conducted under the same experimental conditions as Experiments 2, 7 and 18 (refer to Sections 4.1, 4.2 and 6.2).

Table 6.4 Parameters of temperature measurements with a thin fin

Number	Initial temperature of water in cavity (K)	Temperature difference between sidewalls (K)	*Ra* ($\times 10^9$)	*Pr*
20	295.8	4.0	1.0	6.5
21	294.9	8.0	2.0	6.5
22	295.55	16.0	3.8	6.6
23	295.7	32.0	7.5	6.6

Since the thermal flow around the fin is the focus of this chapter, five thermistors are employed and located in the vicinity of the fin and hot sidewall, three of which are close to and along the sidewall with a distance of 2 mm from the sidewall surface at different heights, and another two of which are placed around the fin. Details of the thermistor locations are shown in Figure 6.19.

Figure 6.20 shows time series of temperatures at five positions measured for $Ra = 3.8 \times 10^9$. Oscillations of temperatures at different points in the vicinity of the hot

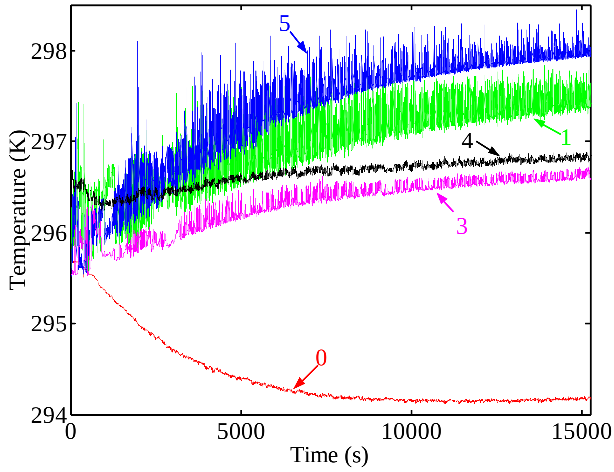

Figure 6.20 Time series of the temperatures at different positions at Ra = 3.8 × 10^9, for the thermistors at the positions given in Figure 6.19

sidewall are distinct, and the measured temperatures eventually approach a quasi-steady state. This is consistent with the flow visualizations in Section 6.2. The increased spread of temperature time series at different heights with time in Figure 6.20 indicates that stratification of the fluid in the cavity is continuously enforced as time increases. Furthermore, due to the presence of the fin, the transition from the start-up to the quasi-steady state persists for a longer time than that in the case without a fin (refer to Section 4.2, Figure 4.12).

For the purpose of illustrating further details of the transition, in the following subsections, the time series of temperatures in different stages are redrawn based on transient features.

6.3.1 Lower intrusion front

Figure 6.21 shows the temperature time series from different thermistors at Ra = 3.8 × 10^9 in the early stage. The temperature time series recorded by Thermistors 0, 1 and 5, which are all close to the sidewall, display distinct features of the LEE, including an overshoot followed by the traveling waves of the temperatures. Subsequently, due to perturbations from the lower intrusion front bypassing the thin fin, the temperature time series from Thermistors 1 and 5, close to the sidewall at the downstream side of the fin, are characterized by strong waves. In contrast to the above-mentioned three temperature time series, the temperature time series from Thermistors 3 and 4, which are further away from the sidewall, remain steady in the initial stage until the lower intrusion front

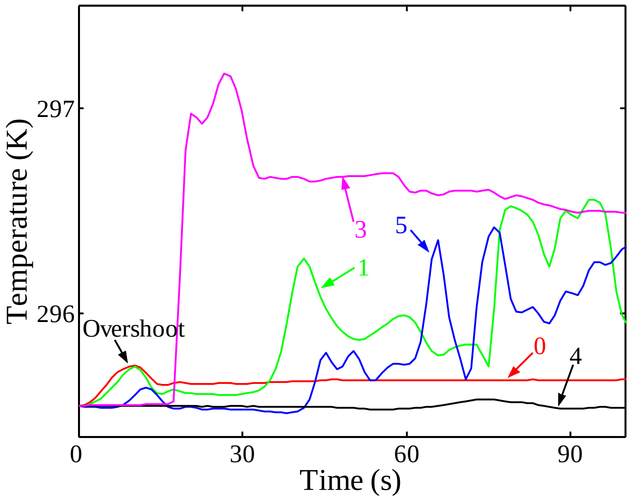

Figure 6.21 Time series of the temperatures at different positions at Ra = 3.8 × 10^9 in the early stage, for the thermistors at the positions given in Figure 6.19

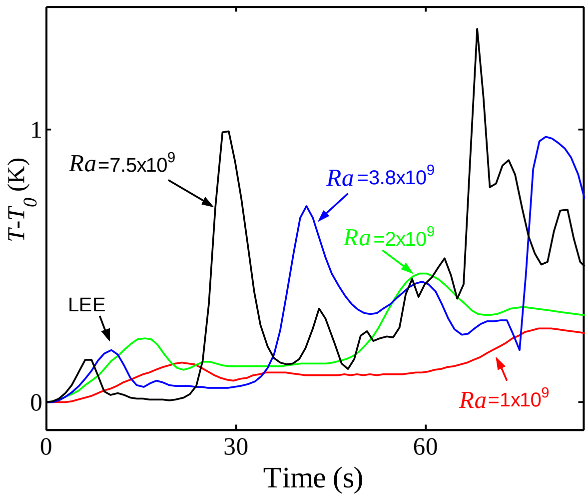

Figure 6.22 Time series of the temperatures at the point (0.498 m, 0.06 m) at different Rayleigh numbers

bypasses the fin. The temperature time series from Thermistor 3 near the tip of the thin fin displays perturbations from the lower intrusion front, and the temperature time series from Thermistors 1 and 5 in turn show similar perturbations as the signal travels downstream. The features characterized by these temperature time series are consistent with those flow visualizations in Figure 6.12. However, it is clear that, since Thermistor 4 is located in the lower corner of the downstream section of the sidewall (i.e. above the fin, see Figure 6.19), the temperature time series from Thermistor 4 is barely affected by the lower intrusion front in this stage.

For the purpose of illustrating the dependence of these early transient features on the Rayleigh number, the temperature time series from Thermistor 1 at different

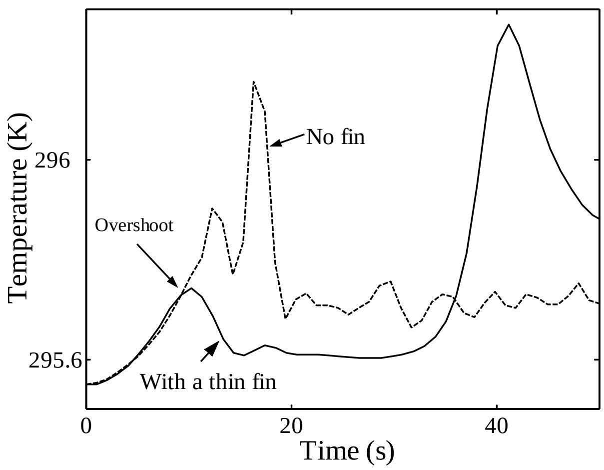

Figure 6.23 The LEE in the cases with and without a thin fin at the point (0.498 m, 0.06 m) at $Ra = 3.8 \times 10^9$

Rayleigh numbers are plotted in Figure 6.22, relative to the initial temperature in each case. As the Rayleigh number increases, the temperature of the thermal boundary layer grows more rapidly during the initial stage (see overshoot in Figure 6.22), and perturbations by the lower intrusion front occur earlier and are stronger.

It is worth noting that the LEE shown clearly in the temperature time series from Thermistors 1 and 5 at the downstream side of the thin fin is different from those in the case without the fin (also refer to Figure 4.14). Figure 6.23 shows the LEE recorded at the same point (0.498 m, 0.06 m) in the two cases with and without the thin fin. It is clear that there is a similar initial growth of the temperature in the two cases with and without the fin. Subsequently, the growth of the temperature finishes earlier in the case with the thin fin and a complete overshoot of the temperature signal results. However, for the case without the fin, the temperature continuously grows until a broken overshoot results. Such a difference between the two cases with and without the fin is because the fin separates the thermal boundary layer into an upper and a lower section before the lower intrusion front bypasses the fin (see Figure 6.11). In each section, there is a leading edge, which is the fin for the upper section and is the bottom of the cavity for the lower section. As a consequence, the distance of Thermistor 1 at the upper section from the leading edge is smaller than that in the case without the fin, and thus a smaller growth of temperature and a complete overshoot in the case with the thin fin result, as seen in Figure 6.23.

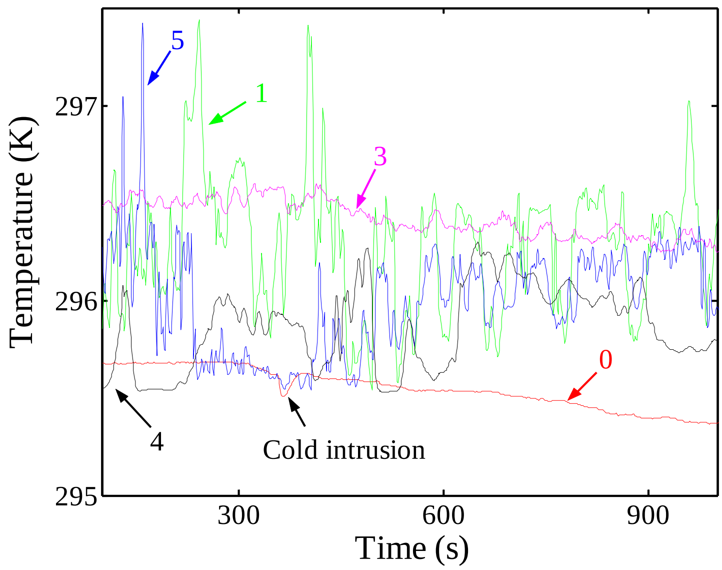

(a) Temperatures at different positions

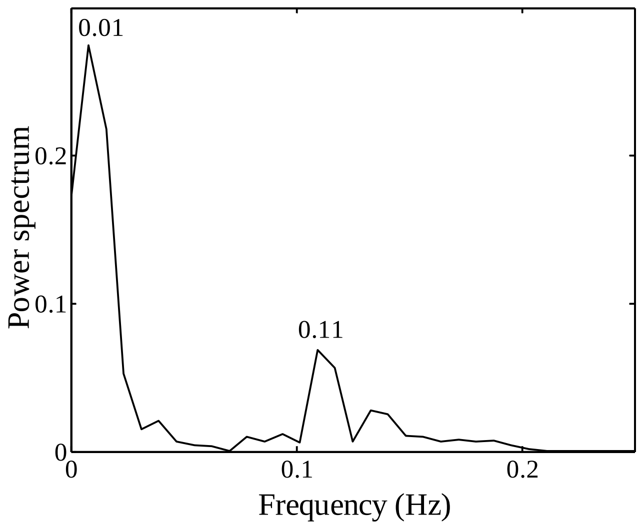

(b) Spectrum of temperature from Thermistor 5

Figure 6.24 Time series of the temperatures in the transitional stage at $Ra = 3.8 \times 10^9$ and spectrum

6.3.2 Temperature time series in the transitional stage

Figure 6.20 indicates that there exist strong perturbations of temperature signals in the early transitional stage. For the purpose of illustrating the details in this stage, Figure 6.24 replots the temperature time series and shows a corresponding spectrum.

As indicated in Figure 6.14, the lower intrusion front and its trailing flow significantly disturb the thermal boundary layer flow, and these perturbations are recorded in the temperature time series (Figure 6.24a). When the trailing flow of the

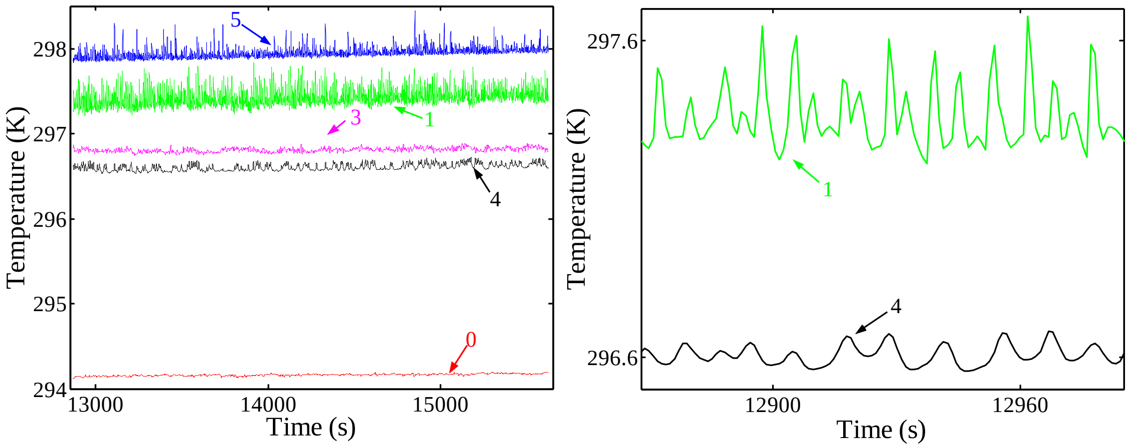

(a) From five thermistors (b) From Thermistors 1 and 4

Figure 6.25 Time series of the temperatures from different thermistors (see Figure 19) in the quasi-stage stage at $Ra = 3.8 \times 10^9$

lower intrusion front is eventually drawn closer to the fin (refer to Figure 6.13d), the temperature time series from Thermistor 4, which is above the fin, also starts to become unstable, and other temperature time series from Thermistors 1 and 5 at the downstream side of the fin still remain unsteady. Figure 6.24(a) shows that the perturbations excited by the lower intrusion front and its trailing flow are so strong that the perturbations induced by the cold intrusion striking the hot sidewall are overwhelmed (refer to the temperature time series from Thermistor 0 in Figure 6.24a). As time elapses, perturbations of the temperatures on the downstream side of the fin become weaker (also refer to Figure 6.20).

The spectrum in Figure 6.24(b) indicates that perturbations of the temperature from Thermistor 5 at the downstream side of the fin in this stage are dominated by two frequencies, which are 0.01 and 0.11 Hz respectively. Clearly, the higher frequency (0.11 Hz) corresponds to oscillations of the thermal flow around the fin, as shown in Figure 6.16.

6.3.3 Oscillations

As shown by the temperature time series in Figure 6.20, the transition of the thermal boundary layer flow approaches a quasi-steady state, which is also observed in the flow visualizations described in Section 6.2.

Figure 6.25 shows the temperature time series in the quasi-steady stage. It is seen in Figure 6.25(a) that the amplitude of the traveling waves does not grow with time, but

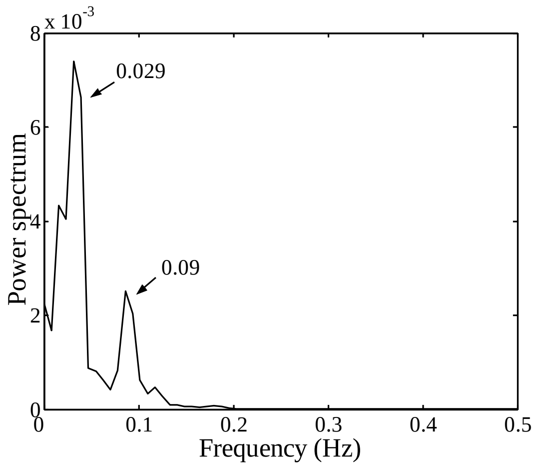

(a) At the point (0.495 m, 0.004 m)

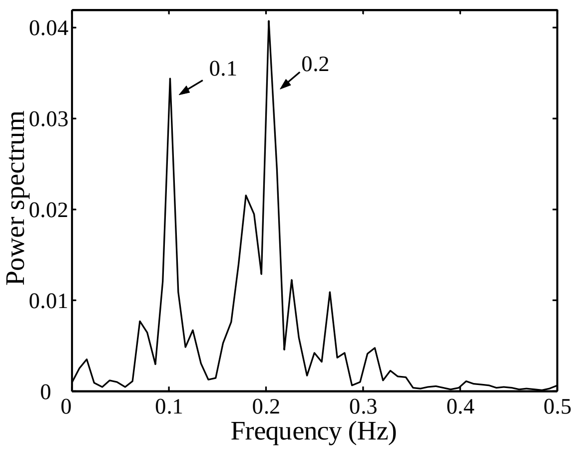

(b) At the point (0.498 m, 0.06 m)

Figure 6.26 Spectra of the temperature time series at different positions at $Ra = 3.8 \times 10^9$

there exists a spatial growth of the waves. For the purpose of illustrating spatial variations, Figure 6.25(b) replots the temperature time series from Thermistors 1 and 4. The temperature signal from Thermistor 4 displays oscillations of the thermal flow around the fin, and that from Thermistor 1 shows downstream perturbations of the thermal boundary layer. The two temperature time series indicate the spatial growth of amplitude and harmonic waves of oscillations after the thermal flow separates from the fin.

The spectra of the temperature time series in the quasi-steady stage are shown in Figure 6.26. The spectrum of the temperature time series from Thermistor 4 in Figure 6.26(a) indicates that the waves in the thermal flow around the thin fin have two frequency modes, 0.029 and 0.09 Hz respectively. The frequency of 0.029 Hz corresponds to those lower-frequency waves (also see Figure 4.18b), and the frequency of 0.09 Hz results from oscillations of the thermal flow around the thin fin (also see Figure 6.16). Figure 6.26(b) shows the spectrum of the temperature time series from Thermistor 1. It is clear that traveling waves in the downstream thermal boundary layer are likewise dominated by two frequencies. As visualized in Figure 6.16, the lower frequency of 0.1 Hz originates from the oscillations of the thermal flow around the thin fin. Furthermore, harmonic waves of oscillations of the thermal flow around the thin fin yield an additional frequency of 0.2 Hz as shown in Figure 6.26(a).

6.4 Summary

In this chapter, the transient development of the thermal boundary layer flows around a square and a thin fin placed at the mid height of the hot wall in a differentially heated cavity is visualized using the shadowgraph technique. Similar to the case without a fin, the natural convection flow with the square and thin fin may be classified into three stages in terms of the development of the thermal boundary layer, which are the initial stage, the transitional stage and the quasi-steady stage.

It is observed in the experiments that the transient flow induced by a fin is different from the case without a fin in the initial stage. Both a smaller square and a larger thin fin are able to block the upstream flow and force it to detach from the hot sidewall and eventually form a lower intrusion front.

Due to the entrainment of the thermal boundary layer, for the case with the square fin, the lower intrusion front reattaches to the hot sidewall after it bypasses the fin. Shadowgraph images show that the interaction between the lower intrusion front around the square fin and the upper thermal boundary layer leads to the collapse of the lower intrusion front when it reattaches to the upper thermal boundary layer. Eventually, the lower intrusion front is convected away.

For the case with the thin fin, the lower intrusion front travels underneath the fin for an extended period of time compared with the case with the smaller square fin, and thus has more time to grow stronger. After the lower intrusion front bypasses the thin fin, it does not reattach to the hot sidewall immediately as it does in the case with the smaller square fin. Instead, the bypassing lower intrusion front moves upwards due to buoyancy effects, and strikes the hot intrusion under the ceiling. The interaction between the lower intrusion front and the intrusion under the ceiling results in distinct turbulent mixing in the vicinity of the top corner. After the large perturbations induced by the lower intrusion front are convected away, entrainment by the thermal boundary layer draws the trailing flow of the lower intrusion front closer to the upper hot sidewall.

With the further development of the flow, a distinct flow around a fin develops. It is observed that, in the transitional stage, the flow around the thin fin separates and oscillates, which is different from the cases with and without a smaller square fin, suggesting that the separation and oscillation of the flow around the fin are dependent on the geometric parameters of the fin.

In the quasi-steady stage, although a similar double-layer structure forms in the lower cavity for both cases with the smaller square and larger thin fin, there are distinct variations of the flow structures in the upper section. Furthermore, it is found that the frequency of oscillations in the case with the thin fin is linearly dependent on the Rayleigh number in the range of present experiments.

The temperature measurements for the case with the thin fin show consistent results with the above-mentioned flow visualizations. The temperature time series from thermistors at different locations clearly characterize the LEE and transient features of the thermal boundary layer in the transition from the start-up to the quasi-steady stage. Furthermore, the spectra of the temperature signals display frequencies of various instabilities of the thermal flow around the thin fin.

The experimental data in this chapter are also used for validating the numerical simulations described in Chapter 7.

7 Numerical simulations of transient natural convection with a fin on the sidewall

Numerical studies of the effect of a fin on the sidewall of a differentially heated cavity on the flow and heat transfer have been extensively reported in the literature, as reviewed in Chapter 1. Most of the previous studies considered only the steady state flow and heat transfer by solving steady or unsteady Navier-Stokes equations. The steady state results are relevant to the cases with low Rayleigh numbers ($<10^7$), but their application to cases with higher Rayleigh numbers ($>10^7$), at which natural convection does not reach a steady state, needs to be reexamined. In this chapter, numerical simulations of transient natural convection in a suddenly differentially heated cavity with one and multiple fins on the hot sidewall are performed for relatively high Rayleigh numbers. First, numerical results for the cases corresponding to the experiments reported in Chapter 6 (i.e. with a square fin and a thin fin) are presented, and then the effects of fin parameters including the dimension, location and number of fins on the flow and heat transfer are discussed.

7.1 Natural convection with a square fin

Natural convection in a suddenly differentially heated cavity with a square fin on the hot sidewall is numerically investigated in this section. Based on the experimental model considered in Section 6.1, a two-dimensional rectangular domain (refer to Figure 3.1), which is H = 0.24 m high and L = 1 m long with a square fin of 10 mm × 10 mm at the mid height of the hot sidewall, is considered. The initial and boundary conditions are given in Section 3.1.3, and the numerical simulation here is for the case of $Ra = 3.8 \times 10^9$ and $Pr = 6.6$ (corresponding to Experiment 14 in Chapter 6, the same Rayleigh number as that in the case without a fin in Chapter 5) in this section. The flow features are compared between the experimental and numerical results, and the heat transfer property is discussed below, based on the numerical simulations below.

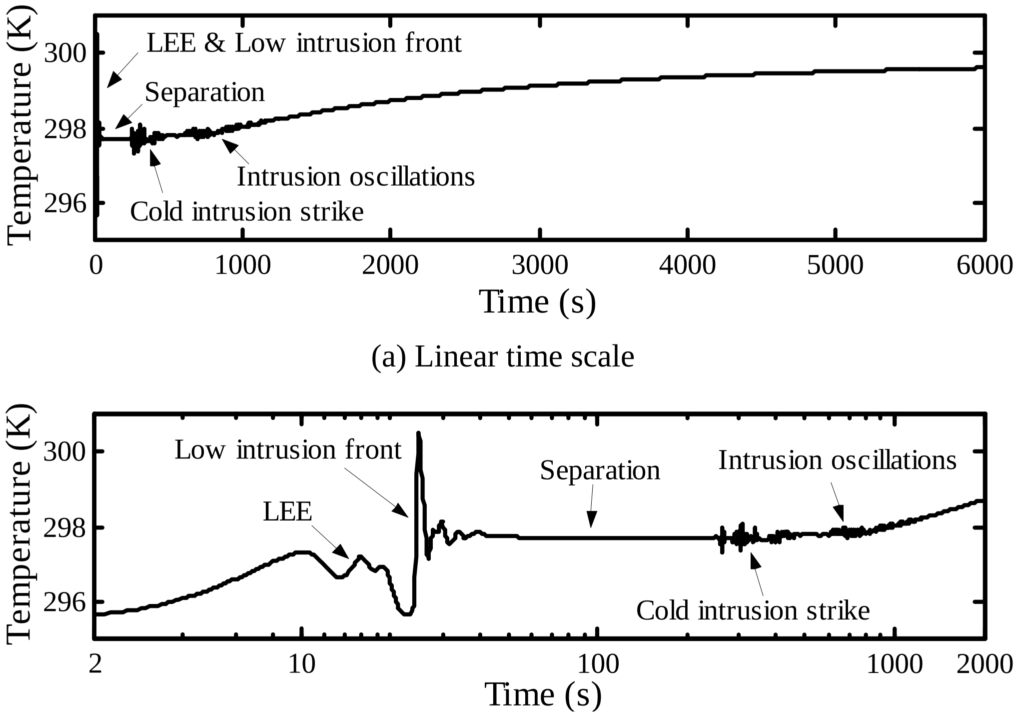

(a) Linear time scale

(b) Logarithmic time scale

Figure 7.1 Time series of the temperature at the point (0.498 m, 0.09 m)

7.1.1 Flow features of transient natural convection

The experimental results presented in Chapter 6 indicate that the development of the vertical thermal boundary layer flow with a square fin may be classified into three stages: the initial stage, the transitional stage and the quasi-steady stage. In this section, the numerical results will be compared with those in the experiments at different stages of the flow development.

Figure 7.1(a) plots a time series of the temperature calculated at the point (0.498 m, 0.09 m), similar to Figure 5.1(a) in Chapter 5. A logarithmic scale plot of the temperature at the same point is shown in Figure 7.1(b) so as to clearly exhibit the important features of the early transition of the thermal boundary layer. Compared with that without a fin (see Figure 5.1), the flow with a square fin displays distinct variations in the initial stage. Figure 7.1(b) indicates that the traveling waves induced by the LEE are weaker than those without a fin (see Figure 5.1). Subsequently, much stronger perturbations of the thermal boundary layer induced by the lower intrusion front completely surpass the traveling waves, as seen in Figure 7.1(b). After the perturbations of the lower intrusion front are convected away, the features of the thermal boundary

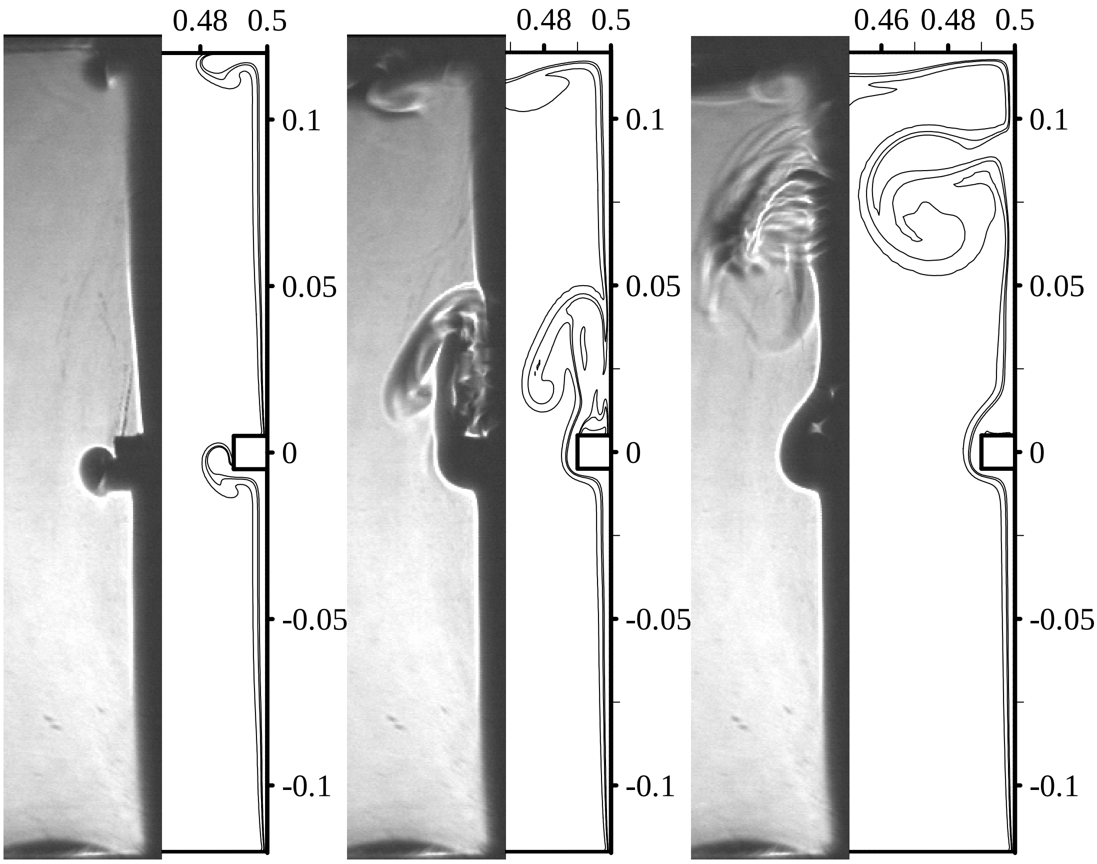

(a) t = 12 s (b) t = 9 s (c) t = 24 s (d) t = 17 s (e) t = 32 s (f) t = 25 s

Figure 7.2 Development of the lower intrusion front

(a), (c), and (e) Shadowgraph images. (b), (d), and (f) Numerical isotherms (contours: 296.56 and 297 K)

layer become similar to the case without a fin. The basic flow features include the separation of the intrusion, the strike of the cold intrusion and intrusion oscillations, as indicated in Figure 7.1(b).

For the purpose of obtaining further insights into the transient flow features, the numerical results are compared with the corresponding experimental visualizations presented in Chapter 6 below. Figure 7.2 shows the shadowgraphs and corresponding isotherms at different times in the initial stage. It is clear that the numerical flow features are similar to those of flow visualizations. However, the numerical flow develops slightly faster than the experimental flow, and the time lag of the experimental flow compared with the numerical one increases with time. This is likely because a relatively smaller Rayleigh number is achieved in the experiment than that in the numerical simulation, as discussed in Chapter 5. Figure 7.2(b) shows that a lower intrusion front forms below the square fin at the early time, and the upper and lower

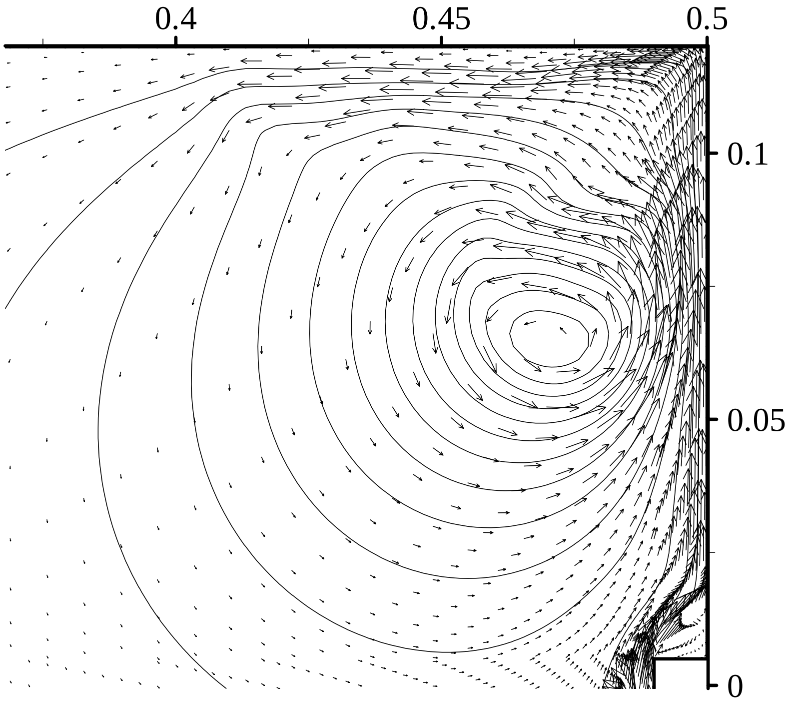

Figure 7.3 Streamlines and velocity vectors at t = 25s (contours from 2×10^{-5} to 2.8×10^{-4} m^2/s with an interval of 2×10^{-5} m^2/s)

sections of the thermal boundary layer flow are almost identical, similar to the experimental flow as shown in Figure 7.2(a). With the passage of time, the lower intrusion front bypasses the square fin and reattaches to the downstream thermal boundary layer due to the entrainment effect, as shown in Figure 7.2(d). Figure 7.2(d) also demonstrates that, after the lower intrusion front is entrained by the thermal boundary layer, the two flows (the lower intrusion front and the upper thermal boundary layer) interact with each other, leading to the breakdown of the flow structure of the upper thermal boundary layer.

With the further development of the flow, the lower intrusion front is convected downstream. Another phenomenon of interest is the formation of an anticlockwise rotation of the lower intrusion front, as seen in Figures 7.2(f), which supports the experimental result shown in Figure 7.2(e). The layered strip patterns in the vicinity of the wall indicate that the interaction between the lower intrusion front and the upper thermal boundary layer may have resulted in temperature waves, as seen in Figure 7.1(b).

The anticlockwise rotation of the lower intrusion front is a result of a non-uniform distribution of the velocity field in the thermal boundary layer. Figure 7.3 shows streamlines and velocity vectors in the vicinity of the upper section of the hot wall. It is

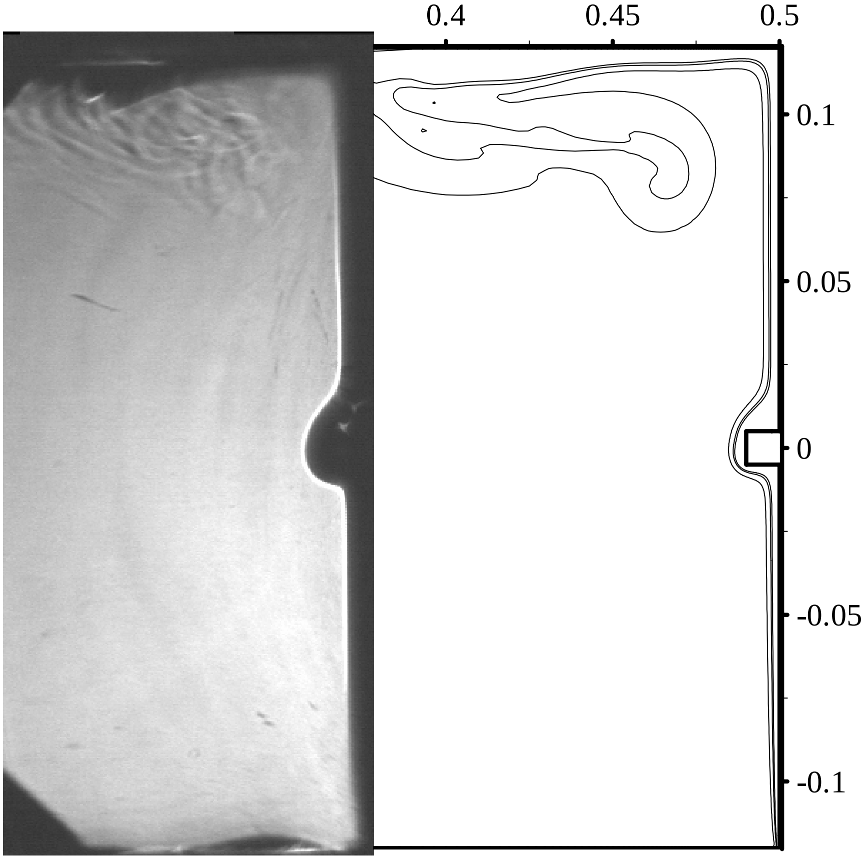

(a) t = 47 s (b) t = 37 s

Figure 7.4 Perturbations of the top intrusion by the lower intrusion front
(a) Shadowgraph images. (b) Numerical isotherms (contours from 294.6 to 296.6 with an interval of 0.5 K)

clear that the distribution of the velocity is non-uniform (see the velocity vectors in the vicinity of the sidewall in Figure 7.3), and the closer to the sidewall the position (except for the viscous inner layer), the larger the velocity. The viscous shear based on such a non-uniform velocity distribution drives the lower intrusion front to rotate anticlockwise while it is convected downstream, and thus enhances the mass and heat transfer of the thermal boundary layer. The temperature signals at the same stage (Figure 7.1b) indicate that the LEE of the upper thermal boundary layer is disturbed and stronger perturbations of the temperature time series are triggered by the lower intrusion front.

Figure 7.4 shows the experimental shadowgraph and numerical isotherms at a later time. It is seen in this figure that the lower intrusion front has merged with the top intrusion. The mixing of the lower intrusion front with the top intrusion has resulted in the disappearance of the earlier separation of the top intrusion (also see e.g. Figure

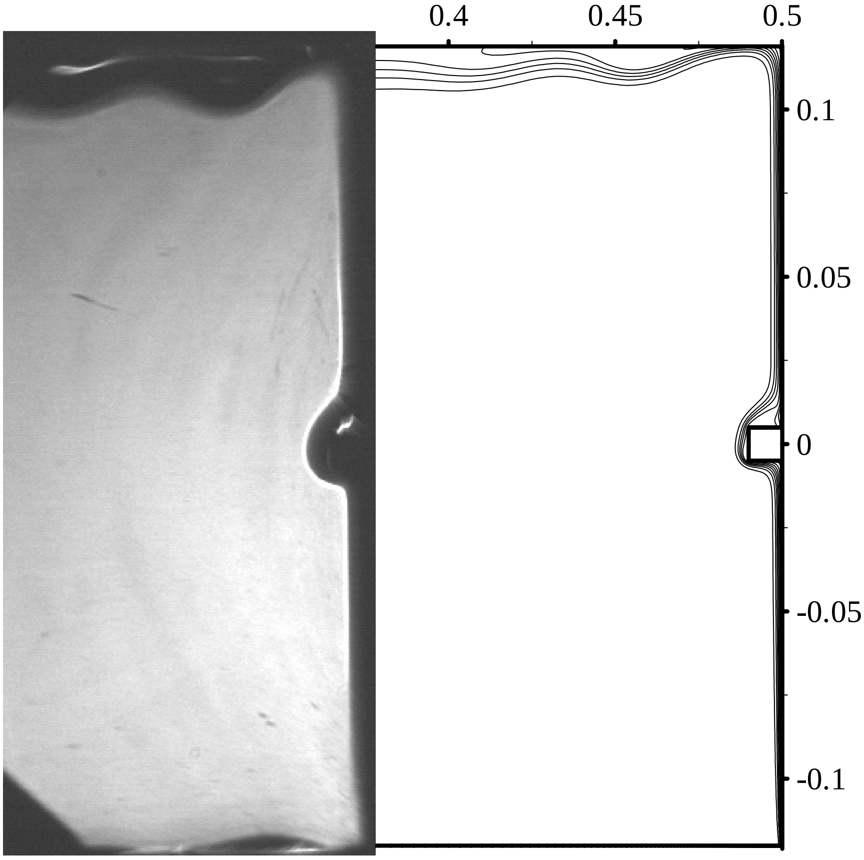

(a) t = 120 s (b) t = 100 s

Figure 7.5 Reappearance of separation and trailing waves of the top intrusion
(a) Shadowgraph images. (b) Numerical isotherms (contours from 288 to 303 K with an interval of 1 K)

5.10). Clearly, the numerical flow (Figure 7.4b) is consistent with the experimental flow (Figure 7.4a).

After the perturbations of the lower intrusion front are convected away, the intrusion under the ceiling becomes steady, and separation and trailing waves of the intrusion reappear, as seen in Figure 7.5. It is clear that the numerical result in Figure 7.5(b) agrees well with the experimental visualization in Figure 7.5(a). However, it is noticeable that the separation and trailing waves of the intrusion shown in the shadowgraph image are less distinct than those without a fin (refer to Figure 5.10).

Figure 7.6 shows the flow structure when the cold intrusion is approaching the hot sidewall. Despite a large time difference between the experimental and numerical flows, the major flow features shown in the numerical simulation (Figure 7.6b) are similar to those observed in the experiment (Figure 7.6a). However, as discussed in Chapter 5 (e.g. see Figure 5.13), due to the presence of various perturbations in the experiment,

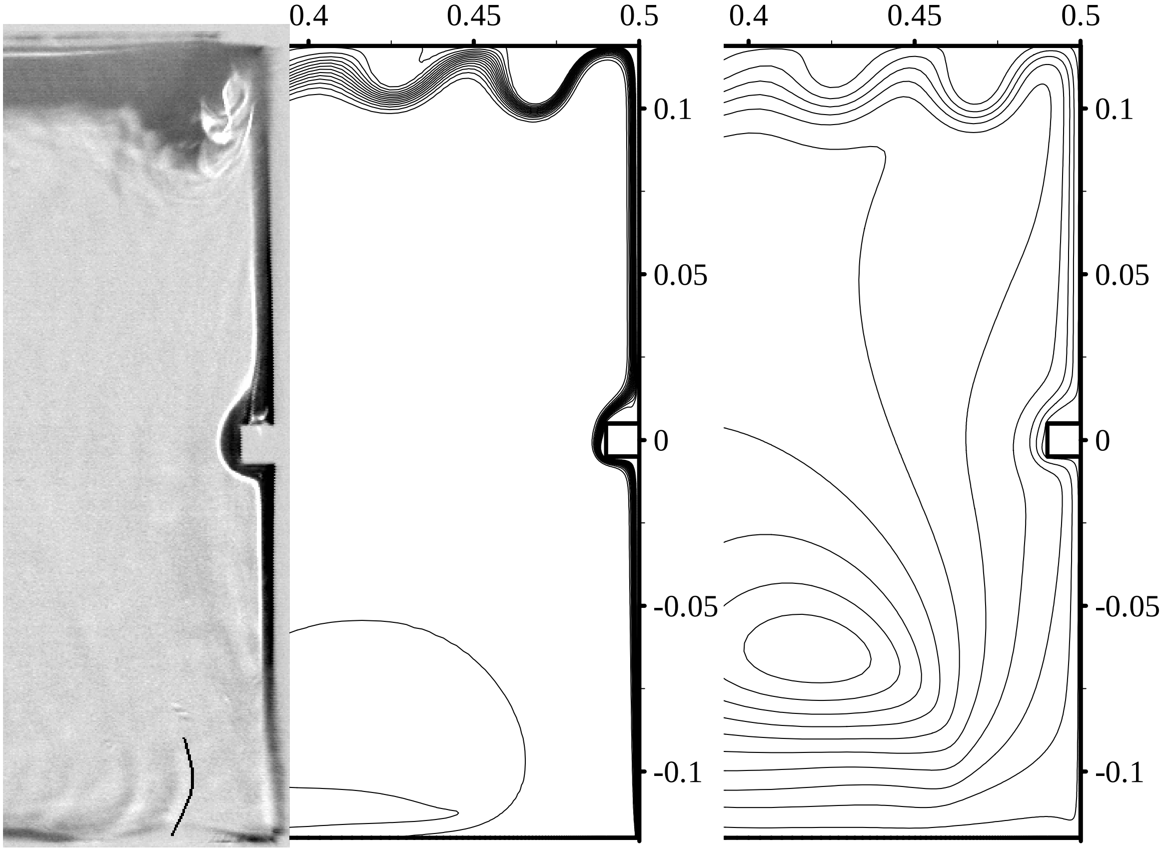

(a) t = 353 s (b) t = 240 s (c) t = 240 s

Figure 7.6 Strike of the cold intrusion to the hot wall

(a) Shadowgraph. (b) Isotherms (contours from 293.23 to 300.19 K with an interval of 0.31 K). (c) Streamlines (contours from 2×10^{-5} to 2.8×10^{-4} m^2/s with an interval of 2×10^{-5} m^2/s)

the shadowgraph image in Figure 7.6(a) shows that the outflow near the top corner is unstable, which is different from the numerical flow (Figure 7.6b). Furthermore, in the experiment, the destabilized roll structure in the top corner causes strong mixing, and results in the disappearance of the downstream trailing waves, as seen in Figure 7.6(a). Similar to the case without a fin, the streamlines in Figure 7.6(c) show that the entrainment of the thermal boundary layer is from the cold intrusion at this time.

As indicated by the temperature plot in Figure 7.1, the development of the thermal boundary layer flow after the cold intrusion strike the hot wall enters a slow transition to a quasi-steady stage. Therefore, following the practice used in Chapter 5 (see e.g. Figures 5.19 to 5.21), the experimental and numerical flows at the same times are compared in the following discussion due to the reduced impact of the timing difference between the experimental and numerical flows.

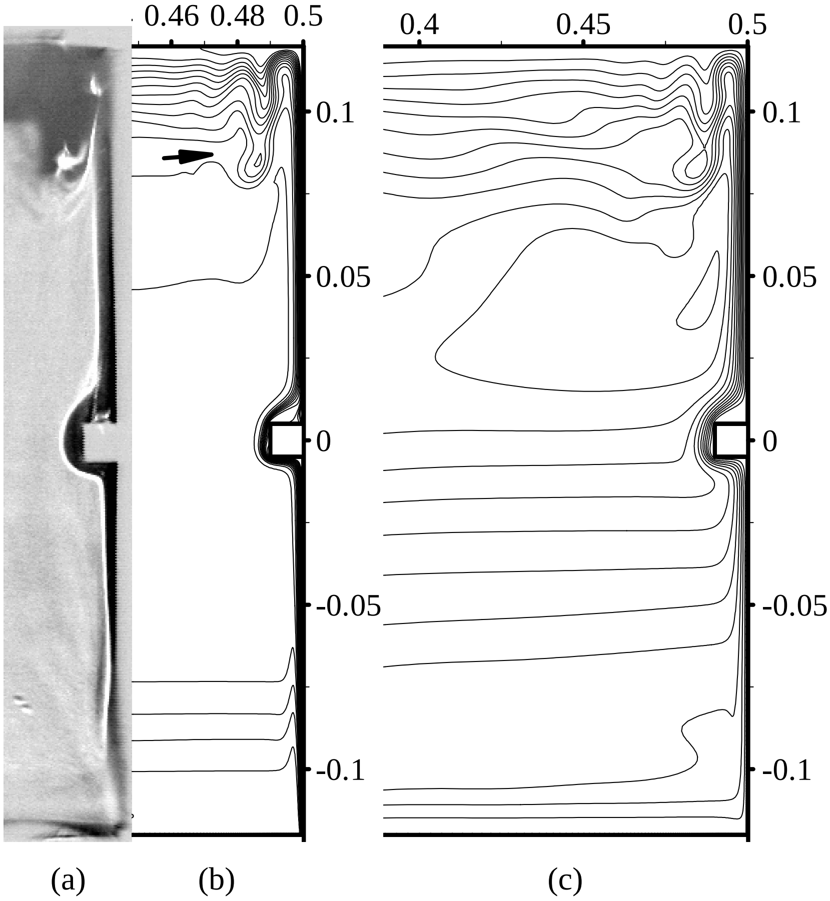

Figure 7.7 Appearance of the outer bright strips at t = 800 s

(a) Shadowgraph. (b) Isotherms (contours from 292.6 to 301.6 K with an interval of 0.5 K). (c) Streamlines (contours from 5×10^{-6} to 6×10^{-5} m^2/s with an interval of 5×10^{-6} m^2/s)

Similar to the case without a fin, a double-layer structure of the thermal boundary layer arises in the lower cavity after the cold intrusion strikes the hot wall, as seen in Figure 7.7(a). In the meantime, a bright strip is also noticeable in the top corner although it is further out from the hot wall. The discussion in Chapter 5 indicates that the two outer bright strips (although the lower bright strip here is less distinct compared to that without a fin, see Figure 5.19a) correspond to the positions of the minima of the second derivative of the temperature.

Clearly, the presence of the square fin does not significantly impact the temperature and flow structures near either the bottom or the top corner (see Figure 7.7 b, c), in comparison with those without a fin (refer to Figure 5.19). A minor variation of the flow structures between the cases with and without a square fin is a circulation adjacent to the downstream thermal boundary layer at this stage. Due to the presence of

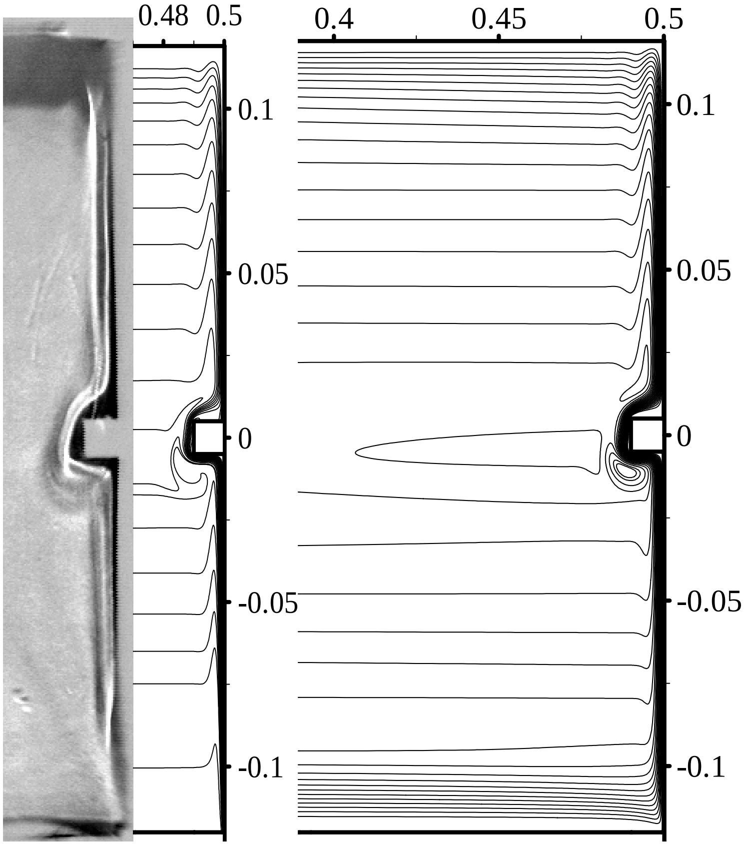

(a) (b) (c)

Figure 7.8 Double-layer structure during the quasi-steady state at t = 8,164s
(a) Shadowgraph. (b) Isotherms (contours from 291.1 to 301.6 K with an interval of 0.5 K). (c) Streamlines (contours from 2.1×10^{-6} to 2.6×10^{-5} m^2/s with an interval of 1.1×10^{-6} m^2/s)

the square fin, the dimension of the circulation is slightly changed compared with that without a fin (see Figure 5.19c). Similar to the case without a fin, the reverse flow resulted from a cavity-scale intrusion oscillation (indicated by the arrow in Figure 7.7b) splits the hot intrusion into two streams: an upper one that moves to the cold wall under the ceiling and a lower one that discharges into the cavity and forms a circulation, trapping cold fluid between the discharge flow and the boundary layer. The intrusion oscillation, likewise, results in the destabilization of the lower intrusion stream, as indicated by the fourth group of waves in the temperature time series in Figure 7.1(b) (also see Figure 4.16).

As time increases, similar to the case without a fin, the upper and lower outer strips gradually extend toward the mid height of the cavity and eventually arrive at the square fin. Figure 7.8 shows the experimental shadowgraph image, numerical isotherms

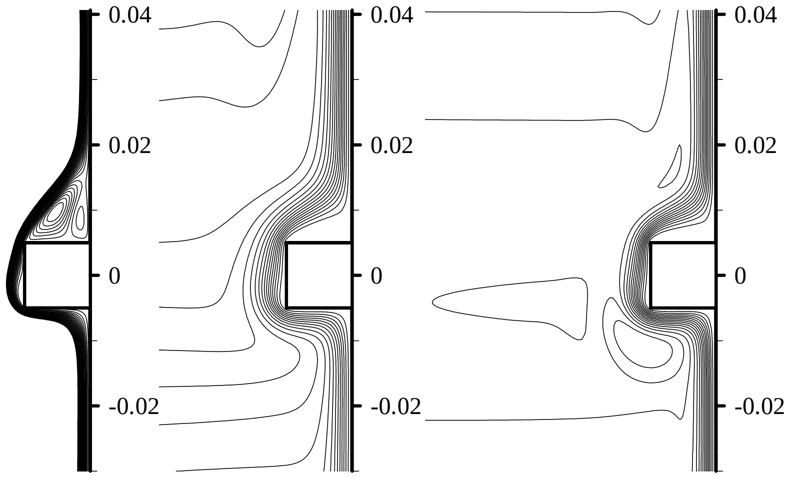

(a) (b) (c)

Figure 7.9 Vortices near the square fin at different times (streamlines)
(a) t = 20 s (contours from 7 × 10^{-7} to 2 × 10^{-5} m^2/s with an interval of 6.9 × 10^{-7} m^2/s). (b) t = 2,000 s (contours from 2.5 × 10^{-6} to 3.7 × 10^{-5} m^2/s with an interval of 2.5 × 10^{-6} m^2/s). (c) t = 8,164 s (contours from 1.7 × 10^{-6} to 2.5 × 10^{-5} m^2/s with an interval of 1.7 × 10^{-6} m^2/s)

and streamlines of the flow adjacent to the hot wall at a much later time. Clearly, due to the presence of the square fin, complex temperature and flow fields around the square fin results. Unlike the case without the fin in which a continuous thermal tongue adjacent to the hot wall forms, the upward thermal tongue here is broken by the square fin. The streamlines in Figure 7.8(c) indicate that three major circulations appear around the square fin, one above, one below and another one on the left of the square fin. Such a multi-circulation structure (Figure 7.8c) with a thermal tongue around the square fin (Figure 7.8b) is a distinct feature of the thermal flow around the square fin at the quasi-steady stage.

In order to observe the development of the multi-circulation flow around the square fin, Figure 7.9 shows the streamlines around the square fin at different times. After the lower intrusion front bypasses the square fin, two circulations first appear at the leeward side of the square fin, as seen in Figure 7.9(a), which are a distinct feature during the initial stage. The double-circulation structure lasts for a long time although weak. As the fluid in the cavity is stratified, the double-circulation structure at the leeward side of the square fin eventually disappears, as indicated in Figure 7.9(b). However, as the transitional flow approaches the quasi-steady state, three circulations form outside the thermal boundary layer around the square fin, as seen in Figure 7.9(c).

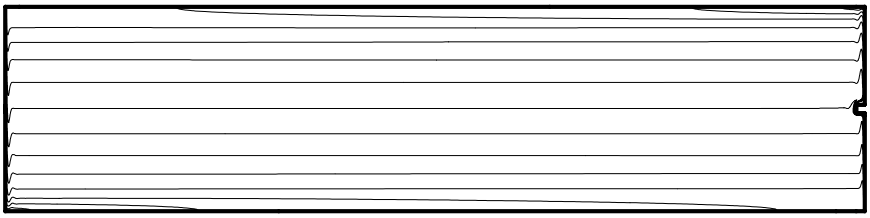

(a) Isothermals (contours from 298.55 to 303.55 an interval of 1K)

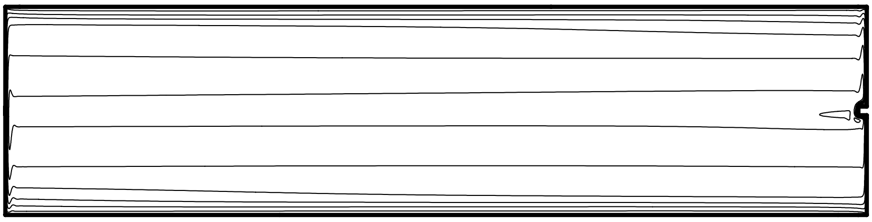

(b) Streamlines (contours from 2×10^{-6} to 2×10^{-5} m^2/s with an interval of 4×10^{-6} m^2/s)

Figure 7.10 Isotherms and streamlines at t = 8,164 s

Apart from the flow adjacent to the hot wall with a square fin, the flows adjacent to the cold wall and in the core are also worth noting. Figure 7.10 shows the isotherms and streamlines of the entire cavity at t = 8,164 s. Although the isothermals and streamlines adjacent to the cold and hot walls are asymmetric (see Figures 7.8b and c), the presence of the square fin has an insignificant impact on the flow and stratification of the core as indicated in Figures 7.10(a) and (b).

7.1.2 Heat transfer

The previous numerical results have demonstrated that the flow development for the case with a square fin is more complex in comparison with that without a fin. Some distinct properties of the flow development have been identified. It is also necessary to examine the correlation between the flow development and the heat transfer properties through the differentially heated cavity. This will be discussed in this section.

Here we define a normalized difference of the heat transfer rate, denoted by $\hat{H}$, as the difference of the heat transfer rate through the hot sidewall between the two cases with and without a fin divided by the heat transfer rate through the hot wall without a fin. That is,

$$\hat{H} = (H_{fin} - H_{nofin}) / H_{nofin} . \tag{7.1}$$

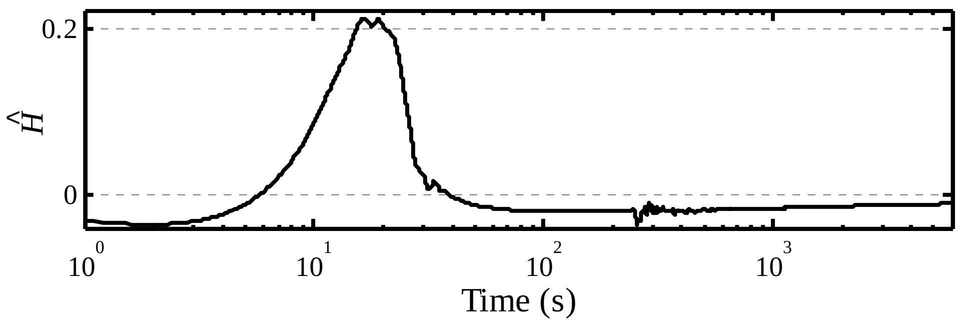

Figure 7.11 Normalized difference of the heat transfer rate of the hot wall between the cases with and without a square fin ($\hat{H}$) against time

It is seen from the above definition that, a positive value of $\hat{H}$ means enhancement of the heat transfer, a negative value means depression of the heat transfer, and a zero value means no effect on the heat transfer. Figure 7.11 plots the time series of the calculated normalized difference of the heat transfer rate. It is clear that the heat transfer rate peaks at approximately 21% in the initial stage, indicating that the heat transfer through the hot wall is significantly enhanced in the early stage. The enhancement of the heat transfer is due to the fact that the presence of the square fin enforces the convection flow adjacent the hot wall, which in turn improve the heat transfer. Figure 7.11 also indicates that the normalized heat transfer rate is positive approximately from 6 s to 36 s. This period corresponds to the time period when the lower intrusion front flushes over the downstream section of the hot wall (see Figures 7.1b and 7.2). That is, the strong convection flow, associated with the lower intrusion front, results in the enhancement of the heat transfer through the hot wall. After the lower intrusion front leaves the hot wall, $\hat{H}$ becomes negative. Since the cold intrusion striking the hot wall leads to instabilities of the thermal boundary layer, $\hat{H}$ displays corresponding fluctuations at approximately t = 240s. As the flow approaches the quasi-steady stage, $\hat{H}$ gradually approaches zero, as seen in Figure 7.11.

In order to estimate the effect of the fin on the local heat transfer of the hot sidewall, the heat transfer coefficient (h) of the hot sidewall is defined as follows,

$$h = \frac{q'}{T_h - T_0}, \tag{7.2}$$

$$q' = k\frac{\partial T}{\partial x}. \tag{7.3}$$

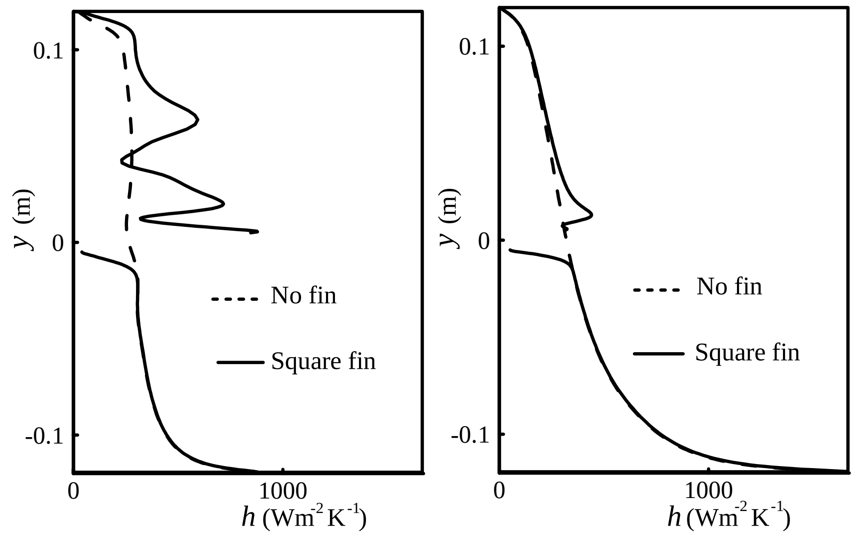

(a) t = 20 s (b) t = 6000 s

Figure 7.12 Heat transfer coefficient of the hot wall with and without a square fin

Figure 7.12 shows the distributions of the calculated local heat transfer coefficients of the hot wall with and without a square fin at the early and quasi-steady stage, respectively. It is seen in Figure 7.12 that, at both the initial and quasi-steady stages, the local heat transfer coefficients in the upstream section of the hot wall for the cases with and without the square fin are identical. However, variations of the heat transfer coefficients in the downstream section of the hot wall and in the vicinity of the square fin between the cases with and without the square fin are noticeable. In particular, in the early stage, large variations of the heat transfer coefficients of the downstream section are evident, and spatial waves can be identified for the case with the square fin, as seen in Figure 7.12(a). This observation also supports the conclusion that the strong convection flow, induced by the lower intrusion front, enhances the heat transfer through the hot sidewall in the early stage. As the thermal boundary layer flow approaches the quasi-steady state, the distributions of the heat transfer coefficients with and without the square fin become similar except in the region near the square fin, as shown in Figure 7.12(b).

In summary, the small square fin changes the flow structure of the thermal boundary layer in the early stage, and in turn significantly enhances the early-stage heat transfer through the hot sidewall by inducing a lower intrusion front. However, as indicated in Figures 7.11, in other stages of the flow development, the presence of the square fin, to some extent, depresses the heat transfer through the hot sidewall. This is consistent with those previously reported results for lower Rayleigh numbers, as reviewed in Chapter 1 (refer to e.g. Bilgen 2005).

7.2 Natural convection with a thin fin

In this section, a numerical simulation of the transient natural convection flow with a thin fin of 40 mm × 2 mm on the hot wall, corresponding to Experiment 18 with Ra = 3.8×10^9 and Pr = 6.6 reported in Section 6.2, is performed. The thin fin here replaces the square fin in Section 7.1, and all other conditions including the initial and boundary conditions as well as the basic flow parameters are the same as those adopted in Section 7.1 (refer to Chapter 3 for more details). The transition of the thermal boundary layer flow with a thin fin is described in this section based on the numerical simulation and compared with the experimental observations. Other features of the flow including wave activities of the thermal boundary layer and the heat transfer properties are also discussed in this section.

7.2.1 Flow features of transient natural convection

As described in Section 6.2, an important feature of the early transition of the thermal boundary layer flow is the formation and evolution of a lower intrusion front. Figure 7.13 shows the comparisons between the recorded shadowgraph images and the computed flows based on flow events rather than the flow time. It is clear that the numerical flow develops slightly faster than the experimental flow, as indicated in Section 7.1, but the basic flow features are very similar between the experimental and numerical results.

The isotherms in Figure 7.13(b) indicate that two intrusion fronts have formed, one underneath the ceiling and the other underneath the thin fin. Since the thin fin in this case is much longer than the square one examined in Section 7.1, both the numerical experimental and numerical results (Figures 7.13a and b) show that the upper and lower sections of the thermal boundary layer are identical. It takes longer time for the lower intrusion front to bypass the thin fin (Figure 7.13d) in comparison with the case with a square fin (see Figure 7.2d). After the lower intrusion front bypasses the thin fin, the similarity between the upper and lower sections of the thermal boundary layer disappears.

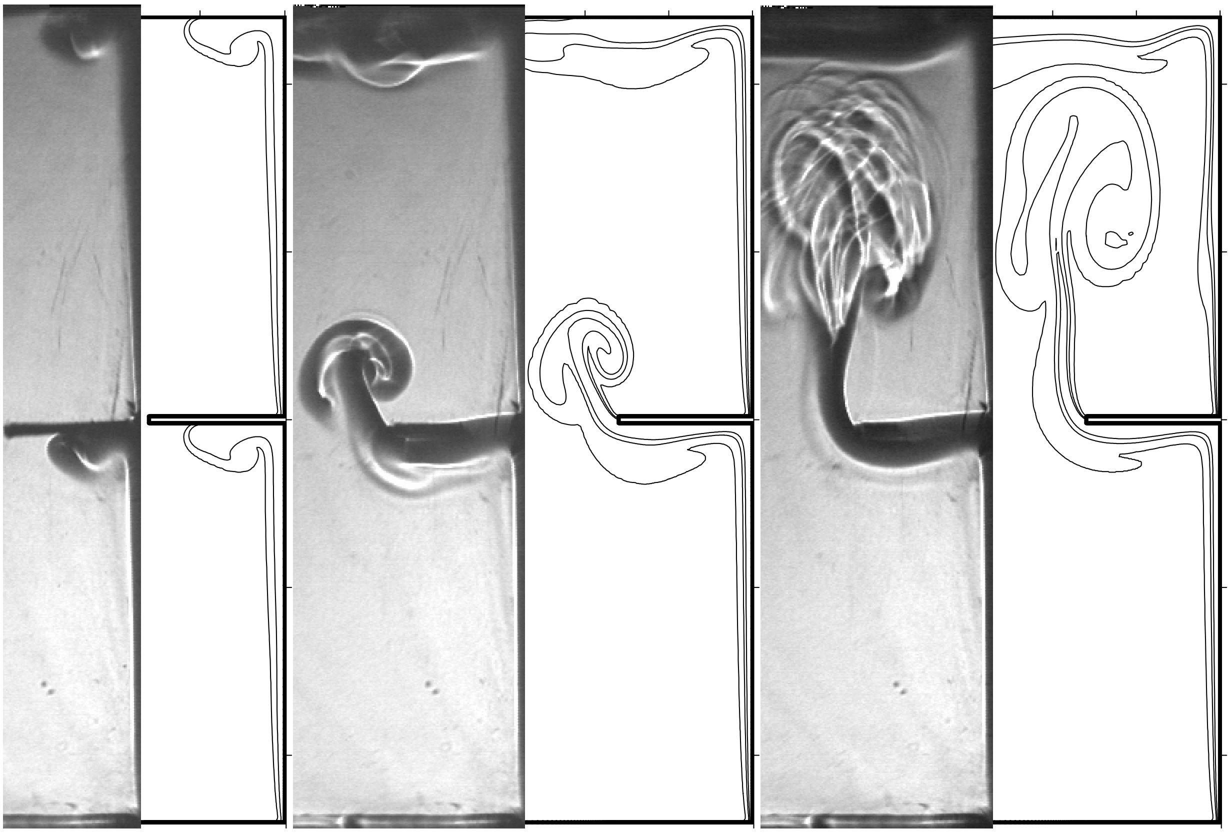

(a) t = 16s (b) t = 12 s (c) t = 30 s (d) t = 24 s (e) t = 41 s (f) t = 34s

Figure 7.13 Development of the lower intrusion front with shadowgraph (a, c, e) and isotherms (b, d, f with contours of 296.56 and 297 K)

Figures 7.13(c) and (d) indicate that the calculated flow is very similar to that observed in the experiment although the numerical flow is ahead for approximately 6 s. Figures 7.13(e) and (f) show that in the subsequent flow development, the lower intrusion front moves directly upwards and strikes the intrusion under the ceiling. This is evidently different from the case with the square fin (refer to Figure 7.2) in which the lower intrusion front reattaches to the downstream thermal boundary layer due to the entrainment effect after it bypasses the square fin. The variation between the cases with the thin and square fins is attributed to the difference in the distance between the lower intrusion front bypassing the fin and the downstream thermal boundary layer. In the present case with the thin fin, the distance is large, and the entrainment effect is not strong enough to draw the rising lower intrusion front to the downstream thermal boundary layer within a short time. Figures 7.13(e) and (f) also display that, although the numerical and experimental results are similar, the flow structure of the broken lower intrusion front observed in the experiment is more complex than that in the

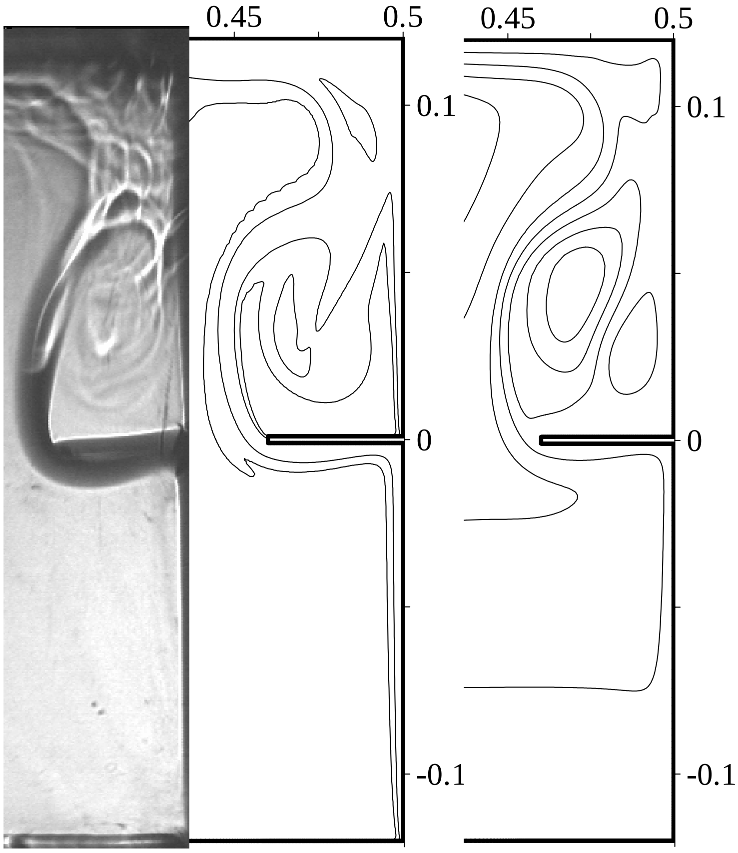

(a) t = 56 s (b) t = 48 s (c) t = 48 s

Figure 7.14 Trailing flow behind the lower intrusion front

(a) Shadowgraph. (b) Isotherms (296.56 and 297 K). (c) Streamlines (contours from 3.2×10^{-5} to 3.5×10^{-4} m^2/s with an interval of 3.2×10^{-5} m^2/s)

numerical simulation. This discrepancy between the experiment and simulation is likely attributed to the presence of various perturbations in the experiment.

After the lower intrusion front strikes the intrusion under the ceiling, it is entrained into the discharge flow and convected away, as indicated in Figure 7.14(a). Although the reattachment of the lower intrusion front to the thermal boundary layer does not occur for the present case with the thin fin, the entrainment effect still draws the trailing flow behind the lower intrusion front to the thermal boundary layer, as shown in Figure 7.14.

In the meantime, a clockwise circulation forms between the reattaching trailing flow and the upper thermal boundary layer, as shown Figure 7.14(a) (the same as Figure 6.13b). The isotherms in Figure 7.14(b) show consistent features with the flow visualization, and the streamlines in Figure 7.14(c) indicate that the clockwise circulation is in fact one of the two circulations forming in this region, which are similar

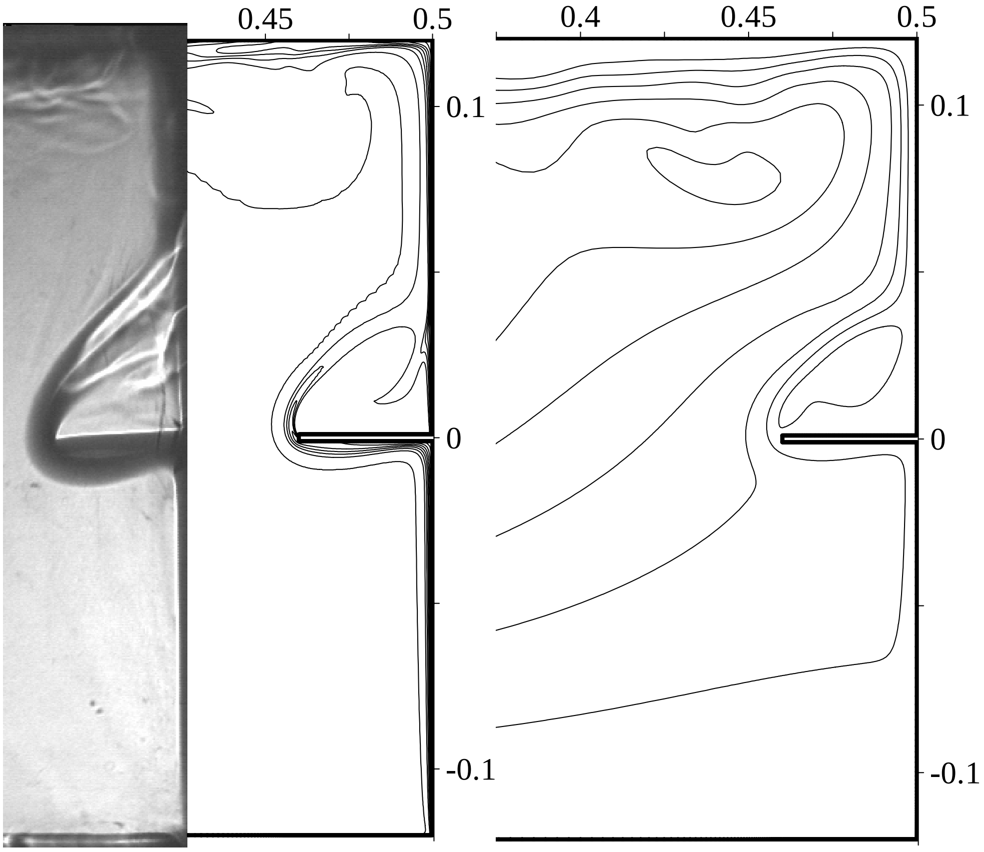

(a) t = 88 s (b) t = 80 s (c) t = 80 s

Figure 7.15 Subsequent development of the trailing flow

(a) Shadowgraph. (b) Isotherms (contour interval of 1 K between 287.56 and 302.56 K). (c) Streamlines (contours from 3.2×10^{-5} to 3.5×10^{-4} m^2/s with an interval of 3.2×10^{-5} m^2/s)

to those forming in the case with the square fin but are evidently of a larger scale (see Figure 7.9a). In the reattachment process, the trailing flow breaks up (Figure 7.14a), and is more complex than that around the square fin.

Figure 7.15 shows the subsequent development of the flow around the thin fin. Clearly, the temperature field in Figure 7.15(b) is consistent with the shadowgraph image in Figure 7.15(a) (the same as Figure 6.13d). After the perturbations induced by the lower intrusion front are convected away, the trailing flow is drawn much closer to the thin fin due to the entrainment effect. The isotherms in Figure 7.15(b) show that the clockwise circulation is still distinct although smaller. The streamlines in Figure 7.15(c) also confirm the existence of the clockwise circulation.

Figure 7.16 shows the temperature and flow structures when the cold intrusion is approaching the hot sidewall. At this stage, the time lag between the experimental and

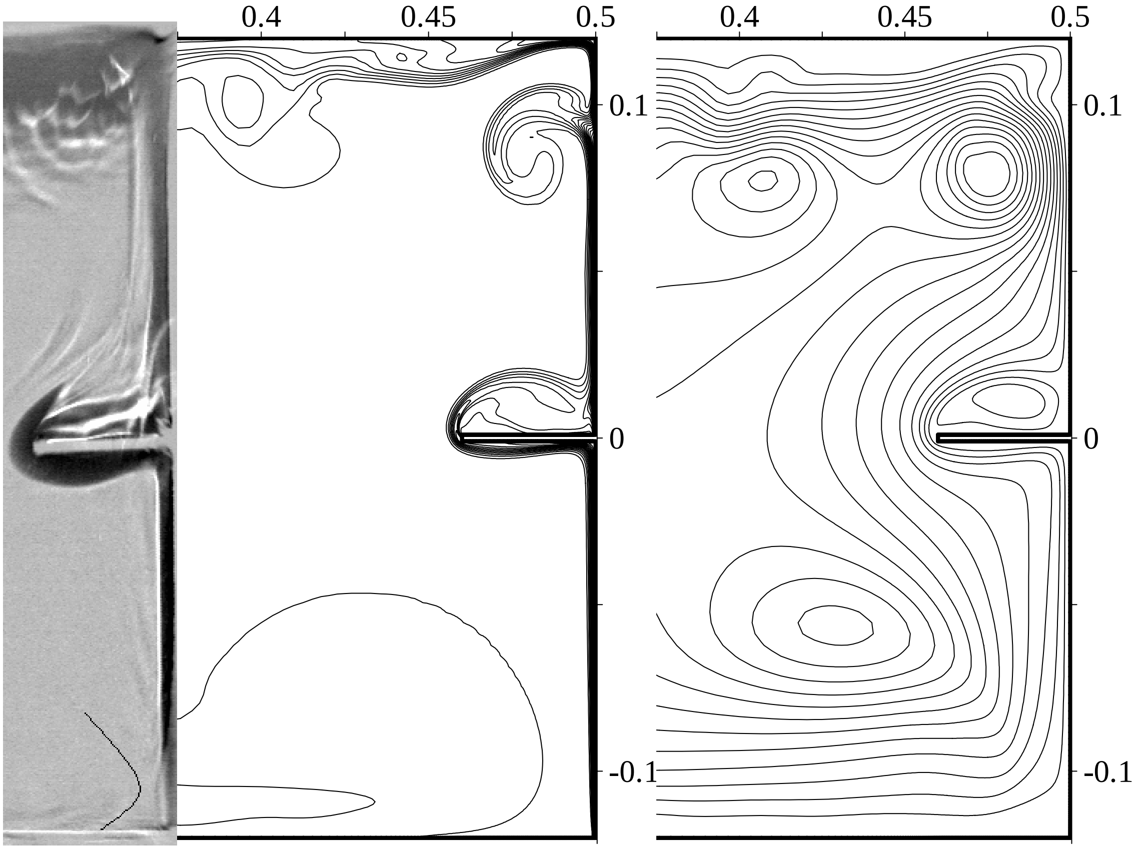

(a) t = 405 s (b) t = 250 s (c) t = 250 s

Figure 7.16 Cold intrusion strikes the hot wall

(a) Shadowgraph. (b) Isotherms (contours from 289.54 to 303.54 K with an interval of 0.5 K). (c) Streamlines (contours from 1.6×10^{-5} to 2.6×10^{-4} m^2/s with an interval of 1.6×10^{-5} m^2/s)

numerical flow development has increased significantly compared with that at the earlier stage of the flow development. The experimental observation in Section 6.2 indicates that, unlike the case with a square fin, there is no clear separation under the ceiling for the case with the thin fin, which is also supported by the numerical results shown in Figures 7.16(b) and (c). This is because the strong perturbations of the thermal flow around the thin fin lead to the breakdown of the separation and trailing waves under the ceiling (see Figure 5.11). Further analyses of the oscillations of the temperature time series will be discussed in Section 7.2.2.

After the cold intrusion strikes the hot wall, the development of the flow enters a slow transitional process, and the time lag between the experimental and numerical flows becomes less important. Therefore, the subsequent comparisons between the

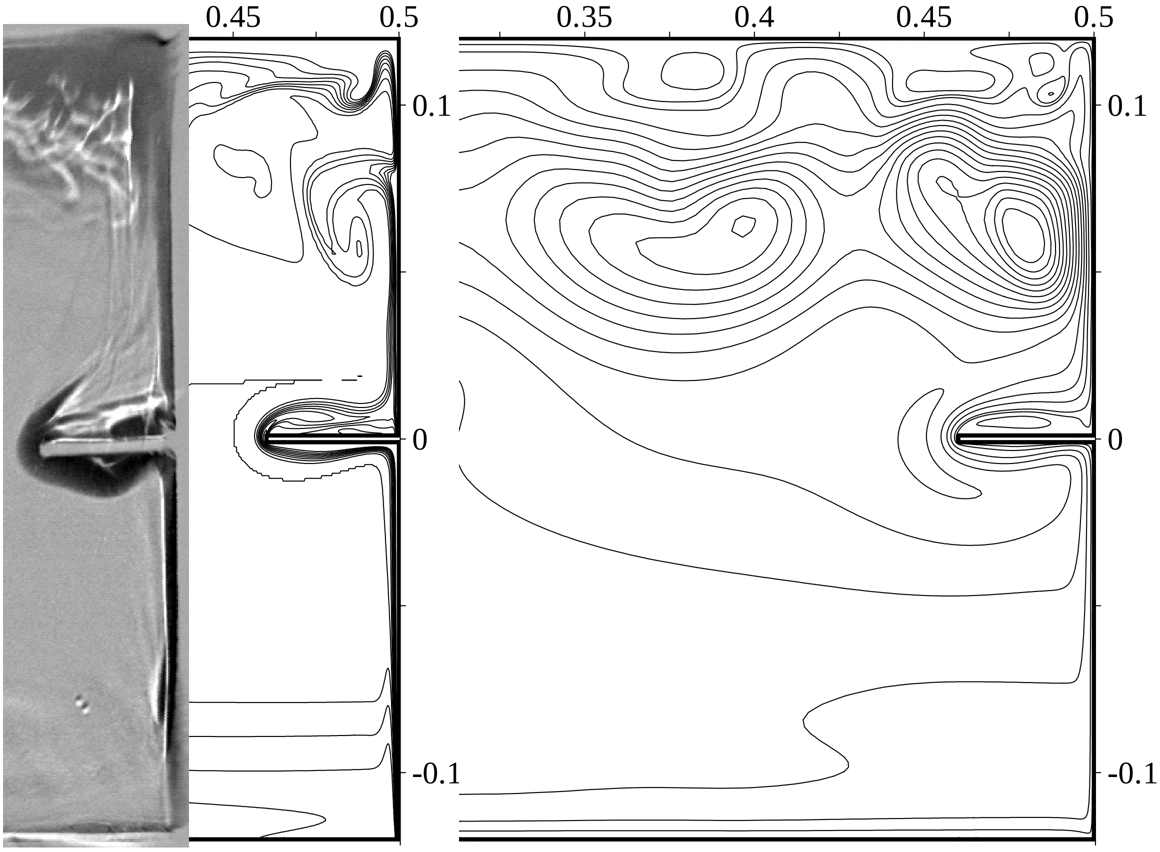

(a) (b) (c)

Figure 7.17 Appearance of the outer bright strip in the lower cavity at t = 700 s
(a) Shadowgraph. (b) Isotherms (contours from 291.55 to 299.55 K with an interval of 0.5 K). (c) Streamlines (contours from 3.1×10^{-6} to 1.6×10^{-4} m^2/s with an interval of 9.9×10^{-6} m^2/s)

experimental and numerical results are carried out based on the same flow time (as performed in Section 7.1).

In the subsequent development of the flow, a double-layer structure of the thermal boundary layer develops. Figure 7.17 (a) shows that a bright outer strip arises outside the thermal boundary layer in the lower cavity. As described in Chapter 5, the calculated isotherms at the same position (Figure 7.17b) display an upward thermal tongue, and the outer bright strip shown in the shadowgraph images corresponds to the positions of the minima of the second derivative of the temperature. Clearly, the presence of the thin fin does not impact on the temperature and flow structures near the bottom corner, in comparison with that without the fin (refer to Figure 5.19). However, the flow structure near the top corner is evidently different from the case without the fin (refer to Figure 5.19) and the case with a square fin (Figure 7.7). In the present case with the thin fin,

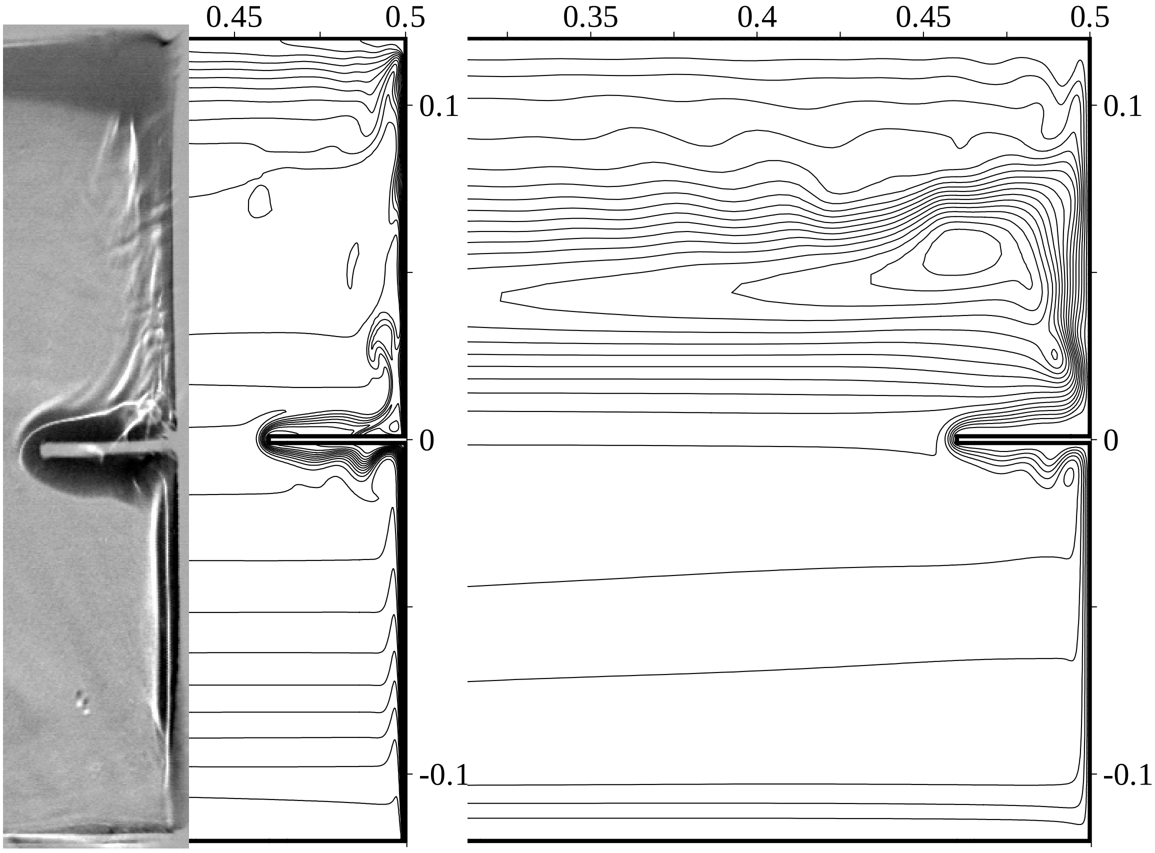

(a) (b) (c)

Figure 7.18 Formation of the double-layer structure in the lower cavity at t = 3200 s
(a) Shadowgraph. (b) Isotherms (contours from 291.55 to 302.55 K with an interval of 0.5 K). (c) Streamlines (contours from 4×10^{-6} to 6.9×10^{-5} m^2/s with an interval of 4×10^{-6} m^2/s)

stronger perturbations lead to the breakdown of the separation and trailing waves of the intrusion, as mentioned previously, and in this case, the reverse flow due to a cavity-scale intrusion oscillation (indicated by the arrow in Figure 7.7b) cannot be observed at this time. In the time period after the cold intrusion strikes the hot wall, the thermal boundary layer flow on the downstream side of the thin fin is oscillatory (also see Section 7.2.2 for details).

Similar to the development of the flow with the square fin, the lower outer bright strip extends toward the thin fin. Figure 7.18 shows the thermal boundary layer flow after the lower outer bright strip arrives at the thin fin. The double-layer structure in the lower cavity (see Figure 7.18a) and the upward thermal tongue (Figure 7.18b) become more distinct. Figures 7.18(a) and (b) also indicate clearly that the flow separates around the thin fin. The separation features will be discussed along with oscillation

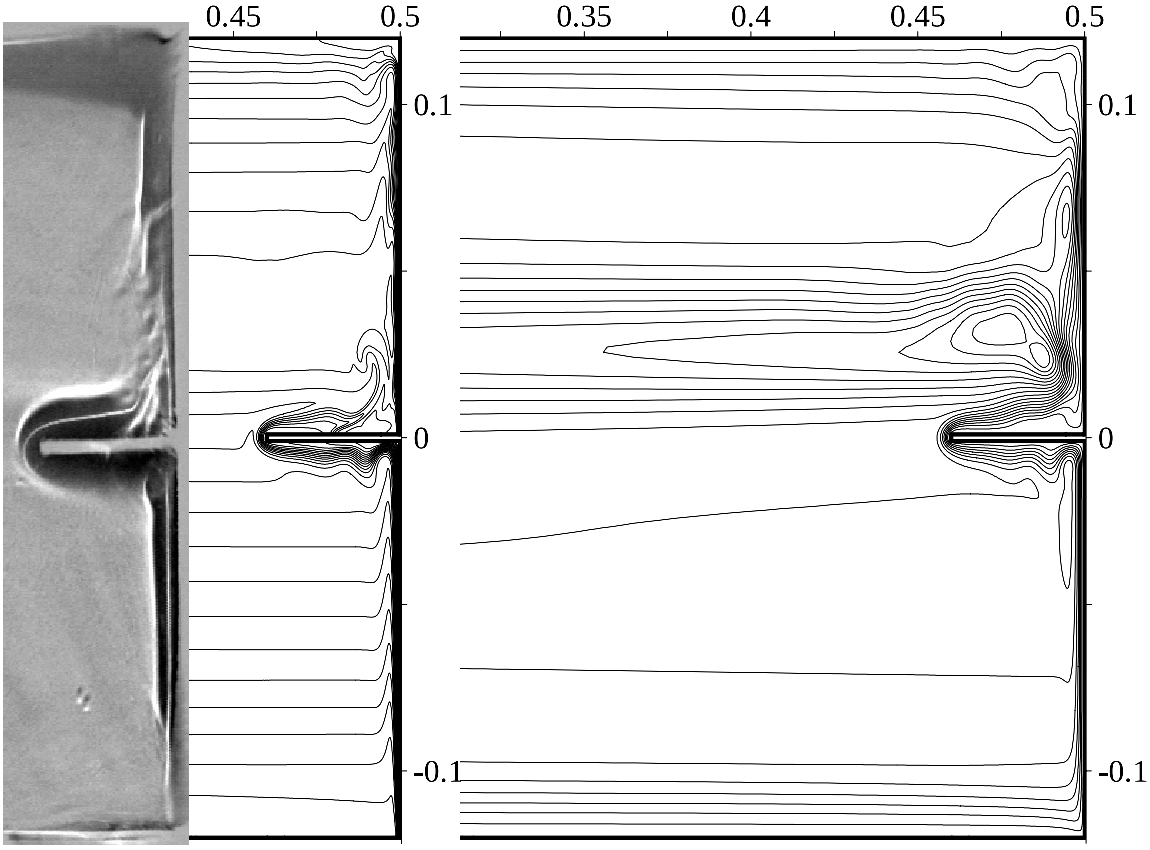

(a) (b) (c)

Figure 7.19 Thermal boundary layer at t = 11700 s

(a) Shadowgraph. (b) Isotherms (contours from 288.55 to 302.55 K with an interval of 0.5 K). (c) Streamlines (contours from 2.5×10^{-6} to 4.2×10^{-5} m^2/s with an interval of 2.5×10^{-6} m^2/s)

features in Section 7.2.2. At this stage, a stable bright strip observed in the case with a smaller square fin (refer to Figure 7.8a) does not form in the top corner (see Figure 7.18a). This is because strong oscillations of the thermal flow separating from the fin and a large-scale circulation in the vicinity of the downstream thermal boundary layer in Figure 7.18(c) disturb the stratified temperature structure near the sidewall (see Figure 7.18b). However, a stable thermal tongue around the tip of the thin fin (above the tip of the thin fin in Figure 7.18b) results, and thus a double-layer structure appears there, as seen in Figure 7.18(a).

As the stratification in the upper cavity is enforced, a clear upward thermal tongue arises near the top corner, as seen in Figure 7.19(b). As a consequence, an outer bright strip appears in the same position in the shadowgraph image, as indicated in Figure 7.19(a). However, the outer bright strip in the upper cavity remains broken as long as

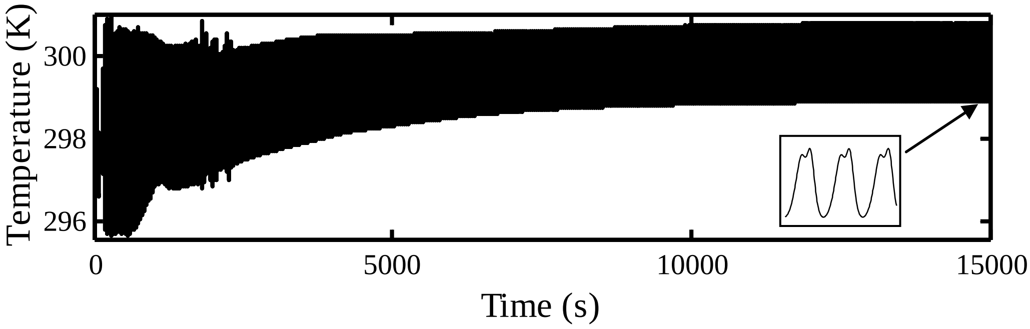

(a) Linear time scale

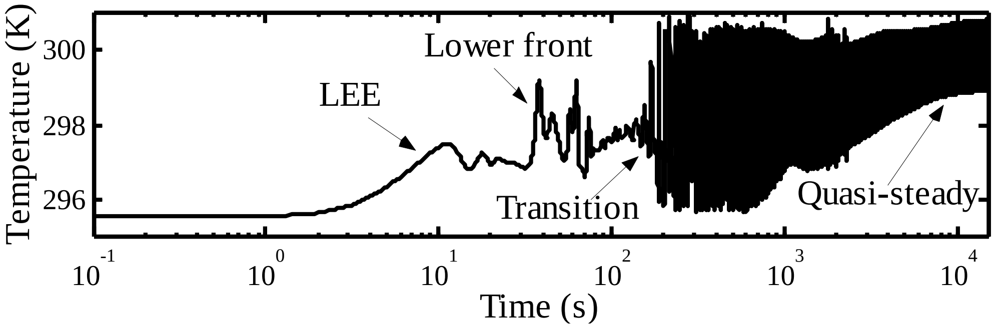

(b) Logarithmic time scale

Figure 7.20 Time series of the temperature at the point (0.498 m, 0.09 m)

the experiment persists. The streamlines in Figure 7.19(c) indicate that a large circulation in the vicinity of the upper thermal boundary layer, similar to that in Figure 7.18(c), may be responsible for the breaking up of the outer bright strip shown in the shadowgraph image (Figure 7.19a). Furthermore, due to the presence of the oscillations of the thermal flow around the fin, the inner bright strip on the downstream side of the fin is also broken (refer to Figure 6.16). Figures 7.19(a) and (b) also indicate that the double-layer structure and the corresponding upward thermal tongue in the lower cavity remain clear and stable.

In summary, the flow development in the case with a large thin fin exhibits some distinct features from the case of a small square fin. Particularly, there are separation and shedding flow around the thin fin, which will be further discussed with oscillation features in the following subsection.

7.2.2 Oscillations of the thermal flow around the fin

For the purpose of illustrating the wave property of the thermal boundary layer flow, a time series of the temperature obtained at the point (0.498 m, 0.09 m) in the thermal boundary layer is plotted in Figure 7.20. Figure 7.20(a) indicates that, for the case with

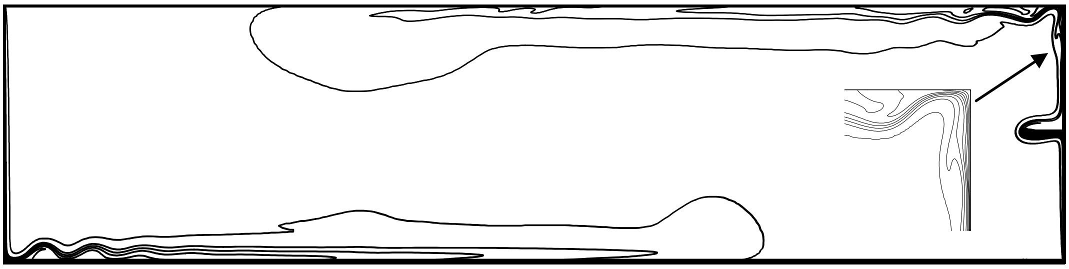

(a) Isotherms (from 287.55 to 303.55 K with an interval of 1 K)

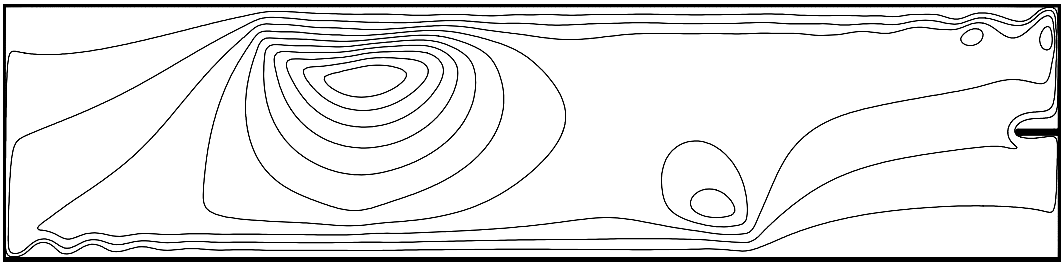

(b) Streamlines (from 3.4×10^{-5} to 3.4×10^{-4} m^2/s with an interval of 3.4×10^{-5} m^2/s)

Figure 7.21 Appearance of oscillations of the flow around the thin fin at t = 170 s

the thin fin, the thermal boundary layer flow eventually approaches a periodic flow (see a zoom in Figure 7.20a and Figure 7.22d). Similar to Figure 7.1, the early transient features are also shown in a logarithmic time scale in Figure 7.20(b). It is seen in this figure that the earlier transient features include the LEE and perturbations from the lower intrusion front. Since the lower intrusion front is not directly entrained into the thermal boundary layer after it bypasses the thin fin (also see Figure 7.13), a complete LEE propagation process in the upper cavity is observed, as shown in Figure 7.20(b). Subsequently, perturbations of the lower intrusion and the reattachment of the trailing flow induce further instability of the thermal boundary layer flow (also see Figure 7.14).

It is worth noting that, compared with the experimental measurements, the calculated temperature waves are apparently stronger, but the development of waves is similar to the measurements in the initial stage (also see Figure 6.21). In addition, the frequencies of the temperature waves in the numerical simulation and experiment are almost identical (approximately 0.11 Hz, also see Figures 6.17, 6.26 and 7.23).

After the lower intrusion front is convected away, the development of the thermal boundary layer enters a transitional stage, as marked in Figure 7.20(b). In the early transitional stage, the amplitude of the temperature waves quickly increases as the cold intrusion is approaching the hot sidewall. Figure 7.21 shows the isotherms and streamlines in this stage, in which the waves near the upper-right corner are present (see

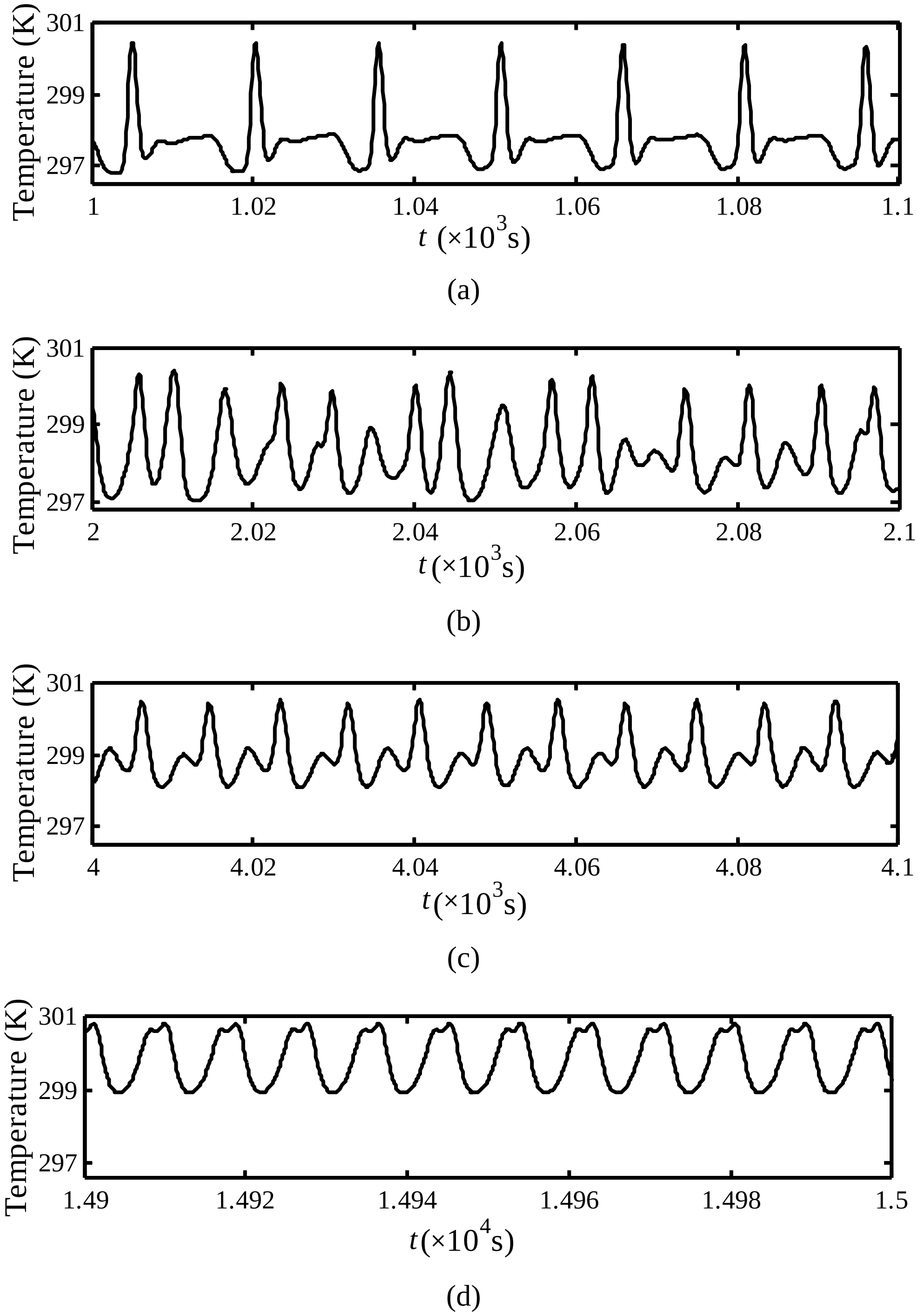

Figure 7.22 Temperature time series at the different stages at the point (0.498 m, 0.09 m)

a zoom in Figure 7.21a). The streamlines in Figure 7.21(b) indicate that the entrainment by the thermal boundary layer is from the lower part of the cavity in the initial stage. It is also seen in Figure 7.21(b) that the circulation under the hot intrusion front is stronger than that near the cold intrusion front.

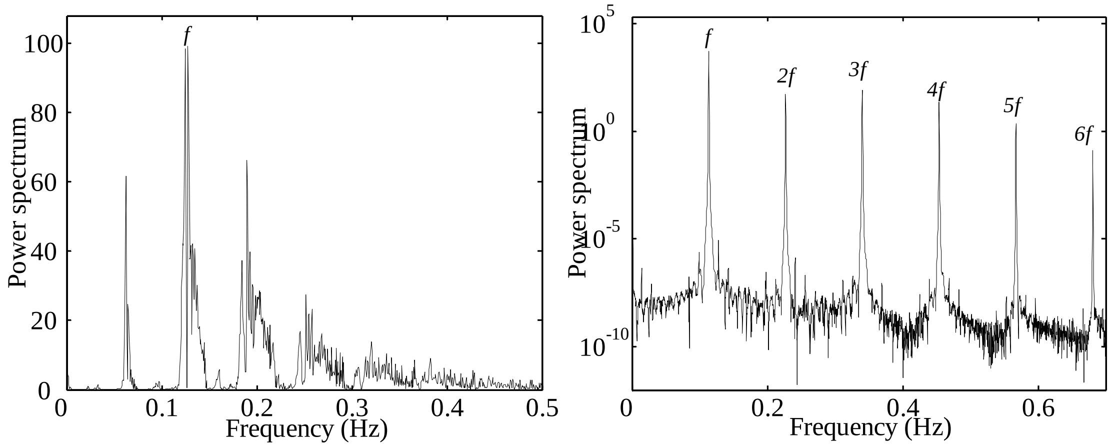

(a) Transitional stage (b) Quasi-steady stage

Figure 7.23 Spectra of the temperature time series at the point (0.498 m, 0.09m)

In order to illustrate the development of the traveling waves of the thermal boundary layer, Figure 7.22 shows time series of the temperatures at different stages. The evolution of the wave modes at different stages is clear. As time increases, the amplitude of the waves decreases, approximately from 3.5 K in the earlier stage (see Figures 7.22a and b) to 2 K in the quasi-steady stage (see Figures 7.22c and d). In the transitional stage (see Figure 7.20b), the frequency adjustment may be observed, and in the quasi-steady stage the double-mode of the waves (see Figure 7.22d) remains.

Figure 7.23(a) shows the spectrum of the temperature time series in the transitional stage (from 200 s to 2000 s), in which the dominant frequency is f = 0.128 Hz with a few additional lower and higher frequency modes. The spectrum of the temperature time series in the quasi-steady stage is shown in Figure 7.23(b). The dominant frequency is reduced to f = 0.113 Hz at the quasi-steady stage (which is consistent with the experimental measurement of 0.11 Hz, see Figure 6.26) with distinct harmonic frequency modes such as 2f, 3f and higher.

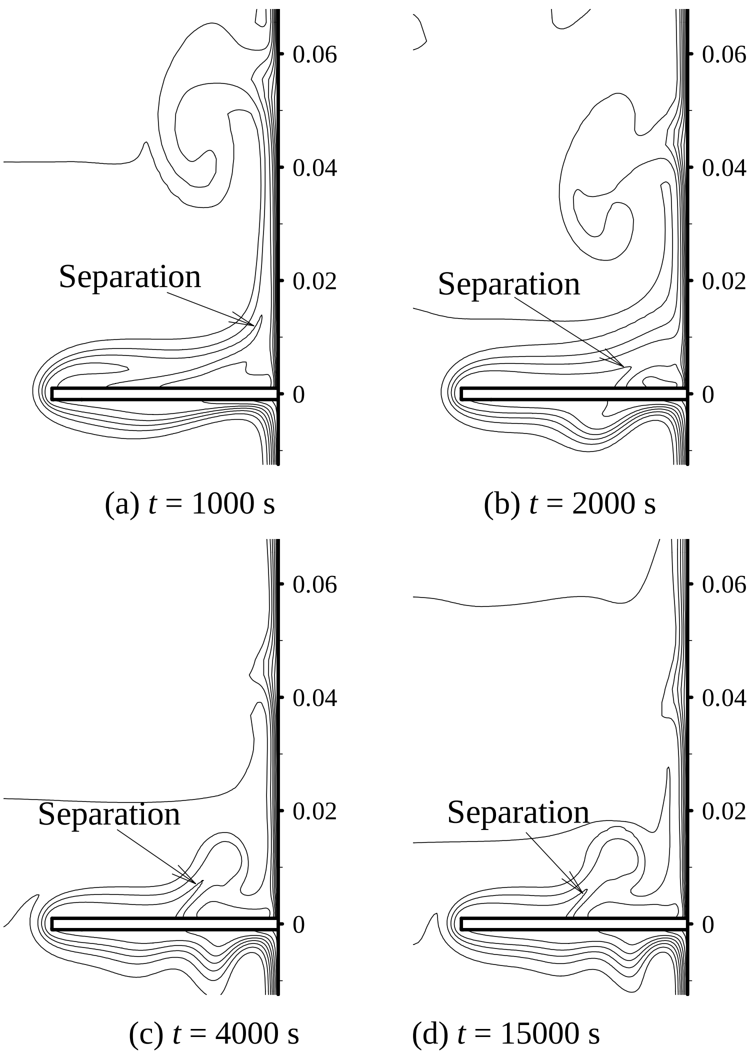

Figure 7.24 Separation and oscillations at different stages (isotherm interval of 1K from 296 K to 303K)

In fact, the development of the wave mode (see Figures 7.22) is largely dependent on the thermal flow around the thin fin. Figure 7.24 shows isotherms near the thin fin at different times. As time increases, the position of the flow separation around the thin fin moves further from the hot wall, and the oscillation of the flow around the thin fin changes accordingly. In the earlier stage, the shedding flow around the thin fin with a relatively larger speed induces stronger traveling waves, as seen in Figures 7.24(a) and (b). However, subsequently, since the separation position of the shedding flow around the thin fin moves further from the hot wall, the shedding flow has less impact on the downstream thermal boundary layer, as shown in Figures 7.24(c) and (d). This is also consistent with the temperature results in Figure 7.22.

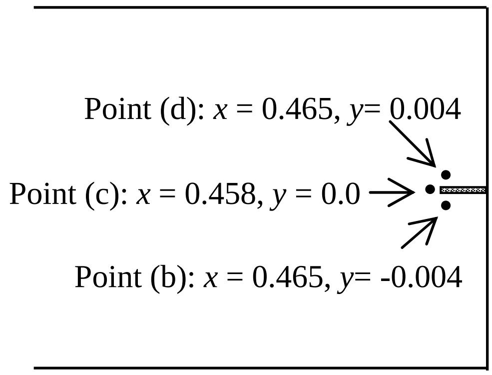

(a) Locations of three points around the fin tip

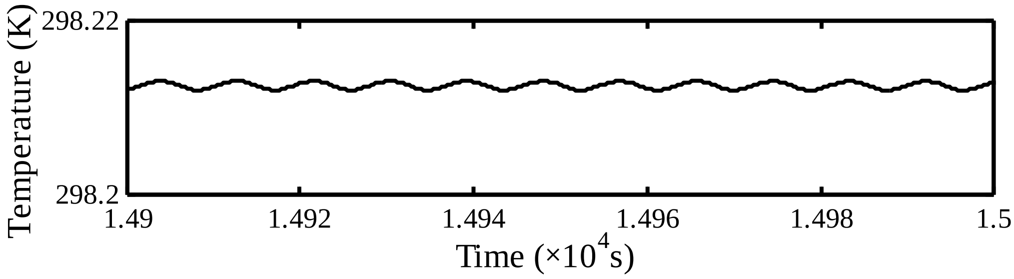

(b) At point (0.465 m, -0.004m)

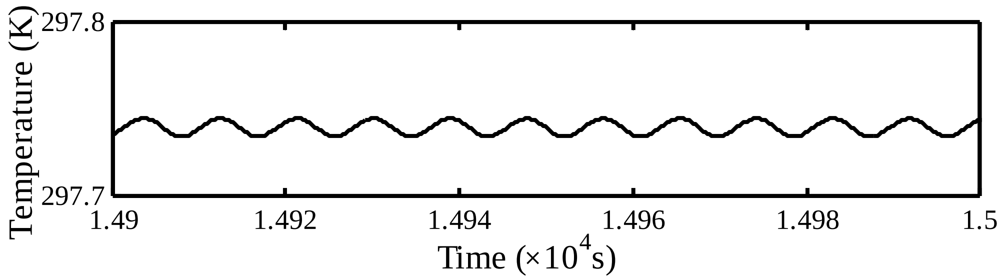

(c) At point (0.458 m, 0)

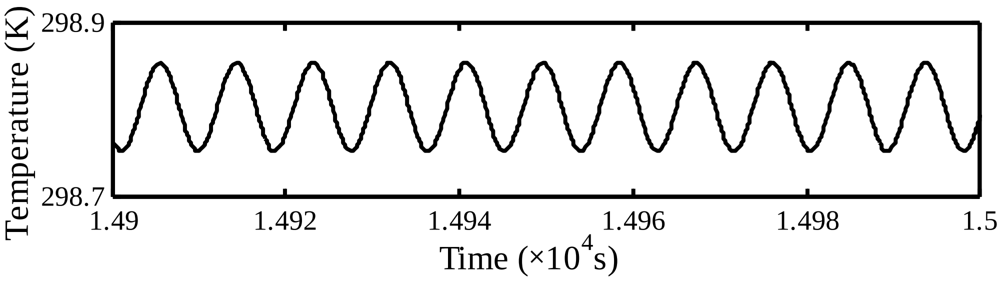

(d) At point (0.465 m, 0.004m)

Figure 7.25 Time series of the temperatures at different points around the tip of the thin fin

In addition to the temporal development of the waves of the thermal boundary layer, the spatial growth of the waves is also an important aspect, particularly around the thin fin. Figure 7.25(a) shows the locations of three points around the thin fin from

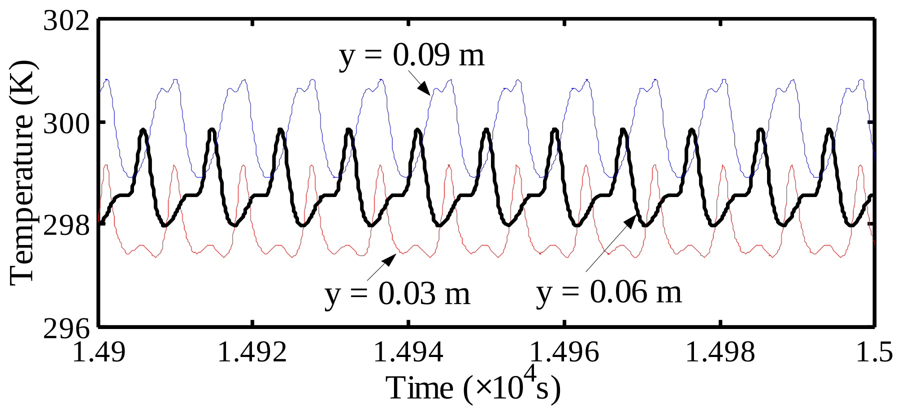

Figure 7.26 Time series of the temperatures at different heights (x = 0.498 m)

which temperature time series in the quasi-steady stage are taken and shown in Figures 7.25(b) to (d). Two of three points are symmetrically located about the fin, and the other near the fin tip (see Figure 7.25a). The flow around the thin fin moves through these points in the order of (b), (c) and (d). It is seen in Figure 7.25 that the amplitude of the waves grows from 0.001 K at Point (b) to 0.1 K at Point (d) (approximately 100 times) while the flow bypasses the thin fin; that is, the instability of the thermal flow around the thin fin significantly amplifies.

Figure 7.26 shows the time series of the temperatures at three heights in the thermal boundary layer at the downstream side of the fin, where the amplitude of the temperature waves grows from 1.8 K at y = 0.03 m to 1.9 K at y = 0.09 m with a total increase of 5%. Compared with the spatial growth near the thin fin, the amplitude growth of the temperature waves in the downstream thermal boundary layer is much smaller.

7.2.3 Heat transfer

As previously described, the thin fin significantly changes the flow and wave features of the thermal boundary layer. It is worth examining the implications of these changes to the heat transfer through the hot wall. Figure 7.27 shows the time series of the normalized difference of the heat transfer rate through the hot wall ($\hat{H}$ refer to Equation (7.1) for the definition). It is clear that $\hat{H}$ is positive for a significantly long period of time with a maximum value of 16% in the early time. This result implies that the oscillation of the thermal flow around the thin fin significantly improve the heat transfer through the hot wall. Figure 7.27 also indicates that, unlike the case with a smaller square fin (see Figure 7.11), $\hat{H}$ approaches zero from the positive side.

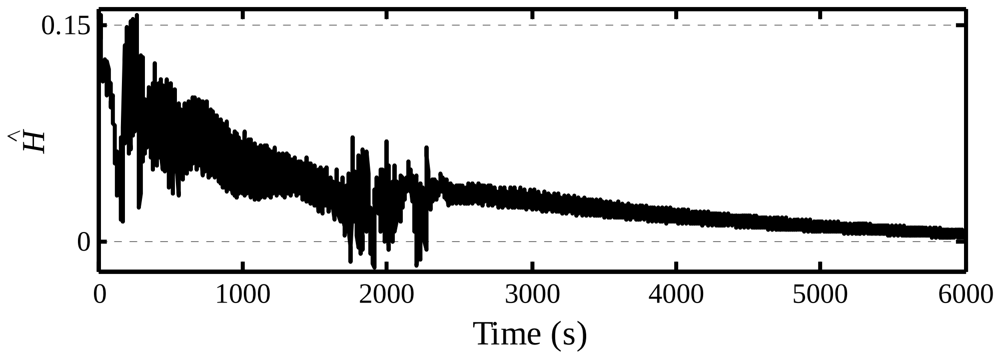

Figure 7.27 Time series of the normalized difference of the heat transfer rate through the hot wall between the cases with and without a thin fin

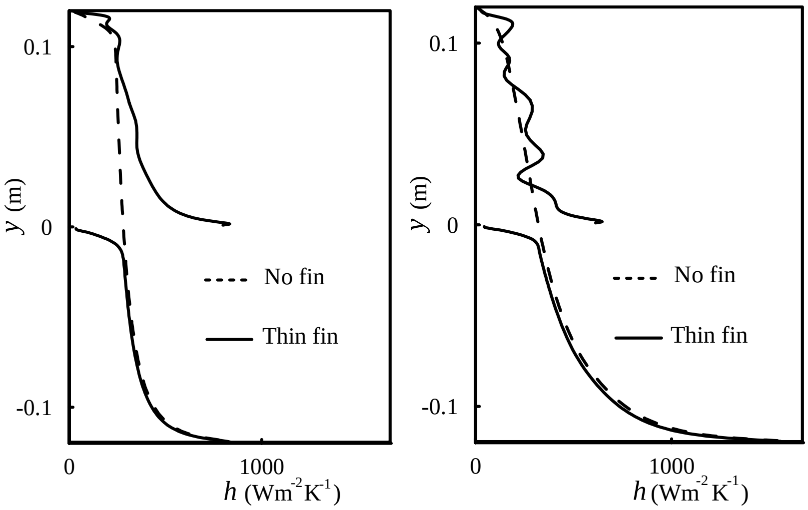

(a) t = 45 s (b) t = 6000 s

Figure 7.28 Local heat transfer coefficients of the hot wall with and without a thin fin

To illustrate the effects of the thin fin on the heat transfer through the hot wall, Figure 7.28 shows the profiles of the local heat transfer coefficients (h) along the hot wall with and without a thin fin at early and quasi-steady states, respectively. Similar to the case with a smaller square fin (see Figure 7.12), the profile of the local heat transfer coefficient in the upstream section of the hot wall with the thin fin is almost identical to that of the case without any fin. Distinct variations of the local heat transfer coefficients in the downstream section of the hot wall and in the vicinity of the fin between the cases with and without the thin fin are noticeable. In particular, in the early stage, the local heat transfer coefficients of the downstream section exhibit distinct variations between the cases with and without the thin fin. Different from the case with the square fin (see

Figure 7.12b), the downstream periodic flow results in a wavy profile of the local heat transfer coefficient in the quasi-steady stage, as seen Figure 7.28(b).

7.3 Effects of fin parameters

In Sections 7.1 and 7.2, the transient natural convection flows in a differentially heated cavity with a smaller square fin and a larger thin fin on the hot wall are numerically investigated respectively. The results have demonstrated that the flow and heat transfer for the two cases display significant variations, indicating that the fin parameter is critical for the transient natural convection flow in a differentially heated cavity. Since the larger thin fin may significantly change the transient natural convection flow in the cavity, further tests of different parameters of the thin fin including its dimension and position and the number of thin fins will be performed in this section.

7.3.1 Dimension of the fin

The numerical results obtained with a 40-mm-long thin fin are discussed and compared with the experiment in Section 7.2. In order to further examine the effects of the dimension of the thin fin on the transient natural convection in the differentially heated cavity, two additional cases with thin fins of 20 mm × 2 mm and 80 mm × 2 mm respectively are numerically simulated here.

Figure 29 plots the calculated time series of the temperatures at the point (0.498 m, 0.09 m) for the smaller thin fin of 20 mm × 2 mm (Figure 7.29a) and the larger thin fin of 80 mm × 2 mm (Figure 7.29b), respectively. For the case with the smaller fin, similar to that with the thin fin of 40 mm × 2 mm discussed in Section 7.2 (refer to Figure 7.20), the thermal boundary layer flow eventually approaches a periodic state, as seen in Figure 7.29(a). Figure 7.29(b) shows that for the case with the larger fin the amplitude of the temperature waves significantly reduces after 5800 s (also see Figure 7.32 for detailed discussion), and the thermal boundary layer also eventually approaches a random wave state (see a zoom in Figure 7.29b) although the amplitude is very small.

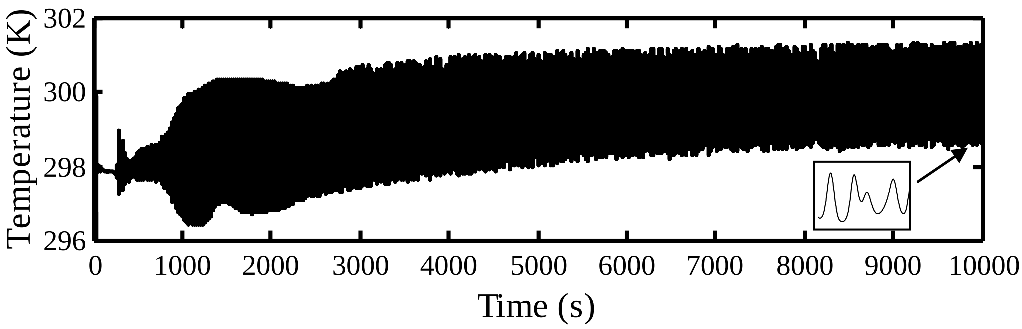

(a) For the case with a fin of 20 × 2 mm^2

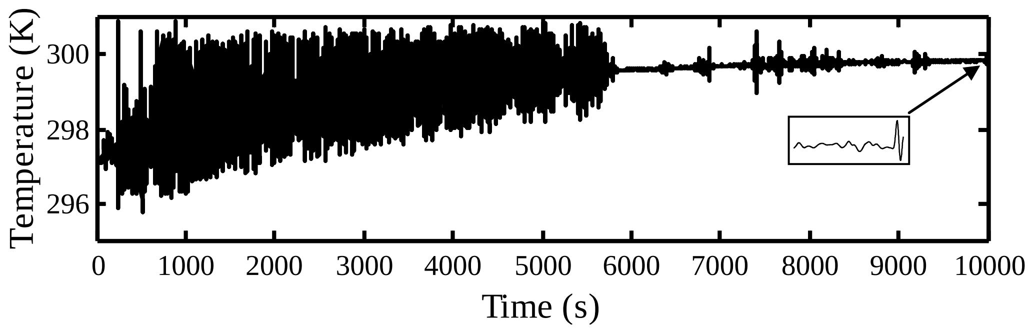

(b) For the case with a fin of 80 × 2 mm^2

Figure 7.29 Time series of the temperatures at the point (0.498 m, 0.09 m)

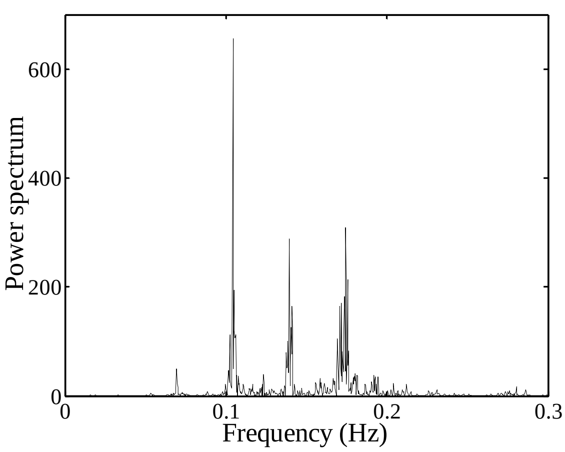

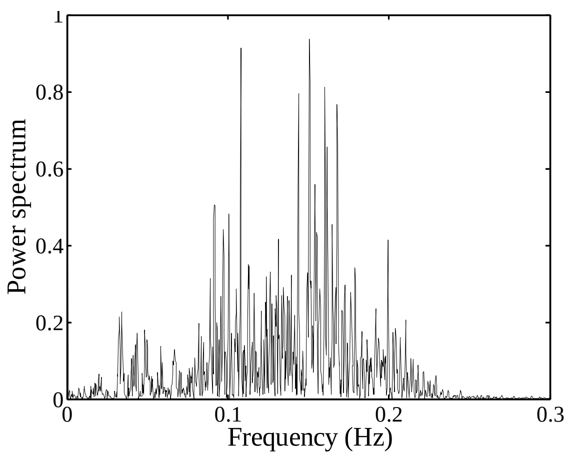

(a) For the case with a fin of 20 × 2 mm^2 (b) For the case with a fin of 80 × 2 mm^2

Figure 7.30 Spectra of the temperature time series at the point (0.498 m, 0.09 m)

Figure 7.30 shows the spectra of the temperature time series in the quasi-steady stage shown in Figure 7.29. For the case with the smaller fin, Figure 7.30(a) indicates that the wave mode has a dominant frequency of f = 0.103 Hz with two additional higher frequencies of 0.14 and 0.175 Hz. However, for the case with the larger fin, the spectrum in Figure 7.30 (b) indicates that, besides a distinct frequency of f = 0.108 Hz, a

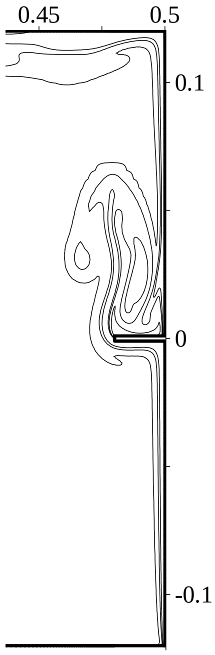

(a) For the case with a fin of 20 × 2 mm^2 at t = 24 s

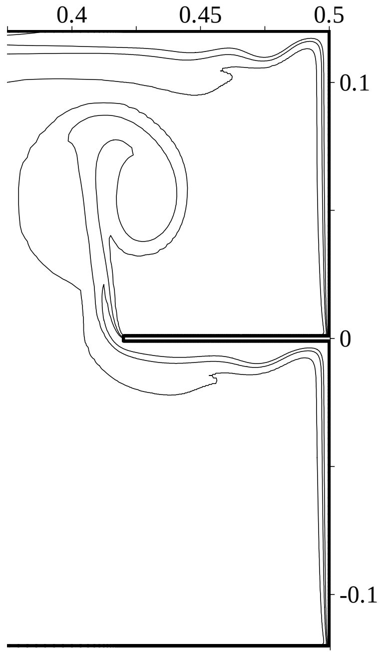

(b) For the case with a fin of 80 × 2 mm^2 at t = 48 s

Figure 7.31 Lower intrusion fronts bypassing the thin fin (isotherms of 296.56, 296 and 297 K)

number of additional higher frequency modes may be observed around f_1 = 0.15 Hz and random.

As indicated in Figures 7.29 and 7.30, the dimension of the thin fin has a clear impact on the temperature wave features. The variations of the temperature wave features are associated with the variations of the thermal boundary layer flow between the cases with different fins.

In order to illustrate the flow features of the thermal boundary layer, Figure 7.31 shows the lower intrusion fronts bypassing the thin fin in the early stage. For the case with the smaller fin, since the lower intrusion front is closer to the hot wall after it bypasses the thin fin, reattachment of the lower intrusion front to the downstream wall occurs immediately after bypassing (Figure 7.31a). The reattachment is similar to the case with the square fin discussed in Section 7.1 (refer to Figure 7.2d), and the early wave features of the temperature series show few variations from those with the square fin. However, for the case with the larger fin, Figure 7.31(b) displays that the development of the lower intrusion front is quite different from that with the smaller fin. In this case, the lower intrusion front moves directly upwards rather than reattaches to the hot wall after bypassing the fin. The development of the lower intrusion front and

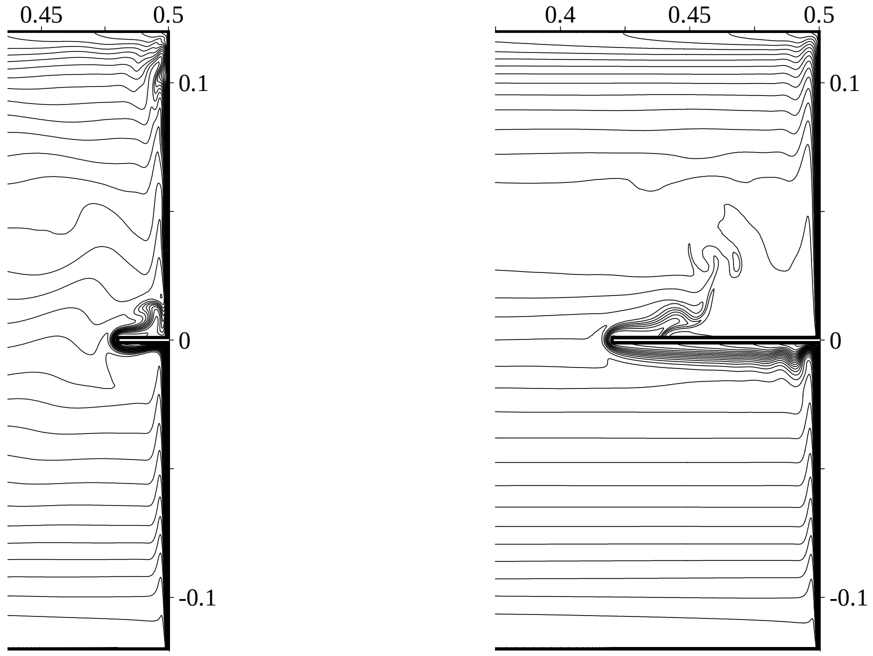

(a) For the case with a fin of 20 × 2 mm^2 (b) For the case with a fin of 80 × 2 mm^2

Figure 7.32 Flows in the vicinity of the hot wall at t = 6000 s (isotherms from 287.94 to 303.16 K with an interval of 0.39 K)

the wave features of the thermal boundary layer in the early stage are similar to the case with the thin fin of 40 mm × 2 mm discussed in Section 7.2 (see Figure 7.13f). Eventually the lower intrusion front strikes the intrusion under the ceiling. Due to the different dimensions of the thin fins, the time it takes for the lower intrusion front to bypass the fin is evidently different.

Figure 7.32 shows the flows in the vicinity of the hot wall in the quasi-steady stage. The isotherms in Figure 7.32(a) indicate that, although the thin fin of 20 × 2 mm^2 is smaller than the other, separation of the flow around the thin fin still occurs. The oscillation of the shedding flow disturbs the thermal boundary layer, which eventually approaches a periodic flow as shown in Figure 7.29(a). For the thin fin of 80 × 2 mm^2, since the position of the flow separation from the thin fin is further away from the hot wall, the shedding flow has less impact on the thermal boundary layer, as seen in Figure 7.32(b). As time increases, the position of separation moves further away from the hot wall. Once the distance between the position of the separation and the hot wall is greater than a critical value, the perturbations to the thermal boundary layer induced by the shedding flow become very weak as seen in Figure 7.29(b). This explains why the amplitude of the temperature waves significantly reduces after approximately 5800 s.

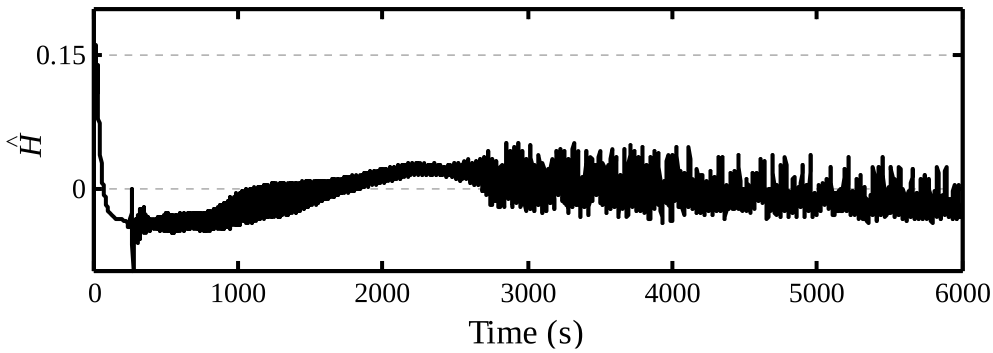

(a) For the case with a fin of 20 × 2 mm^2

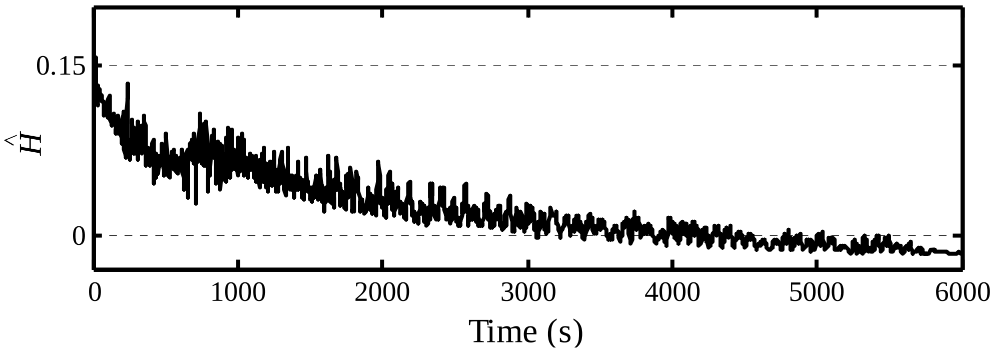

(b) For the case with a fin of 80 × 2 mm^2

Figure 7.33 Normalized difference of the heat transfer rate of the hot wall between the cases with and without a thin fin against time

Figure 7.33 shows the calculated normalized difference of the heat transfer rate through the hot wall against time. For the case with the smaller fin, although the heat transfer is significantly enhanced by up to 16% in the earlier stage, it rapidly reduces below zero and eventually oscillates around zero at the quasi-steady state, as seen in Figure 7.33(a). Figure 7.33(b) indicates that, for the case with the larger fin, the enhancement of the heat transfer, likewise, reaches 16%, but the heat transfer rate through the hot wall slowly decreases with time. The normalized difference of the heat transfer rate becomes negative after approximately 4000 s. Compared with the case with the thin fin of 40 × 2 mm^2 (see Figure 7.27), the heat transfer through the hot wall is less improved by the two fins examined here. This suggests that the dimension of the thin fin has an optimal value in terms of the enhancement of the heat transfer through the hot wall. In order to obtain such an optimal value, a great number of computational cases need to be performed. However, this is out of the scope of this thesis, and thus is not further discussed.

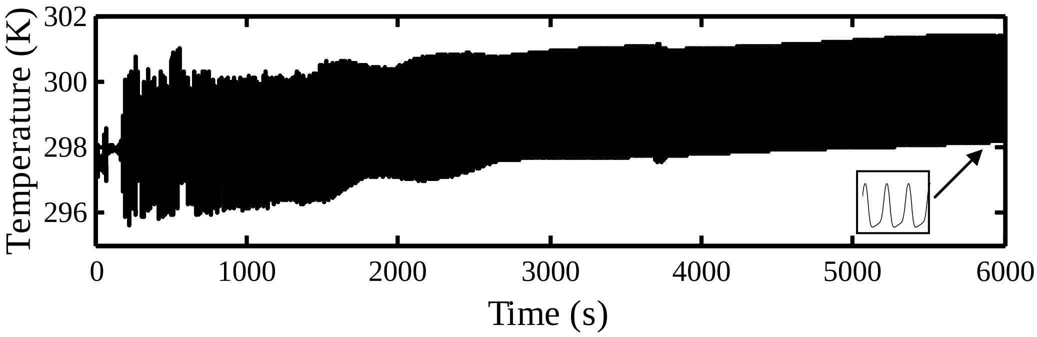

(a) Linear time scale

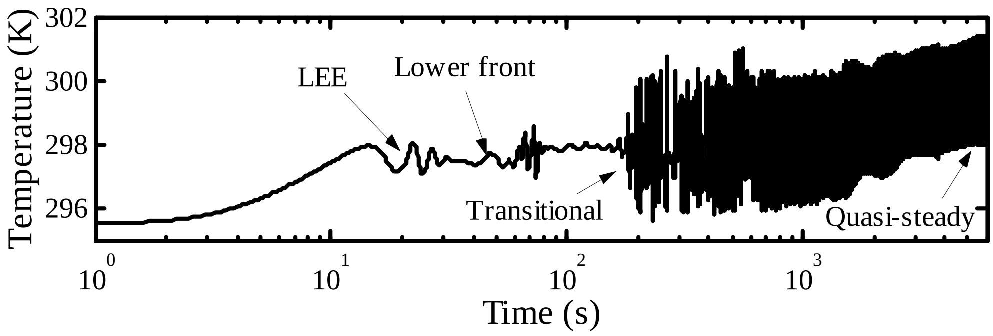

(b) Logarithmic time scale

Figure 7.34 Time series of the temperature at the point (0.498 m, 0.09 m)

7.3.2 Position of the fin

The numerical results in the previous section with different thin fins have demonstrated that the dimension of the thin fin plays an important role in the transient natural convection in a differentially heated cavity. It is worth noting that, in all the above discussions, the fins are placed at the mid height of the hot wall. In this section, the effect of the position of the thin fin on the flow development and heat transfer is investigated by placing a thin fin of 40 × 2 mm^2 at y = -0.06 m (further upstream compared with the previously examined cases).

Figure 7.34 shows a time series of the temperature obtained at the point (0.498 m, 0.09 m) on both linear and logarithmic time scales. Compared with the case with the same fin placed at the mid height of the hot wall (see Figure 7.20), the amplitude of the temperature waves in the quasi-steady stage is greater, as seen in Figure 7.34(a). Moreover, variations of the early-stage flow features between the two cases are also clear. Due to an increased distance between the thin fin and the point where the temperature is monitored in the present case, a complete set of the traveling waves

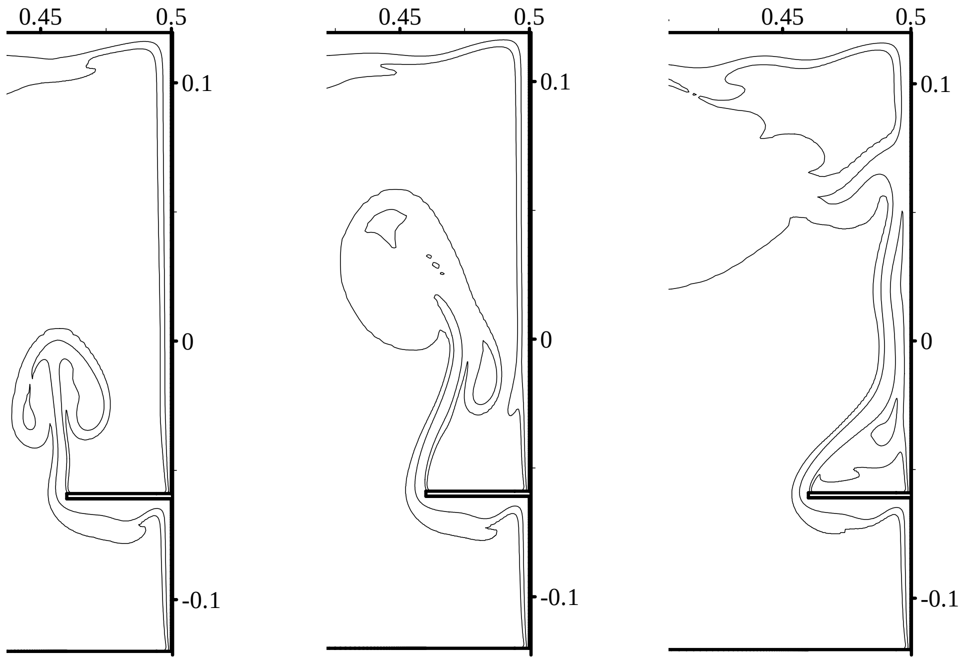

(a) t = 34 s (b) t = 44 s (c) t = 64 s

Figure 7.35 Development of the lower intrusion front in the early stage (isotherms: 296.56 and 296 K)

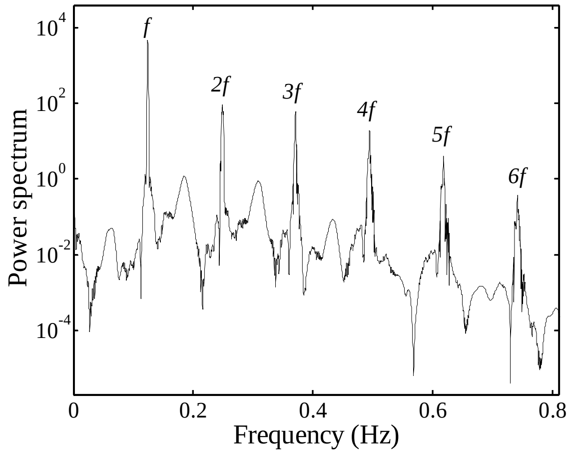

Figure 7.36 Spectrum of the temperature time series at the point (0.498 m, 0.09m)

associated with the propagation of the LEE is observed in Figure 7.34(b). The lower intrusion front is seen to arrive at this point after the passage of the LEE.

In the present case with the thin fin placed at a lower position, the lower intrusion front reattaches to the downstream thermal boundary layer, as shown in Figure 7.35. As a consequence, strong instability of the thermal boundary layer in the early stage is induced (also see Figure 7.34).

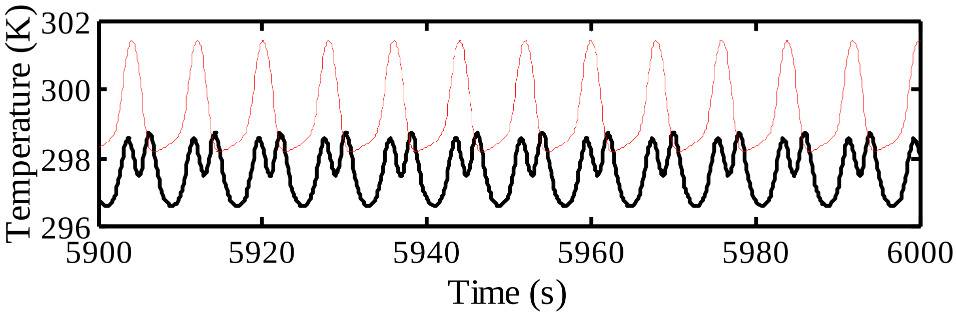

Figure 7.37 Time series of the temperatures at the points (0.498 m, 0.09 m, the dashed line) and (0.498 m, 0 m, the solid line)

The spectrum corresponding to the temperature time series in Figure 7.34 is shown in Figure 7.36. A distinct peak is seen at f = 0.122 Hz, which is evidently a dominant frequency mode. Additional harmonics modes are also seen in Figure 7.36.

In order to observe the spatial propagation of the traveling waves in the quasi-steady stage, Figure 7.37 shows time series of the temperatures at different heights along the thermal boundary layer. An interesting phenomenon shown in this figure is that the temperature waves have two distinct peaks at the lower (upstream) position but only a single peak at the higher (downstream) position.

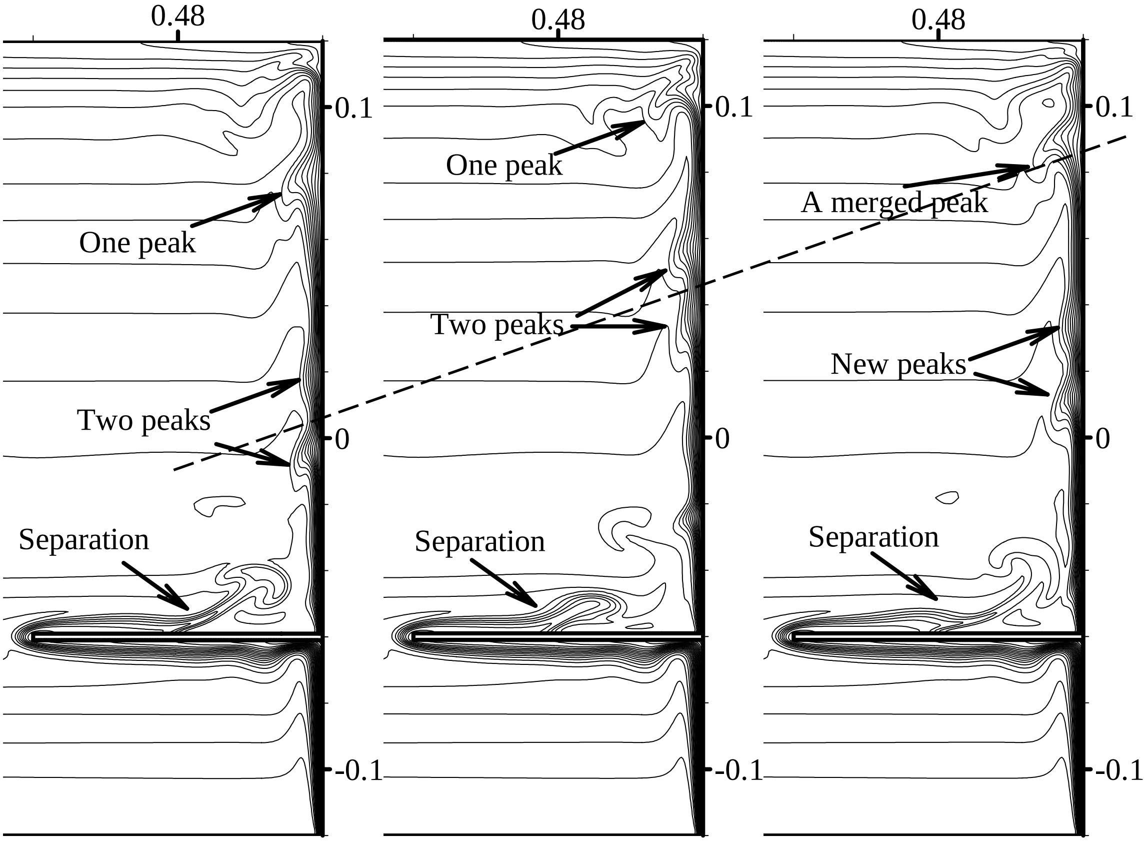

(a) t = 5910 s (b) t = 5915 s (c) t = 5920 s

Figure 7.38 Traveling waves (isotherms from 287.55 to 303.55 K with an interval of 0.41 K)

For the purpose of illustrating the two peak behaviors, Figure 7.38 shows the isotherms in the vicinity of the hot wall at different times in the quasi-steady stage. The shedding flow separating from the fin first induces a two-peak wave, and the two peaks eventually merges into a single one while they propagate downstream, as indicated by the dashed line in Figure 7.38.

As indicated in Figure 7.34, the thin fin at the lower position induces stronger temperature waves, which in turn affects the heat transfer through the hot wall. Figure 7.39 plots the normalized difference of the heat transfer rate through the hot wall against time. The enhancement of the heat transfer by the thin fin at a lower position reaches 17% at the early stage, and persists for a long time approximately at 3% (until 6000 s). Compared with the case with a thin fin at the middle height (also see Figure 7.27), the fin at a lower position obtains a better improvement in enhancing the heat transfer through the finned sidewall.

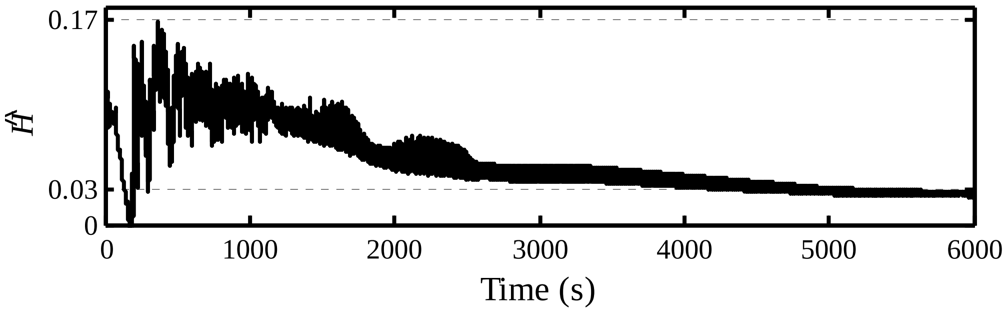

Figure 7.39 Normalized difference of the heat transfer rate of the hot sidewall between the cases with and without a thin fin against time

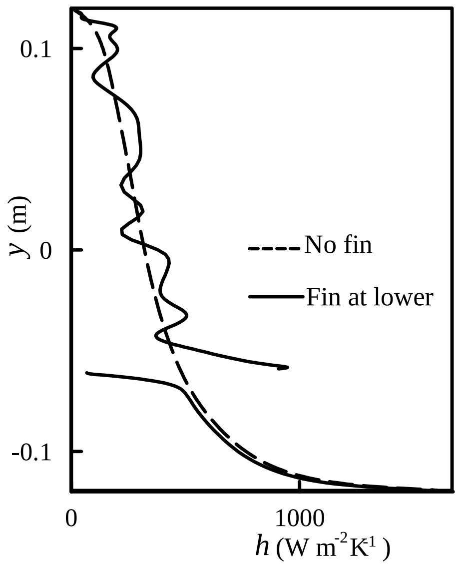

Figure 7.40 Heat transfer coefficient of the hot wall at t = 6000 s

Figure 7.40 shows the local heat transfer coefficients along the hot wall in the quasi-steady stage. Since the thin fin is at a lower position, the downstream section of the thermal boundary layer behind the thin fin is significantly increased, and the perturbations induced by the oscillation of the thermal flow around the thin fin have more room to grow. As a consequence, the heat transfer through the entire hot wall is noticeably enhanced. In summary, compared with other cases, a thin fin at the lower position (upstream) shows a promising result for the enhancement of the heat transfer through a differentially heated cavity.

7.3.3 Three fins on the sidewall

The effects of the fin parameters including the dimension of the fin and its position along the hot wall have been discussed in the previous sections. In this section, another

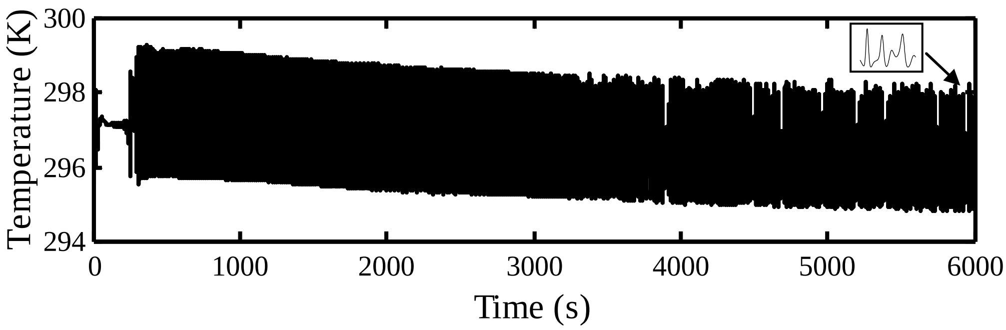

(a) y = -0.03 m

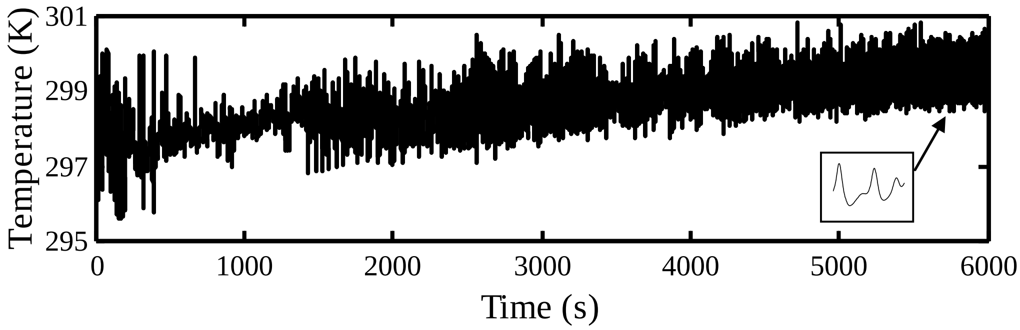

(b) y = 0.03 m

Figure 7.41 Time series of the temperatures at different heights (x = 0.498 m)

important parameter, the number of fins on the hot wall, is also numerically investigated.

Here, three identical thin fins of the same dimensions (20×2 mm^2) evenly distributed along the wall with a spatial interval of 0.058 m between two neighbouring fins and a distance of 0.059 m between the fin and the horizontal wall are considered. Figure 7.41 shows the time series of the temperatures obtained at different heights. The temperature in Figure 7.41(a) is taken at the downstream side of the lowest fin; and the temperature in Figure 7.41(b) is taken at the downstream side of the middle fin. It is clear in Figure 7.41 that the temperature waves behind the lowest thin fin are stronger than those behind the fin at the higher position.

Figure 7.42 shows the corresponding spectra of the above temperature series in the quasi-steady stage. Figure 7.42(a) indicates that the temperature waves on the leeward side of the lowest thin fin have a clear dominant frequency of f = 0.112 Hz with additional higher frequency modes. For the temperature waves on the downstream side of the thin fin at the higher position, the dominant frequency is approximately at f = 0.11 Hz, which is almost the same as that in the case with the fin at the lower position, indicating that the perturbations from the upstream fin are carried downstream to the

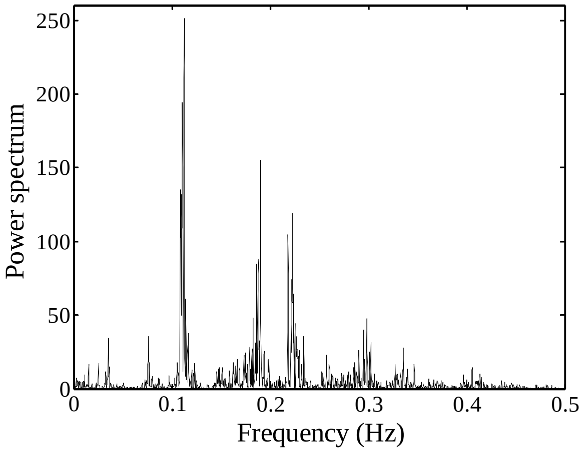

(a) At point (0.498 m, -0.03 m)   (b) At point (0.498 m, 0.03 m)

Figure 7.42 Spectra of the temperature time series at different heights

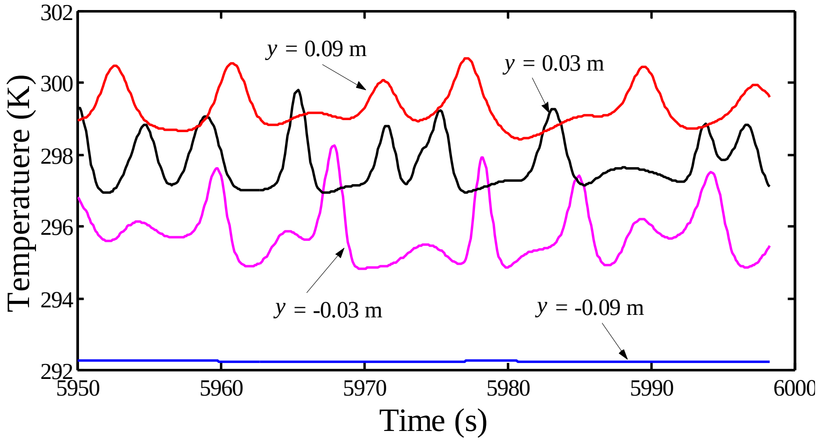

Figure 7.43 Time series of the temperatures at different heights

current location. However, the additional frequency modes at this location are evidently different from that at the lower position.

In order to observe the spatial evolution of the temperature waves in the thermal boundary layer, the time series of the temperatures obtained at different heights in the quasi-steady stage are plotted in Figure 7.43. Since the temperature fluctuation at the upstream side of the lowest fin is much weaker than that at the downstream side of the lowest fin, the wave feature of the temperature signal at the upstream side of the lowest fin cannot be seen clearly when the temperatures obtained at all the locations are plotted on the same scale (the temperature at the lowest position is shown as a straight line in Figure 7.43). It is seen in Figure 7.43 that, apart from the upstream point of the lowest fin, the amplitude of the temperature fluctuations decreases slightly as the monitoring position moves from upstream to downstream. This is different from those in the other

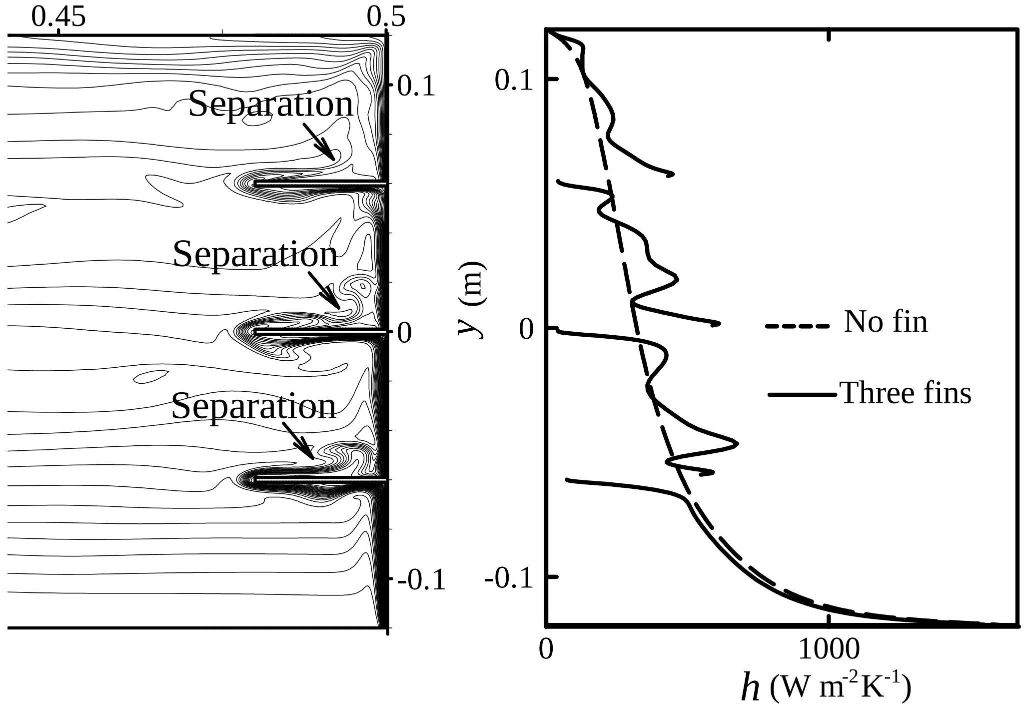

(a) Isotherms (b) Heat transfer coefficient

Figure 7.44 Flow and heat transfer at t = 6000 s (isotherm contours: from 287.55 to 303.55 K with an interval of 0.4 K)

cases with a single fin (see e.g. Figure 7.26) in which the amplitude of traveling waves increases when they propagate on the downstream side of the fin.

Figure 7.44(a) shows the flows in the vicinity of the hot wall in the quasi-steady stage, in which separations of the thermal flow around the thin fins are clear, similar to that of the thermal flow around a single thin fin. Oscillations of the thermal flow separating from the fins trigger the downstream instability of the thermal boundary layer flows, and result in increasing convection flow on the downstream side of the fins. The effect of the increasing convection flow on the local heat transfer coefficient is plotted in Figure 44(b). It is clear that the local heat transfer coefficient on the downstream sides of the fins is greater than that without the fins (the dashed line), implying that the local heat transfer through the hot finned sidewall is enhanced at this time.

Figure 7.45 plots the normalized difference of the heat transfer rate through the hot wall against time. It is clear in this figure that the heat transfer is enhanced by as much as 33% in the initial stage. Compared with the case with a single fin placed at the middle of the hot wall (see Figure 7.33a), the present three-fin configuration produces an improved result in terms of the heat transfer through the hot wall. The enhancement

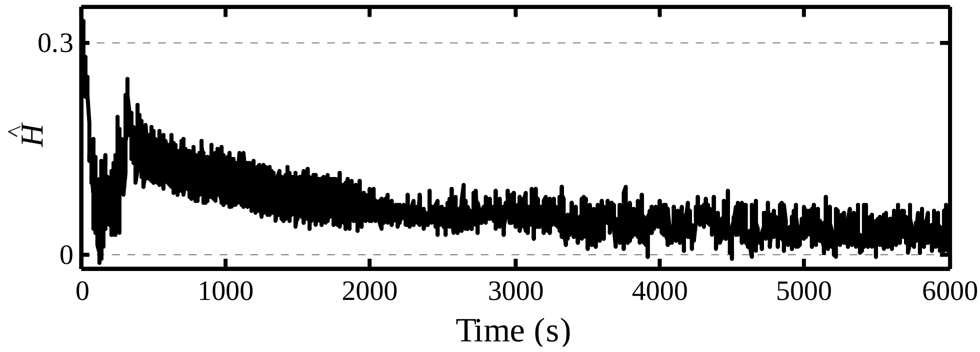

Figure 7.45 Normalized difference of the heat transfer rate of the hot sidewall between the cases with and without a thin fin against time

of the heat transfer through the hot wall here is similar to that in the case of a single fin at the lower position (see Figure 7.39) in the quasi-steady stage.

7.4 Summary

In this chapter, the natural convection flows in a suddenly differently heated cavity with one and three fins placed on the hot wall are numerically simulated. Comparisons between the cases with and without a fin on the hot sidewall indicate that the flows and heat transfer properties are altered by the presence of the fin(s), particularly in the initial stage. The fin, in some sense, blocks the upstream flow and forces it to detach from the hot sidewall. Since the fin parameters are critical for the transient natural convection flow in the cavity, different dimensions, positions and numbers of fin(s) on the hot sidewall have been investigated.

For the case with a small square fin, the numerical flow is consistent with the corresponding flow visualization. Both the experimental and numerical results have shown that, due to the entrainment of the thermal boundary layer, the detached lower intrusion flow reattaches to the downstream thermal boundary layer after it bypasses the fin. The numerical simulation also demonstrates that a double-circulation flow structure arises in the transition of the thermal boundary layer. It is found that the square fin significantly changes not only the flow structures of the thermal boundary layer, but also the heat transfer through the hot sidewall in the early stage.

For the case with a larger thin fin, likewise, there are good agreements between the numerical simulation and experimental visualization. Both the experiment and simulation demonstrate that the lower intrusion front does not reattach to the downstream thermal boundary layer immediately after bypassing the thin fin as it does in the case with the square fin. Instead, it moves directly upwards and strikes the intrusion under the ceiling. In this case, the larger thin fin induces strong perturbations to the thermal boundary layer flow. As a consequence, a periodic flow forms at the quasi-steady stage. Accordingly, the heat transfer through the hot wall is enhanced significantly.

Further numerical investigations indicate that the fin parameters, including its dimension and position and the number of fins, apparently impact on the transient flows and heat transfer. For the case with a single fin placed at the middle of the hot wall, the present numerical results show that there is an optimal length of the thin fin in terms of enhancing the heat transfer. It is also demonstrated that a thin fin placed at a lower position on the hot wall can achieve a better result for the enhancement of the heat transfer. The numerical simulation has also suggested that the heat transfer through the hot wall can be further enhanced by placing multiple fins along the wall compared with that in the case of a single fin at the mid height of the sidewall.

Since this thesis focuses on the fundamental aspects of the differentially heated cavity, some details involving the optimal design parameters for the fin in terms of enhancing heat transfer are not fully resolved here. Despite this imperfection, the numerical results presented in this chapter have significant implications to industrial applications.

8 Conclusions

In this thesis, numerical, experimental and theoretical analyses are employed to investigate transient natural convection in a differentially heated cavity with and without a fin on the sidewall. The emphasis is on the flows in the vicinity of the hot sidewall and around the fin. The transition of the flows from the start-up to a quasi-steady state is numerically and experimentally described, and the transient features of flows are discussed. All the experimental and numerical results presented in this thesis are obtained within a relatively small range of Rayleigh numbers (approximately of the order of 10^9), which are typical Rayleigh numbers in the transitional flow regime. The major findings from the present study are summarized in this chapter, and recommendations for future investigations are also made at the end of this chapter.

8.1 Summary of the present study

8.1.1 Transient natural convection without a fin

The present experimental and numerical results have demonstrated that the transition of the natural convection flow in a differentially heated cavity from the start-up to the quasi-steady state may be classified into three stages, an initial stage, a transitional stage and a quasi-steady stage, based on kinematical features.

In the initial stage, there are two noticeable features: the growth of the thermal boundary layer and the LEE. As described by Patterson and Imberger (1980), the initial growth of the thermal boundary layer is dominated by conduction. The present experimental results confirm the scaling analysis of Patterson and Imberger (1980); that is, the growth of the thickness of the thermal boundary layer is according to the scale of $(\kappa t)^{1/2}$.

The present experimental and numerical results characterize the LEE well. Further discussion of the numerical results indicates that the LEE phenomenon is an interaction between temperature, pressure and velocities. In particular, the pressure perturbations play a key role in the generation and propagation of the LEE. Furthermore, it is confirmed by the present numerical results that the pressure minimum may propagate downstream at the speed which is linearly dependent on time (Figure 5.7). The further discussion of the components of the energy equation demonstrates that the deviation of the numerical solution from the theoretical solution (Goldstein & Briggs 1964) is because the theoretical solution neglects the convection terms.

After the LEE phenomenon, the transition of the natural convection flow in the cavity enters the transitional stage. An important feature of the flow at this stage is the separation of the intrusion from the ceiling and the formation of trailing waves. The mechanism responsible for the separation has been discussed in this thesis, and it is suggested that the vertical pressure gradient induced by the entrainment of the vertical thermal boundary layer is responsible for the separation.

In the subsequent development of the flow, the intrusion triggers instability of the thermal boundary layer adjacent to the opposite (cold) wall when it strikes the opposite wall. The accumulation of the hot fluid carried across the cavity by the intrusion in the opposite corner results in a reverse flow, which moves back toward the hot sidewall and may trigger instability of the flow discharged from the upper end of the vertical thermal boundary layer. Ultimately a cavity-scale oscillation between the two sidewalls forms, and this oscillation dissipates rapidly with time.

The experimental shadowgraph images show that two bright strips appear outside the thermal boundary layer near the top and bottom corners respectively after the intrusion from the opposing side strikes the sidewall. It is confirmed by the numerical simulation that the two bright strips correspond to the minima of the second derivative of the temperature. Both the experimental and numerical results indicate that the two bright strips outside the thermal boundary layer extend toward the middle of the sidewall and meet there, initially with some misalignment but eventually being aligned with each other to form a single bright strip. According to the present shadowgraph observation and the corresponding numerical simulation, the outer and inner bright strips represent a double-layer structure adjacent to the sidewall.

Following the formation of the double-layer structure of the thermal boundary layer, the flow transition enters the quasi-steady stage. The numerical results indicate that the stratification of the interior fluid in the cavity results in a non-monotonic horizontal temperature profile near the hot sidewall, which is related to the double-layer structure. Further discussion concerning the double-layer structure reveals that there are opposing thermal diffusions in the vicinity of the sidewall, directing to the minimum of the temperature profile.

The present shadowgraph observations and direct temperature measurements show that there exist the traveling waves in the thermal boundary layer in the quasi-steady stage. These waves are associated with a convective instability of the thermal boundary layer, and have the same frequency as those induced by the LEE in the initial stage. The amplitude of the traveling waves increases as the stratification of the interior fluid in the cavity is enforced.

8.1.2 Transient natural convection with a fin

For the purpose of controlling the heat transfer through the sidewall, the problem of transient natural convection in a differentially heated cavity with a fin placed on the heated sidewall has been investigated in this thesis. It is demonstrated that the fin may significantly change the transient natural convection flow and in turn enhance or depress the transient heat transfer through the sidewall. Similarly, the transition of the natural convection flow from the start-up to the quasi-steady state may be classified into three stages: an initial stage, a transitional stage and a quasi-steady stage.

In the initial stage, the development of the thermal boundary layer with a fin is different from that without a fin if the fin is sufficiently large. Both experimental and numerical results have demonstrated that, initially, a lower intrusion front forms under the fin. The lower intrusion front eventually bypasses the fin, and the subsequent evolution of the lower intrusion front depends on the dimension of the fin. For the case with a smaller square fin, the lower intrusion front reattaches to the downstream thermal boundary layer, and the interaction between the thermal boundary layer flow and the lower intrusion front leads to the breakdown of the lower intrusion front and strong mixing in the downstream thermal boundary layer. However, for the case with a larger thin fin, the lower intrusion front moves directly upwards and strikes the intrusion under the ceiling. Subsequently, the trailing flow following the lower intrusion front is entrained into the downstream thermal boundary layer. Due to the strong perturbations associated with the lower intrusion front, the early-stage separation and trailing waves of the intrusion under the ceiling disappear in both the above-mentioned cases. Clearly, the lower intrusion front enforces the convection in the downstream thermal boundary layer and significantly enhances the heat transfer through the sidewall (by up to 33% for some computed cases in the thesis).

After the perturbations associated with the lower intrusion front are convected away, the development of the thermal boundary layer flow enters a transitional stage. In this stage, the flow transition exhibits distinct variations between the cases with different fins. The present numerical and experimental results indicate that, for the case with the smaller square fin, the subsequent development of the thermal boundary layer is similar to that of the case without a fin. However, for the case with the larger thin fin, the thermal flow around the fin separates from the fin and oscillates, which in turn triggers instability of the downstream thermal boundary layer flow. It is demonstrated that the evolution of the thermal boundary layer flow in the transitional stage is apparently dependent on the dimension of the fin.

The numerical and experimental results have also demonstrated that different dimensions of the fin may result in different properties of the thermal boundary layer flow in the quasi-steady stage. For the case with the smaller square fin, the flow in the quasi-steady stage is similar to that without a fin. For the case with the larger thin fin, the quasi-steady state flow becomes periodic. The numerically calculated frequencies of the quasi-steady state oscillations of the flow around the thin fin and the instability of the downstream thermal boundary layer flow are consistent with those measured in the experiments. During the transition from the start-up to the quasi-steady state, the perturbations induced by the thin fin enforce the convection of the downstream thermal boundary layer and in turn, enhance the heat transfer through the sidewall.

In order to obtain further insights into the effects of the fin parameters on the transient natural convection and heat transfer through the differentially heated cavity, the effects of the dimension, position and number of the fins are numerically investigated in this thesis. The numerical results of different fin dimensions indicate that there may exist an optimal dimension of the fin for the purposes of either enhancing or depressing the heat transfer through the sidewall. Furthermore, it is revealed that the transient natural convection and heat transfer are sensitive to the position of the fin. The numerical results show that the heat transfer through the sidewall may be enhanced more if the thin fin is placed at a lower position. The present numerical results have also shown that the transient natural convection and heat transfer for the case with three fins on the sidewall are different from those with a single fin.

In summary, the experiments and numerical simulations in this thesis have demonstrated that one or more fins on the sidewall may play an important role in controlling the transient natural convection and heat transfer through a differentially heated cavity in the present Rayleigh number range (the order of 10^9).

8.2 Topics for future studies

Although significant progress regarding the transient natural convection and heat transfer in a differentially heated cavity has been achieved in this thesis, several new research topics have been motivated by the present study, and are worth investigating in future studies.

First of all, the discrepancies between the experiment and numerical simulation of the present study for the case without a fin suggest that the convective instability of the thermal boundary layer flow is worth further studying. In particular, comparisons between the stability analysis of the quasi-steady state thermal boundary layer and the corresponding experiments are desirable. Although a stability analysis of the thermal boundary layer flow adjacent to a flat plate in a stratified ambient was reported by Tao and Le Quere (2003), the distinction between the thermal flows adjacent to a flat plate and in a differentially heated cavity, and the correlations between the thermal boundary layer instability and the stratification of the interior fluid in the cavity need to be further investigated.

Secondly, although numerical results concerning several fin parameters including the dimension, position and number of the fins have been obtained in the present study, it is worthwhile to determine an optimal configuration of the fin in terms of enhancing or depressing the heat transfer through the differentially heated cavity. This investigation is particularly important for many industrial designs and applications.

Finally, due to the limitations of the experimental model, the experimental results of the present study are obtained within only a small range of the Rayleigh numbers for both cases with and without a fin, and the numerical simulations have also been conducted within the same range of the Rayleigh numbers. From the engineering application point of view, it is necessary to extend the experiments and numerical simulations to cover a broader range of the Rayleigh numbers, in particular, the Rayleigh numbers above 10^{10}.

Appendix

i^2erfc = complementary error function integrated two times, defined as follows (also see Goldstein & Briggs 1964),

$$i^2 erfc(\eta) = \int_\eta^\infty i^1 erfc(\zeta) d\zeta = \int_\eta^\infty \int_\zeta^\infty i^0 erfc(\xi) d\xi d\zeta$$

$$i^0 erfc(\eta) = \frac{2}{\sqrt{\pi}} \int_\eta^\infty e^{-\zeta^2} d\zeta$$

References

Ampofo, F 2004, ‘Turbulent natural convection in an air filled partitioned square cavity’, *Int. J. Heat and Fluid Flow*, vol. 25, pp. 103-114.

Ampofo, F 2005, ‘Turbulent natural convection of air in a non-partitioned or partitioned cavity with differentially heated vertical and conducting horizontal walls’, *Exp. Therm. Fluid Sci.*, vol. 29, pp. 94-106.

Armfield, SW & Janssen, RJA 1996, ‘A direct boundary-layer stability analysis of steady-state cavity convection flow’, *Int. J. Heat Fluid Flow*, vol. 17, pp. 539-546.

Armfield, SW & Patterson, JC 1991, ‘Direct simulation of wave interactions in unsteady natural convection in a cavity’, *Int. J. Heat Mass Transfer*, vol. 34, pp. 929-940.

Armfield, SW & Patterson, JC 1992, ‘Wave properties of natural-convection boundary layers’, *J. Fluid Mech.*, vol. 239, pp. 195-211.

Armfield, SW & Patterson, JC 2000, ‘Start-up flow on a vertical semi-infinite heated plate’, *Proc. 7th Australasian Heat and Mass Transfer*, Townsville, pp. 37-43.

Bae, JH, Hyun, JM & Kwak HS 2001, ‘Buoyant convection in a cavity with a baffle under time-periodic wall temperature’, *Numer. Heat Transfer*, Part A, vol. 39, pp. 723-736.

Bajorek, SM & Lloyd, JR 1982, ‘Experimental investigation of natural convection in partitioned enclosures’, *J. Heat Transfer*, vol. 104, pp. 527-532.

Batchelor, GK 1954, ‘Heat transfer by free convection across a closed cavity between vertical boundaries at different temperatures’, *Quart. Appl. Math.*, vol. 12, pp. 209-233.

Bejan, A 1983, ‘Natural convection heat transfer in a porous layer with internal flow obstructions’, *Int. J. Heat Mass Transfer*, vol. 26, pp. 815-822.

Bertolotti, FP, Herbert, T & Spalart, PR 1992, ‘Linear and nonlinear stability of the Blasius boundary layer’, *J. Fluid Mech.*, vol. 242, pp. 441-474.

Bilgen, E (2002), ‘Natural convection in enclosures with partial partitions’, *Renewable Energy*, vol. 26, pp. 257-270.

Bilgen, E 2005, ‘Natural convection in cavities with a thin fin on the hot wall’, *Int. J. Heat Mass Transfer*, vol. 48, pp. 3493-3505.

Bodenschatz, E, Pesch, W & Ahlers, G 2000, 'Recent developments in Rayleigh-Bénard convection', *Annu. Rev. Fluid Mech.*, vol. 32, pp. 709-778.

Brassington, GB, Patterson, JC & Lee, M 2002, 'A new algorithm for analysing shadowgraph images', *J. Flow Visualization & Image Processing*, vol 9, pp. 25-51.

Brooker, AMH, Patterson, JC & Armfeld, SW 1997, 'Non-parallel linear stability analysis of the vertical boundary layer in a differentially heated cavity', *J. Fluid Mech.*, vol. 352, pp. 265-281.

Brooker, AMH, Patterson, JC, Graham, T & Schöpf, W 2000, 'Convective instability in a time-dependent buoyancy driven boundary layer', *Int. J. Heat Mass Transfer*, vol. 43, pp. 297-310.

Brown, SN & Riley, N 1973, 'Flow past a suddenly heated vertical plate', *J. Fluid Mech.*, vol. 59, pp. 225-237.

Catton, I 1978, 'Natural convection in enclosures', *Proc. 6th Int. Heat Transfer Conf.*, Toronto, pp. 13-31.

Cormack, DE, Leal, LG & Imberger, J 1974, 'Natural convection in a shallow cavity with differentially heated end walls. Part 1. Asymptotic theory', *J. Fluid Mech.*, vol. 65, pp. 209-229.

Cormack, DE, Leal, LG & Seinfeld, JH 1974, 'Natural convection in a shallow cavity with differentially heated end walls. Part 2. Numerical solutions', *J. Fluid Mech.*, vol. 65, pp. 231-246.

Cuckovic-Dzodzo, DM, Dzodzo, MB & Pavlovic MD 1999, 'Laminar natural convection in a fully partitioned enclosure containing fluid with nonlinear thermophysical properties', *Int. J. Heat and Fluid Flow*, vol. 20, pp. 614-623.

Daniels, PG & Patterson, J C 1997, 'On the long-wave instability of natural-convection boundary layers', *J. Fluid Mech.*, vol. 335, pp. 57-73.

Daniels, PG & Patterson, JC 2001, 'On the short-wave instability of natural convection boundary layers', *Proc. Roy. Soc. Lond.* A, vol. 457, pp. 519-538.

Davey, A 1973, 'A simple numerical method for solving Orr-Sommerfeld problems', *Q. J. Mech. Appl. Maths.*, vol. 26, pp. 401-411.

De Vahl Davis, G 1983, 'Natural convection of air in a square cavity: a bench mark numerical solution', *Int. J. Mumer. Methods Fluids*, vol. 3, pp. 249-264.

Dol, HS & Hanjalic, K 2001, 'Computational study of turbulent natural convection in a side-heated near-cubic enclosure at a high Rayleigh number', *Int. J. Heat Mass Transfer*, vol. 44, pp. 2323-2344.

Drazin, PG 2001, *Introduction to hydrodynamic stability*, Cambridge University Press, Cambridge, pp. 45-61.

Eckert, ERG, Hartnett, JP & Irvine, TF 1960, 'Flow-visualization studies of transition to turbulence in free-convection flow', *ASME Paper* 60-W-250.

Eckert, ERG & Carlson, WO 1961, 'Natural convection in an air layer enclosed between two vertical plates at different temperatures', *Int. J. Heat Mass Transfer*, vol. 2, pp. 106-120.

Elder, JW 1965a, 'Laminar free convection in a vertical slot', *J. Fluid Mech.*, vol. 23, pp. 77-98.

Elder, JW 1965b, 'Turbulent free convection in a vertical slot', *J. Fluid Mech.* vol. 23, pp. 99-111.

Facas, GN 1993, 'Natural convection in a cavity with fins attached to both vertical walls', *J. Thermophys. Heat Transfer*, vol. 7, pp. 555-560.

Fasel, H & Konzelmann, U 1990, 'Nonparallel stability of a flat-plate boundary-layer using the complete Navier-Stokes equations', J. Fluid Mech., vol. 221, pp. 311-347.

Frederick, RL 1989, 'Natural convection in an inclined square enclosure with a partition attached to its cold wall', *Int. J. Heat Mass Transfer*, vol. 32, pp. 87-94.

Frederick, RL, & Valencia, A 1989, 'Heat transfer in a square enclosure with a partition attached to its cold wall', *Int. Comm. Heat Mass Transfer*, vol. 16, pp. 347-354.

Gadoin, E, Le Quere, P & Daube, O 2001, 'A general methodology for investigating flow instabilities in complex geometries: application to natural convection in enclosures', *Int. J. Numer. Meth. Fluids*, vol. 37, pp. 175-208.

Gebhart, B 1973, 'Instability, transition, & turbulence in buoyancy-induced flows', *Annu. Rev. Fluid Mech.*, vol. 5, pp. 213-246.

Gebhart, B 1988, 'Transient response and disturbance growth in vertical buoyancy-driven flows', *J. Heat Transfer*, vol. 110, pp. 1166-1174.

Gebhart, B & Mahajan, RL 1982, 'Instability and transition in buoyancy induced flows', *Adv. Appl. Mech.*, vol. 22, pp. 231-315.

Gill, AE 1966, 'The boundary-layer regime for convection in a rectangular cavity', *J. Fluid Mech.*, vol. 26, pp. 515-536.

Goldstein, RJ & Briggs, DG 1964, 'Transient free convection about vertical plates and cylinders', *J. Heat Transfer*, vol. 86, pp. 490-500.

Guvenc, A & Yuncu, H 2001, ‘An experimental investigation on performance of fins on a horizontal base in free convection heat transfer’, *Heat Mass Transfer*, vol. 37, pp. 409-416.

Heindel, TJ, Incropera, FP and Ramadhyani, S 1996, ‘Enhancement of natural convection heat transfer from an array of discrete heat sources’, *Int. J. Heat Mass Transfer*, vol. 39, pp. 479490.

Henkes, RAWM 1990, ‘Natural-Convection boundary layers’, PhD thesis, the Delft University of Technology.

Henkes, RAWM & Hoogendoorn, CJ 1993, ‘Scaling of the laminar natural-convection flow in a heated square cavity’, *Int. J. Heat Mass Transfer*, vol. 36, pp. 2913-2925.

Herbert, T 1997, ‘Parabolized stability equations’, *Annu. Rev. Fluid Mech.*, vol. 29, pp. 245-283.

Hieber, CA & Gebhart, B 1971, ‘Stability of vertical natural convection boundary layers: some numerical solutions’, *J. Fluid Mech.* vol. 48, pp. 625-646.

Hyun, JM 1994, ‘Unsteady buoyant convection in an enclosure’, *Adv. Heat Transfer*, vol. 24, pp. 277-320.

Ichimiya, K 2000, ‘Heat transfer enhancement or depression of natural convection by a single square solid element on or separated from a vertical heated plate’, *J. Enhanc. Heat Transfer*, vol. 7, pp. 125-138.

Illingworth, CR 1950, ‘Unsteady laminar flow of gas near an infinite flat plate’, *Proc. Camb. Phil. Soc.*, vol. 46, pp. 603-611.

Imberger, J 1974, ‘Natural convection in a shallow cavity with differentially heated end walls. Part 3. Experimental results’, *J. Fluid Mech.*, vol. 65, pp. 247-260.

Inagaki, T & Komori, K 1995, ‘Heat transfer and fluid flow of natural convection along a vertical flat plate in the transition region: experimental analysis of the wall temperature field’, *Int. J. Heat Mass Transfer*, vol. 38, pp. 3485-3495.

Ivey, GN 1984, ‘Experiment on transient natural convection in a cavity’, *J. Fluid Mech.*, vol. 144, pp. 389-401.

Jaluria, Y & Gebhart, B 1973, ‘An experimental study of nonlinear disturbance behaviour in natural convection’, *J. Fluid Mech.*, vol. 61, pp. 337-365.

Jaluria, Y & Gebhart, B 1974, ‘On transition mechanisms in vertical natural convection flow’, *J. Fluid Mech.*, vol. 66, pp. 309-337.

Janssen, RJA 1994, ‘Instabilities in natural-convection flows in cavities’, PhD thesis, the Delft University of Technology.

Janssen, RJA & Armfield, SW 1996, ‘Stability properties of the vertical boundary layers in differentially heated cavities’, *Int. J. Heat Fluid Flow*, vol. 17, pp. 547-556.

Joshi, Y & Gebhart, B 1987, ‘Transition of transient vertical natural-convection flows in water’, *J. Fluid Mech.*, vol. 179, pp. 407-438.

Kim, HY, Kim, YG & Kang, BH 2004, ‘Enhancement of natural convection and pool boiling heat transfer via ultrasonic vibration’, *Int. J. Heat Mass Transfer*, vol. 47, pp. 2831-2840.

Knowles, CP & Gebhart, B 1968, ‘The stability of the natural convection boundary layer’, *J. Fluid Mech.*, vol. 34, pp. 657-686.

Kwak, HS & Hyun, JM 1996, ‘Natural convection in an enclosure having a vertical sidewall with time-varying temperature’, *J. Fluid Mech.*, vol. 329, pp. 65-88.

Kwak, HS, Kuwahara, K & Hyun, JM 1998, ‘Resonant enhancement of natural convection heat transfer in a square enclosure’, *Int. J. Heat Mass Transfer*, vol. 41, pp. 2837-2846.

Lakhal, EK, Hasnaoui, M, Bilgen, E, & Vasseur, P 1997, ‘Natural convection in inclined rectangular enclosures with perfectly conducting fins attached on the heated wall’, *Heat Mass Transfer*, vol. 32, pp. 365-373.

Le Quere, P 1990, ‘Transition to unsteady natural convection in a tall water-filled cavity’, *Phys. Fluids*, vol. 2, pp. 503-515.

Le Quere, P & Behnia, M 1998, ‘From onset of unsteadiness to chaos in a differentially heated square cavity’, *J. Fluid Mech.*, vol. 359, pp. 81-107.

Lei, C & Patterson, JC 2002, ‘Natural convection in a reservoir sidearm subject to solar radiation: experimental observations’, *Exp. Fluids*, vol. 32, pp. 590-599.

Lei, C & Patterson, JC 2003, ‘A direct stability analysis of a radiation-induced natural convection boundary layer in a shallow wedge’, *J. Fluid Mech.*, vol. 480, pp. 161-184.

Lin, NN & Bejan, A 1983, ‘Natural convection in a partially divided enclosure’, *Int. J. Heat Mass Transfer*, vol. 26, pp. 1867-1878.

Mack, LM 1984, ‘Boundary-layer linear stability theory’, *AGARD Rep.*, No. 709.

Mahajan, RL & Gebhart, B 1978, ‘Leading edge effects in transient natural convection flow adjacent to a vertical surface’, *J. Heat Transfer*, vol. 100, pp. 731-733.

Merzkirch, W 1974, *Flow Visualization*, Academic Press, New York.

Nag, A, Sarkar, A & Sastri, VMK 1993, ‘Natural convection in a differentially heated square cavity with a horizontal partition plate on the hot wall’, *Comput. Method Appl. M.*, vol. 110, pp. 143-156.

Nag, A, Sarkar, A & Sastri, VMK 1994, ‘Effect of thick horizontal partial partition attached to one of the active walls of a differentially heated square cavity’, *Numer. Heat Transfer*, Part A, vol. 25, pp. 611-625

Ooshuizen, PL & Paul, JT 1985, ‘Free convection heat transfer in a cavity fitted with a horizontal plate on the cold wall’, *Advances in Enhanced Heat Transfer*, vol. 43, pp. 101-107.

Ostrach, S 1964, ‘Laminar flows with body forces’, in *theory of laminar flows*, Princeton Univ. Press, Princeton, pp. 528-718.

Ostrach, S 1988, ‘Natural Convection in Enclosures’, *J. Heat Transfer*, vol. 110, pp. 1175-1190.

Paolucci, S & Chenoweth, DR 1989, ‘Transition to chaos in a differentially heated vertical cavity’, *J. Fluid Mech.*, vol. 201, pp. 379-410.

Partankar, SV 1980, *Numerical Heat Transfer and Fluid Flow*, Hemisphere, New York.

Patterson, JC & Armfield, SW 1990, ‘Transient features of natural convection in a cavity’, *J. Fluid Mech.*, vol. 219, pp. 469-497.

Patterson, JC, Graham, T, Schöpf, W & Armfield, SW 2002, ‘Boundary layer development on a semi-infinite suddenly heated vertical plate’, *J. Fluid Mech.*, vol. 453, pp. 39-55.

Patterson, JC & Imberger, J 1980, ‘Unsteady natural convection in a rectangular cavity’, *J. Fluid Mech.*, vol. 100, pp. 65-86.

Plapp, JE 1957, ‘The analytic study of the laminar boundary layer stability in free convection’, *J. Aeron. Sci.*, vol. 24, pp. 318-319.

Ravi, MR, Henkes, RAWM & Hoogendoorn, CJ 1994, ‘On the high-Rayleigh-number structure of steady laminar natural-convection flow in a square enclosure’, *J. Fluid Mech.*, vol. 262, pp. 325-351.

Rhee, HS, Koseff, JR & Street, RL 1984, ‘Flow visualization of a recirculating flow by rheoscopic liquid and liquid crystal techniques’, *Exp. Fluids*. vol. 2, pp. 57-64.

Said, SAM, Habib, MA & Khan, MAR 1997, ‘Turbulent natural convection flow in partitioned enclosure’, *Computers & Fluids*, vol. 26, pp. 547-563.

Schladow, SG 1990, ‘Oscillatory motion in a side-heated cavity’, *J. Fluid Mech.*, vol. 213, pp. 589-610.

Schladow, SG, Patterson, JC & Street, RL 1989, 'Transient flow in a side-heated cavity at high Rayleigh number: a numerical study', *J. Fluid Mech.*, vol. 200, pp. 121-148.

Schöpf, W & Patterson, JC 1995, 'Natural convection in a side-heated cavity: visualization of the initial flow features', *J. Fluid Mech.*, vol. 295, pp. 357-379.

Schöpf, W & Patterson, JC 1996, 'Visualization of natural convection in a side-heated cavity: transition to the final steady state', *Int. J. Heat Mass Transfer*, vol. 39, pp. 3497-3509.

Schöpf, W, Patterson, JC & Brooker, AMH 1996, 'Evaluation of the shadowgraph method for the convective flow in a side-heated cavity', *Exp. Fluids*, vol. 21, pp. 331-340.

Schöpf, W & Stiller, O 1997, 'Three-dimensional patterns in a transient, stratified intrusion flow', *Phys. Rev. Letters*, vol. 79, pp. 4373-4376.

Scozia, R, & Frederick, RL 1991, 'Natural convection in slender cavities with multiple fins attached on an active wall', *Numer. Heat Transfer*, Part A, vol. 20, pp. 127-158.

Settles, GS 2001, *Schlieren and Shadowgraph Techniques*, Springer-verlag, New York.

Severin, J & Herwig, H 2001, 'Higher order stability effects in a natural convection boundary layer over a vertical heated wall', *Heat Mass Transfer*, vol. 38, pp. 97-110.

Shakerin, S, Bohn, M & Loehrke, RI 1988, 'Natural convection in an enclosure with discrete roughness elements on a vertical heated wall', *Int. J. Heat Mass Transfer*, vol. 31, pp. 1423-1430.

Shi, X & Khodadadi, JM 2003, 'Laminar natural convection heat transfer in a differentially heated square cavity due to a thin fin on the hot wall', *J. Heat Transfer*, vol. 125, pp. 624-634.

Stiller, O & Schöpf, W 1997, 'Thermal instability of flows with a horizontal temperature gradient', *Phys. Rev. Lett.*, vol. 79, pp. 1674-1677.

Stiller, O, Schöpf, W, Patterson, JC & Shultz, A 1998, 'Effect of spatial and temporal variations of the boundary temperature on the thermal stability of horizontal flows', *Phys. Rev. E*, vol. 57, pp. 5578-5584.

Szewczyk, AA 1962, 'Stability and transition of the free-convection layer along a vertical flat plate', *Int. J. Heat Mass Transfer*, vol. 5, pp. 903-914.

Tao, J, Le Quere, P. & Xin, S 2004, 'Spatio-temporal instability of the natural-convection boundary layer in thermally stratified medium', *J. Fluid Mech.*, vol. 518, pp. 363-379.

Tasnim, SH & Collins, MR 2004, ‘Numerical analysis of heat transfer in a square cavity with a baffle on the hot wall’, *Int. Comm.. Heat Mass Transfer*, vol. 31, pp. 639-650.

Tasnim, SH & Collins, MR 2005, ‘Suppressing natural convection in a differentially heated square cavity with an arc shaped baffle’, *Int. Comm.. Heat Mass Transfer*, vol. 32, pp. 94-106.

Wright, NT & Gebhart, B 1994, ‘The entrainment flow adjacent to an isothermal vertical surface’, *Int. J. Heat Mass Transfer*, vol. 37, pp. 213-231.

Xu, F, Patterson, JC & Lei, C 2004, ‘Oscillations of the Horizontal Intrusion in a Side-heated Cavity’, *15th Australasian Fluid Mechanics Conference*, Sydney, pp. 779-782.

Xu, F, Patterson, JC & Lei, C 2005a, ‘Observation and simulation of the double layer structure of the thermal boundary layer in a side-heated cavity’, *Proc. 5th Pacific Symposium on Flow Visualisation and Image Processing*, Daydream Island.

Xu, F, Patterson, JC & Lei, C 2005b, ‘Observations of the thermal boundary layer flow along a vertical wall with a square obstruction in a side-heated cavity’, *Proc. 8th Australasian Heat and Mass Transfer Conference*, Perth (in press).

Xu, F, Patterson, JC & Lei, C 2005c, ‘Shadowgraph observations of the transition of the thermal boundary layer in a side-heated cavity’, *Exp. Fluids*, vol. 38, pp. 770-779.

Xu, F, Patterson, JC & Lei, C 2005d, ‘Simulations of the natural convection in a side-heated cavity with a square obstruction on the sidewall’, *Proc. 8th Australasian Heat and Mass Transfer Conference*, Perth (in press).

Xu, F, Patterson, JC & Lei, C 2006, ‘Experimental observations of the thermal flow around a square obstruction on a vertical wall in a differentially heated cavity’, *Exp. Fluids*, vol. 40, pp. 363-371.

Yan, D & Zhang, H 2002, ‘Buoyancy instability in the natural convection boundary layer around a vertical heated flat plate’, *ACTA Mech. Sinica*, vol. 18, pp. 126-132.

Yan, D & Zhang, H 2003, ‘Origin of turbulence in natural convection boundary layer’, *ACTA Mech. Sinica*, in Chinese, vol. 35, pp. 641-650.

Yewell, R, Poulikakos, D & Bejan, A 1982, ‘Transient natural convection experiments in shallow enclosures’, *J. Heat Transfer*, vol. 104, pp. 533-538.

Yu, E & Joshi, Y 2002, ‘Heat transfer enhancement from enclosed discrete components using pin-fin heat sinks’, *Int. J. Heat Mass Transfer*, vol. 45, pp. 4957-4966.

Yucel, N & Turkoglu, H 1998, ‘Numerical analysis of laminar natural convection in enclosures with fins attached to an active wall’, *Heat and Mass Transfer*, vol. 33, pp. 307-314.